Creating directional quantum-limited amplification using multiple parametric drives

by

Tzu-Chiao Chien

Bachelor, Tamkang University, 2008

Master, Kent State University, 2014

Submitted to the Graduate Faculty of

the Dietrich School of Arts & Sciences in partial fulfillment

of the requirements for the degree of

Doctor of Philosophy

University of Pittsburgh

2020

UNIVERSITY OF PITTSBURGH

DIETRICH SCHOOL OF ARTS AND SCIENCES

This dissertation was presented

by

Tzu-Chiao Chien

It was defended on

May 15th 2020

and approved by

Michael Hatridge, Department of Physics and Astronomy

David Snoke, Department of Physics and Astronomy

Roger Mong, Department of Physics and Astronomy

Andrew Zentner, Department of Physics and Astronomy

David Waldeck, Department of Chemistry

Dissertation Director: Michael Hatridge, Department of Physics and Astronomy

Creating directional quantum-limited amplification using multiple parametric drives

Tzu-Chiao Chien, PhD

University of Pittsburgh, 2020

One of the primary requirements for superconducting quantum information processors is high-fidelity, quantum non-demolition qubit readout. In superconducting circuits, we perform measurements with quantum-limited microwave amplifiers. These amplifiers are based on microwave cavities and powered by Josephson-junction based nonlinearities, which we drive to parametrically modulate the circuit and generate gain. However, cavity-based amplifiers generally suffer from a fixed gain-bandwidth product, a limited dynamic range, and the absence of directionality, and so they must be operated with external lossy microwave commercial components such as circulators.

Many of these limitations can be circumvented by combining multiple parametric processes in a few-mode device, in particular by combining parametric drives which produce gain and those which produce gainless photon conversion. By combining balanced gain and conversion processes between a pair of modes, we have demonstrated transmission-only, phase-sensitive, gain-bandwidth-free amplification. We have also used measurements of transmon qubits with this mode of amplification to demonstrate its practical utility. More, by combining multiple instances of imbalanced gain and conversion processes among three modes, we have realized devices with non-reciprocal, transmission-only amplification, matched ports, and a large, gain-independent bandwidth.

One of the biggest challenges in tuning multiple parametric processes is both inherent and dynamically-generated higher order nonlinearities in the device, which shift mode frequencies and parametric coupling strengths with pump power, preventing accurate balancing of the parametric processes. These can be controlled through engineering the Hamiltonian of the nonlinear element, in this thesis either a linearly-shunted Josephson Ring Modulator or SNAIL (Superconducting Nonlinear Asymmetric Inductive eLements), which for certain applied flux values can minimize or even change the sign of higher-order even nonlinearities. Additionally, we have explored a range of circuit parameters, allowing us to also control the

relative size of odd-order nonlinearities. We have developed a series of prototypes which implement these concepts, and have achieved both high-dynamic range singly pumped amplifiers, and a promising platform for multi-parametric devices. We conclude by presenting recent progress towards implementing multiple parametric schemes that generates a practical directional amplifier, and discuss the remaining obstacles to a truly ideal parametric amplifiers

Table of contents

1.0 Introduction 1

1.1 Quantum information 1

1.1.1 Quantum computers are important for reasons[1] 1

1.1.2 The role of measurement in quantum computing 2

1.1.3 Dispersive readout of a superconducting qubit 3

1.1.4 Why do we need a quantum-limited amplifier? 6

1.2 Superconducting parametric amplifiers 8

1.2.1 The state-of-the-art amplifiers 10

1.2.2 Moving towards a directional amplifiers via parametric processes . . 11

2.0 Scattering matrix description of multiple parametric amplifiers 14

2.1 Parametric amplifiers 14

2.2 Phase preserving/sensitive amplification 15

2.2.1 Phase preserving amplifiers 16

2.2.2 Phase-sensitive amplifiers 16

2.3 The scattering matrix 17

2.3.1 Semi-classical equations of motion 18

2.3.2 Basic parametric processes 19

2.3.2.1 Coherent amplification : gain 20

2.3.2.2 Photon hopping : conversion 24

2.4 Coupled mode theory 27

2.4.1 Matrix form of equation of motion 29

2.5 Examples 31

2.5.1 GC amplification 31

2.5.2 How to build a directional device 36

2.5.3 Circulator 40

[1] credit Anja Metelmann

2.5.4 An ideal directional amplifier 44
3.0 Hamiltonian engineering 52
3.1 The Josephson parametric converter 52
3.1.1 The Josephson ring modulator 53
3.1.1.1 The shunted Josephson ring modulator 54
3.1.1.2 Effects of fourth-order terms 59
3.1.2 Consideration of stray inductance and the participation ratio 64
3.1.2.1 Stray inductance 65
3.1.2.2 Participation ratio 68
3.1.2.3 Asymmetry of the ring 71
3.1.3 Circuit design 71
3.1.3.1 Single-ended microstrip JPC 72
3.1.3.2 Single-ended lumped JPC 74
3.1.3.3 Mode flow control - filter JPC 75
3.2 Superconducting Hybridized ARbitrary Cavity-based amplifier (SHARC) . 76
3.2.1 Introduction 76
3.2.2 Theory 78
3.2.3 Design 82
4.0 Experimental results 84
4.1 Evolution of shunted JPC 84
4.1.1 Meander JRM 84
4.1.2 Lightning JPM 86
4.1.3 Kinetic inductance shunted JPM 88
4.1.4 Lumped single-ended kinetic inductance shunted JPC 90
4.1.5 Lumped single-ended aluminum inductance shunted JPC 91
4.2 Measurement of Kerr terms 93
4.3 Multiple parametric processes 94
4.3.1 GC amplification 94
4.3.2 Circulator based on microstrip JPC 102
4.4 Superconducting Hybridized ARbitrary Cavity-based amplifier (SHARC) . 105

4.4.1 SHARC design . . . 106
4.4.2 A single parametric process . . . 107
4.4.3 GC amplifictaion . . . 111
4.4.4 Circulator in SHARC device . . . 112
5.0 Saturation power limitation . . . 114
5.1 Limitation due to Kerr terms . . . 114
5.1.1 Introduction . . . 114
5.1.2 Experimental data and discussion . . . 115
5.2 Optimizing JRM-based amplifiers via full Hamiltonian control . . . 119
5.2.1 Optimizing β and p . . . 119
5.2.2 JPC with third order coupling, relaxing the stiff-pump approximation 120
5.2.3 The effects of participation ratio to Kerr terms . . . 122
5.2.4 Taking advantage of Kerr terms . . . 124
6.0 Conclusions and perspectives . . . 127
Appendix A. Circuit QED . . . 130
A.1 The simple harmonic oscillator . . . 130
A.2 A nonlinear component: Josephson junction . . . 132
Appendix B. Cascaded amplifiers . . . 137
Appendix C. Eigenmodes for an N-Junction N-port Josephson junction ring 139
C.1 Examples . . . 140
C.1.1 2-Junction 2-port device: SQUID and SNAIL . . . 140
C.1.2 3-Junction 3-port device: photon lattice . . . 141
C.1.3 4-Junction 4-port device : JRM . . . 142
Appendix D. Semi-classical solution for the JPC with a single gain process 144
D.1 Third order . . . 144
D.2 Third and fourth orders . . . 148
Appendix E. Fabrication and characterization . . . 150
E.1 Dolan bridge technique . . . 150
E.1.1 Spin-coating . . . 151
E.1.2 Anti-charge layer : only for sapphire substrate . . . 152

E.1.3 Exposure and development 152
E.1.4 Metal deposition 155
E.1.5 Stripping resist 156
E.2 Fabrication details for JPCs 157
E.2.1 JRM 157
E.2.1.1 Edges of the JRM 157
E.2.1.2 Kinetic inductance shunted JRM 158
E.2.2 Microstrip JPC 160
E.2.3 Single-ended lumped JPC 161
E.3 Ambegaokar-Baratoff relation 163
Appendix F. Mathematica 165
Bibliography 172

List of tables

1 **Comparison of Hamiltonian between the mechanical and LC oscillator** 132
2 **Symbols used in circuit element of Fig. 87** 135
3 **First layer: MMA EL 13** 151
4 **Second layer: PMMA 950K A4** 152
5 **Developing recipe** 154
6 **Conditioning recipe** 156
7 **Double angle deposition** 156
8 **Stripping resist** 157
9 **Spin recipe for a thin NbTiN: PMMA 950K A4** 159
10 **Develop recipe for a thin NbTiN** 160
11 **Stripping resist** 160
12 **First layer spin recipe: LOR 5B** 161
13 **Second layer spin recipe: S1805** 162
14 **Develop recipe for MLA** 162
15 **Strip resist for MLA** 163
16 **Variables for a scattering matrix** 170

List of figures

1 **Dispersive readout.** . . . 3
2 **Ideal dispersive readout.** . . . 4
3 **Dispersive readout with higher temperature noise.** . . . 5
4 **Dispersive readout with a HEMT.** . . . 7
5 **Dispersive readout with a cascade amplification.** . . . 8
6 **Schematic of a superconducting parametric amplifier.** . . . 9
7 **Schematic of an actual experiment setup.** . . . 11
8 **Schematic of a basic amplifier.** . . . 14
9 **Phase-preserving amplification.** . . . 17
10 **Phase-sensitive amplification.** . . . 18
11 **Schematic of a typical three-mode device.** . . . 20
12 **Body diagram of gain.** . . . 22
13 **Scattering matrix of gain.** . . . 24
14 **Gain vs power.** . . . 25
15 **Body diagram of conversion.** . . . 27
16 **Scattering matrix for conversion.** . . . 28
17 **An arbitrary N-port network.** . . . 29
18 **Body diagram of GC amplification.** . . . 32
19 **Reflection and transmission of the GC amplification.** . . . 33
20 **Scattering matrix of the GC amplification.** . . . 34
21 **Bandwidth of GC amplification.** . . . 35
22 **GC gain versus normalized pump strength.** . . . 36
23 **Mach-Zehnder interferometer.** . . . 37
24 **GC amplification - paths for S_{ba}.** . . . 39
25 **Body diagram of a circulator.** . . . 40
26 **Signal flow of a circulator for S_{ba}** . . . 42

27 **Scattering matrix of a circulator.** 44
28 **Scattering matrix of a circulator with different phase.** 45
29 **Body diagram of directional amplification.** 46
30 **Scattering matrix for directional amplification.** 48
31 **Scattering matrix for ideal amplification with different κ_b.** 49
32 **An ideal amplification's quantum noise.** 50
33 **Fixed, broad bandwidth for ideal amplification.** 51
34 **Josephson ring modulator.** 53
35 **The circuit diagram for the shunted JRM.** 54
36 **The degeneracy of the ground state.** 58
37 **Gain with the presence of a Kerr.** 61
38 **Conversion with the presence of a Kerr.** 62
39 **GC with the presence of a Kerr.** 63
40 **Kerr terms for shunted JRM.** 64
41 **Linear shunted JRM with stray inductance.** 66
42 **The degeneracy of the ground state with stray inductors.** 67
43 **JRM with external inductors.** 68
44 **Third and Fourth order terms with participation ratio.** 70
45 **Asymmetry effect on the JRM.** 72
46 **Schematic circuit of a microstrip JPC.** 73
47 **Schematic circuit of a lumped JPC.** 74
48 **Filter JPC.** 76
49 **Schematic circuit of SHARC.** 77
50 **SHARC modulation.** 83
51 **Meander JRM SEM.** 85
52 **Lightning JRM SEM and Self-Kerr measurement.** 87
53 **SEM of kinetic inductance shunted JRM.** 88
54 **Kinetic inductance shunted JPM - Kerr measurement.** 89
55 **Lumped kinetic inductance shunted JPC : Fluxsweep and Kerr measurement.** 91

56 **Lumped aluminum inductance shunted JPC : Fluxsweep and Kerr measurement.** . . . 92
57 **Visualization of how to measure Kerrs.** . . . 93
58 **Aligned G and C.** . . . 95
59 **GC properties.** . . . 96
60 **Gain versus pump power.** . . . 97
61 **GC measurement setup.** . . . 97
62 **GC Histogram.** . . . 99
63 **Histogram orthogonal.** . . . 100
64 **Histogram of weak measurement protocol with optimal alignment.** . . . 101
65 **Pulse sequence for quantifying measurement back-action.** . . . 101
66 **GC and GCI.** . . . 102
67 **Reflection of the idler and signal for individual conversion.** . . . 103
68 **Circulator scattering matrix: magnitude versus phase.** . . . 104
69 **Circulator scattering matrix.** . . . 105
70 **SHARC optical/SEM images.** . . . 107
71 **SHARC resonance modulation.** . . . 108
72 **SHARC: gain.** . . . 109
73 **SHARC: conversion.** . . . 109
74 **SHARC: Degenerate gain and Conversion to SNAIL.** . . . 110
75 **SHARC: GC.** . . . 111
76 **SHARC: circulator.** . . . 112
77 **20 dB gain curve for different signal powers.** . . . 116
78 **Saturation power versus pump detuning.** . . . 117
79 $P_{\pm 1\ dB}$ **point for different pump power.** . . . 118
80 **The saturation power for the JRM-based amplifier with various JRM inductance ratio β and participation ratio p.** . . . 121
81 **Saturation power under Soft-pump condition with only third-order coupling.** . . . 122
82 **The effects of participation ratio to Kerr terms.** . . . 123

83 **Taking advantage of Kerr terms.** . . . 125
84 **Saturation hysteresis.** . . . 126
85 **Examples of harmonic oscillators** . . . 131
86 **Schematic circuit of a Josephson junction** . . . 133
87 **Schematic of branch element** . . . 136
88 **Cascaded amplification.** . . . 138
89 **Eigenmdoes of a N-Junction N-Port circuit.** . . . 140
90 **Eigenmdoe of a 2-Junction 2-Port circuit.** . . . 141
91 **Eigenmdoes of a 3-Junction 3-Port circuit.** . . . 142
92 **Eigenmdoes of a 4-Junction 4-Port circuit.** . . . 143
93 **Diagram of phase-preserving amplification.** . . . 146
94 **Saturation of gain curves with different pump detuning.** . . . 149
95 **E-beam exposure.** . . . 153
96 **Double angle deposition.** . . . 155
97 **JRM design in KLayout.** . . . 158
98 **Kinetic inductance shunted JRM design in KLayout.** . . . 159
99 **Coupling capacitor for a microstrip JPC.** . . . 161
100 **Density current measurement.** . . . 164

Acknowledgements

My enriching journey towards a Ph.D. could not have been accomplished without the help of numerous people. I would like to begin by thanking my advisor, Prof. Michael Hatridge, for giving me a chance to work in Hatlab. His enthusiasm and dedication to both research and his students has always been extremely beneficial to me. Michael gave me the freedom to be creative in coming up with new ideas for experiments and solutions. I am grateful for his continued guidance throughout my Ph.D., both academic-wise and and with life in general.

Moreover, I am indebted to my committee members, David Snoke, Roger Mong, Andrew Zentner, and David Waldeck, for taking time out of their busy schedules to guide me on my research. Because of you, I realize there is more physics to learn, and there are different approaches to the same physics problems.

I also want to thank Joe Aumentado and Katrina Cicak. I really enjoyed my time working at NIST. Mainly, I am grateful for both your time in teaching me science and patience for showing me fabrication. Getting to spend two months working at NIST will be an unforgettable memory.

For most of my Ph.D., I had the auspicious opportunity to work with three people: Gangqiang Liu, Olivia Lanes, and Xi Cao. Thank you for always being patient with my questions. Thank you, Gangqiang, for always been there when I needed help. I still remember how you stayed late multiple nights to teach me how to use the measurement equipment. Thank you, Olivia, for always being a good listener when I needed someone to talk to, and overcoming experimental challenges with me together. The truth is you are not annoying; I really enjoy working with you and sometimes you ask questions that I've never even thought about. Thank you, Xi, for teaching me coding skills and always doing me a favor when I needed it. You have such a calming and relaxed demeanor that I never felt quite as stressed when talking to you.

To Pinlei Lu, Chao Zhou, Maria Mucci, and Ryan Kaufman, thank you for a.) being responsible and helpful when lab needed an extra hand b.) being willing to listen to my

anxieties and encouraging me in a positive direction. For Pinlei and Chao, my drinking buddies, there is always a great deal of time that passes between the times we talk or get together, but it never ceases to amaze me that when we gather and after a few drinks, it feels like we can overcome every challenge.

I am also fortunate to have plenty of great friends that have also helped me along the way. Azarin Zarassi taught me plenty of fabrication tricks and discussed interesting physics with me during our daily walks to the coffee store. Chenxu Liu patiently taught me the theoretical parts of the amplifier. Edan Alpern and Sarah Motz are cheerful all the time and bring joy to the lab. People were always laughing when you were around.

Of course, I will never forget the delicious cookies/cakes/meals from Cate. Thank you for refilling our energy when we were exhausted. Also, Hank Hatridge, our little helper, who reminded us when we made a bad decision in the lab. Moreover, thanks for your bold courage in life, for example, reminding others to "get out of the way" when we are stuck at an airport gate whilst tying to board the plane.

I am also thankful to my fiance, Catherine Tsao. I am so grateful for you because you never left my side when I was going through it. You made sure that I had someone who would be with me, to hold my hand, and offer general emotional support. I don't need to tell you what I need, but you always know what it is somehow. Thank you for making time for me no matter how busy you get.

Finally, to my sister, who always make me happy and is willing to share my burden. I was delighted to have you around with me in the last few years. I got to know you better and watched you grow as an independent person. To my parents, who have always believed in me and supported me, you are the reasons for who I am today. Thank you for your unconditional love, and I really love you too.

1.0 Introduction

1.1 Quantum information

1.1.1 Quantum computers are important for reasons[1]

Although classical computers have increased tremendously in speed, many computing problems will forever remain out of reach as they require exponential resources of time and hardware. The classic example of such a problem is decomposing a composite prime number into a product of smaller prime numbers, which is the basis of several important cryptosystems, including RSA [1]. In 1994, Peter Shor demonstrated that prime factorization could be solved efficiently (that is with polynomial resources) on a quantum computer [2]. From another perspective, many physicists have been inspired to study quantum computing based on Richard Feynman's 1992 suggestion: simulating quantum mechanical systems on computers that are themselves quantum mechanical [3].

The massive advantage of quantum computation is that the information content of a register of quantum bits can be entangled, but cannot be copied like classical information. Instead, the two objects are inseparably linked together with information that does not live in any one individual object [4]. Through quantum operations, one can create this entanglement and use it for various applications, such as the speeding up of certain classical computations like Shor's and Grover's algorithms [2, 5], or the realization of quantum teleportation of an independent qubit [6, 7, 8, 9]. The reason that entanglement can be achieved is due to the peculiar property of quantum mechanics: state superposition, which means the information can be represented by both 0 and 1 at the same time. The objects that store this information for quantum computers to process are called quantum bits, or qubits, which are the fundamental component for constructing quantum computers.

A variety of architectures for well characterized qubits have been proposed, including 'natural' quantum systems such as the spin of electrons or nuclei, atomic transitions, or

[1] credit Anja Metelmann

ions [10, 11, 12, 13]. However, the main difficulty of these implementations lies in increasing the coupling strength of qubits while maintaining their intrinsically long lifetimes. Another popular other platform is based on microwave frequency superconducting circuits. Qubits with this approach, often refereed to as superconducting qubits, arise from the macroscopic behavior of the electromagnetic modes of modes formed linear components (inductors, capacitors, transmission lines) together with the nonlinear Hamiltonian of Josephson junctions [14]. These systems are extremely flexible, a sort of 'quantum building block' system in which we can form all parts of our quantum circuits, starting with the qubits themselves, but also including readout and control circuits, from the same set of basic parts. More, superconducting qubits are easily coupled together via electrical components like inductors or capacitors, but also conveniently scaled for fabrication into large systems, and increasingly long-lived. For these reasons, superconducting qubits are leading the race to build a large-scale quantum computer [15, 16].

1.1.2 The role of measurement in quantum computing

To construct a reliable large-scale quantum computer, scientists follow the DiVincenzo criteria [17], which consist of five conditions, one of which is a qubit-specific, measurement capability. For flawless, theoretical machines, the requirements place on the properties and quality of measurement are rather flexible. However, any realistic device will be plagued by errors. Given the analog, continuous nature of quantum bits, the errors can also be continuous and on any part of the machine. Fortunately, we can combat these errors without losing the quantum computer's computational advantage via error correction. In an error corrected machine, add additional components to the machine, and interleave computation with a series of measurements which force the errors on the machine to be local and digital (that is the either have occured or not) [18].

This in turn requires us to carefully construct measurements on the observables of qubits without distorting or destroying the qubit state. As an example, readout of a typical superconducting qubit with a massive detecting tone, about 50000 photons, the cavity reaches a qubit-state-dependent 'bright' (or not) depending on the qubit's state. Such read out can

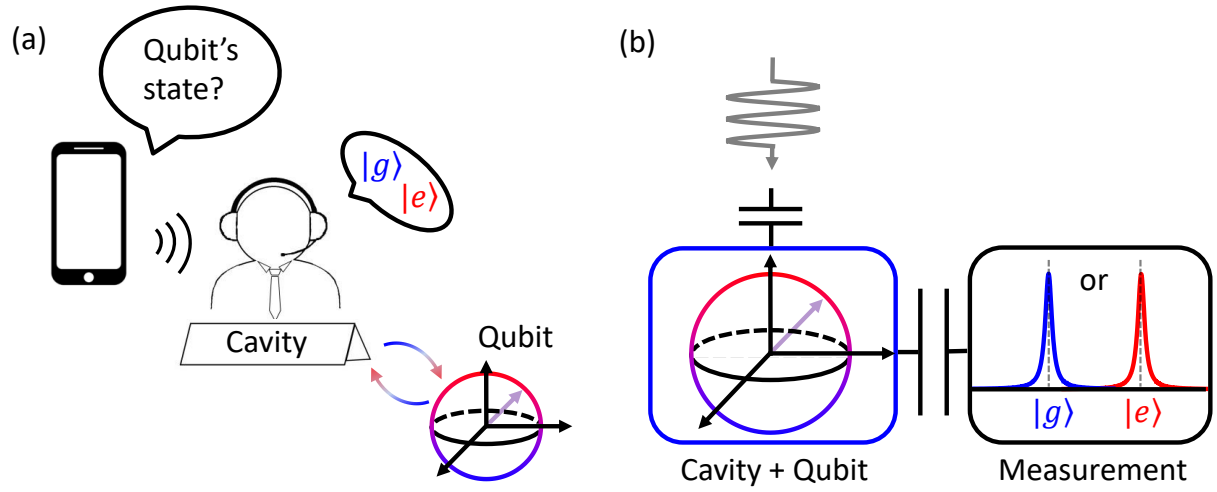

Figure 1: **(a) A cartoon picture of dispersive readout.** In this scheme, the experimenter interrogates the cavity to gain information about the qubit's state without direct contact/energy exchange with the qubit. **(b) Dispersive cavity shifts.** The underlying Hamiltonian for our qubit readout is a state-dependent shift of the cavity's frequency based on the qubit state.

readily be distinguished with high fidelity even in the absence of high-quality amplification. However, the qubit is also excited in the process to an higher, unknown state, and so the state of the qubit cannot be acted back on or corrected [19]. Instead, we need measurements which allow us to know the qubit's state after measurement (also known as Quantum Non-demolition, or QND readout [20]. More, the quantum measurement must work in a single 'shot' so we can determine whether errors have occured in real time. Achieving such readout in superconducting qubits is the primary focus of my thesis.

1.1.3 Dispersive readout of a superconducting qubit

We usually model superconducting qubits as two-level systems, although most have many more levels which can be utilized [21]. These two levels are the ground and excited states, labeled $|g\rangle$ and $|e\rangle$ respectively. Typically, we place a superconducting qubit inside a mi-

crowave cavity, which serves to protect the qubit's information from leaking to the outside world and acts like a customer service representative who reveals the qubit's information only when it receives requests, see Fig. 1 (a). With this measuring mechanism, one will never "talk to" and relax or excite the qubit directly with readout, but can still gain information through the cavity. It is an ideal measurement technique, as it allows accurate qubit measurement in which the qubit's state can be fully known from the measurement outcome. This type of measurement is called dispersive readout, and is the most common method to assess the superconducting qubit's state, see Fig. 1 (b).

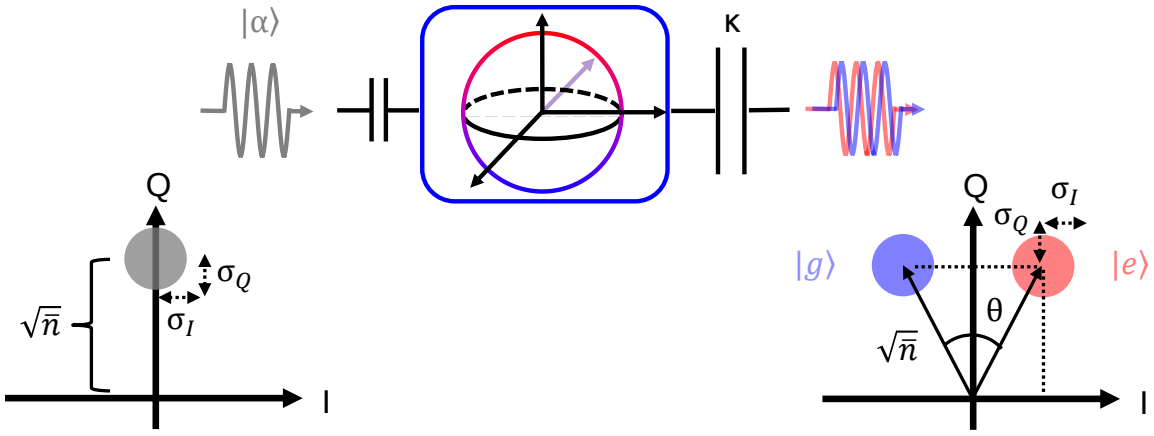

Figure 2: **Ideal dispersive readout.** A coherent input signal travels into a cavity-qubit system and is entangled with the qubit's state. It exits the cavity from the strongly coupled port and is subsequently detected by observers. The act of observing the output state collapses the entangled state which both changes the qubit state and leaves the observer with the information (here the I-quadrature component) indicating the qubit's new state (a basic QND quantum measurement).

The dispersive coupling between the cavity and qubit is achieved by a combination of dipole-dipole interaction and deliberate detuning between the two objects. If the qubit is in a definite state, then the microwave pulse will interact with the cavity whose frequency is shifted (or not). The amount by which the cavity's frequency shifts is parametrized by dispersive shift, χ. The cavity is coupled to the outside world through two capacitors.

Normally, we tend to send in a detecting coherent state, $|\alpha\rangle$ with strength $\sqrt{\bar{n}}$, from the weak capacitor (which is small enough that negligible output signal leaves by this port) and collect the outgoing wave from the strong capacitor, which sets the total bandwidth, κ, of the cavity. The outgoing state can be plotted in a vector space denoting the outgoing pulse's amplitude and phase, which is often called I-Q space, see Fig. 2. In general, the qubit will be in a superposition state, and the light becomes entangled with the cavity's state as it transits the cavity. A 'measurement' occurs when the pulse is either amplified and decoded, or, more likely, suffers loss/damage which allows an external observer to gain information about the pulse.

For measurements based on coherent states of microwave light, the microwave pulse itself has inherent Heisenburg uncertainty σ in both I and Q quadratures due to quantum fluctuations. This noise is typically defined as having a variance of 1/2 photon at the drive frequency [22]. For a projective measurement, which projects the qubit unambiguously onto $|g\rangle$ or $|e\rangle$, then the strength of the pulse, together with the dispersive shift, must be large enough to distinguish the two outcomes.

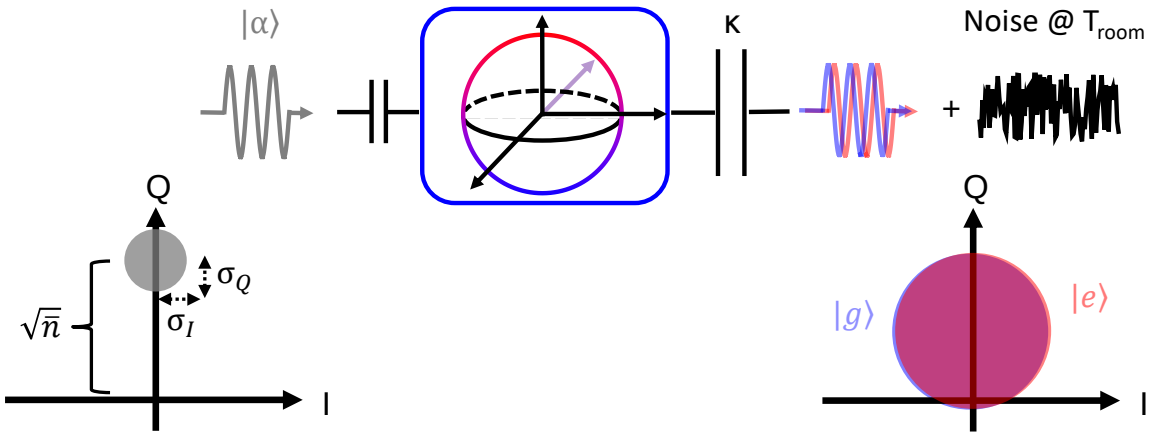

Figure 3: **Dispersive readout with higher temperature noise.** The output signal that travels to room temperature adds thermal noise which makes it difficult to distinguish between the ground and excited states.

However, an actual experiment contains lossy components through which the signal must

pass. This adds additional noise to the signal, which enlarges the output distribution in I-Q space, and shrinks the signal strength, meaning it moves the circle towards to the origin. Splitting (or misrouting) part of the output signal has a similar effect, as it leaks some information to the environment, as if there were other observers. For a successful measurement, the weak (few-photon) qubit signal has to reach detectors at room temperature, which add room temperature noise that is orders of magnitude larger than the quantum noise. Due to all these effects, the ground and excited state distributions in I-Q space can very easily overlap with each other and become unrecognizable, as in Fig. 3.

1.1.4 Why do we need a quantum-limited amplifier?

Therefore, we need to process our readout pulse to render it robust against losses and noisy electronics. An easy way is to amplify the signal with commercial amplifiers. For cryogenic microwave signals, the best semiconductor amplifiers are so-called high-electron-mobility transistor (HEMT) amplifiers [23], which contribute about 40 dB amplification along with tens of photons of noise. This process provides enough gain to suppress further noise contributions from the rest of the readout chain, but it is still degrading the readout SNR by a factor of 50-100, see Fig. 4. In the schematic figure, the signal magnitude increases by $\sqrt{G}$, which is the amplification from the HEMT. However, at the same time, HEMT noise is also introduced into the signal.

Fortunately, however, we can do much better than a commercial HEMT amplifier. Caves has determined that there is a quantum limit on the performance of a phase-preserving amplifier (that is an amplifier which amplifies all input signals equally) [22]. In Caves' limit, the amplifier adds half of a photon at the signal frequency, doubling the noise power of the input signal. Such an amplifier is referred to as 'quantum limited'. Using a quantum-limited amplifier as the first stage in a cascade amplification system, see Fig. 5, the dominant noise is a half of a photon when the quantum-limited amplifier supplies enough gain, typically around $G_1 = 100$, see Appendix B if the following amplifier is a state-of-the-art cryogenic HEMT. It is also possible to amplify one quadrature of a signal noiselessly (say I) at the cost of squeezing away information in the orthogonal quadrature Q, which is known as 'phase-

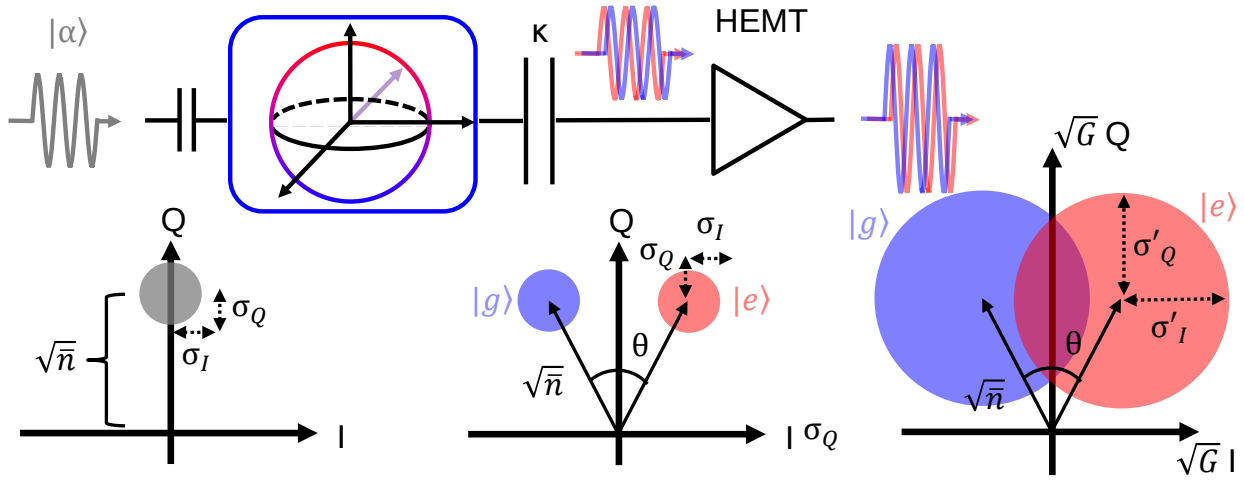

Figure 4: **Dispersive readout with a HEMT.** HEMT provides about 40 dB gain along with tens of photons of noise. A single amplification process is still not good enough to distinguish states. Here $\sigma'_{\mathrm{I,Q}} = \sqrt{(\sigma^2_{\mathrm{I,Q}} + \sigma^2_{\mathrm{HEMT}})}$

sensitive' amplification. At first glance, it should appear that phase-sensitive amplification has the edge due to its lower added noise. However there are practical issues, such as the need to stabilize the amplified quadrature and measurement phases, as well as the inability to distinguish three or more states that do not lie in a line in I-Q space that tend to counteract much of this advantage. As a result, both kinds of amplification are common in superconducting circuits, and both are realized in this thesis.

With this readout setup, we can perform some experiments that were once considered only possible as thought experiments, such as observing quantum jumps [24, 15], individual quantum trajectories [25, 26, 27, 28] and single shot feedback [29, 30, 31], as well as probing the back-action of individual weak measurements [32]. However, the need for ever-higher readout fidelities and ever-larger qubit counts in large-scale quantum machines make quantum-limited amplifiers a very active area of research.

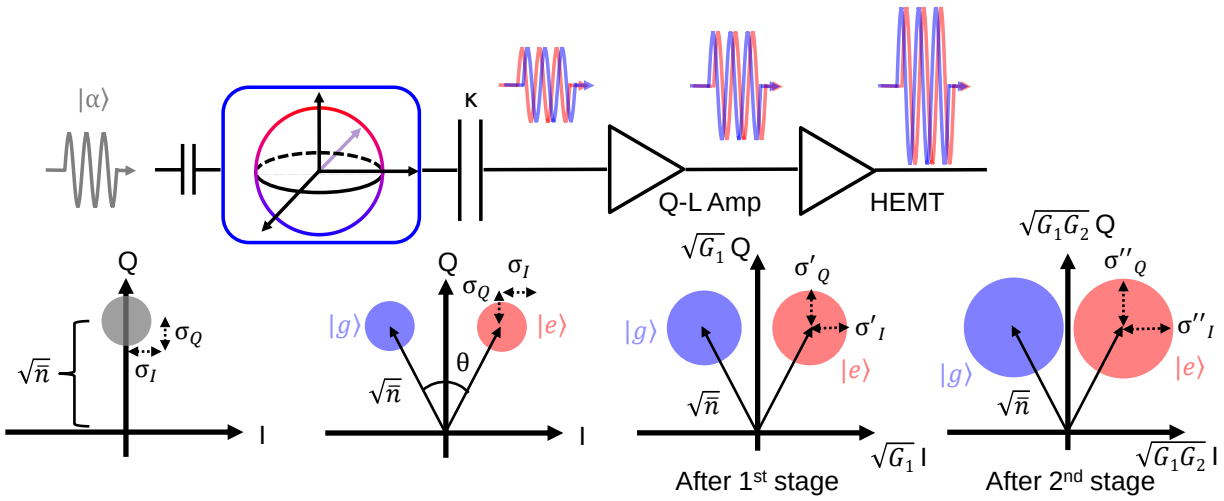

Figure 5: **Dispersive readout with a cascade amplification.** This schematic shows the noise power at different amplification stages. The signal that comes out from the quantum-limited amplifier only has a half of photon of noise, which dominates the overall noise when the quantum-limited amplifiers provide enough gain, $G_1 = 100$.

1.2 Superconducting parametric amplifiers

To obtain a quantum-limited amplifier at microwave frequency, we need a device in close proximity with the qubits (at the bottom stage of a dilution refrigerator at 10 mK) without dissipating heat; Hence, a superconducting amplifier is required. The amplifier must contain non-linear elements to generate the gain process, but again these must be dissipation free, and so are most commonly a Josephson-junction [33, 34, 35], or occasionally a kinetic inductive element [36, 37] or mechanically compliant element [38, 39]. This non-linear element can be thought of as the equivalent of a transistor in a more common, room-temperature amplifier. In such an amplifier (for instance one based on field-effect transistors or FETs) linear amplification is produced when a conductive channel between the source and drain is activated by a DC voltage applied to the device. In other words, the gain process is stimulated by the bias DC voltage.

In a superconducting amplifier, we avoid DC voltages and their concomitant dissipation.

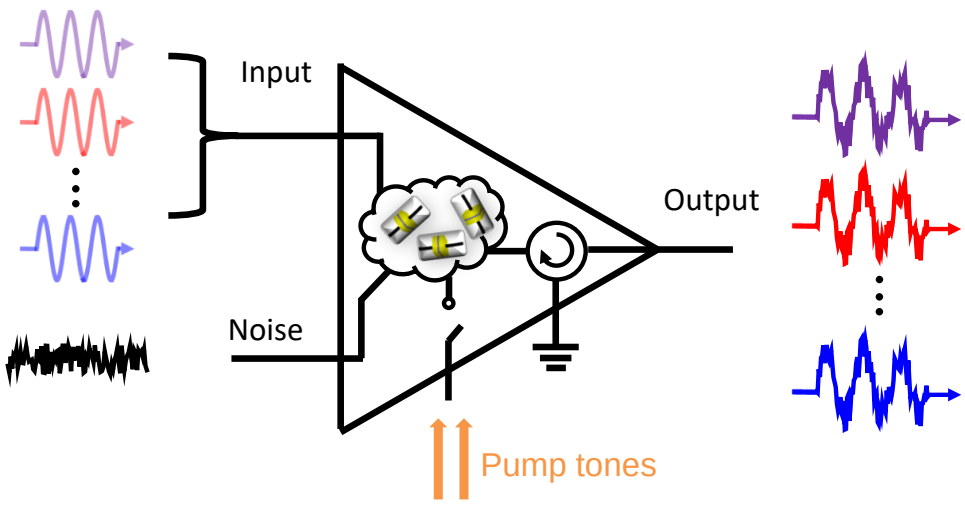

Figure 6: **Schematic of a superconducting parametric amplifier.** An ideal superconducting parametric amplifier can process multiple signals with directional amplification triggered by pumps. The amplified signals only have the minimum amount of noise allowed by quantum mechanics.

Instead, we carefully design a microwave circuit that contains several Josephson junctions and creates the desired Hamiltonian terms, which is similar to the conductive channel in a FET amplifier. Instead of activating the channel with a bias DC voltage, we apply pump tones at specific frequencies to trigger the gain process. An amplifier which generates gain with pumps applied off resonantly to modulate its dynamics is called a parametric amplifier.

Ideal superconducting parametric amplifiers (as pictured in Fig. 6) are operated at temperatures close to absolute zero Kelvin so that Boltzmann energy is small compared to the ground state energy, $k_B T \ll \hbar\omega/2$, so that it's microwave modes start in the ground state, with only quantum fluctuations present. The input port of the amplifier is impedance matched to the transmission line responsible for carrying a weak microwave signal so that no reflection occurs at the same port. By doing so, the input signal embedded with qubit information will not be reflected back to its source, which would have potential negative consequences otherwise.

Furthermore, the amplification process occurs only in a single direction from the input to

the output ports. Also, these amplifiers ideally possess the ability to process multiple (different frequency) signals simultaneously. At present, many have proposed different circuits to build ideal superconducting parametric amplifiers. Their pros and cons will be discussed in the following subsections.

1.2.1 The state-of-the-art amplifiers

Presently, there are two broad categories of superconducting parametric amplifiers: those based on discrete microwave resonances, so-called cavity-based amplifiers, and those based on non-linear transmission lines, so-called traveling-wave parametric amplifiers (TWPAs). We can analyze the functionality of these amplifiers with many of the same parameters. These include the amplifier's quantum efficiency, which describes the noise added during amplification, tunability to match the signal of interest, and instantaneous bandwidth. We also look at the ability to process large amplitude signals, which is typically referred to as the saturation power, or more precisely as $P_{\text{-1 dB}}$, the input power at which the gain falls by 1 dB from its small signal value.

TWPAs are based on a microwave nonlinear transmission line architecture, such as a long kinetic inductance [40, 36] or a periodically repeated section including Josephson junctions [41, 42]. TWPAs can achieve over 3 GHz bandwidth with decent saturation power, on average -95 dBm, and high gain in a single direction. However, they typically adds noise at least $3-4$ times higher than the standard quantum-limit [41, 42].

The other major implementation of nearly quantum-limited parametric devices are cavity based amplifiers containing Josephson junctions, such as Josephson parametric amplifiers (JPAs) [43, 44, 35, 45] and Josephson parametric converters (JPCs) citeBergeal2010a, Bergeal2010. However, these cavity-based amplifiers have saturation power averaging about -120 dBm [46], limited bandwidth of usually less than 100 MHz, and work in reflection. They do, however, achieve a very-nearly quantum limited performance adding $1-2$ times the standard quantum limit [41]. While this difference may not seem exciting compared to TWPAs, the fidelity of reaodut is exponential in the added noise and so factors of two can mean orders of magnitude increases in fidelity.

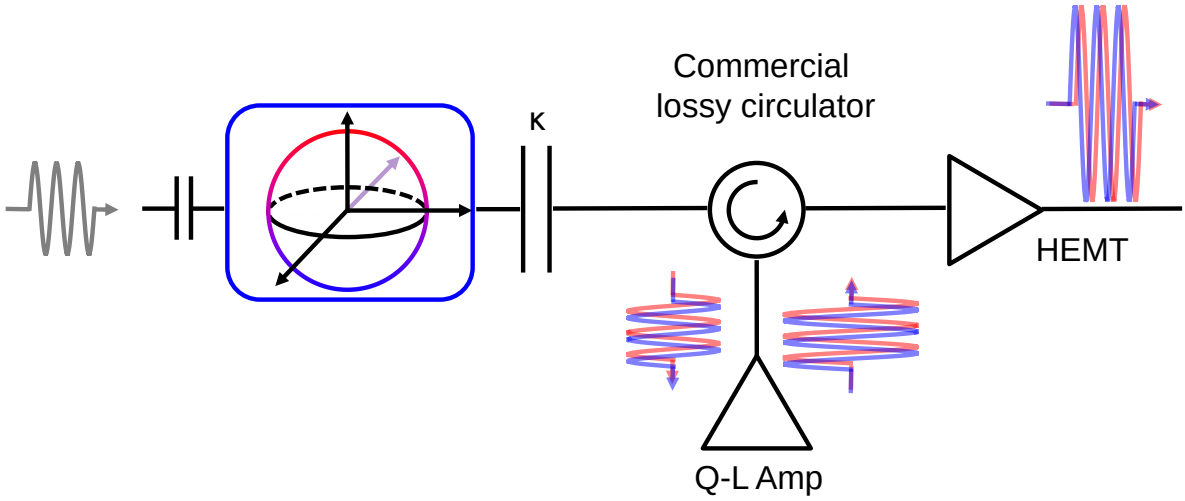

Figure 7: **Schematic of an actual experiment setup.** A schematic measurement setup with a cavity-based amplifier, which required a commercial lossy circulator because the amplifier works in reflection.

Both types of amplifiers require non-reciprocal commercial devices like circulators and isolators for delicate qubit measurements. TWPAs in practice need isolation at the input port since the reflected pump tone and the amplified signal would travel back to the qubits. Similarly, cavity-based amplifiers use circulators for much the same reason, and to also separate input from output because they work in reflection, see Fig. 7. To increase quantum efficiency, lossy and bulky microwave components really should be eliminated. Therefore, a truly directional amplifier which can be operated while directly connected to a qubit/cavity system is a major goal.

1.2.2 Moving towards a directional amplifiers via parametric processes

To build a directional device, like a circulator, one usually uses the Faraday effect induced by large magnetic fields [47] that are incompatible with superconducting devices. Fortunately, people have found that parametric processes can provide equivalent interference and nonreciprocity when we combine several parametric processes in a single de-

vice [48, 49, 50, 51, 52, 53, 54]. For instance, without applying large external magnetic fields, a three-moode, three-port superconducting cavity-based device performs like a circulator when three parametric processes are applied to it [55, 50, 53]. Recently, Metelmann and Clerk have found a pumping scheme to achieve a directional amplifier via parametric processes by introducing an ancillary mode, which is used to absorb the reverse amplified signal and prevent it from traveling into the quantum objects of interest [48, 49].

In this thesis, one major objective is to master building multiple-parametrically coupled devices to realize a directional quantum-limited amplifier. We start by examining how to calculate basic properties of multi-mode, multiply-driven circuits in in Chapter 2. We examine the performance of a number of combinations of modes and pumps which achieve directionality, or other desired features such as gain-independent broad bandwidths.

Furthermore, parametric processes rely on precise control of the Hamiltonian. Any undesired Hamiltonian terms increase the difficulty of operating the device. A common example is fourth-order (Kerr) terms which shift the amplifiers modes as we apply pump tones and complicate device operation. We have developed a generic superconducting circuit analysis that can used for designing the circuit Hamiltonian, see Chapter 3. Using the Josephson Parametric Converter (one of Hatlab's favorite amplifiers) as an example, we exclude Kerr terms by applying a particular external flux through the device. Furthermore, we examine how linear components such as superconducting traces can be used to realize a practical device and modify the Hamiltonian to optimize device performance.

We have also designed a new cavity-based amplifier, Superconducting Hybridized ARbitrary Cavity-based amplifier (SHARC), that is easier for both Hamiltonian engineering and fabrication, as detailed in Chapter 3. Unlike typical parametric amplifiers, SHARC distributes non-linearity between modes by modestly hybridizing linear resonators to a single non-linear mode. The three-wave coupling, which is the source of the amplification process, is not only controlled by the non-linear element but also the strength of hybridization, which provides enormous flexibility in terms of circuit design. We also prove that the SHARC can readily be fabricated and is a very exciting new platform for multiple-parametric processes by demonstrating an array of multi-parametric modes of operation.

In Chapter 5, we have identified a multitude of terms in the Hamiltonian that limit

saturation power. We also detail an optimization method to improve saturation power through circuit engineering which carefully balances the multiple sources of limited power handling in the amplifier. Through the optimization, we regulate the system in such a way that the higher-order Hamiltonian terms, which are both inherent and pump-generated, collaborate and establish exceptional saturation performance.

To conclude, a parametric process to create directional amplification is discussed along with its operating conditions. The process is not limited to superconducting circuits, but can also be applied to optical, mechanical or any three-mode system with desired coupling terms. This implies the quantum information from a superconducting qubit system can be manipulated, amplified, and transferred to other quantum computing platforms, such as optical photons, that have advantages like long distance teleportation [56, 57]. Furthermore, a generic way of analyzing a superconducting circuit is discussed to optimize circuit performance through full Hamiltonian control. This includes improving saturation power; hence, an amplifier for strong input signal processing is possible.

Although we have not yet realized our ideal amplifier, we have made a great deal of progress during my PhD. We have built a number of practical amplifiers and used them to demonstrate high fidelity qubit readout. My amplifiers are in use across the lab, and are currently enabling many quantum-information experiments. We have also made great progress in understanding how to think of devices with a large number of microwave modes and drives, and how to engineer the overall Hamiltonian for good performance. It is my hope that the SHARC will soon allow us to demonstrate practical directional amplification, and in turn, push forward the quest for large-scale quantum information processors.

2.0 Scattering matrix description of multiple parametric amplifiers

2.1 Parametric amplifiers

Routinely, we use electronic devices in all aspects of life to enhance the strength of small electronic signals; for instance, increasing the volume of an audio signal in a cellphone. A circuit that produces an increased version of its input signal is called an amplifier, which can be thought of as a simple box containing some nonlinear components, such as Field Effect Transistors (FET) [58]. FETs have the ability to generate an output signal that is much larger than the input, see Fig. 8 (a). The extent of increase of a signal is the amplification factor or gain (G), which is the signal ratio between output and input powers.

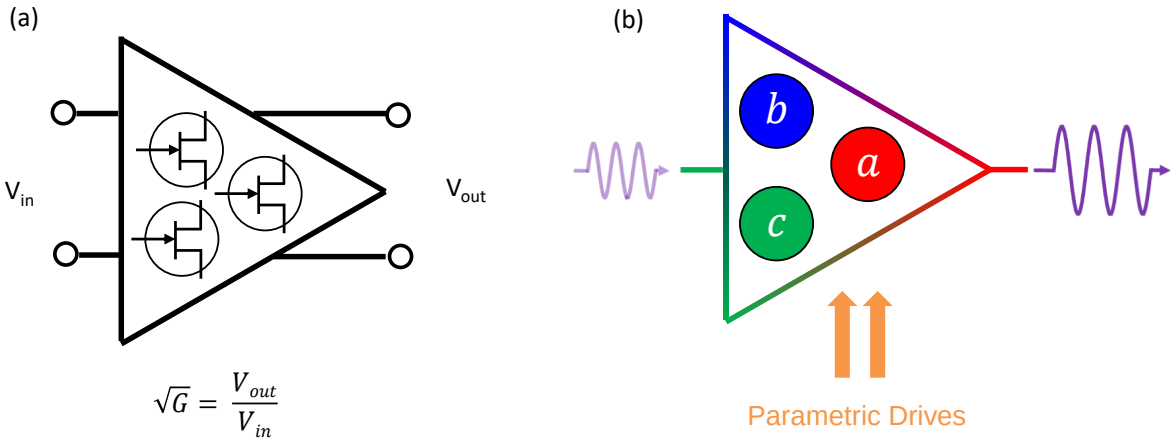

Figure 8: **(a) A schematic of a FET-based amplifier.** The output signal power, which is amplified in a circuit containing FETs, is G times larger than that of input signal power. **(b) A schematic of a cavity-based parametric amplifier.** A three-cavity parametric device amplifies an input signal through parametric processes, which is activated by the parametric drives.

In the superconducting circuit, the block contains a few linear and non-linear modes, the

latter of which contains Josephson junctions as the source of non-linearity [14]. Amplification occurs when pump waves activate parametric non-linearity inherent inside the circuit. This process can be thought of (maybe not so helpfully) as modulating an element's value in the circuit. The canonical example of parametric pumping is a child who kicks their legs on a swing twice per cycle, effectively modulating the length of a (inherently non-linear) pendulum at the right frequency to produce larger oscillations. Thus, we call these types of devices based on non-resonant driving of a nonlinear Hamiltonian 'parametric' amplifiers (paramps) [59].

Parametric amplification can be achieved through either three-wave or four-wave mixing. For three-wave mixing amplification, three electromagnetic waves, pump, signal, and idler, are involved in the interaction, which satisfied the conservation of energy [34, 60, 46]. When both signal and idler do not have the same frequency, the process is referred to as non-degenerate parametric amplification process while a degenerate parametric process produces signal and idler at the same frequency.

Four-wave mixing amplification involves two pump photons converted into one signal and one idler photon [61, 62]. However, four-wave mixing uses fourth-order terms in the Hamiltonian. This circumstance causes problems with configuring parametric processes and limit the performance of paramps, as driving the system causes its frequency to change [35, 63]. Therefore, in this study, the focus is on creating paramps through three-wave coupling terms, though even in these amplifiers the presence of fourth-order terms can cause similar problems, as discussed later in Chapter 3 and 5.

2.2 Phase preserving/sensitive amplification

The most significant advantage of superconducting circuits is that they are dissipation-free and easy to engineer, which makes it possible for superconducting amplifiers to achieve quantum-limited operation [22]. In the past few years, people have proposed different types of superconducting circuits to build quantum-limited amplifiers [34, 64, 35, 65], which allow us to perform experiments that were once only believed possible as thought-experiments [66].

There are two operation modes for paramps, phase-preserving and phase-sensitive, which are determined by what parametric processes are implemented on the device. In phase preserving amplification, the signal does not depend on the relative pump and signal phase, while in phase sensitive amplification one quadrature is amplified while the other is squeezed away.

It is tempting to identify Hamiltonian terms which lead to each of these processes. However, as we will show at length, combining multiple parametric drives in a single device can result in devices where the 'gain' process by itself is phase preserving, but the actual gain produced is phase sensitive, and so we will not try to categorize Hamiltonian terms by gain type.

2.2.1 Phase preserving amplifiers

Amplification is a crucial part of quantum measurements whereby a weak signal is amplified to a detectable level. However, the performance of an amplifier also depends on noise. In the high-gain limit, a phase-preserving amplifier must broaden the output distribution by at least half a quantum (when referred back to its input) at the operating input frequency [67, 68].

Phase-preserving amplification enlarges a coherent input signal with amplitude α, where $\alpha = \sqrt{\bar{\mathrm{I}}^2 + \bar{\mathrm{Q}}^2}$, by amplitude gain $\sqrt{\mathrm{G}}$, where G is the power gain. The noise, symbolized by standard deviation σ, represented as a circle, increased more than $\sqrt{\mathrm{G}}$. Half a photon of additional noise is added into the signal and the radius of circle becomes $\sqrt{\mathrm{G}(\sigma_{\mathrm{I,Q}}^2 + 1/4)}$, see Fig. 9.

2.2.2 Phase-sensitive amplifiers

A coherent input state, on the other hand, will become a squeezed state after phase-sensitive amplification, see Fig. 10. One quadrature of the input signal will be amplified/deamplified depending on pump phase. Added noise to the two quadratures is also affected by this process [69]. For this reason, phase-sensitive amplifiers can reduce quantum noise with squeezing. Also note that $\sigma_{\mathrm{I}}\sigma_{\mathrm{Q}} = \sqrt{\mathrm{G}}\sigma_{\mathrm{I}}\frac{1}{\sqrt{\mathrm{G}}\sigma_{\mathrm{Q}}}$, which means that an ideal

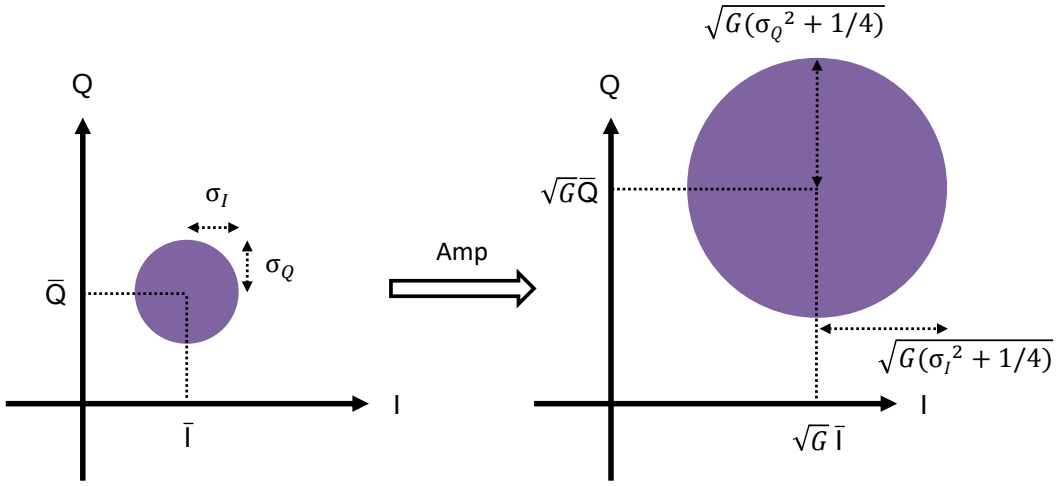

Figure 9: **Phase-preserving amplification.** The coherent input signal centers at $(\bar{\mathrm{I}}, \bar{\mathrm{Q}})$ with a noise disk with standard deviation $\sigma_{\mathrm{I}} = \sigma_{\mathrm{Q}}$. The amplification process enlarges both quadratures. This results in an output signal at the center $(\sqrt{G}\bar{\mathrm{I}}, \sqrt{\mathrm{G}}\bar{\mathrm{Q}})$.

phase-sensitive amplification process preserves the total amount of noise, in contrast to the noise added from phase-preserving amplification. To operate a phase-sensitive amplifier in experiments, one needs to stabilize the pump phase carefully, since which input quadrature is amplified ispump phase-dependent.

2.3 The scattering matrix

Scattering matrices (S-parameters) are based on the concept of incident and exiting waves. By using incident and exiting waves, a linear network can be characterized by a set of simultaneous equations describing the exiting waves from each port in terms of the incident waves at all the ports. The constants that characterize the network under these conditions are called S parameters. To derive these S matrices, we start from the Hamiltonian and the Quantum Langevin equation, then use the input-output relations to obtain the final result.

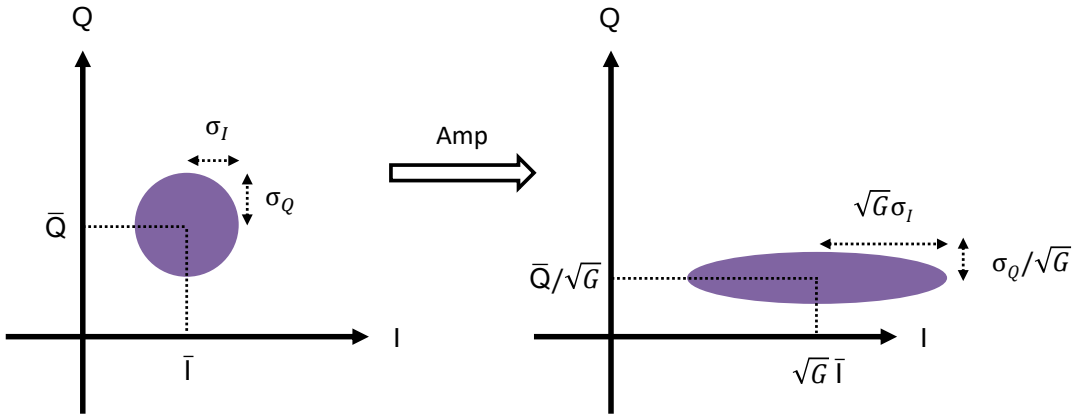

Figure 10: **Phase-sensitive amplification.** The input signal centers at $(\bar{\mathrm{I}}, \bar{\mathrm{Q}})$ and a noise disk with standard deviation $\sigma_{\mathrm{I}} = \sigma_{\mathrm{Q}}$. The amplification process enlarges one quadrature, here I, and deamplifies it along the other. This results in an output signal at the center $(\sqrt{\mathrm{G}}\bar{\mathrm{I}}, \bar{\mathrm{Q}}/\sqrt{\mathrm{G}})$ and a noise disk with standard deviation $\sqrt{\mathrm{G}}\sigma_{\mathrm{I}}$ and $\sigma_{\mathrm{Q}}/\sqrt{\mathrm{G}}$.

2.3.1 Semi-classical equations of motion

Quantum-limited amplifiers can be described by the Hamiltonian of a system and analyzed both classically and quantum mechanically. Some proposals and experiments have proved that amplifiers can perform quantum mechanically [70, 71]. It is also fundamentally interesting to study the classical behavior of the devices. The approach is to start by writing the Heisenberg-Langevin equation for operators, $\hat{o}$:

$$\frac{d\hat{o}}{dt} = \frac{i}{\hbar}[\hat{\mathrm{H}}, \hat{o}] - \frac{\kappa}{2}\hat{o} + \sqrt{\kappa}\,\hat{o}_{\mathrm{in}}(t) \tag{2.1}$$

where $\hat{\mathrm{H}}$ is the Hamiltonian of the system, k is the resonator linewidth (assuming internal loss is negligible), and $\hat{o}_{\mathrm{in}}$ is the propagating field coming into the circuit. Since the modes are bosonic modes, then $[\hat{o}, \hat{o}^{\dagger}] = 1$ has to be satisfied. An internal loss-free system is assumed in this case. Eq. 2.1 shows the usual Heisenberg equation of motion as the first term on the

right-hand side, and the damping term introduced by the coupling between the circuit and the transmission line as the second term on the right. The incoming wave is described by the last term.

To realize the results in the lab frame, one needs to link the circuit's incoming/outgoing waves through the internal signal, which is called input-output theory and is expressed as

$$\hat{a}_{\text{out}} + \hat{a}_{\text{in}} = \sqrt{\kappa_{\text{a}}}\hat{a} \tag{2.2}$$

The semi-classical equation of motion that associates incoming and outgoing waves is derived by combining Eq. 2.1 and Eq. 2.2. To construct the full scattering matrix, $2N$ equation of motions are required, where N is the number of circuit modes. In an extensive system, this derivation becomes complicated and challenging, but still solvable. An example will be discussed in the next subsection followed by the matrix derivation of the equation of motion, which is much easier to construct than the scattering matrix [55].

2.3.2 Basic parametric processes

There have been a number of different proposals and calculation methods to multiple parametric processes, including the schemes discussed in the current work, to produce constructive or destructive interference generate desirable amplifier properties [48, 49, 50, 51, 52, 53, 54]. In our derivation, based on extensive conversation with Joe Aumentado and his work [51], we can accommodate all of these proposals, and base our analysis on simple gain processes as discussed above, together with gainless photon conversion between microwave modes.

We start with a general three-mode system, with the three eigenmodes having distinct frequencies. The circuit is designed in such a way that three modes are coupled to each other through a three-wave mixing element, which provides the desired coupling Hamiltonian $H_{\text{coupling}} \propto \Phi_a\Phi_b\Phi_c$. The detail of how a coupling Hamiltonian is generated will be explained in section 3. As we have discussed in Appendix A, the coupling Hamiltonian can be expressed

as a function of creation and destruction operators. Hence, we obtain

$$\frac{H_{\text{coupling}}}{\hbar} = g_{\text{abc}}\left[\left(\hat{a}+\hat{a}^{\dagger}\right)\left(\hat{b}+\hat{b}^{\dagger}\right)\left(\hat{c}+\hat{c}^{\dagger}\right)\right] \tag{2.3}$$

where g_{abc} (a.k.a. g_3) is the inherent (bias flux-dependent) three-wave mixing strength.

Parametric processes are powerful tools because one can choose terms from H_{coupling} to operate on and eliminate others. Because of this, one can engineer a Hamiltonian of choice with parametric processes. In this section, the basic parametric processes will be discussed followed by constructing a directional amplifier with multiple parametric processes.

From this point forward in this dissertation, I will drop the "hats" on the operators when it is clear from context that it is an operator and not a complex number.

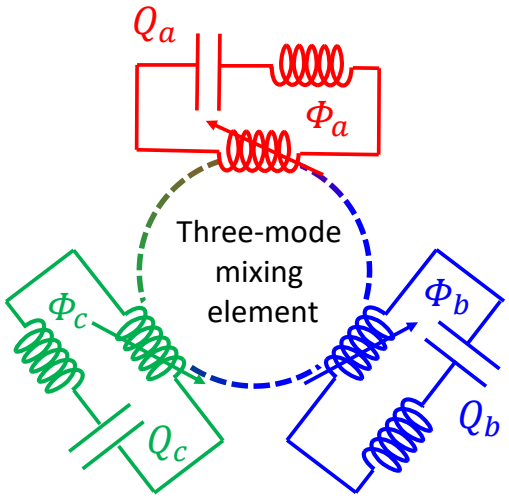

Figure 11: **Schematic of a typical three-mode device.** A typical three-mode device shares the same non-linear inductance contributed from the three wave mixing element, which generates the three wave coupling.

2.3.2.1 Coherent amplification : gain

Using the c mode as a pump mode, meaning sending pump photons into port c at the pump frequency, mode a and mode b can be coupled together by setting the pump frequency

to $\omega_{\rm p} = \omega_a + \omega_b$. When pump frequency $\omega_{\rm p}$ is far away from mode c's frequency, ω_c, the pump is called "stiff", meaning $\hat{c}$ operators can be treated as an average pump wave

$$\hat{c} \xrightarrow{\textbf{stiff}} \langle c \rangle = |\langle c \rangle| \; e^{-i\,(\omega_p t + \phi_p)}$$

where $|\langle c \rangle|$, and $\phi_{\rm p}$ are pump strength and phase, respectively. This approximation is called the stiff pump approximation.

After substituting Eq. 2.3.2.1 into Eq. 2.3, we obtain the Hamiltonian after applying the rotating wave approximation (RWA), which means ignoring all terms which do not rotate at a mode frequency (that is, terms which will be fast-varying after we shift to the modes' joint rotating frame)

$$\frac{H_{\rm coupling}}{\hbar} = g_3[a^\dagger b^\dagger \langle c \rangle + ab\langle c \rangle^*] \tag{2.4}$$

where g_3 is the three-wave mixing interaction.

The first term describes pump photons that are converted into pairs of signal and idler photons at ω_a and ω_b. The second terms indicates the reverse process: signal and idler photons are converted to pump photons. To describe the Hamiltonian of the whole system, we have to consider harmonic oscillator terms as well. Hence,

$$H = \hbar\omega_a a^\dagger a + \hbar\omega_b b^\dagger b + H_{\rm coupling}$$

In the stiff pump approximation, mode c's dynamics at ω_c do not need to be taken into account. Therefore, we do not include mode c's oscillating term in the Hamiltonian. Assuming signals incident on mode $a(b)$ at angular frequency $\omega_{1,2} \simeq \omega_{a,b}$, we can construct equations of motion for $a, b, a^\dagger$ and $b^\dagger$ from Eq. 2.1 in the frequency domain as in [68, 72],

$$\begin{aligned}
\big[\frac{\kappa_a}{2} - i\delta\big]a &= -ig_3\langle c \rangle b^\dagger + \sqrt{\kappa_a}a_{\rm in} \\
\big[\frac{\kappa_b}{2} + i\delta\big]b &= -ig_3\langle c \rangle a^\dagger + \sqrt{\kappa_b}b_{\rm in} \\
\big[\frac{\kappa_a}{2} + i\delta\big]a^\dagger &= ig_3\langle c \rangle^* b + \sqrt{\kappa_a}a^\dagger_{\rm in} \\
\big[\frac{\kappa_b}{2} - i\delta\big]b^\dagger &= ig_3\langle c \rangle^* a + \sqrt{\kappa_b}b^\dagger_{\rm in}
\end{aligned} \tag{2.5}$$

where $\delta = \omega_1 - \omega_a = \omega_b - \omega_2$, which implies that the pump has no detuning. In Appendix D, the detuned scenario will be considered. We then implement the input-output equation, see Eq. 2.2, and can organize the equations in matrix form

$$\begin{bmatrix} a_{\text{out}} \\ b_{\text{out}} \\ a_{\text{out}}^\dagger \\ b_{\text{out}}^\dagger \end{bmatrix} = S \begin{bmatrix} a_{\text{in}} \\ b_{\text{in}} \\ a_{\text{in}}^\dagger \\ b_{\text{in}}^\dagger \end{bmatrix} \quad \text{where} \quad S = \begin{bmatrix} r_{aa} & 0 & 0 & s_{ab} \\ 0 & r_{bb}^* & s_{ba}^* & 0 \\ 0 & s_{ab}^* & r_{aa}^* & 0 \\ s_{ba} & 0 & 0 & r_{bb} \end{bmatrix} \tag{2.6}$$

Based on Eq. 2.6, we realize that a single parametric amplification process links a to $b^\dagger$ as well as $a^\dagger$ and b, as shown in Fig. 12. The coupling diagram can be separated into two sub-diagrams, and since the coupling is for the same gain process, one can analyze a single sub-diagram and derive its scattering matrix.

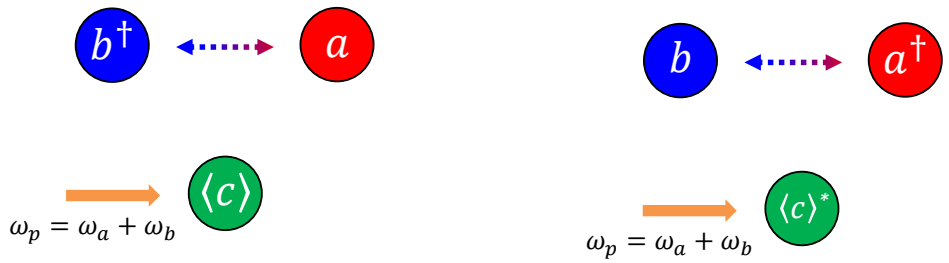

Figure 12: **Body diagram of gain.** Applying a pump drive to mode c at the frequency $\omega_p = \omega_a + \omega_b$. This pump tone is detuned far away from c mode; hence the stiff pump approximation can be applied, and we treat mode c as an average value. The gain process links a creation/annihilation mode to another mode's annihilation/creation operators based on the Eq. 2.6.

The elements of the scattering matrix are given by

$$r_{aa} = \frac{\chi_a^{-1}(\delta)^*\chi_b^{-1}(\delta)^* + \rho_{ab}^2}{\chi_a^{-1}(\delta)\chi_b^{-1}(\delta)^* - \rho_{ab}^2} \text{ and } r_{bb} = \frac{\chi_a^{-1}(\delta)\chi_b^{-1}(\delta) + \rho_{ab}^2}{\chi_a^{-1}(\delta)\chi_b^{-1}(\delta)^* - \rho_{ab}^2} \tag{2.7}$$

$$s_{ab} = \frac{2\rho_{ab}e^{-i\phi_p}}{\chi_a^{-1}(\delta)\chi_b^{-1}(\delta)^* - \rho_{ab}^2} \text{ and } s_{ba} = \frac{2\rho_{ab}e^{i\phi_p}}{\chi_a^{-1}(\delta)\chi_b^{-1}(\delta)^* - \rho_{ab}^2} \tag{2.8}$$

ρ_{ab} is the reduced effective mode coupling and its expression is

$$\rho_{ab} = \frac{2f_{\text{ab}}}{\sqrt{\kappa_a\kappa_b}} \tag{2.9}$$

where $f_{\text{ab}} = g_3|\langle c\rangle|$ is the reduced two-body coupling strength.

The other element in this expression is $\chi_{\text{a,b}}$, which is susceptibility of a mode,

$$\chi_{a,b}^{-1}(\delta) = 1 - i\frac{2\delta}{\kappa_{\text{a,b}}} \tag{2.10}$$

With the scattering Eq. 2.6, we can plot the gain. The scattering matrix element shows the outgoing results at mode j when the system has an incoming signal at mode i. For instance, S_{ab} means one sends a signal into the mode b and collects the results at mode a. The result is shown in Fig. 13. As mentioned at the beginning of this section, coherent amplification generates more photons at each mode. In the plot, the pump condition is about $0.45\sqrt{\kappa_a\kappa_b}$ where $\kappa_a = \kappa_b = 1$, and it results in 20 dB in both reflection and transmission, meaning the output photon number is 100 times more after experiencing the gain process.

When the drive tone of the amplifier has no detuning, $\omega_p = \omega_a + \omega_b$, and the input signals are on resonance with their corresponding mode, the scattering matrix takes a simpler form

$$\begin{bmatrix} \sqrt{G_0} & 0 & 0 & \sqrt{G_0-1}e^{-i\theta_{\text{ab}}} \\ 0 & \sqrt{G_0} & \sqrt{G_0-1}e^{i\theta_{\text{ab}}} & 0 \\ 0 & \sqrt{G_0-1}e^{-i\theta_{\text{ab}}} & \sqrt{G_0} & 0 \\ \sqrt{G_0-1}e^{i\theta_{\text{ab}}} & 0 & 0 & \sqrt{G_0} \end{bmatrix} \tag{2.11}$$

where the zero-detuned, optimal amplifier power gain G_0 is

$$G_0 = \left(\frac{1+\rho_{ab}^2}{1-\rho_{ab}^2}\right)^2 \tag{2.12}$$

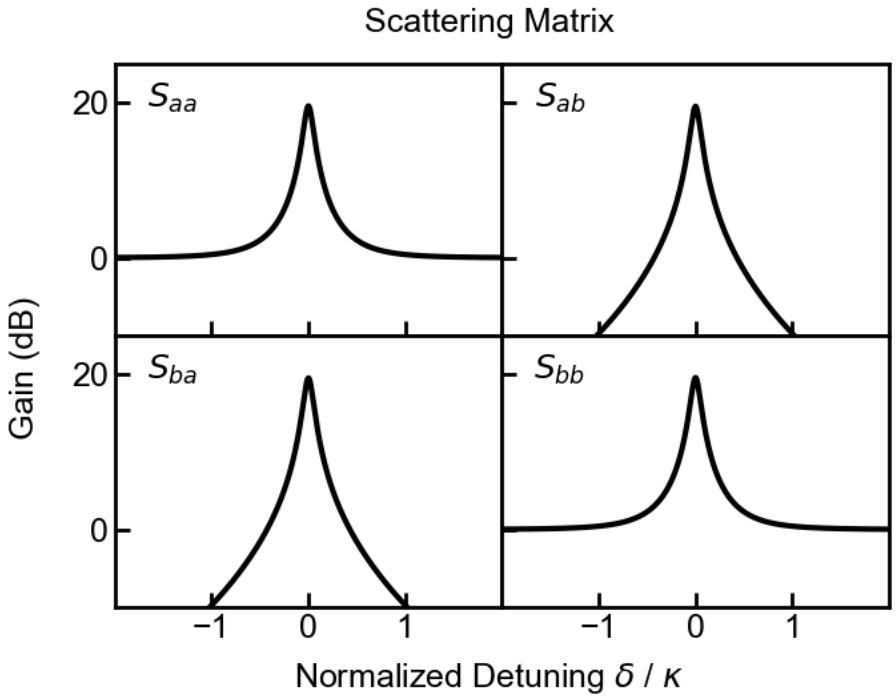

Figure 13: **Scattering matrix of gain.** One basic parametric process is gain. By pumping mode c at the summation of mode a and b frequencies, the pump photons split into two different photons: one photon with mode a's frequency and the other with mode b's frequency. The result suggests that the gain process occurs simultaneously on both reflection and transmission. This plot is generated with $\kappa_a = \kappa_b = 1$ and $f_{ab} = 0.45$

It can be shown that the stability of the amplifier requires that $\rho_{ab} < 1$, as shown in Fig. 14. The amplification becomes unstable when it enters into the region over the red dashed line, which is called the spontaneous parametric oscillations regime. From the Eq. 2.12, we can derive the divergence point where the gain goes to infinity, $f_{\mathrm{ab}} = \sqrt{\kappa_a \kappa_b}/2$.

2.3.2.2 Photon hopping : conversion

In the conversion process, pump photons provide energy to convert the input signal's

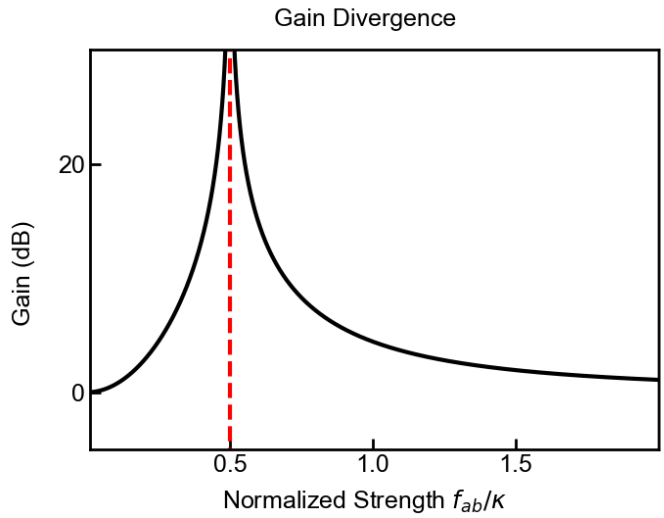

Figure 14: **Gain versus normalized pump strength.** The biggest drawback of the single gain process is that the gain goes to infinity at the critical pump power, P_c. When the pump power is stronger than P_c, the circuit enters the spontaneous parametric oscillation regime, where the system is unstable. $\kappa_a = \kappa_b = 1$ is used to generate this plot.

frequency to another mode's. This is analogous to a photon hopping from one mode to another. For this process, the pump frequency is at the difference of two modes' frequencies instead of the sum, $\omega_p = |\omega_a - \omega_b|$. Again, after assuming the pump tones are far away from mode c, we can apply the stiff pump approximation and the rotating wave approximation to eliminate high oscillation terms. The Hamiltonian of this process is the following

$$\frac{H}{\hbar} = \omega_a a^\dagger a + \omega_b b^\dagger b + g_3[a^\dagger b\langle c\rangle^* + a b^\dagger \langle c\rangle] \tag{2.13}$$

Following the same procedure as for gain, we derive the scattering matrix for the con-

version process

$$\begin{bmatrix} a_{\text{out}} \\ b_{\text{out}} \\ a^{\dagger}_{\text{out}} \\ b^{\dagger}_{\text{out}} \end{bmatrix} = S \begin{bmatrix} a_{\text{in}} \\ b_{\text{in}} \\ a^{\dagger}_{\text{in}} \\ b^{\dagger}_{\text{in}} \end{bmatrix} \quad \text{where} \quad S = \begin{bmatrix} r_{aa} & s_{ab} & 0 & 0 \\ s_{ba} & r_{bb} & 0 & 0 \\ 0 & 0 & r^{*}_{aa} & s^{*}_{ab} \\ & 0 & s^{*}_{ba} & r_{bb} \end{bmatrix} \tag{2.14}$$

where

$$r_{aa} = \frac{\chi_a^{-1}(\delta)^* \chi_b^{-1}(\delta) - \rho_{ab}^2}{\chi_a^{-1}(\delta)\chi_b^{-1}(\delta) + \rho_{ab}^2} \text{ and } r_{bb} = \frac{\chi_a^{-1}(\delta)\chi_b^{-1}(\delta)^* - \rho_{ab}^2}{\chi_a^{-1}(\delta)\chi_b^{-1}(\delta) + \rho_{ab}^2} \tag{2.15}$$

$$s_{ab} = \frac{2\rho_{ab}e^{-i\phi_p}}{\chi_a^{-1}(\delta)\chi_b^{-1}(\delta) + \rho_{ab}^2} \text{ and } s_{ba} = \frac{2\rho_{ab}e^{i\phi_p}}{\chi_a^{-1}(\delta)\chi_b^{-1}(\delta) + \rho_{ab}^2} \tag{2.16}$$

ρ_{ab} is the reduced effective mode coupling and is given by

$$\rho_{ab} = \frac{2g_{\text{ab}}}{\sqrt{\kappa_a \kappa_b}} \tag{2.17}$$

where $g_{\text{ab}} = g_3|\langle c \rangle|$ is called the reduced two-body coupling strength.

The Eq. 2.14 is very similar to that of gain, but with a difference in the coupling terms. We note that the conversion process links both modes' creation/annihilation operators together, see Fig. 15. Using gain and conversion processes as examples, the body diagram can be separated into two parts, and we see there is no connection between these two. This implies that the creation and annihilation photons from the same mode will not interfere with each other. As a result, the process must be phase preserving.

To show the photon hopping process, we use the scattering matrix plot in Fig. 16, and S_{aa} and S_{ba} as examples. For these two cases, we inject a signal into mode a and measure reflection and transmission. This plot uses variables $\kappa_a = \kappa_b = 1$ and $g_{\text{ab}} \simeq 0.45\sqrt{\kappa_a \kappa_b}$. In reflection, we observe a -20 dB dip on resonance, which implies that around 99 % of photons are not reflected back. In transmission, we notice 0 dB on resonance, and this tells us that the photons are converted from mode a to b. This phenomena also appears when the input signal is at mode b. It is important to note that our derivation, which begins from a discussion of creation and annihilation operators inherent computes in the photon-number basis. In

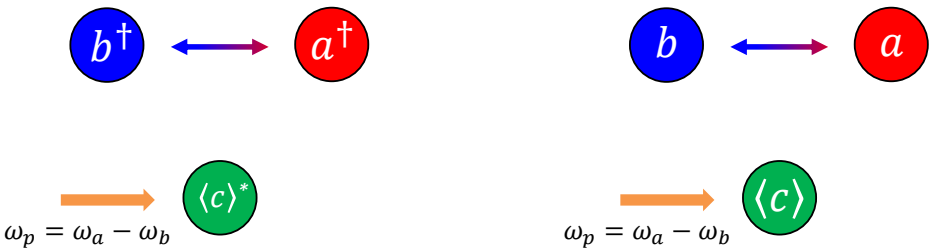

Figure 15: **Body diagram of conversion.** The pump tone is applied on the mode c at the difference of two other modes' frequencies. This process links a mode's creation/annihilation mode to another mode's creation/annihilation operators.

measurements or calculations based on microwave power, the observed result will not be 0 dB, rather larger or smaller (if the photons are converted up or down, respectively) by the ratio of the input/output frequencies involved. Students should watch out for this factor, particularly in Microwave Office simulations, which are not based on quantum Hamiltonian.

2.4 Coupled mode theory

The response of multi-mode coupled systems can be challenging to understand using conventional approaches that focus on the Hamiltonian or the resulting coupled equations of motion, especially in cases with several modes. However, the basic properties available to a system, such as impedance matching, gain, bandwidth, directionality, isolation, etc., are actually determined by the structure of the network topology created by the couplings. In this section, a pictorial representation of this network can be useful in understanding these

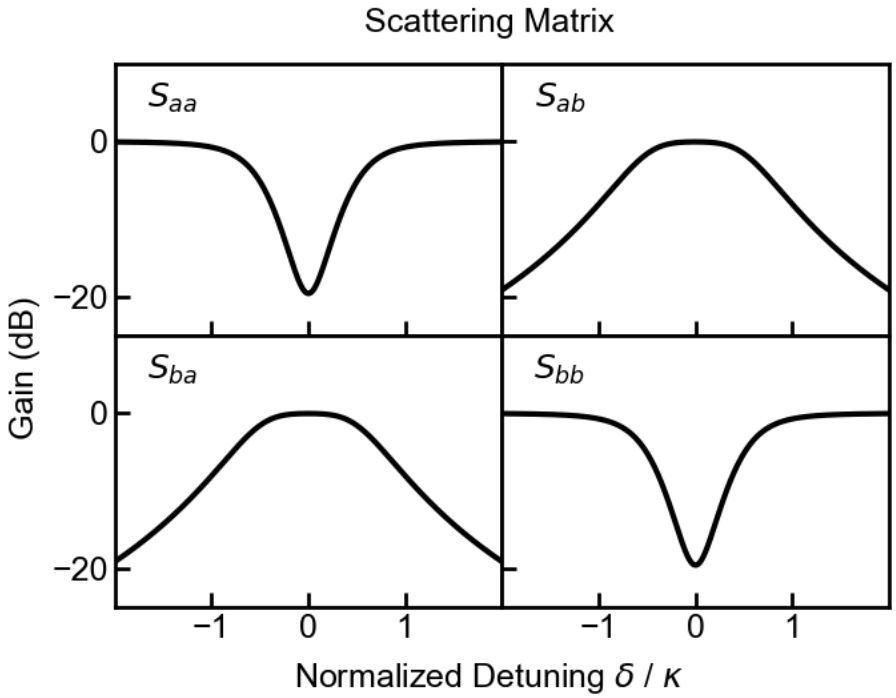

Figure 16: **Scattering matrix for conversion.** The other standard process is called conversion. Instead of summing the modes' frequencies, this process uses the difference in frequencies. The process converts the input signal to another mode's frequency. In other words, the photon hops from one port to another through conversion.

otherwise obfuscated properties.

This section contains an outline to organize the problem by use of directed graphs, following Aumentado's methods [51]. These graphs serve as a representation of the matrix that encapsulates the Langevin equations of motion for the normal mode representation. The the basic formulation of a general coupled mode theory is presented using general language so that the specific implementation is less important, and the number of modes in the problem can be easily increased. Thus, a pictorial representation is introduced to organize and understand coupled mode systems.

2.4.1 Matrix form of equation of motion

We begin by considering an arbitrary N-mode, N-port system, as depicted in Fig. 17. The system contains N eigenmodes and each mode has a port with which to communication to the outside. The ports in Fig. 17 may be any type of transmission line or waveguide that can send and receive the propagating modes. If one of the physical ports of the network supports more than one propagating mode, additional electrical ports can be added to account for these modes. Other than the number of modes, the modes must be coupled to each other through a type of coupling, gain or conversion.

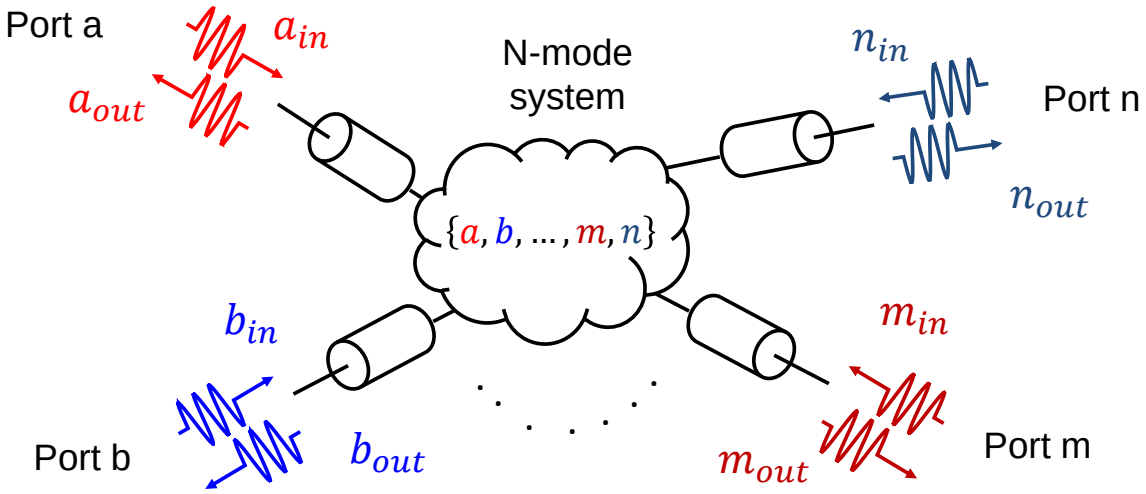

Figure 17: **An arbitrary N-port network.** An Arbitrary N-modes system with N-ports. Each mode has a dedicated port to send and receive signals.

To construct the scattering matrix in a matrix form, we must define the following parameters, $V_{\text{sys}}, V_{\text{in}}$ and V_{out}. If this network is considered as a circuit diagram, the input and outgoing signals can be represented as the voltage at the port. V_{sys} describes the mode's response inside the system while V_{in}, and V_{out} represent incoming and outgoing waves.

$$V_{\text{sys}} = \left[a, b, \cdots, n, a^\dagger, b^\dagger, \cdots, n^\dagger\right]$$

$$V_{\text{in}} = \left[a_{in}, b_{in}, \cdots, n_{in}, a^\dagger_{in}, b^\dagger_{in}, \cdots, n^\dagger_{in}\right]$$

$$V_{\text{out}} = \left[a_{out}, b_{out}, \cdots, n_{out}, a^\dagger_{out}, b^\dagger_{out}, \cdots, n^\dagger_{out}\right]$$

We can rewrite Eq. 2.1 in matrix form

$$MV_{\text{sys}} = \gamma V_{\text{in}} \tag{2.18}$$

where $\gamma = Diag(\sqrt{\kappa_a}, \sqrt{\kappa_b}, \cdots, \sqrt{\kappa_n}, \sqrt{\kappa_a}, \sqrt{\kappa_b}, \cdots, \sqrt{\kappa_n})$ and M is a coupling matrix that describes how a set of modes are connected.

Likewise, we can rewrite Eq. 2.2 in a matrix form,

$$V_{\text{sys}} = \gamma^{-1}(V_{\text{out}} + V_{\text{in}}) \tag{2.19}$$

Combine Eq. 2.18 and Eq. 2.19, and therefore, we obtain the scattering matrix in full matrix form

$$S = \gamma M^{-1}\gamma - \mathbb{1} \tag{2.20}$$

The form of Eq. 2.20 gives the scattering matrix directly, and it indicates that as long as we know the couplings between each mode, represented in the M-matrix, and also the mode's κ, which lives in γ, we can calculate the scattering matrix right away without deriving them from the $2N$ equations of motion. This scattering matrix can be used for an N-eigenemode, M-port system, where $M < N$, which is very common for a system that has inherent high-Q modes, such as microwave filters.

This theory can be applied to optical systems, such as beam-splitters, nonlinear crystals, and cavities, and used in microwave circuits such as couplers, filters, diodes, and implemented in mechanical oscillator systems. Even a system with microwave, optical, and mechanical modes coupled with each other can also benefit from the theory. The theory only requires users to know the number of eigenmodes and how they couple with each other and the

outside world. This theory is focused on the issues of computing the scattering in systems where many modes are parametrically coupled, and have arbitrary complex coupling rates linking these modes.

Graphical representations can be constructed from the M-matrix. The graphs serve as a tool to account for various terms in the problem of scattering between modes, as well as a way to develop intuition for the simple or complex problems of frequency conversion, amplification, and non-reciprocity as we move to coupled mode problems involving 3 or more modes. This method has the advantage of organizing terms according to their corresponding physical process and can be used to determine the scattering between modes by inspection.

2.5 Examples

2.5.1 GC amplification

For the first example, a pair of parametric couplings are applied between two cavity modes, each coupled to an input/output port. The pair of parametric couplings activate the interaction between both cavities through gain and conversion processes as shown in Eq. 2.21. The coherent interaction will thus be described by a quadratic Hamiltonian. This pumping scheme is proposed by A. Metelmann and A. Clerk in ref. [48, 49]. The Hamiltonian is a linear superposition of the processes

$$H_{\text{int}} = g_g(a^\dagger b^\dagger c + abc^\dagger) + g_c(ab^\dagger c + a^\dagger bc^\dagger) \tag{2.21}$$

where g_g and g_c are three-wave coupling strengths for the gain and conversion process respectively.

Based on what we have learned from the coherent amplification and photon conversion processes, we know $a/a^\dagger$ should connect to $b/b^\dagger$ through conversion and $b^\dagger/b$ via the gain process, as shown in Fig. 18. Each arrow in the coupling diagram indicates a specific parametric strength and phase.

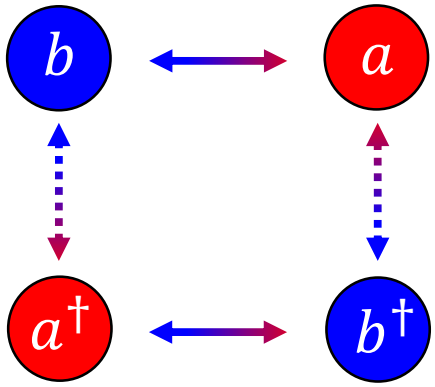

Figure 18: **Body diagram of GC amplification.** Start with a three-mode system and apply both gain and conversion pumps simultaneously on the c mode. Because mode c is treated as the pump mode and not involved in the parametric process, mode c is not shown in the coupling diagram. The dashed lines represent the gain process, which couples a/b to $b^\dagger/a^\dagger$, and the solid lines are the conversion process, which couples $a/b^\dagger$ to $b/a^\dagger$.

Assume modes a and b communicate with the outside at the rates κ_a and κ_b, respectively. We can construct the M-matrix with the basis $\left(a, b, a^\dagger, b^\dagger\right)$.

$$\begin{bmatrix} \kappa_a/2 - i\delta & ie^{-i\phi_{\mathrm{ab}}} g_{\mathrm{ab}} & 0 & ie^{-i\theta_{\mathrm{ab}}} f_{\mathrm{ab}} \\ ie^{i\phi_{\mathrm{ab}}} g_{\mathrm{ab}} & \kappa_b/2 - i\delta & ie^{-i\theta_{\mathrm{ab}}} f_{\mathrm{ab}} & 0 \\ 0 & -ie^{i\theta_{\mathrm{ab}}} f_{\mathrm{ab}} & \kappa_a/2 + i\delta & +ie^{i\phi_{\mathrm{ab}}} g_{\mathrm{ab}} \\ -ie^{i\theta_{\mathrm{ab}}} f_{\mathrm{ab}} & 0 & -ie^{-i\phi_{\mathrm{ab}}} g_{\mathrm{ab}} & \kappa_b/2 + i\delta \end{bmatrix} \tag{2.22}$$

where $g_{\mathrm{ab}} = g_c|c|$ and $f_{\mathrm{ab}} = g_g|c|$ with pump phase θ_{ab} and ϕ_{ab}, respectively. With the M-matrix, we can calculate the S-matrix and obtain the equation of gain and reflection for GC amplification.

$$\sqrt{G}(\delta) = \frac{ige^{i\phi_{\mathrm{ab}}}}{f^2 - g^2 + (\delta/\kappa_a + i/2)(\delta/\kappa_b + i/2)} \tag{2.23}$$

$$\sqrt{R}(\delta) = \frac{-f^2 + g^2 - (\delta/\kappa_a - i/2)(\delta/\kappa_b + i/2)}{f^2 - g^2 + (\delta/\kappa_a + i/2)(\delta/\kappa_b + i/2)} \tag{2.24}$$

where $g = g_{\mathrm{ab}}/\sqrt{\kappa_a \kappa_b}$ and $f = f_{\mathrm{ab}}/\sqrt{\kappa_a \kappa_b}$ are the normalized coupling strengths for conversion and gain processes respectively.

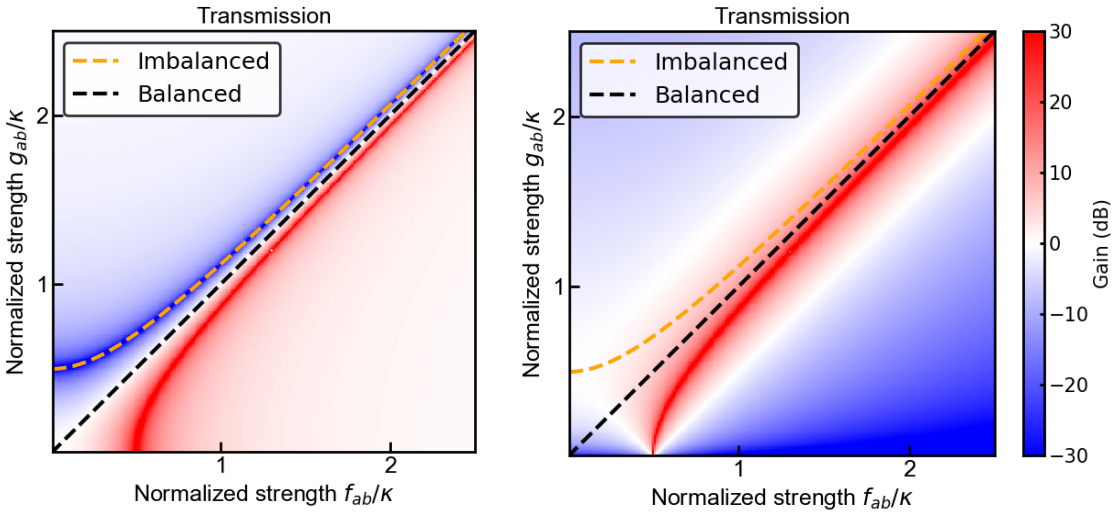

Figure 19: **Reflection and transmission of the GC amplification.** The GC amplification behavior is plotted for both reflection and transmission as a function of g_{ab} and f_{ab}. In these plots, $\kappa_a = \kappa_b = 1$ is assumed. In the plot, we observe transmission gain as both pump powers become stronger. When both pump strengths are the same, indicated as a black dashed line, reflection shows unity gain regardless of the power. Moreover, we observe when $g_{\mathrm{ab}} = \frac{1}{2}\sqrt{\kappa_a \kappa_b + 4f_{\mathrm{ab}}^2}$, reflection is deep blue, which implies there is no signal appearing in reflection. This is one of the criteria for an ideal amplifier. We called this GC-Imbalanced amplification.

By applying a pair of parametric gain and conversion couplings at the same time, the device properties are completely changed. The simplest way to check this is to plot reflection and transmission of the device on resonance, $\delta = 0$, as shown in Fig. 19. In the plot, the magnitude response is plotted in dB with red above 0 dB, and blue below 0 dB. Again, κ_a and κ_b are assumed to be 1 in this plot. In reflection, note the upper triangle of the plot is all blue, indicating that the conversion process dominates the behavior while the lower triangle is a faded red, showing that the gain process is stronger.

When the pump strengths are the same (i.e. balanced), then 0 dB is observed in reflection,

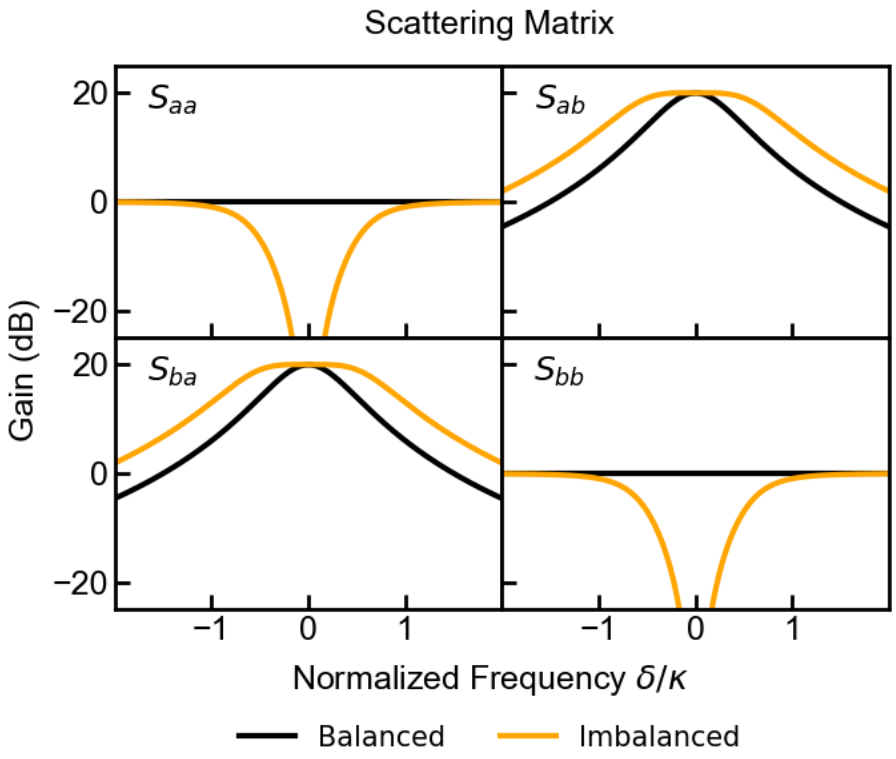

Figure 20: **Scattering matrix of the GC amplification.** When both parametric processes' power are equivalent, the rate of generating photons is the same as that of converting. The result implies that in reflection, S_{aa} and S_{bb}, only receive one photon, therefore unity gain can be observed. Alternatively, When the converting rate is higher than the rate of generating photons, then no any photon exists in reflection. Therefore, a large dip is found. For both cases, gain only appears in transmission, S_{ab} and S_{ba}. An interesting outcome is that in the imbalanced scenario, bandwidth is larger.

as shown by a black dashed line along the diagonal. Following the black line in transmission, the gain appears as pump strength becomes stronger, and we obtain a device with gain in transmission with only unity in reflection. Interestingly, when the conversion pump satisfies this condition, $g_{\mathrm{ab}} = \frac{1}{2}\sqrt{\kappa_a\kappa_b + 4f_{\mathrm{ab}}^2}$, we obtain amplification where there is no signal in reflection but gain in transmission, which is the criteria for a matched device.

We also plot the scattering matrix as a function of δ for both scenarios. Reflection in

Fig. 20 shows very different performance compared to a single parametric process. For the balanced case, gain and conversion processes destructively interfere with each other, hence a flat line at 0 dB. The result suggests the gain and conversion processes are interfering with each other and cancel out all the reflective signal; thus leaving only a copy of the original input signal. However, a large dip is observed in the imbalanced case. The results imply the conversion process overpowers the gain to create a considerable dip. In the transmission case, there is transmission gain under both cases, but the imbalanced case displays a larger bandwidth than that of the balanced case.

We adjust the pump power to achieve a different GC gain and compare the bandwidths. Amazingly, the bandwidth remains the same regardless of the gain in both cases, see Fig. 21. The results of GC amplification are unique when compared to a single parametric process. Without changing hardware, we achieve a bi-directional amplifier by turning on two parametric processes. Hence, this suggests the possibility of creating a non-reciprocal directional amplifier using multiple parametric processes.

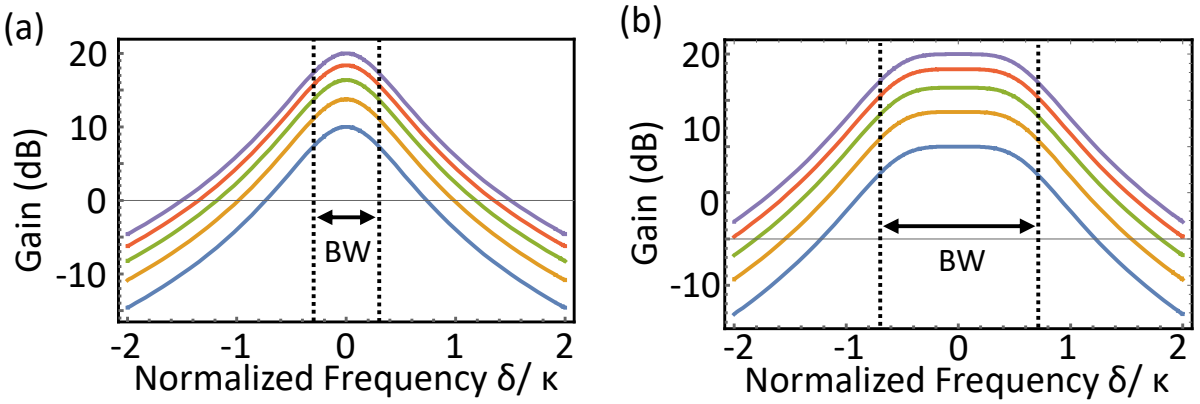

Figure 21: **(a) Bandwidth of GC balanced.** We compare bandwidth with different GC gain and find the bandwidth remains the same regardless of the gain. **(b) Bandwidth of GC imbalance.** Similar to the balanced case, in the imbalanced case there is no gain-bandwidth product.

The other important property of the GC amplification process is that gain does not diverge, see Fig. 22. However, the amplification process requires higher pump strength to reach 20 dB compared with a single parametric amplification process, which is indicated

with a red line. The plot shows transmission gain for all pumping schemes.

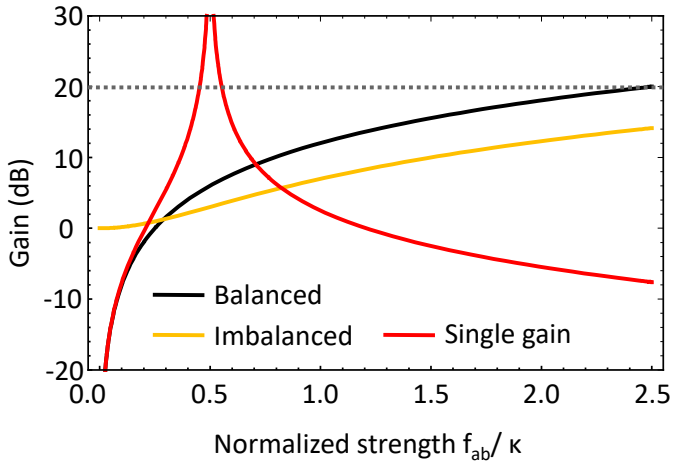

Figure 22: **GC gain versus normalized pump strength.** GC amplification requires at least five times more pump strength to reach 20 dB gain compared to a single gain process. Also, GC amplification does not diverge.

2.5.2 How to build a directional device

Parametric processes not only turn on the desired inherent coupling terms but also introduce extra pump phases into signals. In some parametric processes, such as a single parametric process and GC amplification, the pump phase does not affect the output magnitude. If we can generate a parametric scheme that allows us to use the pump phase to create interference, then directionality of the device can be engineered. This idea is very similar to the Mach-Zehnder interferometer [73, 74], see Fig. 23.

Mach-Zehnder interferometers consist of two paths: an upper and lower. We can assume the upper and lower path lengths are the same for light travelling from the source to the detector. For the simplest case, there is no extra phase shift as the light goes through the beam-splitter. Also, the mirrors are identical, just like a beam-splitter. The beam-splitter is a perfect 50-50 component, meaning the photons have 50 % chance of going to either

the upper or lower paths. The lower path collects only the path phase whereas the upper path gathers path phase and a phase shift contributed from the sample. When photons are detected, the phase difference between the two paths is θ, the phase from the sample. Hence, the outcome is affected by θ.

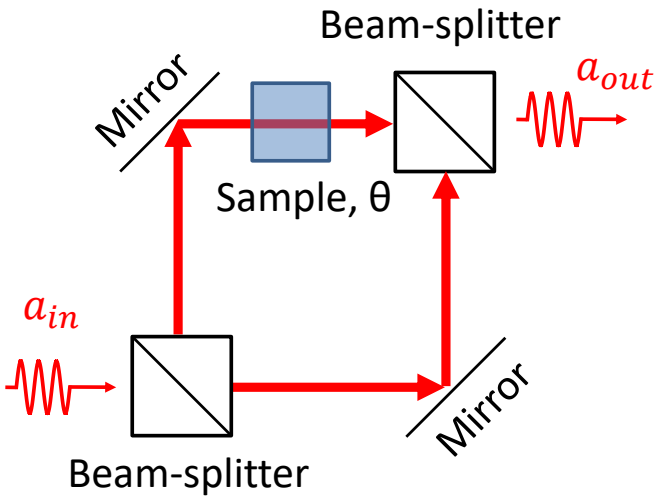

Figure 23: **Mach-Zehnder interferometer.** An input signal splits into two and travels along different paths. The sample arm provides additional phase θ. These two paths meet at the output port and detection will show constructive or destructive interference dependent on θ.

A similar concept can be applied to parametric processes. The coupling diagram indicates how signal flows from the input to the output. The input signal is the source in the interferometer, and the outcomes are the outgoing waves. The number of paths depends on the number of parametric processes; i.e. more paths are generated as more pumps are introduced.

In principle, the Mach-Zehnder interferometer is a reciprocal device, meaning when the incoming/outgoing ports switch roles, the result remains the same as long as the sample is also reciprocal. Alternatively, the parametric processes do not guarantee reciprocity because the reverse processes introduce an opposite sign in pump phase. Another difference from the Mach-Zehnder interferometer is that the strength of photons on each path is the same, so the

interference is affected only by phase shifts. However, parametric processes can control the strength of the coupling; hence, the strength of the paths can be different. Before discussing the details of these findings, it is useful to review the equation of scattering matrix, Eq. 2.20 and focus on how to calculate a scattering matrix element S_{ij}

$$\begin{aligned} S_{ij} &= \sqrt{\kappa_i \kappa_j} M^{-1}_{\mathrm{ij}} \\ &= \sqrt{\kappa_i \kappa_j} \frac{1}{|M|} C_{\mathrm{ji}} \\ &\propto C_{\mathrm{ji}} \end{aligned} \tag{2.25}$$

Note that $M^{-1} = C^T/|M|$.

From Eq. 2.25, the scattering matrix is related to the inverse of the coupling matrix, M^{-1}, which is determined by the co-factor matrix, C. This implies that by calculating C_{ji}, the properties of S_{jk} if $|M| \neq 0$ will be revealed.

I used this method to analyze GC amplification on resonance again, using S_{ba} and S_{ab} as examples. From the M-matrix of the GC amplification Eq. 2.22, we can write down C_{ab}

$$C_{\mathrm{ab}} = \begin{vmatrix} ie^{i\phi_{\mathrm{ab}}} g_{\mathrm{ab}} & ie^{-i\theta_{\mathrm{ab}}} f_{\mathrm{ab}} & 0 \\ 0 & \kappa_a/2 & -ie^{i\phi_{\mathrm{ab}}} g_{\mathrm{ab}} \\ -ie^{i\theta_{\mathrm{ab}}} f_{\mathrm{ab}} & -ie^{-i\phi_{\mathrm{ab}}} g_{\mathrm{ab}} & \kappa_b/2 \end{vmatrix} \tag{2.26}$$

$$= ig^3_{\mathrm{ab}} e^{i\phi_{\mathrm{ab}}} - if^2_{\mathrm{ab}} g_{\mathrm{ab}} e^{i\phi_{\mathrm{ab}}} + i\frac{\kappa_a \kappa_b}{4} g_{\mathrm{ab}} e^{i\phi_{\mathrm{ab}}}$$

Note that C_{ab} in Eq. 2.26 has three terms, and each term specifies how signal flows from a to b. The term on the right side indicates the path shown in Fig. 24 (a). It is a simple path from a to b but there is an interaction between $a^\dagger$ and $b^\dagger$ via the conversion process. The second path indicates that the signal passes through $b^\dagger$ via the gain process, then $a^\dagger$ through conversion, and finally back to b via the gain process. The last term has a single path from a to b with $a^\dagger$ and $b^\dagger$ coupled to ports through κ.

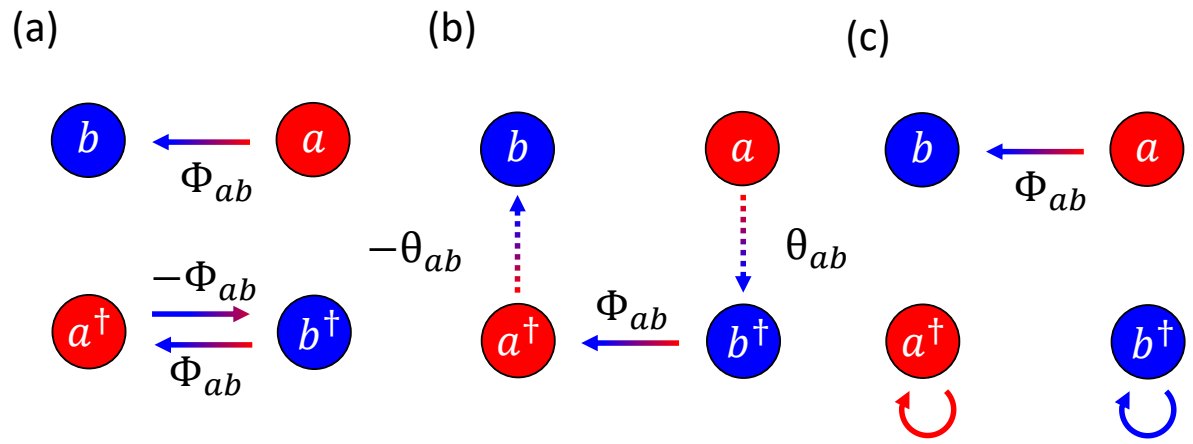

Figure 24: **(a) Path 1.** The input signal travels from a to b under the influence of $a^\dagger$ and $b^\dagger$ coupled via conversion. **(b) Path 2.** The input signal travels from a to $b^\dagger$ then to $a^\dagger$ and then to b. **(c) Path 3.** The input signal travels from a to b under the influence of $a^\dagger$ and $b^\dagger$ coupled to output ports.

Similarly, the same calculation can be performed for C_{ba}

$$C_{\mathrm{ba}} = \begin{vmatrix} ie^{-i\phi_{\mathrm{ab}}} g_{\mathrm{ab}} & 0 & ie^{-i\theta_{\mathrm{ab}}} f_{\mathrm{ab}} \\ -ie^{i\theta_{\mathrm{ab}}} f_{\mathrm{ab}} & \kappa_a/2 & -ie^{i\phi_{\mathrm{ab}}} g_{\mathrm{ab}} \\ 0 & -ie^{-i\phi_{\mathrm{ab}}} g_{\mathrm{ab}} & \kappa_b/2 \end{vmatrix} \tag{2.27}$$

$$= ig_{\mathrm{ab}}^3 e^{-i\phi_{\mathrm{ab}}} - if_{\mathrm{ab}}^2 g_{\mathrm{ab}} e^{-i\phi_{\mathrm{ab}}} + i\frac{\kappa_a \kappa_b}{4} g_{\mathrm{ab}} e^{-i\phi_{\mathrm{ab}}}$$

The only difference for C_{ba} is that because signal flows in the opposite direction, all the phases must flip sign; hence, $\phi_{\mathrm{ab}} \to -\phi_{\mathrm{ab}}$. However, ϕ_{ab} and $-\phi_{\mathrm{ab}}$ are only global phases in these two equations, therefore the magnitudes of S_{ab} and S_{ba} are unaffected by the phase. Using this calculation, we prove that GC amplification is a bi-directional parametric process.

2.5.3 Circulator

In this subsection, the realization of a circulator through multiple parametric processes is discussed. Because the device is made of superconducting circuits, theoretically it has no dissipation energy and does not require large magnetic fields to achieve non-reciprocity.

The purpose of a circulator is to convert photons from one port to another by turning on the conversion processes between modes, see Fig. 25. The system must be expanded to a three-eigenmode circuit, and each mode has a port, as in commercial three-port circulators. The conversion process does not require coupling between creation and annihilation photons; therefore, the coupling diagram of the circulator can be separated into two parts. We can now proceed to the next step of constructing the M-matrix.

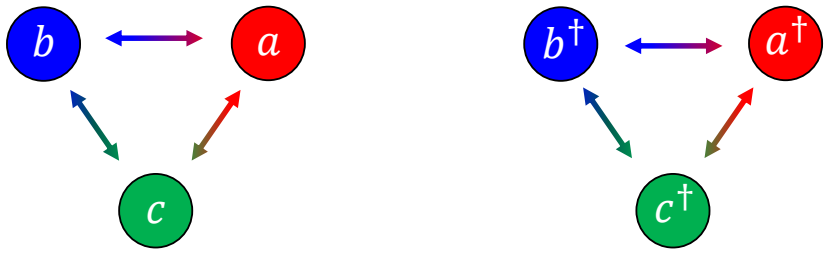

Figure 25: **Body diagram of a circulator.** The principle underlying a circulator can be imagined as photons hopping from one port to another. In this study, each port ties to an eigenmode; therefore photon hopping can be achieved through conversion processes.

The M-matrix can be constructed using an understanding of the coupling scheme and the number of modes.The matrix has four blocks, where the off-diagonal parts are the description of the coupling between creation and annihilation modes, as shown in Eq. 2.28. The upper/lower part of the diagonal blocks indicates that the annihilation/creation photons are associated with one another through the conversion process. To analyze this multi

parametric process, we can calculate upper or lower blocks on the diagonal.

$$\begin{bmatrix} \kappa_a/2 - i\delta & ie^{-i\phi_{\rm ab}}g_{\rm ab} & ie^{-i\phi_{\rm ac}}g_{\rm ac} & 0 & 0 & 0 \\ ie^{i\phi_{\rm ab}}g_{\rm ab} & \kappa_b/2 - i\delta & ie^{-i\phi_{\rm bc}}g_{\rm bc} & 0 & 0 & 0 \\ ie^{i\phi_{\rm ac}}g_{\rm ac} & ie^{i\phi_{\rm bc}}g_{\rm bc} & \kappa_c/2 - i\delta & 0 & 0 & 0 \\ 0 & 0 & 0 & \kappa_a/2 + i\delta & -ie^{i\phi_{\rm ab}}g_{\rm ab} & -ie^{i\phi_{\rm ac}}g_{\rm ac} \\ 0 & 0 & 0 & -ie^{-i\phi_{\rm ab}}g_{\rm ab} & \kappa_b/2 + i\delta & -ie^{i\phi_{\rm bc}}g_{\rm bc} \\ 0 & 0 & 0 & -ie^{-i\phi_{\rm ac}}g_{\rm ac} & -ie^{-i\phi_{\rm bc}}g_{\rm bc} & \kappa_c/2 + i\delta \end{bmatrix} \tag{2.28}$$

From the M-matrix, we can track the input signal, for instance, at ω_a and track its flow to port b at ω_b. There are two paths which are shown in Fig. 26. Before explaining the calculation of the scattering matrix, it is useful to prove that this pumping scheme indeed generates a non-reciprocal property. To do so, we use S_{ba} and S_{ab} as examples.

$$\begin{aligned} C_{\rm ab} &= \begin{vmatrix} ie^{i\phi_{\rm ab}}g_{\rm ab} & ie^{-i\phi_{\rm bc}}g_{\rm bc} \\ ie^{i\phi_{\rm ac}}g_{\rm ac} & \kappa_c/2 \end{vmatrix} \\ &= e^{i(\phi_{\rm ac}-\phi_{\rm bc})}g_{\rm ac}g_{\rm bc} + i\frac{\kappa_c}{2}g_{\rm ab}e^{i\phi_{\rm ab}} \end{aligned} \tag{2.29}$$

On the right side of Eq. 2.29, the first term indicates that the signal passes c before reaching b, while the second term is the direct path from a to b with c mode's self-correction due to the coupling to the outside world. Similarly, we achieve $C_{\rm ba}$ with the same method, shown in Eq. 2.30

$$\begin{aligned} C_{\rm ba} &= \begin{vmatrix} ie^{-i\phi_{\rm ab}}g_{\rm ab} & ie^{-i\phi_{\rm ac}}g_{\rm ac} \\ ie^{i\phi_{\rm bc}}g_{\rm bc} & \kappa_c/2 \end{vmatrix} \\ &= e^{-i(\phi_{\rm ac}-\phi_{\rm bc})}g_{\rm ac}g_{\rm bc} + i\frac{\kappa_c}{2}g_{\rm ab}e^{-i\phi_{\rm ab}} \end{aligned} \tag{2.30}$$

Similar to the GC amplification example, when the flow is reversed, all phases must flip in sign.

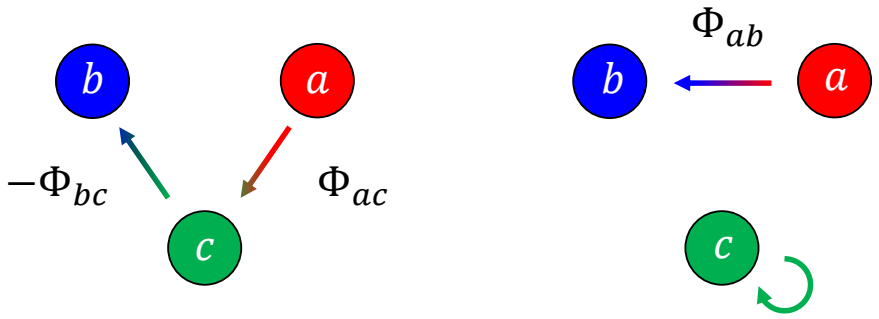

Figure 26: S_{ba} **: Signal flow of a circulator.** From the M-matrix, we can determine how the signal flows from the one port to another. Parametric drives provide energy for the input photons to hop to other modes and carries a pump phase. S_{ba}, for example, has the input signal coming into the mode a, then to mode b directly with a new pump phase ϕ_{ab}. It can also go through mode c with an additional phase, $\phi_{\mathrm{ac}} + \phi_{\mathrm{bc}}$. The interference at mode b depends on these path phases.

To produce non-reciprocity, we must generate constructive interference on paths in one direction but destructive interference in the opposite direction. To do so, the weight of each term should be the same, i.e. the condition has to satisfy $g_{\mathrm{ac}}g_{\mathrm{bc}} = \kappa_c g_{\mathrm{ab}}/2$. Under this condition, we can rewrite the equations

$$C_{\mathrm{ab}} = g_{\mathrm{ac}}g_{\mathrm{bc}}\left[e^{i(\phi_{\mathrm{ac}}-\phi_{\mathrm{bc}})} + e^{i(\phi_{\mathrm{ab}}+\pi/2)}\right]$$
$$C_{\mathrm{ba}} = g_{\mathrm{ac}}g_{\mathrm{bc}}\left[e^{-i(\phi_{\mathrm{ac}}-\phi_{\mathrm{bc}})} + e^{-i(\phi_{\mathrm{ab}}-\pi/2)}\right]$$

We assume there cannot be constructive interference on C_{ab} and destructive interference on C_{ba}. Then by setting $C_{\mathrm{ba}} = 0$, another constraint can be obtained, $\phi_{\mathrm{ac}} - \phi_{\mathrm{bc}} = \phi_{\mathrm{ab}} + \pi/2$. After applying this constraint to C_{ab}, we obtain $C_{\mathrm{ab}} = 2g_{\mathrm{ac}}g_{\mathrm{bc}}e^{i(\phi_{\mathrm{ab}}+\pi/2)}$. This indicates that $S_{ab} \neq S_{ba}$; hence, it is directional between a and b. If the same assumption is applied to all

scattering elements, S_{ac}, S_{ca}, S_{bc} and S_{cb}, then we obtain all constraints

$$\begin{cases} g_{\rm ab}g_{\rm ac} = \kappa_a g_{\rm bc}/2 \ \text{ and } \ \phi_{\rm ab} - \phi_{\rm ac} = \phi_{\rm bc} + \pi/2 \\ g_{\rm ab}g_{\rm bc} = \kappa_b g_{\rm ac}/2 \ \text{ and } \ \phi_{\rm ab} - \phi_{\rm bc} = \phi_{\rm ac} + \pi/2 \\ g_{\rm ac}g_{\rm bc} = \kappa_c g_{\rm ab}/2 \ \text{ and } \ \phi_{\rm ac} - \phi_{\rm bc} = \phi_{\rm ab} + \pi/2 \end{cases}$$

We arrive at the condition for a circulator after organizing the above equations

$$\begin{cases} g_{\rm ab} = \sqrt{\kappa_a\kappa_b}/2 \\ g_{\rm ac} = \sqrt{\kappa_a\kappa_c}/2 \ \text{ and } \ \phi_{tot} = \pm\pi/2 \\ g_{\rm bc} = \sqrt{\kappa_b\kappa_c}/2 \end{cases} \tag{2.31}$$

where $\phi_{\rm tot} = \phi_{\rm ab} + \phi_{\rm bc} + \phi_{\rm ac}$ and $\phi_{\rm tot} = \pi/2$ is for circulating counter-clockwise and $\phi_{\rm tot} = -\pi/2$ is for clockwise. The result shows that we can use parametric processes to generate a directional device. Also, the flow direction can be controlled by the pump phases by balancing the strength for each pump.

Using our understanding of the M-matrix, the next step is taken to build a scattering matrix. The scattering matrix is plotted in Fig. 27 with $\kappa_a = \kappa_b = \kappa_c = 1$ and the pump strength satisfying the above conditions, Eq. 2.31. When the total phase $\phi_{\rm tot} = -\pi/2$, the signal flow is clockwise in the coupling diagram and reversed to counterclockwise when the phase flips in sign.

This circulating condition described above is for the ideal case where the overall pump phase is well controlled. In an actual experiment, phase drifting or phase fluctuation must be considered. Therefore, it is helpful to plot the scattering as a function of $\phi_{\rm tot}$, as shown in Fig. 28. As illustrated on the plot, if a perfect circulator is not needed because the reflection is not required to be $-\infty$ dB and the transmission does not need to be 0 dB, then there is an operating window of about 0.3 π.

Using the circulator as an example of a directional device, we can build a directional amplifier based on the circulator. It is clear that a gain process must to be applied to have appropriate gain; however, which two modes should be used and the conditions for ideal amplification must be addressed.

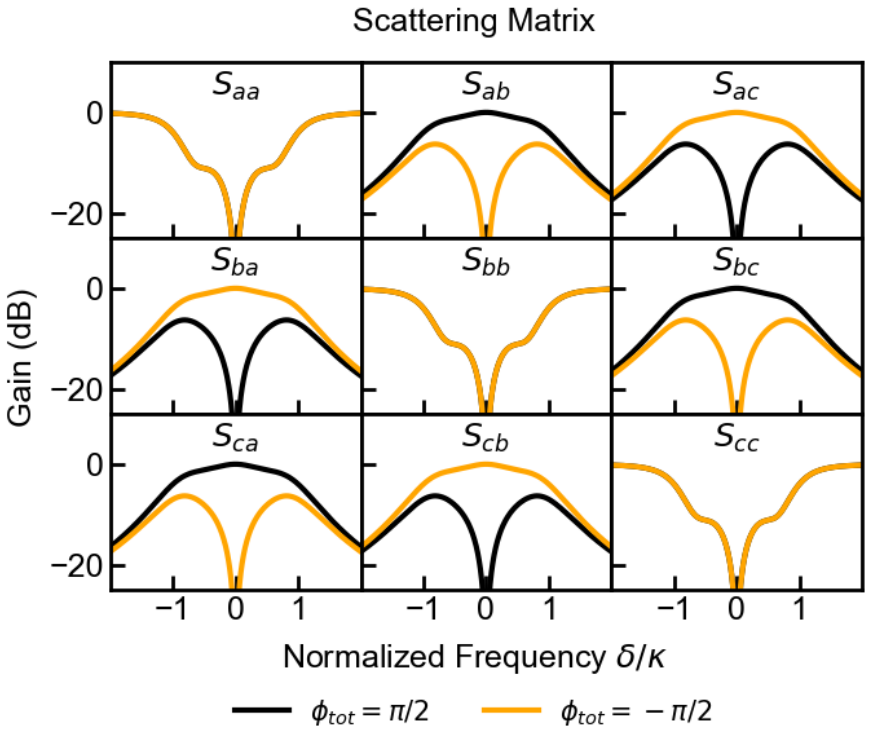

Figure 27: **Scattering matrix of a circulator.** This pumping scheme results in a circulator, which is a matched device with directionality dependent on ϕ_{tot}.The plot is generated with $\kappa_a = \kappa_b = \kappa_c = 1$ and $g_{\text{ab}} = g_{\text{ac}} = g_{\text{bc}} = 0.5$.

2.5.4 An ideal directional amplifier

An ideal amplifier has to be directional, meaning the signal can be amplified from a port that is connected to an object of interest, such as a qubit, to a output port, which connects the amplification chain. The amplification must be large so that the amplified signal will not be immersed in the thermal noise introduced from the amplification chain at higher temperature stages, such as a HEMT amplifier. However, we must minimize the reverse signal from the back-action, i.e. signal reflected from the posterior chain that enters from the output port and returns to the protected port. Hence, the device should amplify the

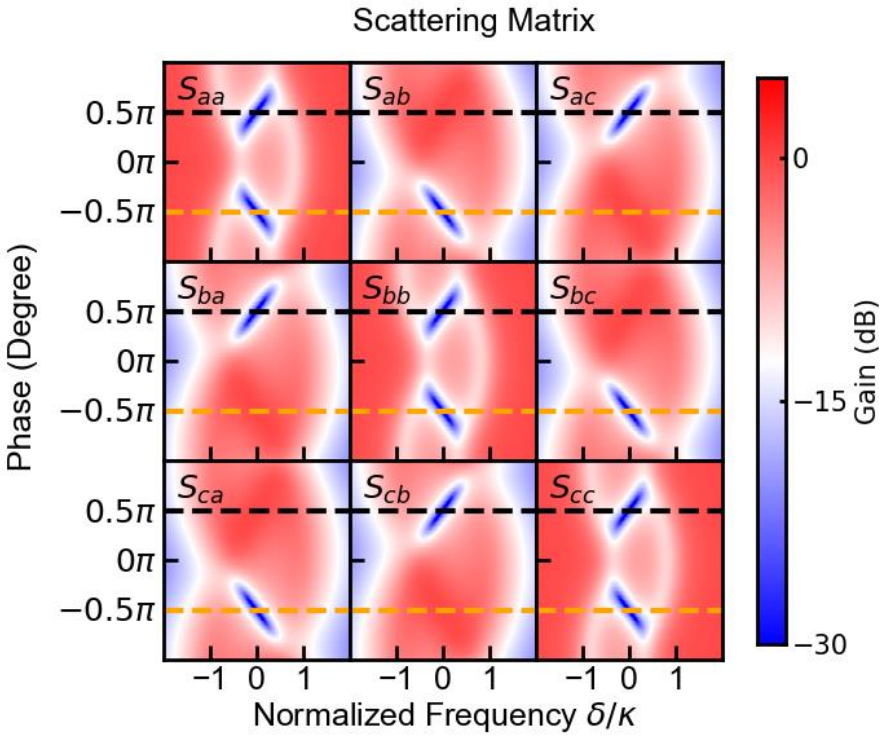

Figure 28: **Scattering matrix of a circulator with different phase.** The plot shows magnitude response for each scattering element as a function of δ and ϕ_{tot}. The dark blue indicates at least -30 dB. The circulator's direction is controlled by the overall phase, ϕ_{tot}. Completely constructive and destructive interference only occurs when $\phi_{\text{tot}} = \pm\pi/2$. The horizontal dashed black and orange lines correspond to the curves in Fig. 27.

signals and it also needs to be a matched device to avoid reflection and protect the object of interest.

Furthermore, state-of-the-art quantum computers require one amplifier along with a commercial circulator for each qubit; this configuration wastes space in a dilution refrigerator. If ideal directional amplifiers could be used for reading out multiple qubits, then it would be more practical. These constraints suggest that these amplifiers require large bandwidth to cover a range of qubit frequencies and also have the capability of processing huge or multiple

signals together.

In the previous section, we discussed the pumping scheme to create a circulator. Directional amplifiers are created based on the circulator and additional parametric processes, such as gain between modes a and b, as well as modes a and c. Using the described parametric processes, we can produce the coupling diagram shown in Fig. 29. This illustrated pumping scheme has 2 GC amplifications on top of a circulator.

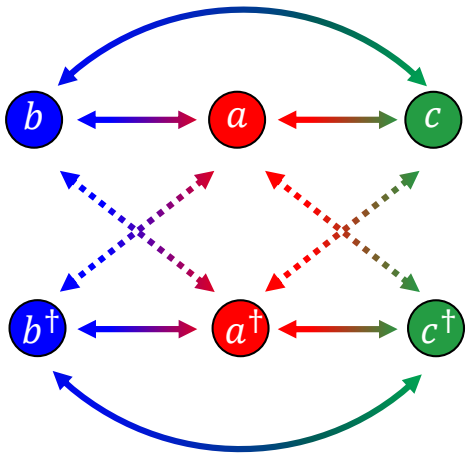

Figure 29: **Body diagram of directional amplification.** Directional amplification is built on the circulator with additional gain processes between mode a and b as well as mode a and c.

To further analyze the scheme, we examine the M-matrix with the basis $\left(a, b, c, a^\dagger, b^\dagger, c^\dagger\right)$.

$$\begin{bmatrix}
\kappa_a/2 - i\delta & ie^{-i\phi_{\mathrm{ab}}} g_{\mathrm{ab}} & ie^{-i\phi_{\mathrm{ac}}} g_{\mathrm{ac}} & 0 & ie^{-i\theta_{\mathrm{ab}}} f_{\mathrm{ab}} & ie^{-i\theta_{\mathrm{ac}}} f_{\mathrm{ac}} \\
ie^{i\phi_{\mathrm{ab}}} g_{\mathrm{ab}} & \kappa_b/2 - i\delta & ie^{-i\phi_{\mathrm{bc}}} g_{\mathrm{bc}} & ie^{-i\theta_{\mathrm{ab}}} f_{\mathrm{ab}} & 0 & 0 \\
ie^{i\phi_{\mathrm{ac}}} g_{\mathrm{ac}} & ie^{i\phi_{\mathrm{bc}}} g_{\mathrm{bc}} & \kappa_c/2 - i\delta & ie^{-i\theta_{\mathrm{ac}}} f_{\mathrm{ac}} & 0 & 0 \\
0 & -ie^{i\theta_{\mathrm{ab}}} f_{\mathrm{ab}} & -ie^{i\theta_{\mathrm{ac}}} f_{\mathrm{ac}} & \kappa_a/2 + i\delta & -ie^{i\phi_{\mathrm{ab}}} g_{\mathrm{ab}} & -ie^{i\phi_{\mathrm{ac}}} g_{\mathrm{ac}} \\
-ie^{i\theta_{\mathrm{ab}}} f_{\mathrm{ab}} & 0 & 0 & -ie^{-i\phi_{\mathrm{ab}}} g_{\mathrm{ab}} & \kappa_b/2 + i\delta & -ie^{i\phi_{\mathrm{bc}}} g_{\mathrm{bc}} \\
-ie^{i\theta_{\mathrm{ac}}} f_{\mathrm{ac}} & 0 & 0 & -ie^{-i\phi_{\mathrm{ac}}} g_{\mathrm{ac}} & -ie^{-i\phi_{\mathrm{bc}}} g_{\mathrm{bc}} & \kappa_c/2 + i\delta
\end{bmatrix} \tag{2.32}$$

where, $g_{\mathrm{ij}}, \phi_{\mathrm{ij}}$ and $f_{\mathrm{ij}}, \theta_{\mathrm{ij}}$ are the conversion and gain process's strength and phase between mode i and j. Also, κ_i is linewidth of mode i. Because the pumping scheme builds on the

circulator and GC amplification, we can apply the pumping condition for the circulator and GC imbalanced that results in a matched device.

$$\begin{cases} g_{\mathrm{ab}} = \frac{1}{2}\sqrt{\kappa_a\kappa_b + 4f_{\mathrm{ab}}^2} \\ g_{\mathrm{ac}} = \frac{1}{2}\sqrt{\kappa_a\kappa_c + 4f_{\mathrm{ac}}^2} \\ g_{\mathrm{bc}} = \frac{1}{2}\sqrt{\kappa_b\kappa_c} \end{cases} \quad \text{and} \quad \begin{cases} \phi_{\mathrm{ab}} + \phi_{\mathrm{bc}} + \phi_{\mathrm{ac}} = \pm\pi/2 \\ \theta_{\mathrm{ab}} = \phi_{\mathrm{ab}} \\ \theta_{\mathrm{ac}} = \phi_{\mathrm{ac}} \end{cases} \tag{2.33}$$

Under these conditions, we can explore this scheme's scattering matrix using parameters $\kappa_a = \kappa_b = \kappa_c = 1$ and $f_{\mathrm{ab}} = f_{\mathrm{ac}} = 5$, see Fig. 30. At first glance, we notice that the directionality appears by operating as a circulator through controlling $\phi_{\mathrm{tot}} = \phi_{\mathrm{ab}}+\phi_{\mathrm{ac}}+\phi_{\mathrm{bc}} = \pm\pi/2$. Because one port must be used for protecting the quantum objects of interest, it implies that all signals/noise sources from other ports not be amplified into the protected port (at least one term must have unity transmission to allow quantum fluctuations to reach the qubit port, or the scattering matrix will be unphysical). When $\phi_{\mathrm{tot}} = \frac{\pi}{2}/-\frac{\pi}{2}$, then mode b/c has a deep dip on resonance in reflection and there is no signal flowing from port a. There is another signal from S_{bc}/S_{cb} showing 0 dB on resonance, as required.

The output port a receives an amplified signal from the protected port, whether the protected port is port b or c depends on the ϕ_{tot}. Moreover, the reverse signal, S_{ba}/S_{ca}, is again $-\infty$ dB, and the result implies no signal flows in the reverse direction. To sum up, the protected port can be chosen by ϕ_{tot}, and the information from the protected to the output port is amplified but the reverse is not true. This suggests that this pumping scheme is a candidate for directional amplification. All combinations of protected ports and output ports are feasible for this matched linewidth case, but other combinations require adjusting which pairs of modes are linked with gain processes.

Because the device is quantum-limited, each port must receive a minimum amount of quantum noise based on the Heisenberg uncertainty principle [68, 22, 67]; hence, vacuum fluctuations from port c/b must exist. Fortunately, port c/b at $\phi_{\mathrm{tot}} = \frac{\pi}{2}/-\frac{\pi}{2}$ is an ancillary port used for absorbing the reverse-gain signal from the output port. Note the ancillary port is not physically connected to any output lines that go out to room temperature. Therefore, the ancillary port will only send vacuum noise to the protected port, which is the minimum amount of noise allowed by the quantum mechanics.

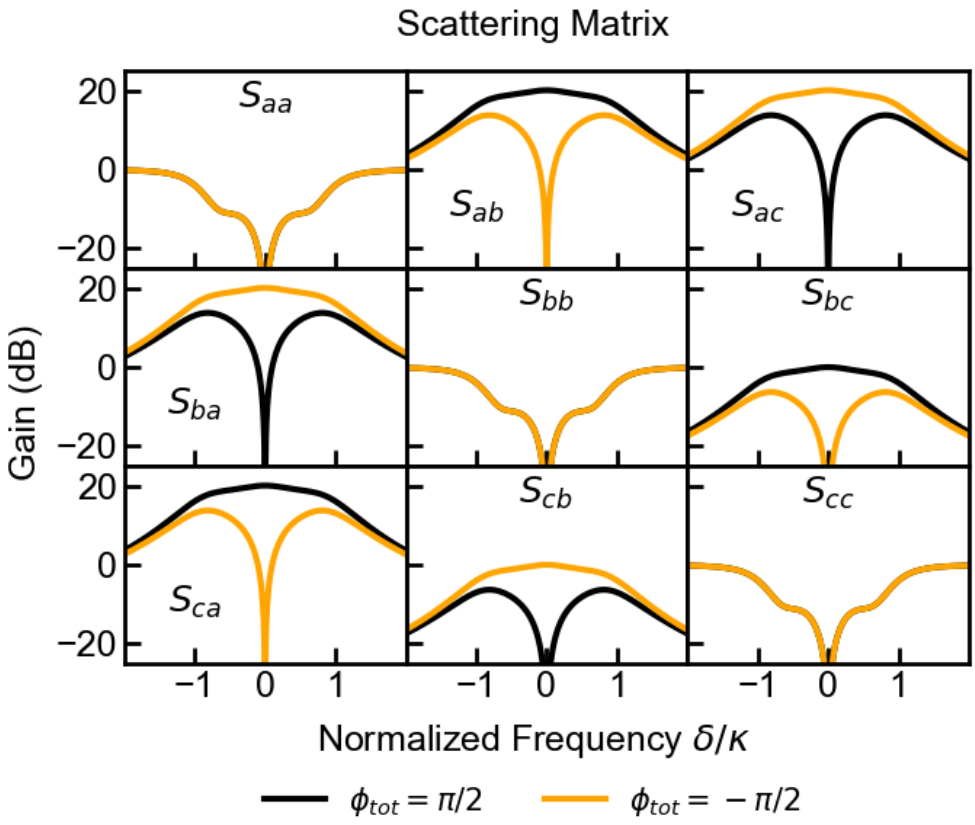

Figure 30: **Scattering matrix for directional amplification.** The pumping scheme depicted preserves the properties from GC imbalance and the circulator. Directionality depends on ϕ_{tot}, where $\phi_{\text{tot}} = \phi_{\text{ab}} + \phi_{\text{ac}} + \phi_{\text{bc}}$. When $\phi_{\text{tot}} = \pi/2$ or $-\pi/2$, the protected port will be mode b or c, respectively. Transmission gain appears from the protected port to the output port a. The other port can be an ancillary port that absorbs the back-action and prevents it from leaking into the protected port. In this plot, $\kappa_a = \kappa_b = \kappa_c = 1$ and $f_{\text{ab}} = f_{\text{ac}} = 5$.

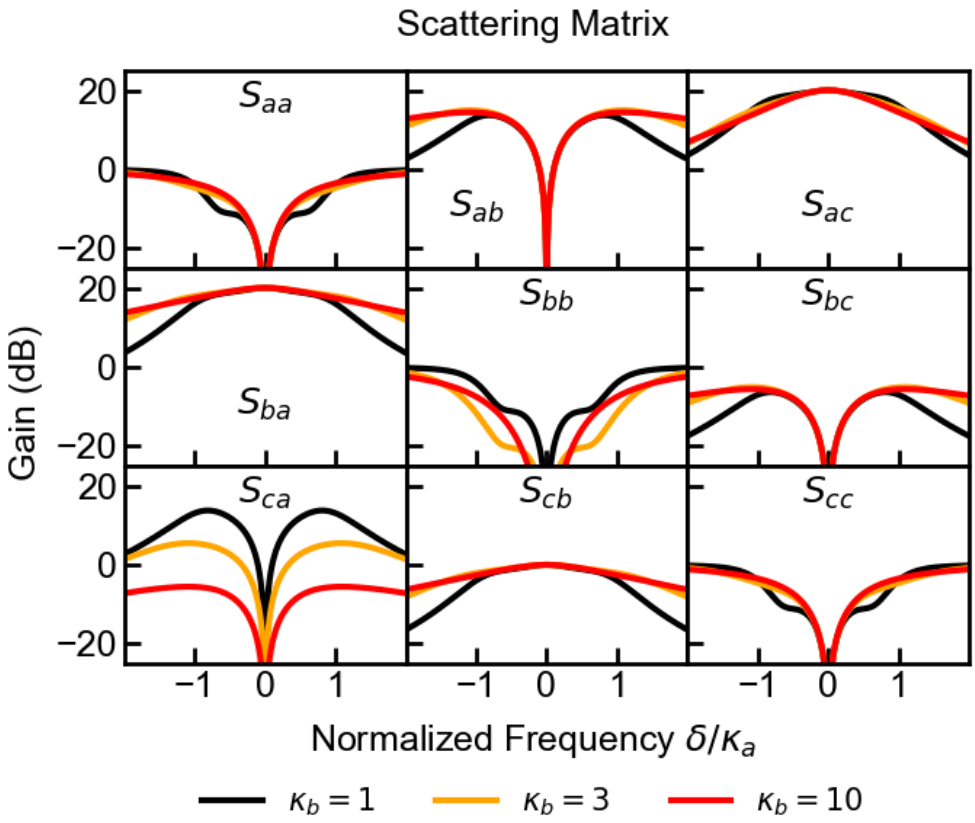

Figure 31: **Scattering matrix for ideal amplification with different κ_b.** The condition for plotting this scattering matrix is the same as Fig. 30 but for different value of κ_b at fixed $\phi\text{tot} = -\pi/2$. The purpose of varying κ_b is to minimize signal flow into the protected port when $\delta \neq 0$. When $\kappa_b = 1$, two humps appear up in S_{ca}. This indicates that when the back-action signals are off-resonance, the quantum objects will be affected. However, this situation significantly improves when κ_b becomes larger. That is, when κ_b is ten times larger, we can suppress the reverse-gain to less than unity.

However, to have multiple qubits read out by the amplifier, it is insufficient to focus on resonance, because the output cavities' frequencies are not all the same. We must be concerned with off-resonance signals. Note that the reverse transmission from the output to protected ports has significant strength when the signal is off-resonance. Another scattering element of concern is the vacuum noise from the ancillary to the output ports. These issues are addressed separately.

From the previous plot, we have assigned all κ to be the same. However, to absorb the reverse-gain, $\kappa_{ancillary}$ has to be larger than the others. In Fig. 31, we have plotted the scattering matrix with different κ_b. All the requisite properties are preserved but with better modification of the reverse-gain from the output port, S_{ca}. As κ_b becomes larger, the reverse-gain becomes suppressed.

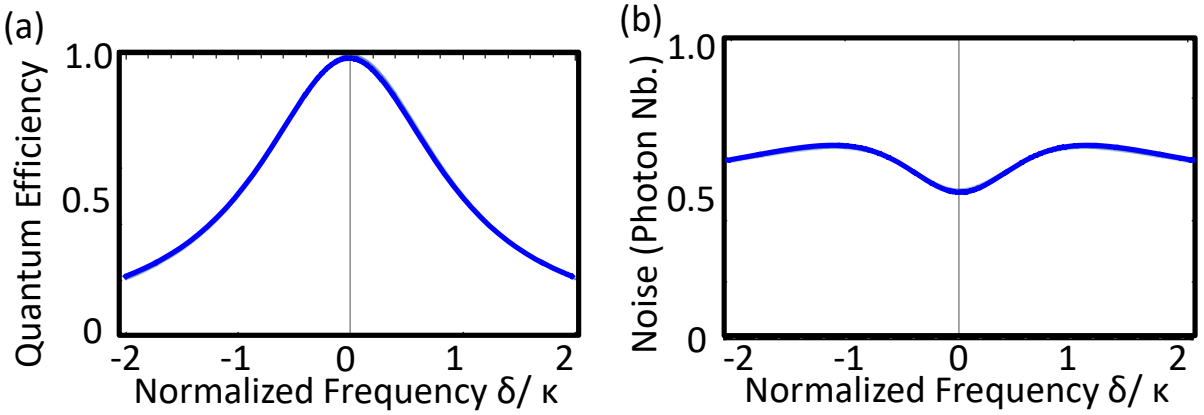

Figure 32: **(a) Quantum output efficiency.** This plot represents the loss in quantum efficiency due to additional noise being added to the output signal due to unwanted additional gain processes. **(b) Noise emitted into the protected port.**This plot represents the output fluctuations from the amplifier protected port, in units of photon number. The rise above the quantum limit of 0.5 photon at non-zero detuning is due to the finite reverse gain into the protected port from the output port.

However, the behavior of S_{ab} remains the same and becomes stronger when the signal is one κ away from resonance. In this case, b port is only connected to the vacuum noise. If we add amplified vacuum noise on the top of amplified qubits' signals, will it significantly disturb the quantum measurement?

In Fig. 32, we calculated the performance of the amplifier with regard to measurement. The figure indicates quantum output efficiency. With efficiency equaling 1, we can distinguish qubit's state with 100 % certainty, hence, we want the efficiency to be close to 1. The ideal point is still on resonance, with $\delta = 0$, where the quantum efficiency is perfect and only a minimum amount of noise is added into the protected port. For the off-resonant signal, the quantum efficiency drops due to the amount of noise added into the output port, which is coming from the ancillary port. If we are satisfied with 80 % quantum efficiency (nowadays, the average efficiency is around 60 % [75, 15, 76]), the operating window is about 1 κ. For the protected port, the vacuum noise will rise up to around 0.7 photons in the operation window, which will slightly heat up the qubit's readout cavity.

Another noticeable property of the pumping scheme: it preserves the absence of gain-bandwidth limitation characteristic of GC and GCI amplification. In Fig. 33, we compare the bandwidth with different transmission gains (solid lines), and the bandwidth remains the same, shown in light orange. Dashed lines representing reverse gain become larger when the gain is higher. This plot is generated with 10 $\kappa_a = 10\ \kappa_b = \kappa_c$.

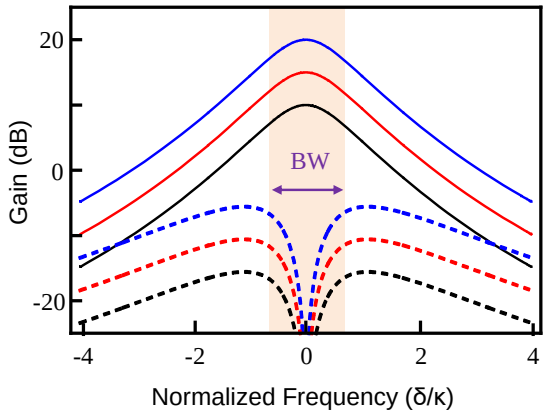

Figure 33: **Fixed bandwidth for directional amplification.** The pumping scheme preserves one of properties from GC amplification: no gain-bandwidth limitation.

3.0 Hamiltonian engineering

There are two common approaches to create a controllable quantum system. The first approach is to search for systems that exist in nature and circumspectly isolate individual parts of those system, such as single atoms and ions. Their behavior can only be described by quantum physics. However, the properties of particles are something we cannot control and often, we only have access to the system through weak interactions [77, 78, 79, 80].

The second approach is to create hand-made systems. For example, we can fabricate superconducting electronic circuits. The biggest advantage of building this quantum system is the massive amount of flexibility in how we design them. Subject only to the engineering limitations of our fabrication techniques, we can tune and tweak all the operating parameters to precisely what we want them to be.

Furthermore, we can build simple electronic circuits that have a larger size compared to natural atoms, and use them to generate macroscopic quantum behavior.

3.1 The Josephson parametric converter

A generic three-mode coupling system can be schematized as three modes shared with a mixing element, which provides the coupling terms as shown in Fig. 11 [34, 33, 64]. One example is the Josephson Parametric Converter (JPC). The JPC has three inherent modes coupled with each other through a mixing component, with the Josephson Ring modulator (JRM) sitting at the center of the device and providing not only the modes' inductance but also the nonlinearity. In this section, I will discuss the properties of the JPC and derive its Hamiltonian.

3.1.1 The Josephson ring modulator

One of the most common three-wave mixing elements in the superconducting circuit is the Josephson Ring Modulator (JRM). It was first invented at Yale in 2010 [34, 33] and has since been successfully embedded in the JPC and operated as a quantum-limited amplifier. It naturally has three inherent, orthogonal modes coupled to each other. However, the original design, see Fig. 34 (a), suffered from an intrinsic instability when the external magnetic flux through the ring exceeded a half flux quantum.

In 2012, N. Roch, E. Flurin et al. solved the instability problem by shunting the JRM with four identical linear inductors while keeping the symmetry of the ring to preserve the desired coupling [70, 81]. This method divides the loop inside the JRM into four sub-loops and releases the burden on each Josephson junction from the external flux, see Fig. 34 (b). In this section, we will derive the Hamiltonian of the shunted JRM and discuss its properties.

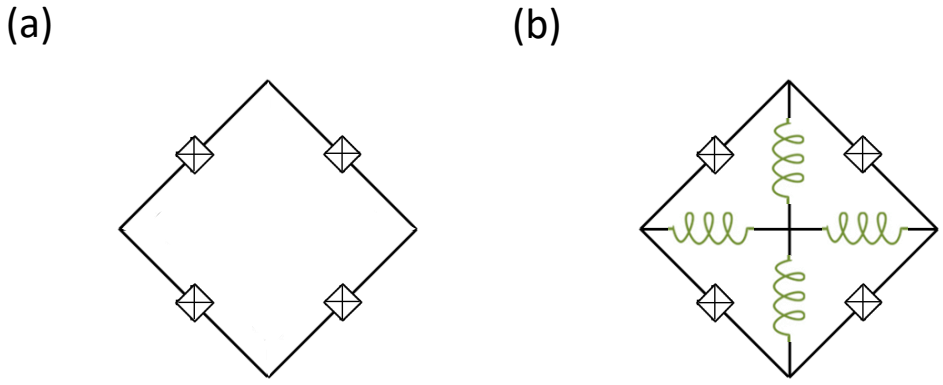

Figure 34: **(a) 4-JJs Josephson ring modulator.** The JRM ring consists of four Josephson junctions on the outside. **(b) Shunted Josephson ring modulator.** JRM with shunted linear inductances.

3.1.1.1 The shunted Josephson ring modulator

The strategy to extend the stability range of the JRM is to implement shunted inductors through a ring as shown in Fig. 35 (a). Four identical linear inductors link the four nodes together, hence defining four sub-loops, one per junction. Note that the circuit keeps the symmetry of the original ring which is essential to preserve a pure three-wave mixing Hamiltonian. Using the Josephson junctions' and linear inductors' Hamiltonian, we obtain

$$\begin{aligned} H_{\text{ShuntedJRM}} = &- E_J \left(\cos(\varphi_a) + \cos(\varphi_b) + \cos(\varphi_c)\cos(\varphi_d)\right) \\ &+ \frac{E_L}{2}\left(\varphi_\alpha^2 + \varphi_\beta^2 + \varphi_\gamma^2 + \varphi_\delta^2\right) \end{aligned} \tag{3.1}$$

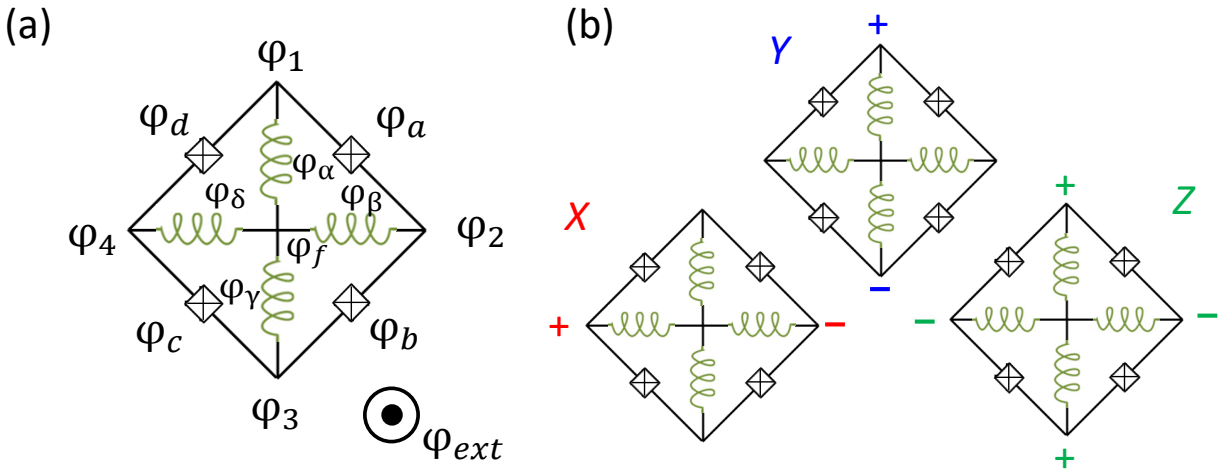

Figure 35: **(a) The circuit diagram for the shunted JRM.** The shunted JRM consists of a ring of four identical Josephson junctions shunted by four linear inductors. **(b) Eigenmodes.** The modes X, Y are differential modes while mode Z lives on all nodes of the ring.

We can replace each phase across the junction with functions of the nodes' phases.

$$\begin{cases} \varphi_a = \varphi_2 - \varphi_1 + \frac{\varphi_{\text{ext}}}{4} \\ \varphi_b = \varphi_3 - \varphi_2 + \frac{\varphi_{\text{ext}}}{4} \\ \varphi_c = \varphi_4 - \varphi_3 + \frac{\varphi_{\text{ext}}}{4} \\ \varphi_d = \varphi_1 - \varphi_4 + \frac{\varphi_{\text{ext}}}{4} \end{cases} \quad \text{and} \quad \begin{cases} \varphi_\alpha = \varphi_1 - \varphi_f \\ \varphi_\beta = \varphi_2 - \varphi_f \\ \varphi_\gamma = \varphi_3 - \varphi_f \\ \varphi_\delta = \varphi_4 - \varphi_f \end{cases}$$

φ_f is a floating point; hence, we can set it to zero. The normal modes of the circuits can be found by expanding the Hamiltonian up to the second order in $\varphi_{1,2,3,4}$. It can then be expressed as a function of the inductance matrix $\mathcal{L}$ and the flux vector $\boldsymbol{\varphi}_{\mathbf{nodes}} = (\varphi_1, \varphi_2, \varphi_3, \varphi_4)$.

$$H_{\text{ShuntedJRM}} = \boldsymbol{\varphi}_{\mathbf{nodes}} \frac{\mathcal{L}^{-1}}{2} \boldsymbol{\varphi}_{\mathbf{nodes}}{}^T + o(|\boldsymbol{\varphi}_{\mathbf{nodes}}|^2)$$

where

$$\mathcal{L}^{-1} = \begin{bmatrix} E_L{+}2E_J\cos\left(\frac{\varphi_{\text{ext}}}{4}\right) & \text{-}E_J\cos\left(\frac{\varphi_{\text{ext}}}{4}\right) & 0 & \text{-}E_J\cos\left(\frac{\varphi_{\text{ext}}}{4}\right) \\ \text{-}E_J\cos\left(\frac{\varphi_{\text{ext}}}{4}\right) & E_L{+}2E_J\cos\left(\frac{\varphi_{\text{ext}}}{4}\right) & \text{-}E_J\cos\left(\frac{\varphi_{\text{ext}}}{4}\right) & 0 \\ 0 & \text{-}E_J\cos\left(\frac{\varphi_{\text{ext}}}{4}\right) & E_L{+}2E_J\cos\left(\frac{\varphi_{\text{ext}}}{4}\right) & \text{-}E_J\cos\left(\frac{\varphi_{\text{ext}}}{4}\right) \\ \text{-}E_J\cos\left(\frac{\varphi_{\text{ext}}}{4}\right) & 0 & \text{-}E_J\cos\left(\frac{\varphi_{\text{ext}}}{4}\right) & E_L{+}2E_J\cos\left(\frac{\varphi_{\text{ext}}}{4}\right) \end{bmatrix}$$

The normal modes of the JRM are directly given by the eigenmodes of the inductance matrix. They can be expressed as a combination of node fluxes, which are eigenvectors of $\mathcal{L}^{-1}$:

$$\begin{cases} \varphi_X = \varphi_3 - \varphi_1 \\ \varphi_Y = \varphi_4 - \varphi_2 \\ \varphi_Z = \frac{1}{2}(\varphi_2 + \varphi_4 - \varphi_3 - \varphi_1) \\ \varphi_W = \frac{1}{2}(\varphi_1 + \varphi_2 + \varphi_3 + \varphi_4) \end{cases} \tag{3.2}$$

The coefficient 1/2 in both φ_Z and φ_W is used for consistency with the JRM derivation in [82]. One can solve without 1/2 and still achieve the same results. We can generalize this derivation to an N-Junction, N-port ring, see Appendix C. This technique is valid with all superconducting circuits [83]. The W mode is not coupled to the ring since its eigenvalue

is zero. This is due to the fact that all nodes have the same flux, hence, no current goes through the junctions. Therefore, the ring is coupled to three orthogonal modes: X and Y are differential modes and Z is a common mode that lives on all nodes as represented in Fig. 3.1. We can use the same method to derive eigenmodes of an N-JJ and N-port ring, which is useful when we have to design multiple-mode systems, as mentioned in Appendix C.

$$\begin{aligned} H_{\text{ShuntedJRM}} = &- 4E_J \cos\Big(\frac{\varphi_X}{2}\Big) \cos\Big(\frac{\varphi_Y}{2}\Big) \cos(\varphi_Z) \cos\Big(\frac{\varphi_{\text{ext}}}{4}\Big) \\ &- 4E_J \sin\Big(\frac{\varphi_X}{2}\Big) \sin\Big(\frac{\varphi_Y}{2}\Big) \sin(\varphi_Z) \sin\Big(\frac{\varphi_{\text{ext}}}{4}\Big) \\ &+ \frac{E_L}{4}\left(\varphi_X^2 + \varphi_Y^2 + 2\varphi_Z^2\right) \end{aligned}$$

One can expand the Hamiltonian around the minimum points of the ground state energy. Here, we assume the minimum point is $\boldsymbol{\varphi_{min}} = (\varphi_{Xmin}, \varphi_{Ymin}, \varphi_{Zmin})$ and $\boldsymbol{\varphi} = (\varphi_X, \varphi_Y, \varphi_Z)$.

$$\begin{aligned} H_{\text{ShuntedJRM}} = &\frac{1}{4}\left[E_L + 2E_J \cos\Big(\frac{\varphi_{\text{ext}}}{4}\Big) \cos(\boldsymbol{\varphi_{min}}) + 2E_J \sin\Big(\frac{\varphi_{\text{ext}}}{4}\Big) \sin(\boldsymbol{\varphi_{min}})\right]\left(\varphi_X^2 + \varphi_Y^2\right) \\ &\frac{1}{2}\left[E_L + 4E_J \cos\Big(\frac{\varphi_{\text{ext}}}{4}\Big) cos(\boldsymbol{\varphi_{min}}) + 4E_J \sin\Big(\frac{\varphi_{\text{ext}}}{4}\Big) \sin(\boldsymbol{\varphi_{min}})\right]\varphi_Z^2 \\ &+ H_{\text{higher-order}}\left(\varphi_X, \varphi_Y, \varphi_Z\right) \end{aligned} \tag{3.3}$$

where

$$\begin{aligned} \cos(\boldsymbol{\varphi_{min}}) &= \cos\Big(\frac{\varphi_{Xmin}}{2}\Big) \cos\Big(\frac{\varphi_{Ymin}}{2}\Big) \cos(\varphi_{Zmin}) \\ \sin(\boldsymbol{\varphi_{min}}) &= \sin\Big(\frac{\varphi_{Xmin}}{2}\Big) \sin\Big(\frac{\varphi_{Ymin}}{2}\Big) \sin(\varphi_{Zmin}) \end{aligned}$$

Comparing Eq. 3.3 and the inductance energy in Eq. A.1, we obtain the inductance expression

$$\begin{aligned} L_{X,Y}^{-1} &= \frac{1}{2\varphi_0^2}\left[E_L + 2E_J \cos\Big(\frac{\varphi_{\text{ext}}}{4}\Big) \cos(\boldsymbol{\varphi_{min}}) + 2E_J \sin\Big(\frac{\varphi_{ext}}{4}\Big) \sin(\boldsymbol{\varphi_{min}})\right] \\ L_Z^{-1} &= \frac{1}{\varphi_0^2}\left[E_L + 4E_J \cos\Big(\frac{\varphi_{\text{ext}}}{4}\Big) cos(\boldsymbol{\varphi_{min}}) + 4E_J \sin\Big(\frac{\varphi_{\text{ext}}}{4}\Big) \sin(\boldsymbol{\varphi_{min}})\right] \end{aligned}$$

The higher order terms can be calculated from Eq. 3.1.1.1.

$$H_{\text{higher-order}}\left(\varphi_X, \varphi_Y, \varphi_Z\right) = \sum_{i=3}^{\infty} \sum_{n,m,l=0}^{i} \frac{F_{nml}\left(\boldsymbol{\varphi_{min}}\right)}{n!m!l!} \varphi_X^n \varphi_Y^m \varphi_Z^l, \quad \text{for} \;\; n+m+l=i \tag{3.4}$$

The power of the expression is determined by i while the coefficient takes the following form

$$F_{nml}\left(\boldsymbol{\varphi_{min}}\right) = \left.\frac{\partial^{n+m+l} H_{\text{ShuntedJRM}}\left(\boldsymbol{\varphi}\right)}{\partial\varphi_X^n \partial\varphi_Y^m \partial\varphi_Z^l}\right|_{\boldsymbol{\varphi}=\boldsymbol{\varphi_{min}}}$$

The general and most recognized three-wave mixing term can be calculated from the above equation with $i = 0$ at the stable solution, $\boldsymbol{\varphi_{min}} = (0, 0, 0)$.

$$H_{\text{mixing}}\left(\varphi_X, \varphi_Y, \varphi_Z\right) = -E_J \sin\Big(\frac{\varphi_{\text{ext}}}{4}\Big)\varphi_X\varphi_Y\varphi_Z$$

When the ground state energy is degenerate or the ring has an asymmetry caused by non-identical junctions or sub-loop areas, one will find $\varphi_{min} \neq (0, 0, 0)$, which will generate additional three-wave mixing, such as degenerate amplification coupling terms. We will discuss this case in section 3.1.2.3.

We now introduce a dimensionless parameter that we will use to characterize our circuits. $\beta = E_{\text{shunt}}/E_J = L_J/L_{\text{shunt}} = \phi_0^2/L_{\text{shunt}}E_J$, measures the strength of the shunt inductors relative to the effective inductance of the Josephson junctions. We note that $\beta = 0$ is the case when the JRM is unshunted. To see this, in an unshunted-JRM model, the center node and the inner shunted linear inductance are fictitious, i.e. there should be no energy contribution from these linear inductors, which means $E_{\text{shunt}} = 0, \beta = 0$. To make sure the expansion is valid throughout the entire external flux range, β should be sufficiently large to ensure that $\varphi_1 = \varphi_2 = \cdots = 0$ is the global minimum of $H_{\text{ShuntedJRM}}$ and hence the JPC has a single, well-defined ground state at the null point.

We can now analyze the degeneracy of the ground states of the shunted JPC. Specifically, to find the degeneracy of the ground state we count the number of global minima of $H_{\text{ShuntedJRM}}$. We numerically find the global minima of the JRM Hamiltonian by forming a set of possible minimum points by randomly seeding a numerical minimum with initial values of φ_1, φ_2, φ_3, and φ_4. From this set, we select the minima that correspond to the smallest values of $H_{\text{ShuntedJRM}}$, and finally we discard repeated points. In Fig. 36 (a), we plot the degeneracy of the JRM ground state as we sweep the external magnetic flux and the shunting parameter β. The blue region in the plots correspond to conditions under which

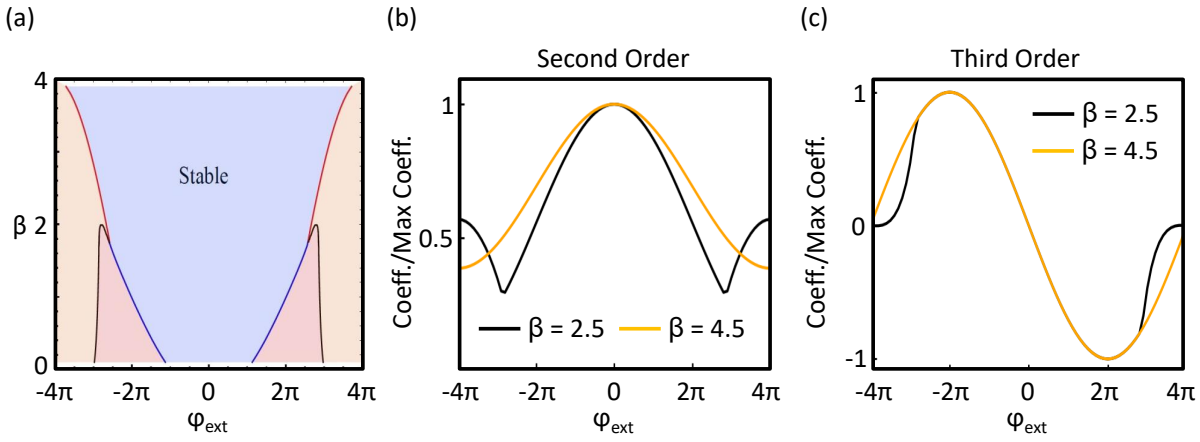

Figure 36: **(a) The degeneracy of the ground state without stray inductance.** We sweep the shunt parameter β and external magnetic flux φ_{ext}. The blue, orange and red region show the parameter regimes where the JRM ground state is non-degenerate, two-fold degenerate and four-fold degenerate. The non-degenerate regime is considered stable. The red, blue, and black lines show the phase boundaries between stable/two-fold, stable/four-fold and two-fold/four-fold regimes. **(b) Normalized second order term with different β.** We show the corresponding dynamics for two different values of β. When the circuit has no degeneracy, there exists only one lobe over a whole flux quantum. When the circuit has degeneracy, two side humps will appear in the degenerate regime.**(c) Normalized third order term with different β.** Similarly, we can plot the same case but for the third order term, where we see that the only difference is inside the degenerate regime. The three wave mixing term becomes weaker toward $\pm 4\pi$.

the JRM has a single global minimum; hence,the JPC has a non-degenerate ground state, while the orange and red regions corresponds to doubly- and quadruply-degenerate ground states.

As we decrease the inductance of the shunts, states with circulating currents move up in energy, and hence the ground state degeneracy is lifted. In other words, larger β corresponds to less degeneracy. In the absence of stray inductors, all even order terms (beyond 2^{nd} order) in $H_{\text{ShuntedJRM}}$ become zero when the external magnetic flux bias is set to 2 π. We find that at this flux bias, the ground state is non-degenerate for $\beta > 1.0$, which is the minimum requirement for operation of the nulled JPC. Additionally, we find that the ground state is non-degenerate for all values of the magnetic flux bias when $\beta > 4.0$.

The easiest way to observe the degeneracy of the circuit is to monitor the flux response of the mode's frequency, as shown in Fig 36 (b). In the stable regime, the ground state energy has node flux combination, $\varphi_1 = \varphi_2 = \varphi_3 = \varphi_4 = 0$. If the whole flux range has only the stable solution, we observe one huge lobe. When it enters the degenerate regime, the current configuration changes, and a tiny lobe can be seen toward $\pm 4\ \pi$. By fitting the experimental result to the theory, we can determine the β of the device.

Another interesting side effect in the degenerate regime is that the $\varphi_X \varphi_Y \varphi_Z$ term becomes smaller when it tends towards $\pm 4\ \pi$. In an ideal scenario, meaning all Josephson junctions are identical and the sub-loop areas are the same, all third-order terms will gradually vanish towards the end of a flux quantum. If there is any asymmetry of the ring, other third-order terms will appear and even become significant, which will be discussed in 3.1.2.3.

3.1.1.2 Effects of fourth-order terms

To operate the JRM in a stable regime over the whole φ_{ext}, E_J on the outside arm of the ring has to be at least four times larger than that of E_L. However, to explain the detailed behavior of the device, the higher order terms need to be taken into account. In this section, we expand the Hamiltonian one higher order up to fourth-order, and explain how these terms in the Hamiltonian affect multiple parametric processes.

The JRM Hamiltonian expanded up to fourth order can be obtained from Eq. 3.3. Similar

to the third order terms, the fourth order terms are

$$H_{\text{fourth}}\left(\varphi_X,\varphi_Y,\varphi_Z\right)=\sum_{n,m,l=0}^{4}\frac{F_{nml}\left(\varphi_{Xmin},\varphi_{Ymin},\varphi_{Zmin}\right)}{n!m!l!}\varphi_X^n\varphi_Y^m\varphi_Z^l \quad , \quad \text{for} \;\; n+m+l=4 \tag{3.5}$$

After the rotating wave approximation, some terms in Eq. 3.5 will not survive, which leads us to

$$H_{\text{Kerr}}\left(\varphi_X,\varphi_Y,\varphi_Z\right)=\sum_{n,m,l=0}^{4}\frac{F_{nml}\left(\varphi_{Xmin},\varphi_{Ymin},\varphi_{Zmin}\right)}{n!m!l!}\varphi_X^n\varphi_Y^m\varphi_Z^l \tag{3.6}$$

$$\text{for} \;\; n+m+l=4 \;\; \text{and} \;\; n,m,l\in 0,2,4$$

We can define two different kinds of fourth order terms (Kerr terms): Self-Kerr and Cross-Kerr. Self-Kerr describes the mode's non-linearity with respect to its own occupation, such as the anharmonicity of the qubit. Typically it is expressed as $H_{\text{Self-Kerr}}\propto\varphi_X^4\propto\varphi_Y^4\propto\varphi_Z^4$. The other type of Kerr, Cross-Kerr, indicates how a mode's frequency is affected by another mode and usually is expressed as $H_{\text{Cross-Kerr}}\propto\varphi_X^2\varphi_Y^2\propto\varphi_X^2\varphi_Z^2\propto\varphi_Y^2\varphi_Z^2$.

With the presence of these Kerr terms, multiple parametric processes become extremely hard to operate. When too many photons enter the modes, the Kerr terms become non-negligible, and it influences the mode's frequency. As previously discussed, multiple parametric processes rely on interference, which depends on pump and mode frequencies. If mode frequencies are shifted away due to the Kerr terms, the pump is no longer on the optimal condition, and hence multiple parametric processes will no longer be correctly tuned.

As an example, let us consider only one Kerr in the system, K_{XY}, for now. The harmonic terms of mode a become

$$H_X=\frac{1}{4}\left[E_L+2E_J\cos\!\left(\frac{\varphi_{\text{ext}}}{4}\right)\cos(\boldsymbol{\varphi_{min}})+2E_J\sin\!\left(\frac{\varphi_{\text{ext}}}{4}\right)\sin(\boldsymbol{\varphi_{min}})+4K_{XY}\varphi_Y^2\right]\varphi_X^2$$

where K_{XY} is from the *Eq.* 3.6 with $n=m=2$ and $l=0$.

From the above equation, we notice that the second-order terms of mode X, which are equivalent to the mode's frequency, are altered by the Kerr term, 4 $K_{XY}\varphi_Y^2$. φ_Y^2 is linked to the photon number in mode Y, which will be modified due to the pump strength.

In the Fig. 37, the color represents the strength of pump power for the single gain process, starting from weak (light blue) to strong (dark blue). When the power becomes stronger, more photons enter mode Y; therefore, $K_{XY}\varphi_Y^2$ becomes non-negligible and affects the bare mode frequency. Due to the shift, the pump condition is no longer at the sum of two modes' frequencies with detuning. Therefore, we can observe that the peak shifts away from resonance at the origin. For a single pump process, this is not a big deal. One can adjust the pump frequency to move the gain peak back to where it originally was. Because K is negative, in reflection, the gain peak will shift to lower frequency when pump strength is increased. Meanwhile, in transmission, the peak must move to a higher frequency due to the conservation of energy.

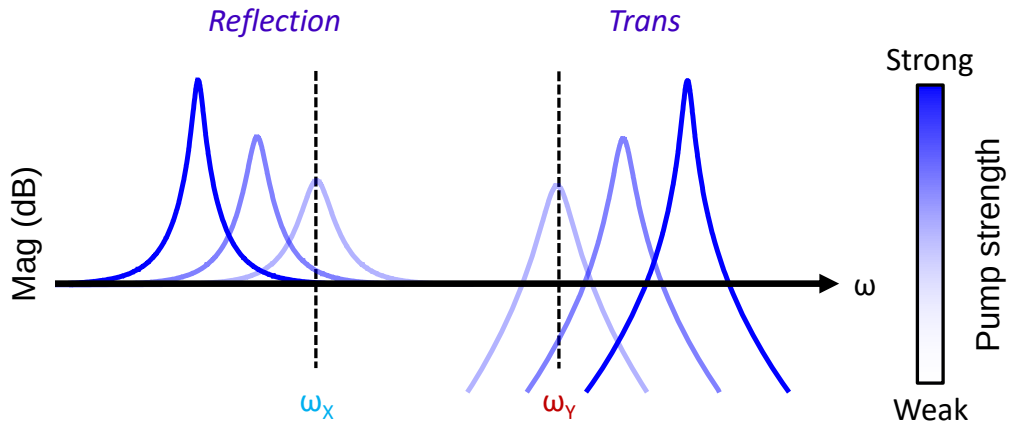

Figure 37: **Gain with the presence of a Kerr.** When the pump power becomes stronger, from light blue to dark blue, the effect of the Kerr term becomes observable. The gain peak will be shifted away from the bare resonance when the power becomes stronger.

Similarly, we can perform another basic parametric process, conversion, with the presence of the same Kerr term, K_{ab}. Mode a's frequency moves to lower frequency when the pump power becomes larger, see Fig. 38. Again, it is not a big deal if one only needs a conversion

process. However, Kerr shifts become a problem for multiple parametric processes. For example, using GC amplification with the presence of a single Kerr, K_{XY}, relies heavily on interference between modes. If one does not match, then the properties of the parametric process will not be ideal. As we can see in Fig. 39, when both processes are on, in reflection the gain peak and conversion dip align right on top of each other. However, in transmission, we notice that gain and conversion do not align together.

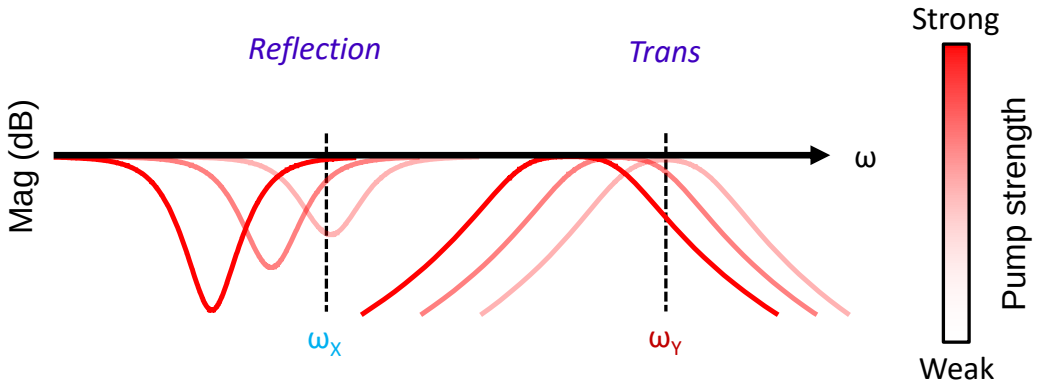

Figure 38: **Conversion with the presence of a Kerr.** When the pump power becomes stronger, the effect of the Kerr term becomes observable. The conversion dip/peak is shifted to lower frequency in reflection/transmission.

In the previous example, we have only considered one Kerr term, which affects multiple parametric processes. In principle, we can fine-tune the pump frequency and power until the pump conditions match our pumping scheme. However, in a real experiment, we have to consider all different kinds of Kerr terms and even higher-order terms, which increases the difficulty of pumping at the right condition. Therefore, an ideal scenario is to engineer circuits that produce only the desired terms in the Hamiltonian.

To build a pure three-wave mixing device, we have to control the Hamiltonian and make sure undesired terms are small or even nonexistent. All circuits that involve Josephson junctions have higher-order terms after Taylor expanding their Hamiltonia. However, we note that even order terms in the expression of H_{Kerr} have a common coefficient $\cos\left(\frac{\varphi_{\text{ext}}}{4}\right)$. This

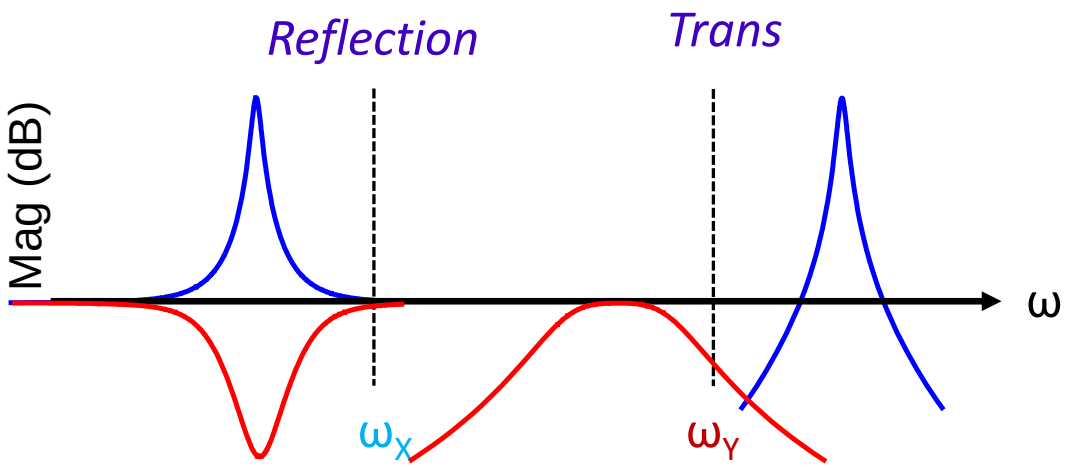

Figure 39: **GC with the presence of a Kerr.** With the presence of K_{ab}, when both gain and conversion processes are simultaneously turned on at a fixed pump power (dark green from the previous two figures), we observe the peak of gain and dip of conversion that align with each other in reflection but not transmission.

coefficient goes to zero automatically when $\varphi_{\text{ext}} = \pm 2\ \pi$, which implies that by controlling the external flux, Kerr terms can be eliminated.

In some papers [84, 46], the JRM is shunted with larger Josephson junctions, which gets rid of the hysteresis problem that exists in a 4-Josephson junction ring. If we compare the fourth order terms between linear-shunted and Josephson-shunted designs, see from Fig. 40, Cross-Kerr indeed is zero at $\pm 2\ \pi$; however, Self-Kerr is zero only for the linear shunted design. Due to this reason, throughout the rest of my thesis I will only focus on the linear-shunted JRM.

In section 5, we also present another drawback of the fourth-order Kerr. We present experimental data and theoretical calculations showing that the Kerr terms inherent in Josephson junctions are the dominant factor for limiting saturation power. The Kerr-based theory has the unusual property of causing saturation at both lower and higher gains, depending on bias conditions.

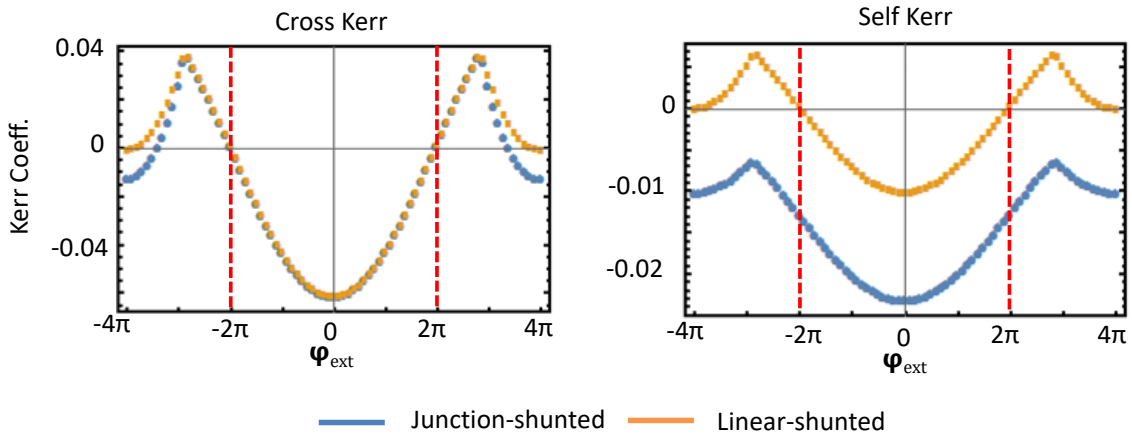

Figure 40: **Kerr terms for shunted JRM.** We can shunt the JRM with linear/non-linear inductors. However, to control Kerr terms, we prefer linear components. Cross-Kerr can be cancelled in both cases when the external flux is at $\varphi_{\text{ext}} = \pm 2\ \pi$. However, we are not so lucky on the Self-Kerr. It crosses the zero point only when the JRM is shunted with linear components.

3.1.2 Consideration of stray inductance and the participation ratio

In this subsection, I want to build a bridge between the Hamiltonian and fabrication. Every metal we put down on the circuit affects device performance, such as the trace connected from the input/output ports to the JRM or the metal used to send the signal from the trace to Josephson junctions. To understand the whole picture of the circuit, every piece of metal used to fabricate the device plays a role in the Hamiltonian. This is a crucial point in design considerations and underlines the importance of Hamiltonian engineering.

There are two major components in the circuit that we want to take into account: stray inductance and external inductance. Stray inductance is introduced by the trace connected from the Josephson junction to the node of the JRM. This connection is necessary, of course, but we cannot design it to be so long that the stray inductance dominates the whole circuit.

External inductance usually comes from the resonator that hooks up to the ring. As per the discussion in the section 3.1.3, when external resonators are used to drive the JRM, external inductance will exist in the resonators.

3.1.2.1 Stray inductance

The effective circuit diagram of our inductively shunted JRM is depicted in Fig. 41. The key ingredients of the model are (1) the Josephson junctions, (2) the shunt inductors labeled L_{shunt}, and (3) the stray inductance on the outer arms of the JRM, labeled L_{stray}. In this setup, the outer ring of the JRM, which contains the Josephson junctions, is the source of the non-linear couplings between the modes of the JPC. The shunt inductors are used to control the degeneracy of the ground state of the JPC at finite magnetic flux bias. They lift the energy of states in which current flows through the shunt inductors, thus preventing the device from switching to these undesired configurations. The stray inductors are an inherent property of the aluminum traces which we use to make the outer ring of our JRM.

The circuit is described by the Hamiltonian $H_{\text{JRM}} = H_{\text{shunt}} + H_{\text{out}}$, composed of the shunt Hamiltonian

$$H_{\text{shunt}} = \sum_{i=1}^{4} \frac{\phi_0^2}{2L_{\text{shunt}}} \left(\varphi_i - \varphi_f\right)^2 ,$$

and the outer ring Hamiltonian

$$H_{\text{out}} = \sum_{i=1}^{4} H_{\text{seg}} \left(\varphi_{i+1} - \varphi_i - \varphi_{\text{ext}}/4\right) .$$

Here, φ_i is the superconducting phase at the i-th vertex of the JRM, see Fig. 41, and we use the notation $\varphi_5 = \varphi_1$. The phase gain due to the externally applied flux bias in each of the four outer arms of the JRM is $\varphi_{\text{ext}}/4$. The energy of an outer ring segment phase biased to φ is

$$H_{\text{seg}}(\varphi) = \min_{\chi} \frac{\phi_0^2}{2L_{\text{stray}}}(\varphi - \chi)^2 - E_J \cos(\chi), \tag{3.7}$$

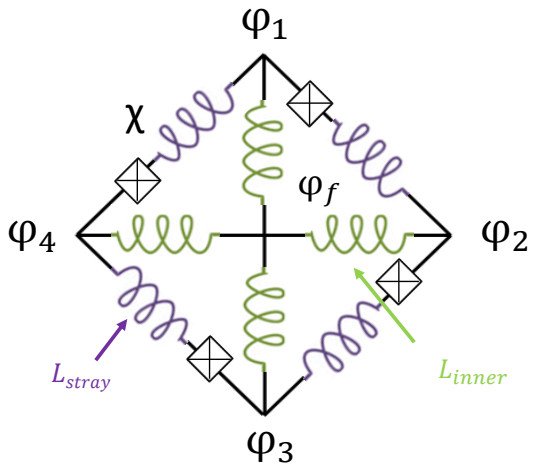

Figure 41: **Linear shunted JRM with stray inductance.** To calculate a more realistic Hamiltonian, we have to consider stray inductance, which appears from the metal trace used to connect Josephson junctions.

and the minimization with respect to χ results in a transcendental equation that ensures that the current in the outer inductor is identical to the current in the Josephson junction.

Next, we analyze the non-linear couplings between the JPC modes. Here, we focus on the case in which the JPC has a non-degenerate ground state centered on $\varphi_1 = \varphi_2 = \cdots = 0$. We obtain the non-linear couplings between the normal modes of the JPC by taking derivatives of H_{JRM} with respect to the canonical variables. For the self- and cross-Kerr terms we find:

$$K_{XX} = \frac{1}{4!}\frac{\partial^4 H_{\text{JRM}}}{\partial \varphi_X^4} = \frac{1}{6} H_{\text{seg}}^{(4)}(\varphi_{\text{ext}}/4) = K_{YY} = K_{ZZ},$$
$$K_{XY} = \frac{1}{4}\frac{\partial^4 H_{\text{JRM}}}{\partial \varphi_X^2 \partial \varphi_Y^2} = H_{\text{seg}}^{(4)}(\varphi_{\text{ext}}/4) = K_{XZ} = K_{YZ}.$$

Observe that all of the Kerr terms are proportional to the fourth derivative of $H_{\text{seg}}(\varphi)$ with respect to φ evaluated at $\varphi = \varphi_{\text{ext}}/4$. The cosine Hamiltonian of the junction means that the Kerr naturally passes through zero, if the desired flux configuration holds to the

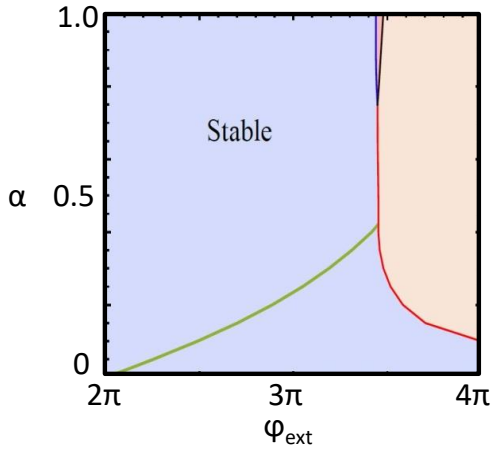

Figure 42: **The JRM's ground state degeneracy with stray inductors.** We fix $\beta = 4.5$, and calculate the ground state degeneracy as we sweep the stray parameter α and external magnetic flux φ_{ext}. The green line shows the position of the nulling point. The nulling point shifts to higher external magnetic flux as we increase the stray parameter α and finally hit the unstable regime.

required flux. Moreover, all six Kerr terms vanish identically at a single null point. In the absence of stray inductance, $L_{\text{stray}} \rightarrow 0$, the null occurs at $\phi_{\text{ext}} = 2\,\pi$; the null point persists and shifts towards $\phi_{\text{ext}} = 4\pi$ as L_{stray} increases.

We now introduce another dimensionless parameter that we will use to characterize our circuits. $\alpha = L_{\text{stray}}/L_J = L_{\text{stray}}E_J/\phi_0^2$ measures the strength of the Josephson junction with respect to the stray inductance. Preferably $\alpha \ll 1$ to ensure that the Josephson energy dominates the stray inductance. At the same time, β should be sufficiently large to ensure that $\varphi_1 = \varphi_2 = \cdots = 0$ is the global minimum of H_{JRM} and hence the JPC has a single, well defined ground state at the null point. For the case $\alpha = 0$, the non-degeneracy of the ground state for all values of φ_{ext} is ensured by setting $\beta > 4$.

Now, we take stray inductance into account. The stray inductors increase the inductance

of the segments of the outer ring of the JRM, effectively decreasing β (as compared to the case $\alpha = 0$). In Fig. 42, we fix $\beta = 4.5$ and sweep the parameter α and external magnetic flux φ_{ext}. We notice that as we increase α, the region of degenerate ground states reappears near maximal magnetic flux bias. Further, we observe that as we increase α the Kerr nulling point moves from $\varphi_{\text{ext}} = 2\pi$ towards $\varphi_{\text{ext}} = 3.5\ \pi$, at which point it hits the degenerate ground state region, corresponding to $\alpha \approx 0.4$.

3.1.2.2 Participation ratio

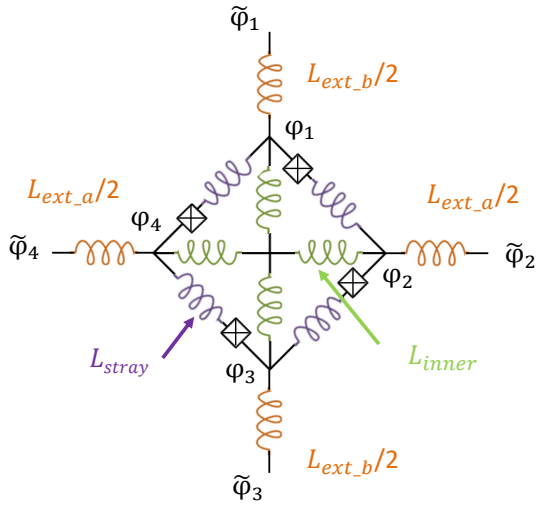

Figure 43: **JRM with external inductors.** The external inductors act as a flux divider to redistribute the flux across the JRM.

In this subsection, we focus on the effects of participation ratio by introducing external linear inductors in series with the JRM circuit, L_{ext} as shown in Fig. 43. When resonators are connected to the JRM, the flux injected from the microwave ports is shared between the JRM and the external resonators and hence the JRM nonlinearity is attenuated. To model this effect, four outer linear inductors L_{ext} are added in series with the JRM circuit. These external inductance and the JRM can be treated as a "flux-divider" type circuit. Further, as the input-output ports are connected to the outer nodes and there are no capacitors

connecting the inner nodes to ground, we treat the fluxes of outer nodes ($\tilde{\varphi}_j$) as free coordinates, while the inner node fluxes (φ_j) are restricted by the Kirchhoff's current relation. The potential energy of JRM becomes

$$\begin{aligned} H &= H_{\text{Lext}} + H_{\text{ShuntedJRM}} \\ &= \sum_j \frac{\varphi_0^2}{L_{\text{ext}}} (\tilde{\varphi}_j - \varphi_j)^2 + H_{\text{ShuntedJRM}} \end{aligned}$$

We introduce a new variable, participation ratio, p, to indicate how much energy is distributed to the JRM with given external inductance. Participation ratio is defined as

$$\begin{aligned} p_i &= \frac{L_{\text{i}}}{L_{\text{i}} + L_{\text{ext}_{\text{i}}}} \\ p_{\text{ext}_{\text{i}}} &= \frac{L_{\text{ext}_{\text{i}}}}{L_{\text{i}} + L_{\text{ext}_{\text{i}}}} \end{aligned} \tag{3.8}$$

where $i \in X, Y, Z$.

From Eq. 3.8, we can see that p_i and $p_{\text{ext}_{\text{i}}}$ is smaller than 1. To describe how much flux is distributed to the JRM, we can express the mode's flux as a function of participation ratio and original φ_i

$$\varphi_{p_i} = p_i \varphi_i$$

We can further combine above equation into $H_{\text{ShuntedJRM}}$ and calculate how participation changes the Hamiltonian. Using three-wave mixing and Kerr terms without the effect of stray inductance as examples, we obtain

$$H_{\text{mixing}} \left(\varphi_{P_X}, \varphi_{P_Y}, \varphi_{P_Z}\right) = \sum_{n,m,l=0}^{3} \frac{F_{nml} \left(\varphi_{P_{X}min}, \varphi_{P_{Y}min}, \varphi_{P_{Z}min}\right)}{n!m!l!} \varphi_{P_X}^n \varphi_{P_Y}^m \varphi_{P_Z}^l$$

$$\text{for } \; n + m + l = 3$$

$$H_{\text{Kerr}}\left(\varphi_{P_X},\varphi_{P_Y},\varphi_{P_Z}\right)=\sum_{n,m,l=0}^{4}\frac{F_{nml}\left(\varphi_{P_{X}min},\varphi_{P_{Y}min},\varphi_{P_{Z}min}\right)}{n!m!l!}\varphi_{P_X}^{n}\varphi_{P_Y}^{m}\varphi_{P_Z}^{l}$$

$$\text{for}\ \ n+m+l=4\ \ \text{and}\ \ n,m,l\in 0,2,4$$

From the above equations, we notice that the coefficient of each term is modified by participation ratio. Naively, one would think participation only reduces each term's strength but leaves the form of each of the Hamiltonian terms alone. But actually, it fundamentally changes each term in the Hamiltonian and this can even be observed in the modulation of the flux response. This is because L_i is also a function of φ_{ext} and hence, the participation ratio is different across the whole range of external flux, see Fig. 44.

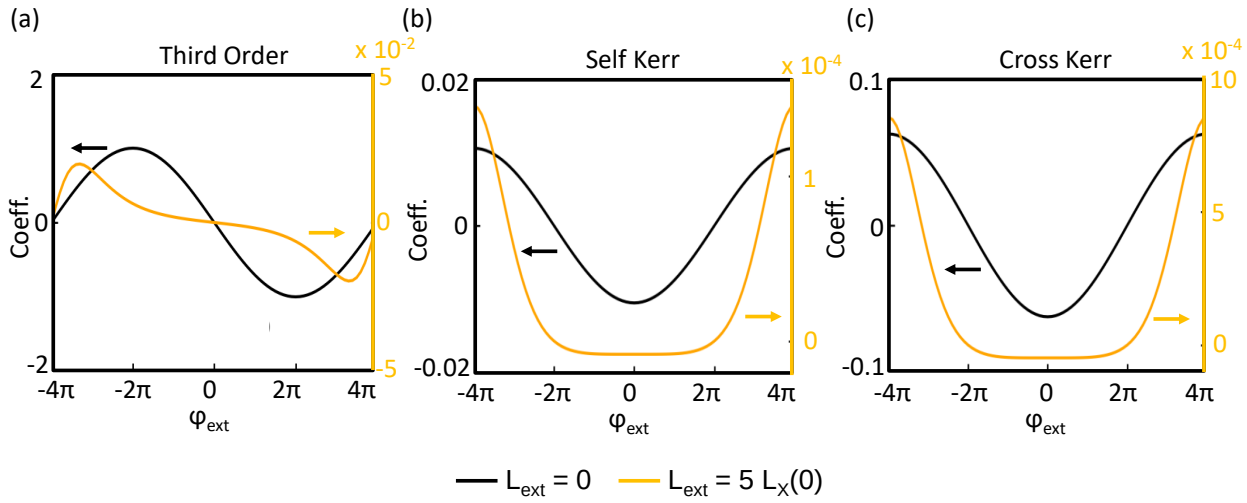

Figure 44: **(a) Third order term with participation ratio.** The black line is without consideration of participation ratio while the yellow line has external inductance five times larger than mode X's inductance at $\varphi_{\text{ext}}=0$. The magnitude of the coefficient is reduced by at least 100 times. The shape is distorted as well. **(b) and (c) Kerr terms with participation ratio.** Similarly, the magnitude is significantly smaller when the participation ratio is taken into account. Also, the yellow line shows a flat regime around $\varphi_{\text{ext}}=0$.

With the presence of the participation ratio, the minimum and maximum of the third order coefficient appear around $\varphi_{\text{ext}}=\pm 4\ \pi$ instead of at $\varphi_{\text{ext}}=\pm 2\ \pi$. For Kerr terms, both

Self- and Cross-Kerr have a sinusoidal pattern with a global minimum right at $\varphi_{\text{ext}} = 0$. When the participation ratio is taken into account, the minimum shows up for a range instead of a single point. Also, sharp rising points are located at $\varphi_{ext} = \pm 2\ \pi$.

3.1.2.3 Asymmetry of the ring

In an actual experiment, an ideal shunted JRM, including identical junctions and sub-loops, can be a challenge to realize due to the limitations of fabrication, which will be discussed in the Appendix E. The asymmetric ring not only changes coefficients of the Hamiltonian, but also creates additional terms. The most significant impact is in the third-order terms. As we have discussed early in this section, the most general three-wave mixing term, Eq. 3.1.1.1, can be achieved at the stable solution, $\boldsymbol{\varphi_{min}} = (0, 0, 0)$. However, when asymmetric junctions are introduced, the stable solution deviates from the original one, and might become $\varphi_{\{Xmin,Ymin,Zmin\}} \neq 0$. Due to this reason, we can obtain degenerate gain couplings, such as $\varphi_X^2\varphi_Z, \varphi_Y^2\varphi_Z$, see Fig. 45 (a). Moreover, asymmetric sub-loops create different periodic patterns in the system, as shown in Fig. 45 (b) and (c).

3.1.3 Circuit design

To form a JPC, external resonators have to connect to the JRM in a differential fashion to drive the modes. One can use a hybrid to generate a voltage difference across two ends of the JRM; this type of operation is often referred to as differential amplification. However, using a hybrid has some drawbacks: (a) hybrid is too big to integrate on-chip with the JPC, the easiest way is to use a commercial one, which is lossy and bulky; therefore it degrades quantum efficiency. (b) the input signal splits into two parts after a hybrid. This implies that the physical cable length from the hybrid to the chip is essential since the cable length contributes an additional phase to the signal. Due to all the above reasons, people have changed from the hybrid design to single-ended designs. In this section, two main single-ended designs will be discussed.

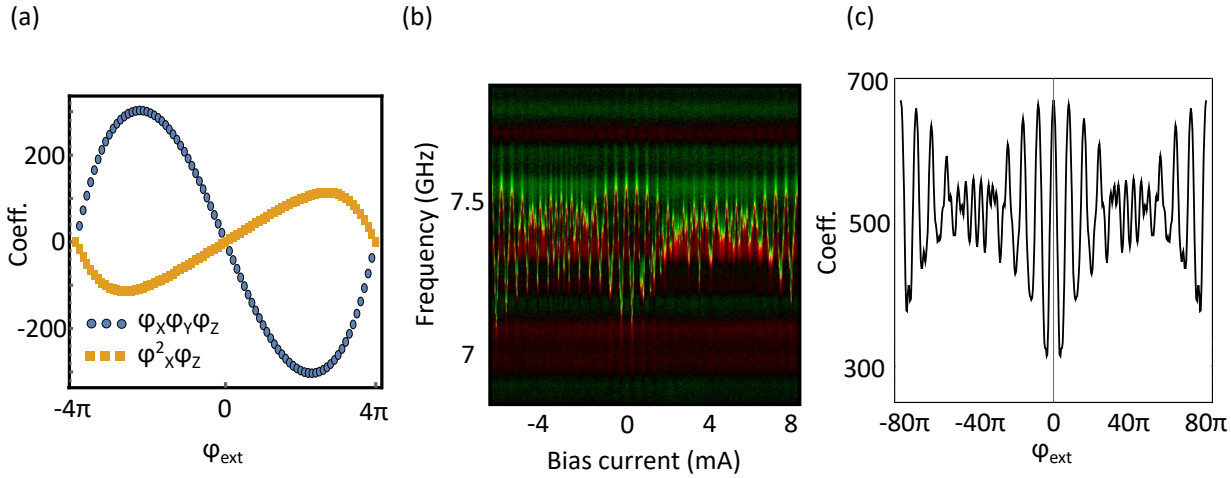

Figure 45: **(a) Degenerate and non-degenerate gain on an asymmetric JRM.** Assuming two junctions on the ring are 0.2 times larger than others at $\beta = 4.5, \alpha = 0$ and $p = 1$, the JRM has the ground state energy solution at $\varphi_{Xmin,Ymin,Zmin} \neq 0$, which introduces the opportunity of creating degenerate gain coupling terms. **(b) and (c) Frequency modulation with asymmetric sub-loops from experimental result and theory.** Different area of sub-loops are introduced in the ring and it causes a few periodic patterns to coexist and interfere in the frequency modulation, which is associated with the second-order term of the Hamiltonian.

3.1.3.1 Single-ended microstrip JPC

The microstrip JPC consists of two $\lambda/2$ resonators, which meet at a central ring of Josephson junctions, the JRM. The horizontal (red) mode is labeled X, the vertical (blue) mode Y, and there is the third, common mode Z, which lives in both two resonators. The mode's frequency is defined by the length of a $\lambda/2$ resonator, which means the geometric inductance is also determined once the frequency is fixed. This design is straightforward in terms of fabrication; however, it provides no flexibility for controlling participation ratio.

Resonant modes X and Y are each capacitively coupled to a single microwave port, and

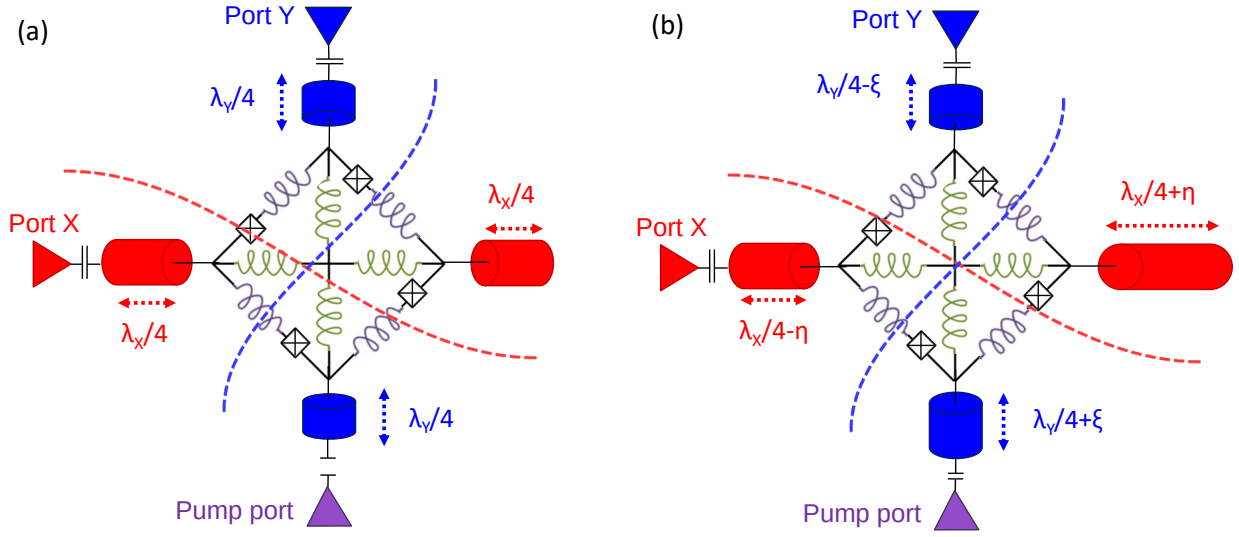

Figure 46: **(a) Schematic circuit of a microstrip JPC with the ring at the center.** When the ring is placed at the center of two resonators, the zero voltage point on both modes tends to shift towards the output port due to the coupling capacitor, which causes cross-talk between two modes. **(b) Schematic circuit of microstrip JPC with the ring shifted.** To minimize the leakage due to coupling capacitors, the ring is shifted by η and ζ in horizontal and vertical directions, respectively.

the pump is weakly coupled via a weak capacitor, see Fig. 46 (a). Due to the coupling capacitors, the ring is not located at the zero voltage point of two resonators, which means cross-talk between resonators occurs. To minimize this leakage, the ring is shifted away from the center by η and ζ in the horizontal and vertical directions, respectively, see Fig. 46 (b).

3.1.3.2 Single-ended lumped JPC

In order to have full control over participation ratio, the microstrip platform has to be replaced. We shift our design to lumped circuits, which have a physical device size much smaller than the wavelength of the mode frequency. The typical dimension of the microstrip JPC design, which is limited by the length of $\lambda/2$ resonator, is about 8 mm by 11.5 mm. For the lumped design, the size of the JPC is about 200 μm by 200 μm, which yields the possibility of integrating a JPC with other microwave components such as filters.

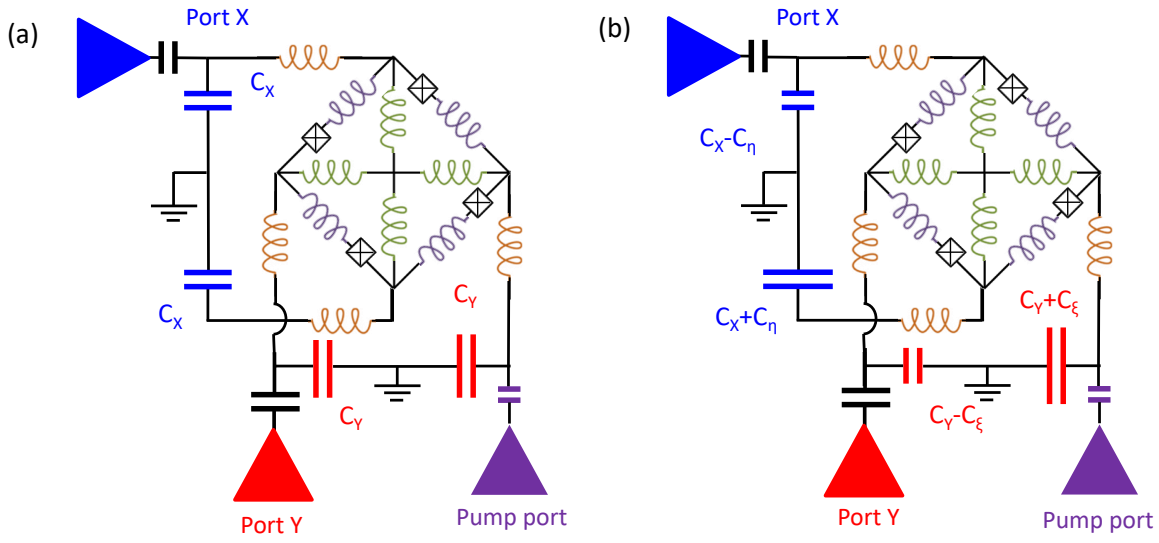

Figure 47: **(a) Schematic circuit of a lumped JPC.** A ring is in parallel with capacitors to form resonators. Similar to the microstrip JPC, coupling capacitors makes one end of capacitance larger than the other end; hence, cross-talk between modes appears. **(b) Schematic circuit of a lumped JPC with modification on capacitors.** To minimize the leakage due to coupling capacitors, the mode capacitors are not identical.

The single-ended lumped JPC implements two sets of capacitors connected to the inductance part, which has both the JRM and external inductance controlled by the length of metal fabricated on the device, as shown in Fig. 47 (a). When the coupling capacitors are also considered in the circuit, they cause the capacitance of one end of the LJPC to be larger than the other, which causes cross talk. A compensating asymmetry in external capacitance needs to be introduced into the circuit to suppress cross-talk, see Fig. 47 (b).

The single-ended lumped design shows flexibility in Hamiltonian engineering. All the components in the circuit can be individually tweaked. In section 5, we demonstrate a single-lumped design JPC with saturation power about -100 dBm, which is 20 dBm higher than typical JRM-based amplifiers, through optimization of the circuit via Hamiltonian engineering. However, the price we have to pay for building the single-ended lumped JPC is an increase in the difficulty of fabrication, which will be discussed in Appendix E.

3.1.3.3 Mode flow control - filter JPC

The common mode, Z, lives on all nodes, which indicates that it leaks out to all the output ports. To collect all of the information of mode Z, one has to use hybrids to collect mode Z's signal from all the ports, which will be very similar to an FPJA or a multiple hybrid system [64, 50]. If all signals are collected from a single port, we have to use a diplexer to separate the signals from different frequencies, which adds another commercial component and degrades quantum efficiency.

Signal flow control, meaning each mode has an individual input and output port, is required to create a multi-port device. One way to solve this problem is by using bandpass filters to prevent modes from leaking to undesired ports. A schematic filter JPC circuit diagram is shown in Fig. 48. Each bandpass filter only allows the signal within its working band to pass; therefore, an individual output port only receives one mode's signal. However, the bandpass filters' functionality depends on how many resonators are used. In Fig. 48 (b), a filter JPC's optical image is shown and left/top/right corresponds to port $X/Y/Z$'s. Each port has a two-resonator based bandpass filter. In a single device, we have engineered nine resonators instead of only three JPC modes. This method of signal control is not efficient,

therefore a better platform for multiple parametric processes is required.

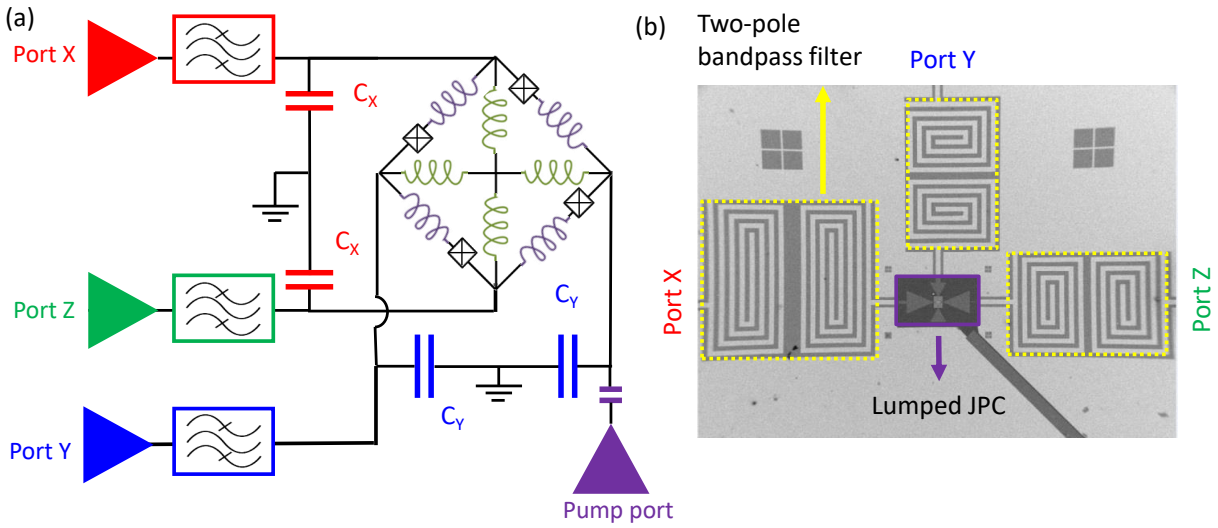

Figure 48: **(a) Schematic circuit of the filter JPC.** An example of a lumped JPC integrated with bandpass filters. Each filter only allows one eigenmode's frequency to pass. **(b) Optical image of the filter JPC.** The real device with a single-ended lumped JPC integrated with bandpass filters, which are two-pole filters.

3.2 Superconducting Hybridized ARbitrary Cavity-based amplifier (SHARC)

3.2.1 Introduction

In recent years, the potential of superconducting qubits as a quantum computing architecture has grown tremendously [21, 85]. This is due in part to quantum limited, Josephson-junction based parametric amplifiers (JPAs), which are able to enhance qubit signals while adding the minimum amount of noise and back-action allowed by quantum mechanics [22]. In these devices, gain is achieved by intensely driving the non-linear Hamiltonian of a circuit containing one or more Josephson junctions to parametrically couple together one or more microwave modes [72]. Paramps regularly enable experiments with single-shot, high-fidelity quantum non-demolition measurements of superconducting quantum bits [24, 32, 86].

At present, there are two families of parametric amplifiers: those based on discrete microwave resonances, and those based on nonlinear transmission lines, so-called Traveling Wave Parametric Amplifiers (TWPAs). TWPAs have superior instantaneous bandwidth and saturation power, but their typical reported noise performance is a factor of a few higher than resonant mode-based JPAs, and, although they are directional amplifiers, reflected pump and signal tones still often require operation with external circulators [41, 42, 87]. On the other hand, resonator-based JPAs (the focus of this work) contain typically far fewer Josephson junctions, are far easier to fabricate and operate very near the quantum limit. Their limitations are a fixed gain-bandwidth product, low input saturation powers, and lack of directional amplification (that is, they amplify in reflection and so must be operated with external circulators) [88, 34, 63].

A number of multiple parametric processes have been proposed to break reciprocity in both optical systems and superconducting circuits. Nonreciprocal quantum amplifiers have also been developed largely in the context of superconducting circuits. They typically involve engineering complex interference between parametric processes within a few eigenmodes.

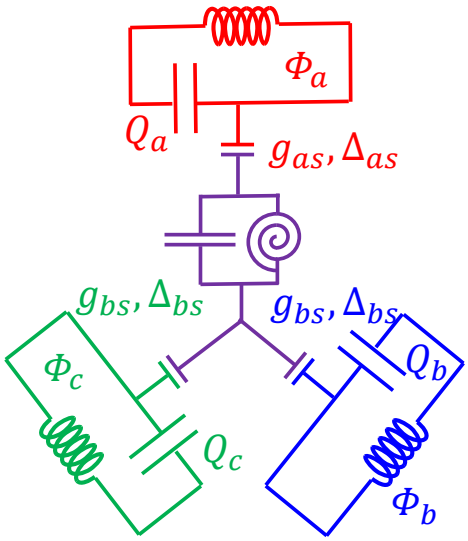

Figure 49: **Schematic circuit of SHARC.** Three LC resonators capacitively hybridize with a three-wave mixing element, the SNAIL. Due to the hybridization, non-linearity distributes between LC resonators as well as the SNAIL to resonators.

In this work, we have come up with a new platform, the Superconducting Hybridized ARbitrary Cavity-based amplifier (SHARC). It is suitable for multiple parametric processes. It has a three-wave mixing element placed at the center of the chip surrounded by an arbitrary number of cavity modes. These cavity modes hybridize with the three-wave mixing element through either capacitive or inductive mode coupling. By controlling the hybridization strength and mode frequencies, the cavity modes' photons can be preserved with additional three-wave coupling between cavity modes, see Fig. 49.

The SHARC has a great advantage over previous designs in terms of mode engineering. By coupling the desired number of cavity modes to the three-wave mixing element, all cavities are coupled together. Furthermore, individual components on the device correspond to one variable in the Hamiltonian, which provides a huge convenience for the multiple parametric amplifier community. Moreover, each mode has an individual input/output port, which implies that no external commercial hybrid or diplexer is required to process the outgoing signals. In this design, the three-wave mixing element is the Superconducting Nonlinear Asymmetric Inductive eLements (SNAIL), which was invented by Yale [89, 65].

The SNAIL has two arms: one arm with three identical Josephson junction in an array while the other arm has only a single Josephson junction that is α times smaller. It is a two-port component, similar to the JRM, that provides three-wave mixing terms at certain external bias flux.

3.2.2 Theory

Let us start with assuming there are N cavities coupled with a SNAIL operated at one of its fourth-order cancellation points. The Hamiltonian is

$$\frac{H_{\text{SHARC}}}{\hbar} = H_0 + H_1 + H_{\text{nonlinearity}} \tag{3.9}$$

where

$$H_0 = \omega_s s^\dagger s + \sum_{j=1}^{N} \omega_j a_j^\dagger a_j$$

$$H_1 = \sum_{j=1}^{N} g_j^* s^\dagger a_j + g_j s a_j^\dagger$$

$$H_{\text{nonlinearity}} = g_3(s^\dagger s^\dagger s + s s s^\dagger)$$

H_0 describes the linear resonance of each mode, H_1 is the coupling between cavity modes and the SNAIL and $H_{\text{nonlinearity}}$ is the higher order terms inherent from the SNAIL mode. Assuming the wave function of the system can be described by

$$|\boldsymbol{\varphi}\rangle = |\varphi_s, \varphi_1, \varphi_2, ..., \varphi_N\rangle$$

Now, we treat g_j, g_{s3}^m and g_{s4}^m small compared to ω_s and ω_j. By doing so, we can perform a perturbative analysis and find the dressed states of the system. To find the dressed states, let us ignore $H_{\text{nonlinearity}}$ for now. Because H_1 elements are smaller than those in H_0, we want to diagonalize using a perturbative approach in the orders of g_j.

Expanding Eq 3.9 and solving the perturbation to the first order for the SNAIL state, we obtain

$$H_0 \left|\varphi_s^{(1)}\right\rangle + H_1 \left|\varphi_s^{(0)}\right\rangle = E_s^{(0)} \left|\varphi_s^{(1)}\right\rangle + E_s^{(1)} \left|\varphi_s^{(0)}\right\rangle$$

Operating through by $\left\langle\varphi_s^{(0)}\right|$, the first term on the left-hand side cancels the first term on the right-hand side. This leads to the first-order energy shift

$$E_s^{(1)} = \left\langle\varphi_s^{(0)}\right| H_1 \left|\varphi_s^{(0)}\right\rangle$$

To obtain the first-order correction to the eigenstates, we act H_1 on the unperturbed state $\left|\varphi_s^{(0)}\right\rangle$ and combine with the above equation

$$\begin{aligned} H_1 \left|\varphi_s^{(0)}\right\rangle &= \sum_{j=1}^{N} \left|\varphi_j^{(0)}\right\rangle \left\langle\varphi_j^{(0)}\right| H_1 \left|\varphi_s^{(0)}\right\rangle + \left|\varphi_s^{(0)}\right\rangle \left\langle\varphi_s^{(0)}\right| H_1 \left|\varphi_s^{(0)}\right\rangle \\ &= \sum_{j=1}^{N} \left|\varphi_j^{(0)}\right\rangle \left\langle\varphi_j^{(0)}\right| H_1 \left|\varphi_s^{(0)}\right\rangle + E_s^{(1)} \left|\varphi_s^{(0)}\right\rangle \end{aligned}$$

Now we combine the above equation and the Hamiltonian

$$(E_s^{(0)} - H_0)\left|\varphi_s^{(1)}\right\rangle = \sum_{j=1}^{N} \left|\varphi_j^{(0)}\right\rangle \left\langle\varphi_j^{(0)}\right| H_1 \left|\varphi_s^{(0)}\right\rangle$$

Multiply $\left\langle\varphi_j^{(0)}\right|$ on the both sides of the above equation

$$(E_s^{(0)} - E_j^{(0)})\left\langle\varphi_j^{(0)}\middle|\varphi_s^{(1)}\right\rangle = \left\langle\varphi_j^{(0)}\right| H_1 \left|\varphi_s^{(0)}\right\rangle$$

We see that the above $\left\langle\varphi_j^{(0)}\middle|\varphi_s^{(1)}\right\rangle$ gives us the component of the first-order correction along $\left|\varphi_j^{(0)}\right\rangle$. Thus, in total, we get

$$\left|\varphi_s^{(1)}\right\rangle = -\sum_{j=1}^{N} \frac{g_j}{\Delta_j} \left|\varphi_j^{(0)}\right\rangle$$

where $\Delta = E_j^{(0)} - E_s^{(0)}$. Likewise, we can find the first correction to the cavity states

$$\left|\varphi_j^{(1)}\right\rangle = \frac{g_j^*}{\Delta_j} \left|\varphi_s^{(0)}\right\rangle$$

Therefore, the dressed states are

$$\begin{aligned} |\tilde{\varphi}_s\rangle &= \left|\varphi_s^{(0)}\right\rangle - \sum_{j=1}^{N} \frac{g_j}{\Delta_j} \left|\varphi_j^{(0)}\right\rangle \\ |\tilde{\varphi}_j\rangle &= \left|\varphi_j^{(0)}\right\rangle + \frac{g_j^*}{\Delta_j} \left|\varphi_s^{(0)}\right\rangle \end{aligned} \tag{3.10}$$

To obtain the nonlinearity, we have to expand $H_{\text{nonlinearity}}$ in the dressed states basis. Substitute $|\tilde{\varphi}_j\rangle$ into $|\tilde{\varphi}_s\rangle$

$$\begin{aligned} |\tilde{\varphi}_s\rangle &= \left|\varphi_s^{(0)}\right\rangle - \sum_{j=1}^{N} \frac{g_j}{\Delta_j} \left(|\tilde{\varphi}_j\rangle - \frac{g_j^*}{\Delta_j} \left|\varphi_s^{(0)}\right\rangle \right) \\ &\approx \left|\varphi_s^{(0)}\right\rangle - \sum_{j=1}^{N} \frac{g_j}{\Delta_j} |\tilde{\varphi}_j\rangle \\ |\varphi_s\rangle &\approx |\tilde{\varphi}_s\rangle + \sum_{j=1}^{N} \frac{g_j}{\Delta_j} |\tilde{\varphi}_j\rangle \end{aligned}$$

Based on Eq. 3.10, we can construct the unitary matrix that is used for changing the basis with the basis $(\varphi_s, \varphi_1, \varphi_2, \cdots, \varphi_N)$.

$$U = \begin{bmatrix} 1 & -\delta_1 & -\delta_2 & \cdots & -\delta_N \\ \delta_1 & 1 & 0 & \cdots & 0 \\ \delta_2 & 0 & 1 & \cdots & 0 \\ \vdots & \vdots & \vdots & \ddots & \vdots \\ \delta_N & 0 & 0 & \cdots & 1 \end{bmatrix}$$

where $\delta_j = g_j/\Delta_j$. We can calculate $s = U^{-1}\tilde{s}U$

$$s = \frac{1}{det(U)} \begin{bmatrix} C_{11} & -C_{11}\delta_1 & -C_{11}\delta_2 & \cdots & -C_{11}\delta_N \\ 0 & 0 & 0 & \cdots & 0 \\ 0 & 0 & 0 & \cdots & 0 \\ \vdots & \vdots & \vdots & \ddots & \vdots \\ 0 & 0 & 0 & \cdots & 0 \end{bmatrix}$$

Note that $C_{11} = 1$ and $det(U) = 1 + \sum_{j=1}^{N} \delta_j^2 \approx 1$, therefore, we obtain

$$s = \tilde{s} - \sum_{j=1}^{N} \delta_j \tilde{a}_j$$

To see three-wave coupling between cavity modes, we can substitute the above expression into $H_{\text{nonlinearity}}$

$$\begin{aligned} H_{\text{nonlinearity}} =& g_3 \tilde{s}^\dagger \tilde{s}^\dagger \tilde{s} - \sum_{j=1}^{N} g_3 \delta_j \tilde{s}^\dagger \tilde{s}^\dagger \tilde{a}_j \\ & - 2\sum_{j=1}^{N} g_3 \delta_j \tilde{s}^\dagger \tilde{a}_j^\dagger \tilde{s} + 2\sum_{i,j=1}^{N} g_3 \delta_i \delta_j \tilde{s}^\dagger \tilde{a}_i^\dagger \tilde{a}_j \\ & + \sum_{i,j=1}^{N} g_3 \delta_i \delta_j \tilde{a}_i^\dagger \tilde{a}_j^\dagger \tilde{s} - \sum_{i,j,k=1}^{N} g_3 \delta_i \delta_j \delta_k \tilde{a}_i^\dagger \tilde{a}_j^\dagger \tilde{a}_k + h.c. \end{aligned} \tag{3.11}$$

The first line on the right-hand side is the coupling for the SNAIL mode itself and the SNAIL with a linear mode. The second line is the coupling between SNAIL and cavity modes with $\tilde{s}$ and $\tilde{a_j}$ as pump modes. The third line is the coupling between cavities with $\tilde{s}$ and $\tilde{a_k}$ as pump modes. The strength of the three-wave mixing is modified by the amount of cavities operators in each term.

Assuming δ are small, we can obtain the SHARC Hamiltonian by combining Eq. 3.11 with harmonic terms of dressed states

$$\begin{aligned} H_{\text{SHARC}} = \hbar\omega_{\tilde{s}}\tilde{s}^\dagger\tilde{s} + \sum_{i=1}^{N}\hbar\omega_{\tilde{a}_i}\tilde{a}^\dagger\tilde{a} \\ + g_3\tilde{s}^\dagger\tilde{s}^\dagger\tilde{s} - \sum_{j=1}^{N} g_3\delta_j\tilde{s}^\dagger\tilde{s}^\dagger\tilde{a}_j \\ - 2\sum_{j=1}^{N} g_3\delta_j\tilde{s}^\dagger\tilde{a}_j^\dagger\tilde{s} + 2\sum_{i,j=1}^{N} g_3\delta_i\delta_j\tilde{s}^\dagger\tilde{a}_i^\dagger\tilde{a}_j \\ + \sum_{i,j=1}^{N} g_3\delta_i\delta_j\tilde{a}_i^\dagger\tilde{a}_j^\dagger\tilde{s} - \sum_{i,j,k=1}^{N} g_3\delta_i\delta_j\delta_k\tilde{a}_i^\dagger\tilde{a}_j^\dagger\tilde{a}_k + h.c. \end{aligned}$$

where $\delta_j = g_j/\Delta_j$ and $\Delta = E_j^{(0)} - E_s^{(0)} = \hbar(\omega_j^{(0)} - \omega_s^{(0)})$

3.2.3 Design

Generically speaking, the SHARC is composed of three different parts: a SNAIL, linear modes, and coupling components. Each part plays a role in the SHARC's Hamiltonian Eq. 3.2.2. Linear modes determine mode frequency, ω_j, while a coupling component decides how strongly a mode hybridizes with the SNAIL, g_j. The SNAIL has inherent three-wave mixing strength, g_3, and SNAIL mode frequency ω_s. Similar to the JPC, we want to operate the SHARC at a nulling point where Kerr and higher even-order terms are minimized. Also, because the circuit is based on hybridization, we have to design nulling points at the point where linear modes and SNAIL are not hybridized too strongly, see Fig. 50.

When generalizing SHARC to an N-linear mode system, we want to design a SNAIL whose avoided crossings only include one cavity to avoid forbidden zones occupying the whole external flux range. The miniature modulation can be achieved by either introducing participation ratio or reducing the inherent SNAIL's second-order terms.

In Fig. 50, a nulling point is placed outside of forbidden zones, where at least 10 % of a mode hybridizes with the SNAIL. In this example, the SNAIL modulates from around 2 GHz to 8 GHz and passes three forbidden zones. Three resonances are 3.5, 5, and 6.5 GHz with g_2 coupling 0.13, 0.14 and 0.15 GHz, respectively. When designing a real device, High

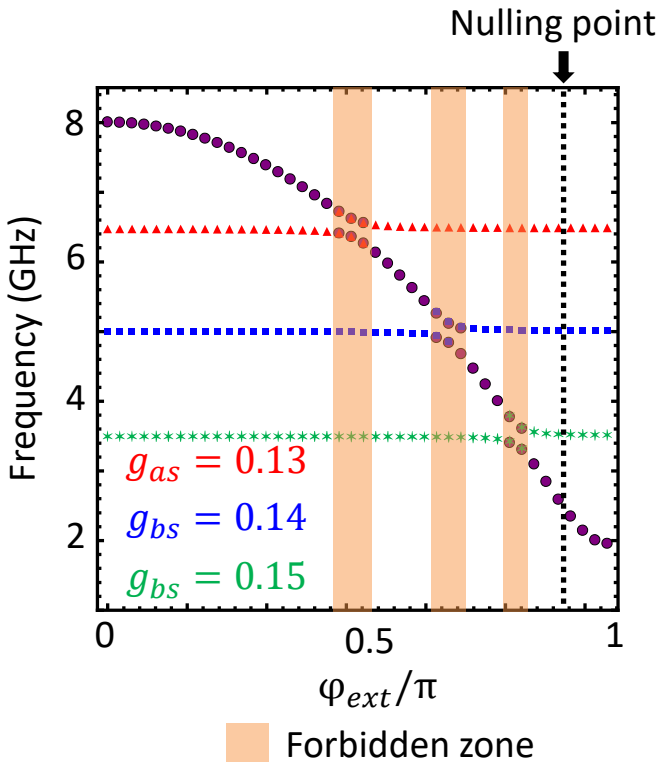

Figure 50: **SHARC modulation.** The SHARC needs to be operated at a nulling point where undesired terms can be suppressed. We have to place nulling points outside the forbidden zones where at least 10 % of mode's hybridize with the SNAIL. g_2 coupling in the unit of MHz are listed in the figure. Bare mode frequencies are 3.5, 5 and 6.5 GHz.

Frequency Structure Simualtor (HFSS) is useful for determining not only modes frequencies but g_2 coupling with a giving geometry.

4.0 Experimental results

4.1 Evolution of shunted JPC

Constructing a pure environment or device for a desired Hamiltonian, which allows one to perform multiple parametric processes efficiently, is not an easy task, especially when the circuit is formed by Josephson junctions. Suppressing undesired terms generated from the junctions while retaining desired terms strong enough to pump it is one of the biggest challenges. Based on the discussion in the previous section, our goal for building a JRM-based amplifier is to satisfy at least $\beta > 4$ and $\alpha \ll 1$. This condition sounds straightforward, however there are some fabrication limitations that stop us from achieving these goals.

In the first part of this section, we will show the evolution of the JRM that was designed and fabricated for better Hamiltonian engineering. Along with it, I will explain the pros and cons of each design and how to solve or overcome the difficulties that were encountered for each. Each design leads us toward an ideal JRM-based multiple parametric amplifier.

The second half of this section focuses on performing multiple parametric processes on the device, and finally, using it to measure a qubit. When a new pumping scheme is applied to a device, a challenge that always shows up is tuning the parametric processes during the intermediate stages. When the pump conditions are not ideal, we need to know how to identify whether either the pump's power or frequency needs to be adjusted in order to produce the right quantum interference.

We want to point out that the first three subsections in the evolution of shunted JRM are directed toward a single-ended microstrip JPC, see section 3.1.3.1. I will compare the difference with the microstrip JPC and the single-ended lumped JPC in the last subsection.

4.1.1 Meander JRM

The very first linear inductor shunted-JRM we have fabricated is inspired by N. Roch [90]. A piece of metal about 20 μm long meanders from one node of the JRM to the center of

the ring with the same pitch, which yields the same area to the sub-loops see Fig. 51 (a). Within the size of a ring about 20 μm x 20 μm, four meandering linear inductors with length varying from 10 μm to 30 μm or even longer can be placed in a ring.

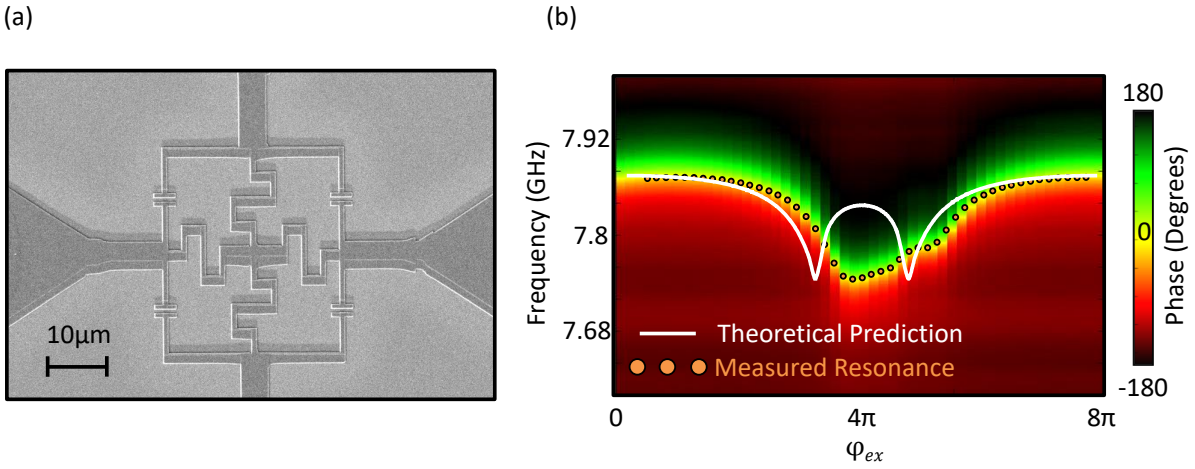

Figure 51: **(a) Meander JRM SEM.** We squeeze the meander inductors into the ring. The top/left and bottom/right inductors are identical for the purpose of keeping sub-loop area the same. **(b) Experimental and theoretical resonance response.** We can extract α and β from the SEM image and produce the theoretical prediction of the resonance response, which is very different from the experimental results. The experimental results indicate β should be larger.

To figure out β of the device, we can fit the tunability of the resonant frequency to the theoretical model with the assumption that the Josephson junction's area and critical current are known, see Appendix E. In the Fig. 51 (a), we identify the junction's size, which is 2.4 μm^2, with around 25 μm aluminum connections from node to the junction. The ring is shunted by about 40 μm of metal. With these parameters, we calculate that α and β are 0.37 and 3.4, respectively, and plot the theoretical prediction of the flux tunability, which is shown in white in Fig. 51 (b). However, the experimental response does not show the minor lobe, which implies that β must be greater than 4. This implies that the real β is larger than what we expect. The meandering inductor contributes more inductance, which we believe

comes from the mutual inductance.

To control the Hamiltonian, we must have a component that is well understood and easy to control. Theoretically, we can find out the mutual inductance from the meander inductance. However, it depends heavily on the geometry of the inductor and size of the ring, which we change from design to design. To make our lives easier, we came up with the second version of the JRM: Lightning JRM.

4.1.2 Lightning JPM

Instead of squeezing meandering inductors in a ring, we extend the ring and stretch the meander inductors to a lightning-like shape. By doing so, we can eliminate the effect of mutual inductance. In the Fig. 52 (a), the ring size is about 100 μm by 100 μm. To minimize α, we have to increase the junction's inductance; hence, a physically smaller Josephson junction, 1 μm^2, is used in this design. This design yields α and β to be 0.35 and 3.8. From Fig. 52 (a), we can still observe a minor lobe, which indicates β is smaller than 4. Even though β is still not ideal, we perform a measurement to identify nulling points.

In order to characterize the self- and cross-Kerr terms for a given mode/pair of modes, a pump tone is applied that is fixed 5 line widths away from the resonant frequency, while a second, weak tone is swept through the mode's resonant frequency with a Vector Network Analyzer(VNA) (see Appendix 4.2). The Kerr amplitude is seen as a shift in resonant frequency with increasing pump power [91]. Nulling points at which the resonant frequency remains fixed are shown in Fig. 52 (b).

From Fig. 52 (b), we can identify four nulling points. However, by mapping these four points to the resonance modulation data, we notice that the two nulling points close to 4 π belong in an unstable regime, where we do not want to operate the device. The other two nulling points seem very reasonable. However, the biggest challenge of this design is the nonuniform external flux through each sub-loop. Due to this reason, we can not assume the node's phase satisfies our requirement, $\varphi_1 = \varphi_2 = \varphi_3 = \varphi_4 = 0$. This indicates that the Hamiltonian of the circuit might be different from what we expect.

When it comes to circuit design, we usually only consider parameters related to the

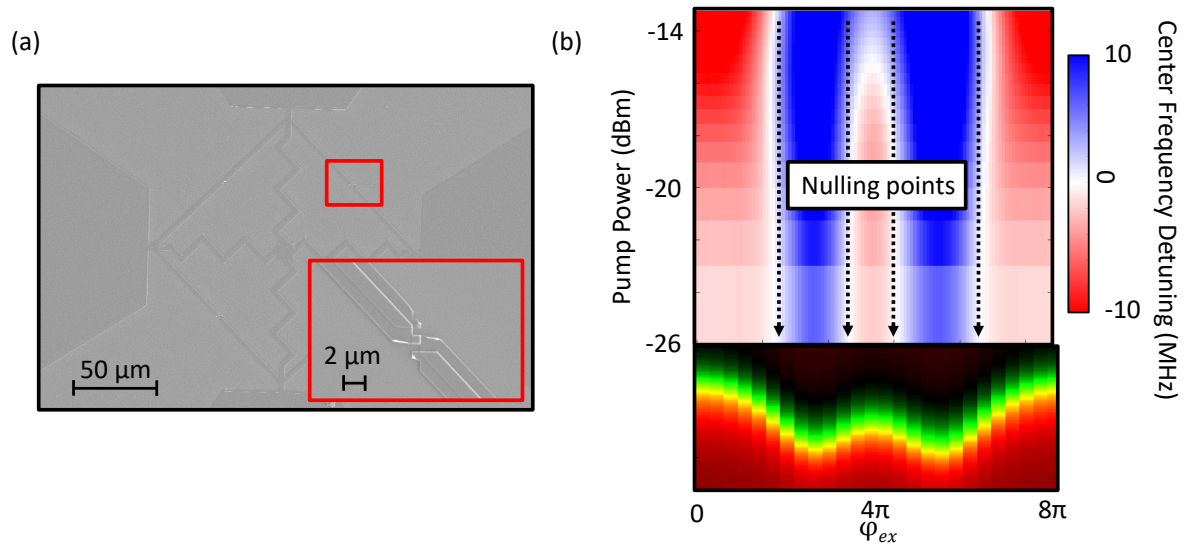

Figure 52: **(a) Lightning JPM SEM.** SEM image of the lightning JPM. The ring size is significantly larger when compared to the meander JRM design. To compensate L_{stray}, we have to use smaller Josephson junctions to keep α small. **(b) Self-Kerr measurement.** We performed the Kerr measurement mentioned in Appendix 4.2 and found four nulling points.

Hamiltonian directly and often ignore some physical designs that will affect the circuit's behavior. The lightning JRM is a perfect example. If we convert the design into a schematic circuit, everything seems very reasonable. However, the experimental challenge, in this case, is uniformity of the external field, which often yields additional design limitations. The ideal scenario is to have four identical magnets that control flux through each sub-loop. However, it is hard to realize experimentally, since the sub-loops are only a few μm away from each other. The easy solution for this is to keep the size of the ring under around 25 μm by 25 μm. This leads us to our final version of the JRM: Kinetic inductance shunted JPM.

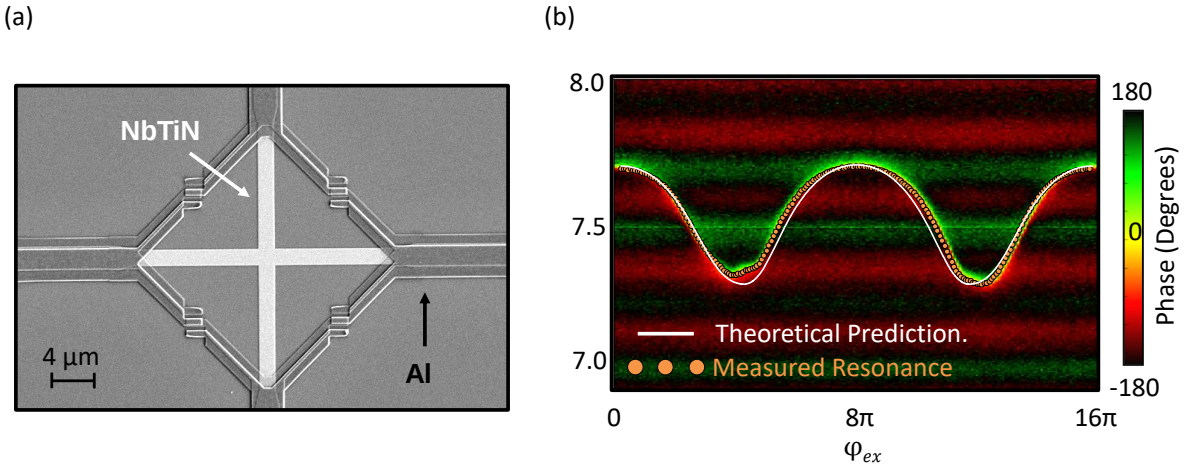

Figure 53: **(a) SEM image of Kinetic inductance JPM.** The ring is about 20 μm by 20 μm, which is small enough to ensure uniform external field. The white cross at the center is the thin NbTiN. **(b) Resonance modulation with fitting result.** From the image (a), we extract $\alpha = 0.07$ and $\beta = 4.3$. Using these parameters to plot the resonance modulation (in white), the prediction shows good agreement with the experimental results.

4.1.3 Kinetic inductance shunted JPM

We form a JPC by embedding the JRM at the intersection of two, single-ended microstrip resonators, as in [92]. The target parameters, junction $I_0 = 2$ μA, $\beta > 4$ and $\alpha \ll 1$, were fabricated using either meandering shunt inductances [93, 81] or kinetic-inductance shunts. We achieved superior control using kinetic-inductance shunts, due to the smaller physical size, and hence smaller α due to reduced stray inductance on the outer arms of the JRM.

To fabricate our JRM, we first sputter a film of 10 nm thick of NbTiN onto a PMMA mask on which a cross with widths and lengths of 2 and 15 μm respectively has been written via Electron Beam Lithography. The PMMA layer is subsequently lifted off with acetone. The resulting shunt inductors have $L_{\text{shunt}} \simeq 75$ pH, about five times their geometric value. Next, standard double-angle aluminum deposition is used to create the outer ring of the JRM.

As NbTiN does not form a native oxide, good contact to the upper (aluminum) portion of the circuit is achieved with only a standard, gentle Argon/Oxygen cleaning step prior to deposition of the first layer of aluminum, see Fig. 53(a).

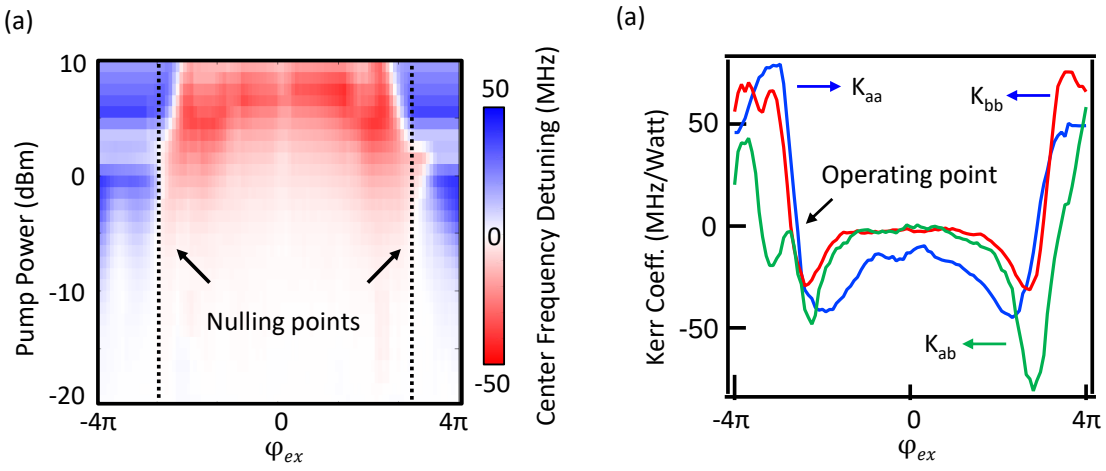

Figure 54: **(a) Measurement of mode a's self Kerr vs. applied flux.** For each flux point, we represent the shift away from the small-signal resonant frequency with a blue/white/red color for positive/zero/negative Kerr, respectively. The two cancellation points (where the plot remains white for all pump powers) are indicated with vertical dashed black lines.**(b) Effective Kerr terms.** We fit the data acquired in this protocol to a polynomial function of applied drive power. The linear coefficient of the function, which we recorded as MHz/Watt of driving power at room temperature, is proportional to the relevant Kerr term of the Hamiltonian.

With the power of the kinetic inductance boost, we can fabricate a ring that has $\beta = 4.3$ and $\alpha = 0.07$. With all these known parameters, we can compare the theoretical prediction of resonance modulation to the experimental results. There is a bit of discrepancy, which might be caused by the uncertain external inductance, see Fig. 53 (b). The next step is to identify nulling points from Kerr measurement mentioned in Appendix 4.2. This flux bias point as shown in Fig. 54 (a), is represented by a dotted black line. For each bias current result, we can fit it to the polynomial function and the linear term of the fitting result is

proportional to the Kerr. By fitting all bias currents, all Kerr terms as a function of the bias current can be extracted as shown in Fig. 54 (b) in order to identify an operating point for multiple parametric processes. (Note : All GC amplification results is taken with this single-ended microstrip kinetic inductance shunted JRM device at the operating point mentioned in Fig. 54 (b))

So far, we have embedded different types of JRMs in the single-ended microstrip JPC. Microstrips have inherent geometric inductance, which implies that the Hamiltonian is modified by participation ratio, as we have mentioned in section 3.1.2.2. The length of microstrips determines the resonance of modes, which also defines geometric inductance. From the point of view of fabrication, we want the ability to control every parameter in a device independently. Therefore, the singled-ended lumped design comes into play. The lumped JPC has the JRM connected to capacitors to form resonators directly, which implies that the inductance in the circuit comes entirely from the JRM. The fabrication details will be discussed in Appendix E.

4.1.4 Lumped single-ended kinetic inductance shunted JPC

Without the effect of participation ratio, the Hamiltonian coefficient of the JRM should be more significant since the inductance energy only comes from the JRM. One way to observe this directly is to measure resonant frequency modulation. As we have shown in Fig. 55 (a), the smallest modulation in the plot is almost 2 GHz, which is at least two times larger than that of the single-ended microstrip JPC. We notice that there are two resonances that appear in this data, one with 2 GHz of modulation, the other with about 4 GHz, which can be understood by comparing the second-order coefficient of the JRM Hamiltonian, Eq. D.2. The larger modulation corresponds to the common mode or mode Z. We further fit the results to the theory with $\beta = 5$, $\alpha = 0.06$ and the participation ratio close to 0.78. Theoretically, the participation ratio should be 1. However, capacitors that connect from a CPW port to the JRM have a certain length, which will also contribute to external inductance.

From this data, we also notice that the common mode leaks out the same port as the

signal mode, which confirms that bandpass filters are required to control the signals. We further perform the Kerr measurement, and we notice that indeed this device has nulling points almost on $\varphi_{\text{ext}} = 2\ \pi$, which is a good agreement with the theoretical prediction, see Fig. 55 (b). Overall, the lumped JPC indeed has larger coefficient terms, and nulling points show up at the desired external flux. However, signal control is needed to separate modes' signals to different spatial ports.

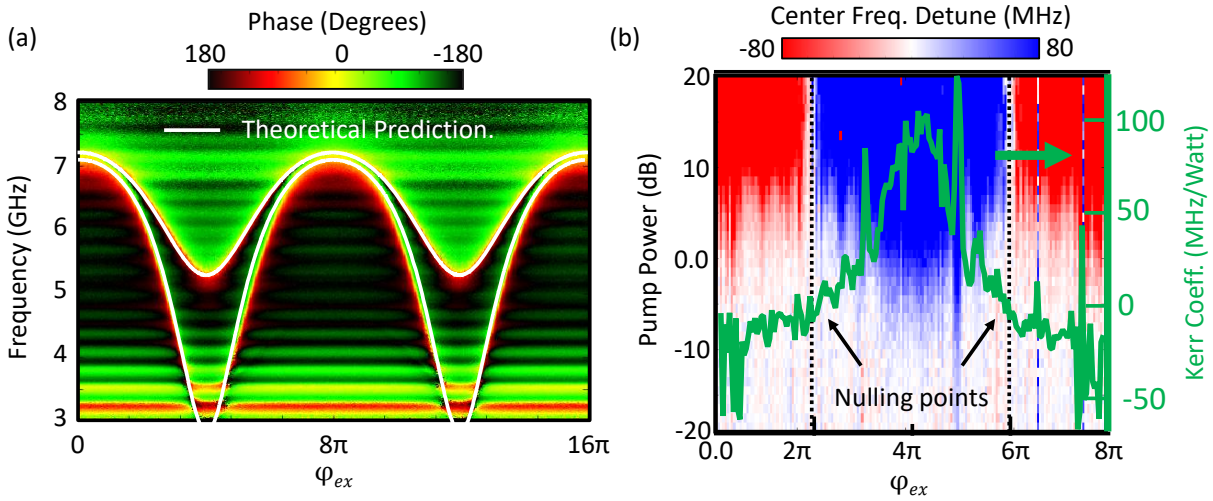

Figure 55: **(a) Resonant frequency modulation.** The lumped kinetic inductance shunted JPC has larger modulation because of almost unity participation ratio. The theoretical prediction uses $\beta = 5$, $\alpha = 0.06$ and $p = 0.72$ at $\varphi_{\text{ext}} = 4\pi$. **(b) Measurement of Self-Kerr.** For each flux point, we represent the shift away from the small-signal resonant frequency, with positive/zero/negative Kerr as a blue/white/red color, respectively. We fit the data acquired in this protocol to a polynomial function of applied drive power, and the linear coefficient of the function, which we recorded as MHz/Watt of driving power at room temperature, is proportional to the relevant Kerr term of the Hamiltonian.

4.1.5 Lumped single-ended aluminum inductance shunted JPC

From [94], we learn that saturation power scales linearly with Josephson junction's size for the JRM-based amplifiers, which usually implies small coupling terms. With the advantage

of the lumped JPC, we can fabricate large Josephson junctions without worrying about whether the third order mixing term of the Hamiltonian is too small. The price we have to pay is to allow α to be larger than 0.1. In Fig. 56 (a), this device has 4 μm^2 Josephson junctions on the outside of 20 μm by 20 μm ring. It has a modulation of resonant frequency less than 1 GHz, which is considerably smaller than the lumped kinetic inductance shunted JPC. By fitting to the theory, we obtain $\beta = 5.8$, $\alpha = 0.24$ and $p = 0.16$ at $\varphi_{\text{ext}} = 4\ \pi$. As we have mentioned, the stray inductance has significantly modified the behavior of the Hamiltonian, which can be seen in Fig. 56 (b). Nulling points shift toward to $\varphi_{ext} = 4\ \pi$ due to the stray inductance.

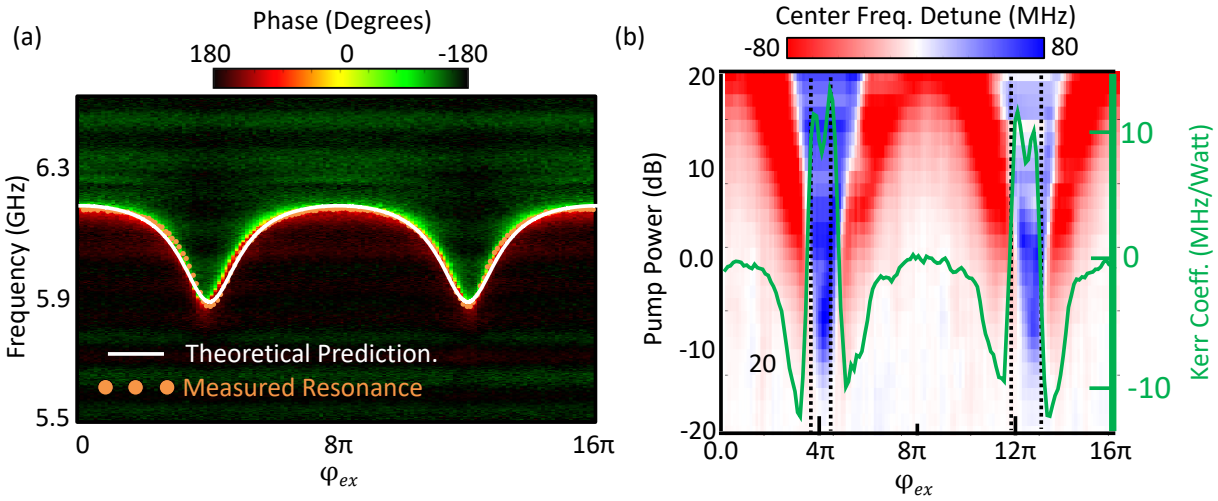

Figure 56: **(a) Resonant frequency modulation.** The lumped aluminum inductance shunted JPC has relatively smaller modulation compared with the kinetic inductance shunted JPC. The theoretical prediction uses $\beta = 5.8$, $\alpha = 0.24$ and $p = 0.16$ at $\varphi_{ex} = 4\ \pi$. **(b) Measurement of Self-Kerr.** Nulling points are closer to $\varphi_{ext} = 4\ \pi$ due to large value of α.

Interestingly, the saturation of this device performs very well, and it is almost the same as the traveling wave parametric amplifier, which has saturation power about -100 dBm [41, 87]. The detailed discussion of saturation power is in section 5.2.4.

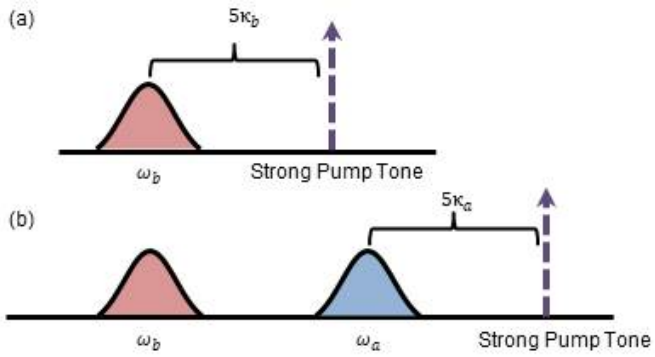

Figure 57: **(a) Visualization of how to measure self Kerr.** We prepare a pump tone that is 5 times the linewidth away from the mode frequency and observe the shift of the mode frequency. **(b) Visualization of how to measure cross Kerr.** Similarly, for the cross Kerr, we monitor the change of mode frequency on mode a while varying the strength on the pump tone which is five linewidths away from mode b.

4.2 Measurement of Kerr terms

We need to quantify the strength of the Kerr terms inherent to our amplifier in order to find when they go to zero. To do this, we perform Self-Kerr and Cross-Kerr duffing sweeps across a wide range of flux. The self Kerr terms, $a^\dagger a a^\dagger a$ and $b^\dagger b b^\dagger b$, can be measured by applying a strong pump tone five linewidths away from the respective resonant frequencies as shown in Fig. 57 (a). We then sweep the flux and the pump power and measure the detuning from the resonant frequencies. In Fig. 54 (a), we plot negative detuning in red and positive in blue which allows us to quickly identify where these terms go to zero, since zero detuning, representing no fourth-order effects, is plotted in white. The cross Kerr, $a^\dagger a b^\dagger b$ is measured similarly, but this time we apply a tone five linewidths away from the mode a and measure the effect of the mode b, as seen in Fig. 57 (b). With a high enough pump power, it becomes easy to distinguish the red/blue regions, and thus, the crossing zone in the middle where the specific fourth-order term goes to zero. This flux bias point as shown Fig. 54 (a), is represented by a dotted black line. For each bias current result, we can fit

it to the polynomial function and the linear term of the fitting result is proportional to the Kerr. By fitting all bias currents, all Kerr terms as a function of the bias current can be extracted and is shown in Fig. 54 (b).

Our recent work in ref [94] has complicated this picture. When the geometric inductance introduced from microstrips that form the $\lambda/2$ resonators is taking into account, nulling points for the self and cross Kerrs appear at slightly different points. Moreover, the dynamic Kerr which is generated by strong pump tones also affects the measurement of Kerr [65]. However, we can still use this method and identify the best operating point where all Kerr terms are minimized.

4.3 Multiple parametric processes

In this section, we perform GC amplification and build the circulator mentioned in chapter 2. The device we have used to get these results is a kinetic inductance shunted JPC at an operating pointing where Kerr terms are minimized.

First, we identified the mode a and b frequencies ,which are 7.4668 GHz and 4.8715 GHz respectively, and pumped at their sum, tuning the applied pump power to achieve 20 dB gain in reflection (G). We repeated the process with the pump at the difference frequency (C), tuning the applied pump power to find a 20 dB dip in reflection. These bias powers are each very close to the critical values, and tell us the room temperature ratio of applied microwave powers required to balance the G and C processes. We next tuned the applied pump frequencies until they link to identical idler frequencies in transmission through the device see Fig. 58 (a) and (b). We also compared the experimental result to the theoretical plot and found really good agreement.

4.3.1 GC amplification

Turning on both drives simultaneously achieves GC amplification. If we start GC amplification with 20 dB gain and -20 dB conversion, then based on theoretical predictions, around

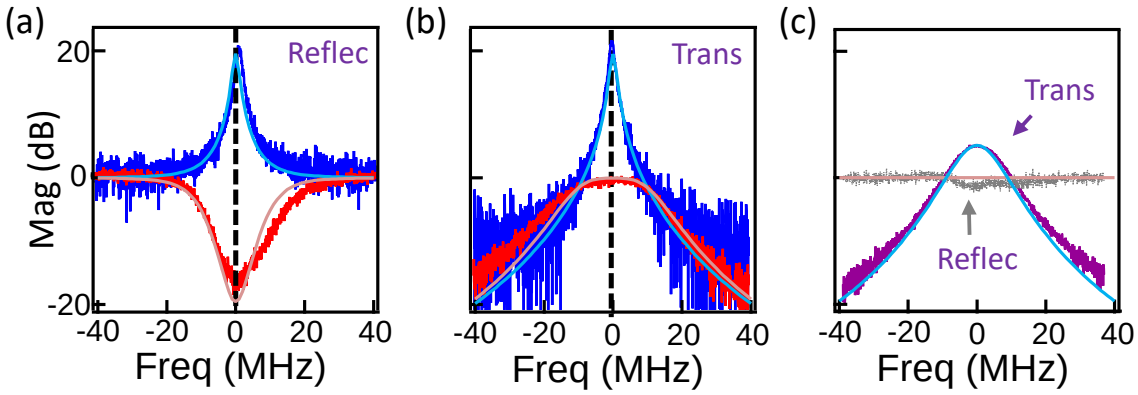

Figure 58: **(a) Measured reflection gain and conversion.** Reflection of 20 dB gain (blue) and −20 dB conversion (red) are shown in this figure compared with the theory plot, shown in a light color. The peak and dip of gain and conversion are aligned. **(b) Measured transmission gain and conversion.** Similar to figure (a), but we measure in transmission. Again, the peak can dip are aligned. **(c) GC amplification.** With the gain and conversion aligned, both parametric processes will interfere with each other and result in the GC amplification. Again, we compared the experimental and theoretical plot and found good agreement.

5 dB transmission gain will be achieved with only unity gain in reflection, see Fig. 58 (c). We control GC gain by increasing/decreasing both pumps simultaneously while maintaining the ratio established above. Measured GC amplification gain strengths between 8 and 15 dB, along with reflection performance, are shown in Fig. 59 (a). All transmission gain curves are measured with a VNA. An external mixer at the difference frequency converts device outputs from the idler mode back to the input, signal mode, frequency. The VNA is sensitive only to a single frequency, thus all gains shown are phase-preserving, and so for large gains, the phase-preserving gain peak sits ~ 6 dB below the phase-sensitive gain of the device, so that the maximum phase-sensitive gain for the 15.5 dB curve (which we will use for qubit output) is 21.5 dB. Above 10 dB gain, the frequency of the pump tones had to be adjusted slightly to account for the imperfectly nulled higher order terms, which shifted the device's

modes, and hence, the frequency of peak gain, to lower frequencies. At the same time, the reflection curves at this higher power start to show small disturbances away from unity (see Fig. 59 (a)). For clarity in these experiments, the amplifier is shifted slightly below the cavity frequency, which is evident as a notch to the right of the gain peaks.

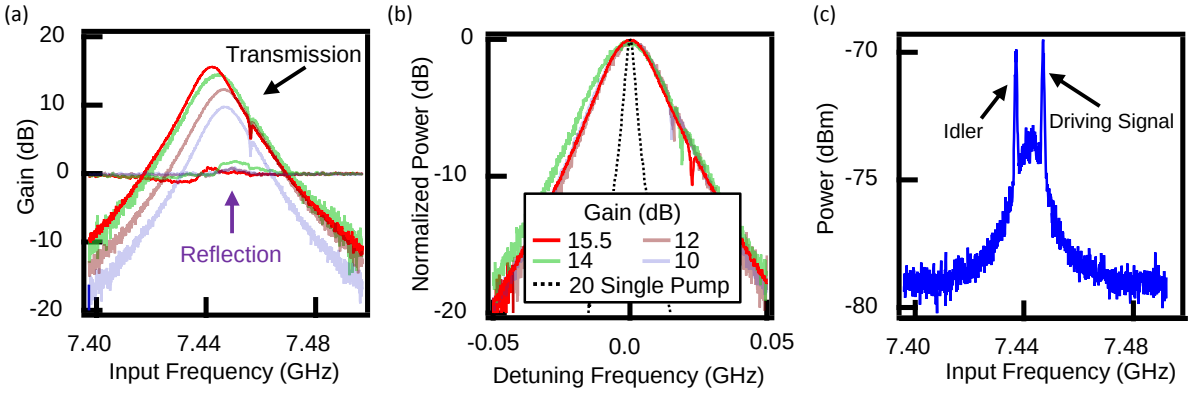

Figure 59: **(a) Measured transmission and reflection coefficients.** For phase-preserving gains between 8 and 15 dB, we found gain in transmission, with near unity gain in reflection. The notch at 7.45 GHz is the cavity response, which we have deliberately detuned away from for behavioral clarity. **(b) Bandwidth comparison.** Gain curves from part (a) are normalized relative to their peak gain and center frequency and are plotted together to show the fixed bandwidth regardless of the gain. The black dashed curve represents the gain peak and bandwidth of a 20 dB, phase-preserving singly-pumped process. **(c) Phase sensitivity.** Here we show a spectrum analyzer (received power) trace when the GC amplifier is driven with a fixed tone 5 MHz detuned from its center frequency. The presence of a symmetrically detuned idler tone below the center frequency is a clear demonstration of the phase-sensitive nature of this device's gain.

The other crucial feature of these gain curves is that they demonstrate the same bandwidth regardless of gain (see Fig. 59 (b)). We compare these bandwidths with the standard 20 dB for one single pump amplification process represented by the black dashed curve. The GC amplifier shows 14 MHz of phase-preserving bandwidth. In contrast, a singly-pumped gain response of 20 dB only has a bandwidth of 2.33 MHz in the same device. This bandwidth is approximately six times larger, in good agreement with theory.

We also show a spectrum analyzer (received power) trace when the GC amplifier is driven with a fixed tone 5 MHz detuned above its center frequency in Fig. 59 (c). The presence of a symmetrically detuned tone below the center frequency is a clear demonstration of the phase-sensitive nature of this device's gain. Collectively, Fig. 59 demonstrates all key predicted features of GC amplification; fixed bandwidth, 0 dB gain in reflection, and phase-sensitive amplification in transmission.

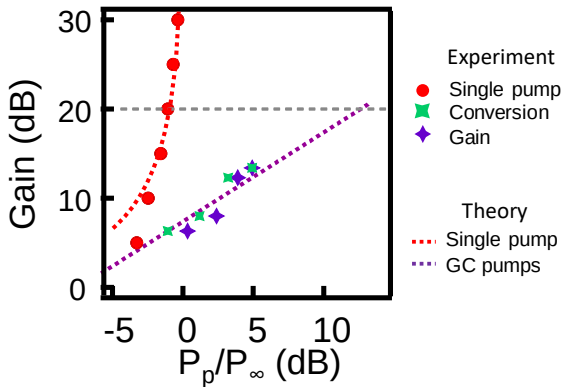

Figure 60: **Gain versus pump power.** The pump power required to obtain gain on resonance for a single pump and GC amplification processes.

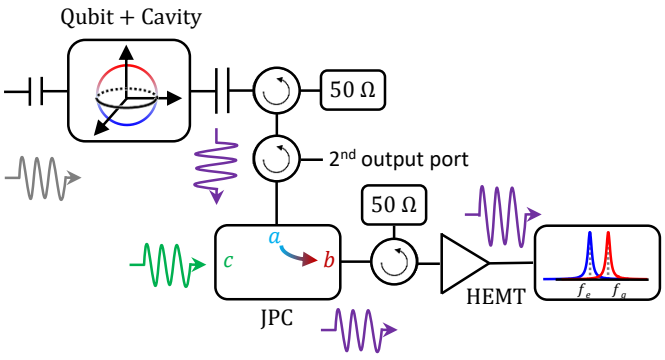

Figure 61: **Schematic of quantum measurement experiment.** A quantum limited amplifier, the Josephson parametric converter (JPC), is used in transmission to measure a transmon qubit mounted inside a 3D cavity.

The other notable property of GC amplification is that unlike a single parametric process, the gain of GC is a linear function of the (matched) pump powers for each parametric process. Here we record the pump power used to achieve gain on resonance for different parametric processes, as shown in Fig. 60. The pump power is normalized to the critical power, P_∞, which point where the gain of a singley-pumped, phase-preserving gain diverges [34]. The curved dashed line is the single pump process theory prediction that allowed us to extract P_∞. The red dots are the experimental pump power applied to the device for different gains. In contrast, the linear dashed line is the prediction of GC amplification as a function of pump power for individual (matched) pumps G and C. We note it shows no divergence. For 5 dB GC gain, G and C pump strength have to be about P_∞. To reach 20 dB GC gain, each pump power has to be around 10 times stronger than P_∞.

To demonstrate that our Kerr-nulled, GC pumped device is a practical, quantum-limited amplifier we also performed phase-sensitive strong/projective measurements on a superconducting transmon qubit. All further qubit measurements are performed in the configuration shown in Fig. 61. The qubit is first prepared in the superposition state $|\Psi\rangle = (|g\rangle + |e\rangle)/\sqrt{2}$, we determined the optimal alignment of the device's amplified quadrature by finding the largest separation between ground and excited states when projective measurement is performed, as shown in Fig. 62 (a). Rotating the relative pump phase by 180° from this optimal point moves the signal to the squeezed quadrature, so that the $|g\rangle$ and $|e\rangle$ states overlap, as seen in Fig. 62(b). Both histograms contain $80,000$ measurements. We also measured spontaneous quantum jumps between the $|g\rangle$ and $|e\rangle$ state when the phase was rotated to the optimal alignment and the cavity was driven for 7.5 μs, as shown in Fig. 62 (c).

Finally, we calculate the quantum efficiency of our amplifier via the back-action of deliberately weak measurements on the qubit's state, as in [32, 76]. The pulse sequence is detailed in Fig. 65. For phase-sensitive amplification, only one microwave quadrature can be received at room temperature. In a qubit measurement, this confines the qubit back-action to a single plane on the Bloch sphere, determined by which quadrature is amplified. To calibrate our quantum efficiency (η), we use the amplifier aligned as in Fig. 62 (b), resulting in a pure back-action on the qubit's phase, shown in Fig. 63. We found that our quantum efficiency was $\eta = 55$ %, in good agreement with the efficiency of the device when operated as

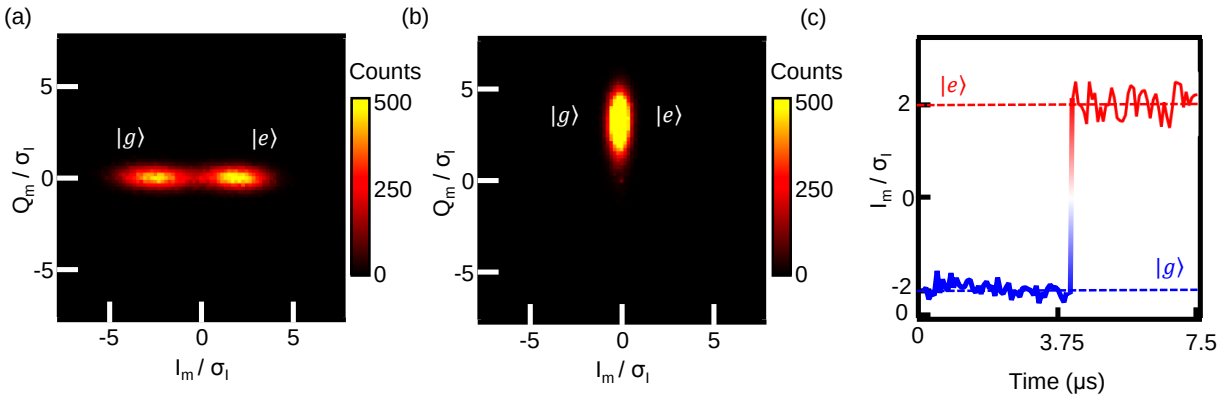

Figure 62: **(a) Histogram of strong measurement with optimally aligned cavity drive and amplifier phase.** This histogram consists of $80,000$ shots in which the qubit is prepared in the state $|\Psi\rangle = (|g\rangle + |e\rangle)/\sqrt{2}$ and projectively measured. The cavity drive has been aligned to the center (phase-sensitive point) of the GC amplifier and the relative phases of the cavity drive and amplifier aligned to maximize the projectivity of the measurement. **(b) Histogram of strong measurement with orthogonally aligned cavity drive and amplifier phase.** By rotating the relative phase of cavity drive and amplifier by 90° compared to part a, we show that the states of the qubit after projective measurement now completely overlap. **(c) Quantum jumps.** Here we demonstrate the ability to perform rapid QND measurements by continually monitoring the qubit and observing a well resolved quantum jump in its evolution.

a phase-preserving amplifier at the same bias point. We also performed weak measurements with the amplifier aligned optimally as in Fig. 62 (a) (for which the back-action is only on the qubit's z-coordinate,shown in Fig. 64.)

The standard way to perform back-action measurement is shown in Fig. 65. We first strongly read out the qubit and record the outcome, which will be used to prepare the qubit in the ground state with state selection. Then the qubit is rotated by the +y axis and measured with a variable measurement strength, and the outcome is recorded again. For the final tomography, phase measures the x, y, or z component of the qubit with a strong

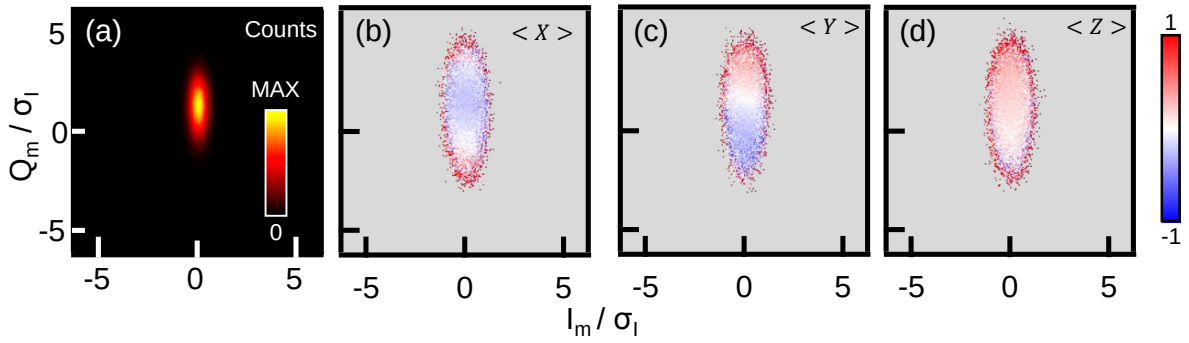

Figure 63: **(a) Histogram of weak measurement protocol with orthogonal alignment (Q-quadrature amplified) to determine quantum efficiency of the GC amplifier.** Each plot contains 80,000 measurements. **(b)-(d) Conditional expectation value of X/Y/Z after weak measurement plotted versus measurement outcome.** Sinusoidal oscillation in both X and Y are a non-classical stochastic Ramsey process. Together with the nearly constant outcomes for Z, these plots show how an orthogonally-aligned measurement provides a 'kick' around the equator of the bloch sphere.

measurement pulse.

If we take the qubit to originally be oriented along the Y-axis and the I quadrature to be perfectly squeezed, the back-action corresponds to stochastic, trackable motion of the qubit state in the x-y plane, with the extent of the motion varying with the strength of the measurement. For weak strength, the back-action looks like a stochastic rotation in the x-y plane with the degree of rotation encoded in Qm.

By increasing conversion's pump power, we alter the pumping scheme from the balanced case to imbalanced. In reflection, we indeed observe a dip instead of 0 dB. Theoretically, the GC imbalanced scheme should have -∞ dB. However, in the experiments, we compromise at -10 dB dip. In transmission, we observe that the bandwidth for the imbalanced case indeed is more significant than that of a balanced situation, see Fig. 66. GC imbalanced requires more conversion power to achieve the same amount of gain. In this case, the conversion is

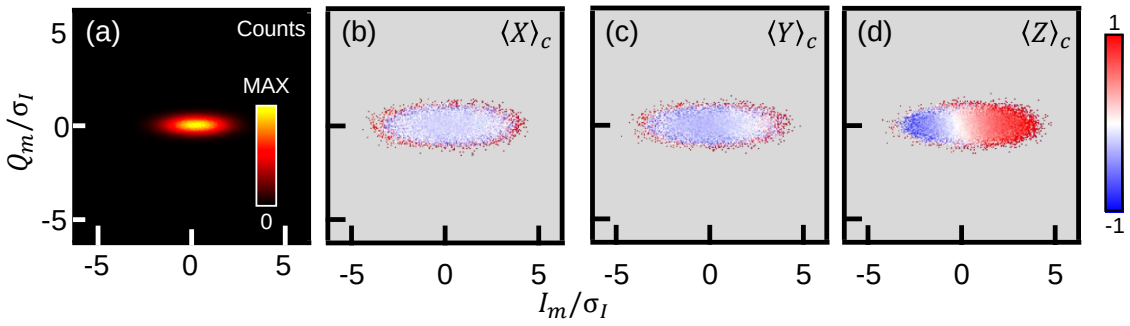

Figure 64: **(a) Histogram of weak measurement protocol with optimal alignment (I-quadrature amplified) to determine quantum efficiency of the GC amplifier.** Each plot contains $80,000$ measurements. **(b)-(d) Conditional expectation values of X/Y/Z after weak measurement plotted versus measurement outcomes.** These plots show how an optimally-aligned measurement provides a 'kick' around the Y-Z plane of the bloch sphere.

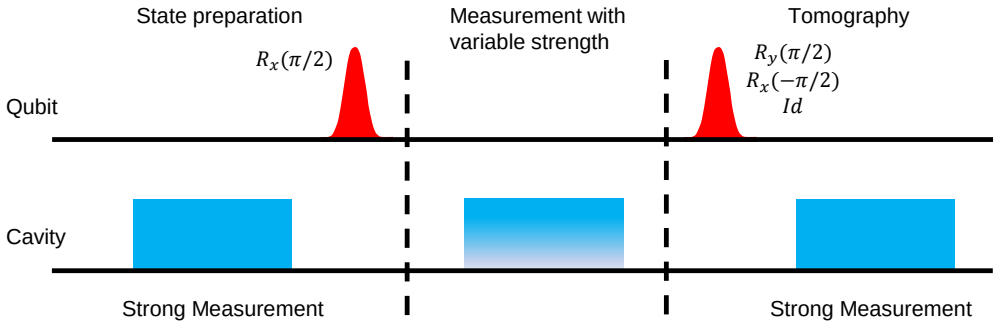

Figure 65: **Pulse sequence for quantifying measurement back-action.** We first strongly read out the qubit and record the outcome, which will be used to prepare the qubit in the ground state by postselection. Then, the qubit is rotated by the +y axis and measured with a variable measurement strength, and the outcome is recorded. The final tomographs, phase measures the x, y, or z component of the qubit Bloch vector with a strong measurement pulse.

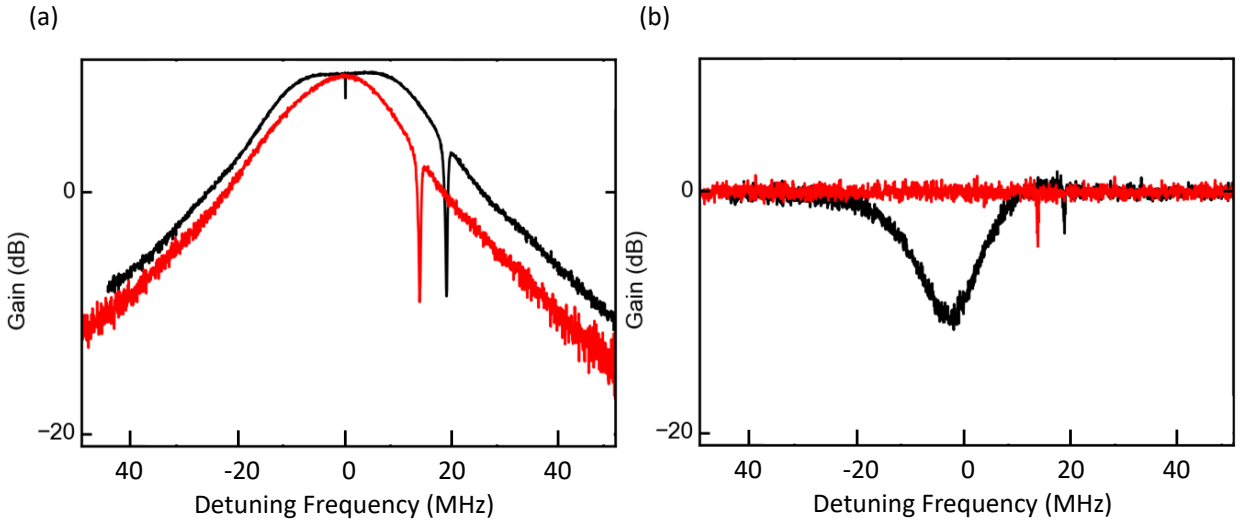

Figure 66: **(a) and (b)Transmission and reflection of GC and GCI.** We align GC and GCI's peak together for the purpose of comparison. We observe about −10 dB dip in reflection for the imbalanced case but 0 dB for the balanced. GCI's bandwidth is wider than that of GC.

strong enough to make fourth-order terms significant, and hence the mode's frequency is shifted, which caused the notch to appear at a different frequency.

4.3.2 Circulator based on microstrip JPC

Furthermore, we can implement the circulator on this device. The configuration of measurement is still the same as the GC amplification, see Fig. 61; therefore, we do not have full control of the common mode. However, we can still perform the circulator and look at its behavior on the signal and idler modes. To start the experiment, we need to identify the common mode's frequency, which is 6.232 GHz.

Before firing up all conversion processes, we have to check each conversion process carefully. As we have mentioned in section 2.5.3, all the pump strengths need to be the same. To verify this condition, we have to turn on one pump at a time and measure the reflection

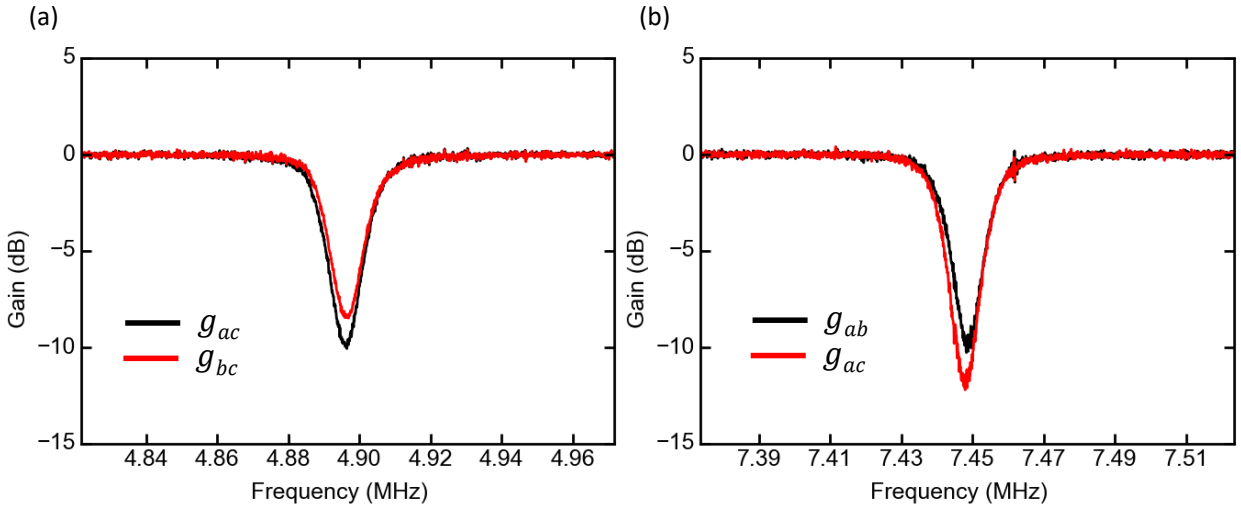

Figure 67: **(a) and (b) Reflection of the idler and signal for individual conversion.** Measure reflection on the idler and signal mode for individual conversion pump. To have the interference process working, we have to make sure the dip appears at the same frequency and the magnitude is about the same.

and transmission of the conversion process. If all the pumps have the same strength, then in the reflection we should observe the dip of about the same magnitude. Furthermore, we have to make sure the conversion processes really happen at the right frequency. Each mode connects with two conversion processes, and the dip in the reflection should appear at the same frequency with the individual process is on. Using mode a as an example, it experiences two conversion processes: g_{ab} and g_{ac}. When one of these two processes is on, the dip in reflection for mode a should appear at the same frequency ω_a with about the same magnitude, see Fig. 67 (a) and (b). Even though we do not have full access to the common mode, measuring the idler and common modes is sufficient to proceed to the next step.

Once all pumps have the right frequency and power, we can turn on all of them simultaneously. The value of minimizing fourth-order terms for the multiple parametric processes can be seen once all conversion processes are on. We should observe that the dip in reflection remains at the same frequency. If it is shifted away from the origin point, this implies the

four-order terms have become significant. Operating the kinetic inductance shunted JPC around null points, we can turn on all pumps without worrying about the shift of mode frequency. The last step is finding the right phase condition. Recall that circulation appears only when $\varphi_{\text{tot}} = \pm\pi/2$, which can be controlled by varying one generator's phase. By changing one pump's phase, we can generate magnitude versus phase plots, see Fig. 68. In our experiment setup, we can only drive the common mode but not receive the entirety of its signal. Therefore, only six elements from the circulator matrix can be obtained.

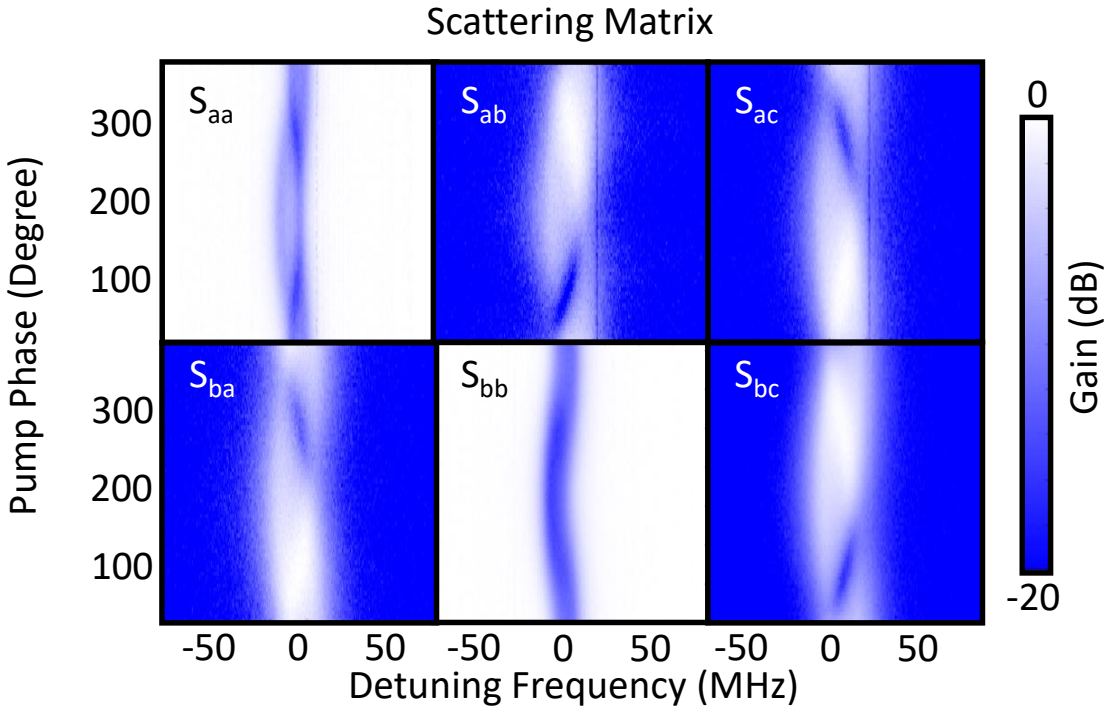

Figure 68: **Circulator scattering matrix: magnitude versus phase.** Six elements from the circulator matrix can be obtained. The plot shows how magnitude changes with phase.

From Fig. 68, we identify the phase where the circulator appears, in this case, $\phi_p = 260°$ and 80°. The performance of the circulator at these phases can be plotted and is shown in Fig. 69.

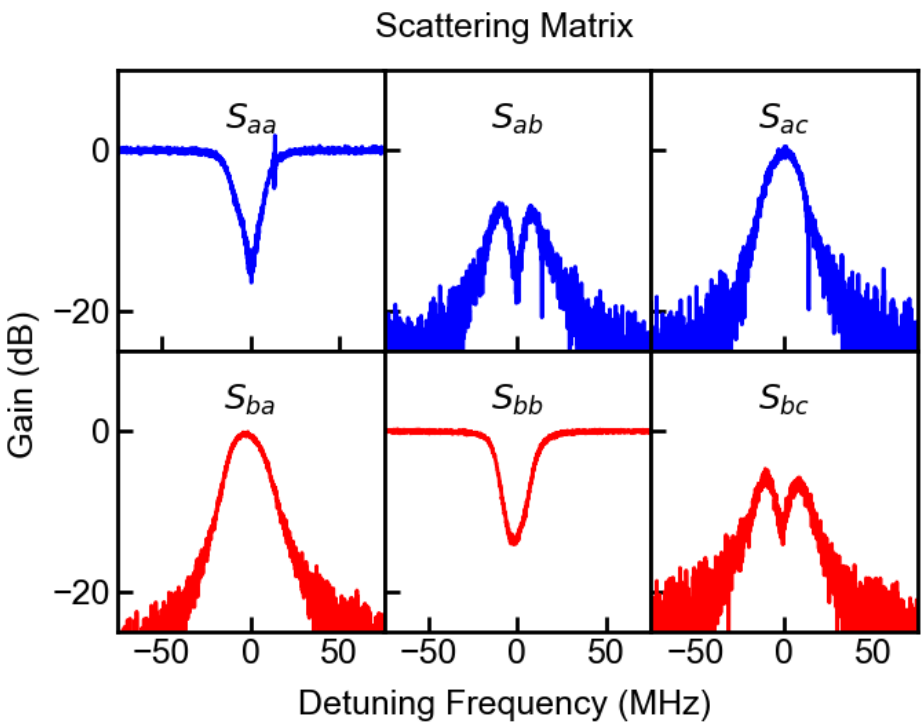

Figure 69: **Circulator scattering matrix.** We plot six elements of a circulator's scattering matrix when $\phi_p = 80°$.

4.4 Superconducting Hybridized ARbitrary Cavity-based amplifier (SHARC)

As we have mentioned in the previous section, the common mode can leak out to all the ports, which implies that without 180° hybrids or using filters with the JPC, we cannot collect the whole signal of the common mode. Collecting a complete signal for a mode at an individual spacial single port is always a considerable challenge for multiple parametric processes. Furthermore, some have proposed multi-mode parametric processes to integrate mechanical, optical, or microwave mode systems [48, 49, 50, 51, 52, 53, 54]. To expand the number of modes on JRM-based circuits is quite a hurdle.

In contrast, with SHARC as a platform for multiple parametric processes, the above challenges can be overcome in a relatively straightforward fashion. By engineering the modes' frequencies on individual resonators, each spatial port only talks to one mode. Therefore,

all ports are spread out spatially and in the frequency domain. Nonlinearity between modes appears after they modestly hybridize with a three-wave mixing element. As we have mentioned in section 3.2, there is no limitation of the number of modes. As long as modes couple to the nonlinear element, then nonlinearity will naturally live between modes.

4.4.1 SHARC design

To fabricate the SHARC, we first clean a silicon wafer with a gentle Argon/Oxygen ion cleaning step prior to deposition of uniform 150 nm thick aluminum on the top of a silicon wafer with PLASSYS following an etching and a standard double angle deposition. The etching process produces the desired eigenmodes, which are LC lumped resonators. These modes are capacitively coupled to CPW traces for sending/receiving signals. To hybridize modes with a three-wave mixing element, SNAIL in our device, we fabricate interdigital capacitors, which are fabricated half by the etching process and half by the standard double angle process. SNAIL is fabricated by the standard double angle process, see Fig. 70. In our design, the biggest junction is 5 μm^2, and the smallest junction is 1 μm^2. LC resonators and SNAIL are fabricated in a way that they share the same ground plane to avoid the any issues related to a dirty ground.

It is worth mentioning that the SNAIL mode can be used as a pump mode, which implies that it can strongly couple to a CPW trace and allow pump photons to come into and out of the device easily. This is an essential advantage for multiple parametric processes, especially for pump schemes that require strong pump power to create ideal amplification.

In our design, mode a is about 5.406 GHz, mode b is about 7.442 GHz, and mode c is 8.496 GHz. The SNAIL mode modulates from around 4.6 GHz to 6.6 GHz. From the resonance modulation, we observe the energy splitting due to the coupling between the SNAIL and mode a. By fitting the resonance modulation to the theoretical prediction, which is shown as a red-dot line in Fig. 71, we can figure out this hybridization strength is around 150 MHz. Also, from the theory, the forbidden zone, where the mode hybridizes at least 10 % with the SNAIL, can be found and indicate as light orange in the figure. The following measurements are taken when the device is operated at around -0.42 mA, as shown in the

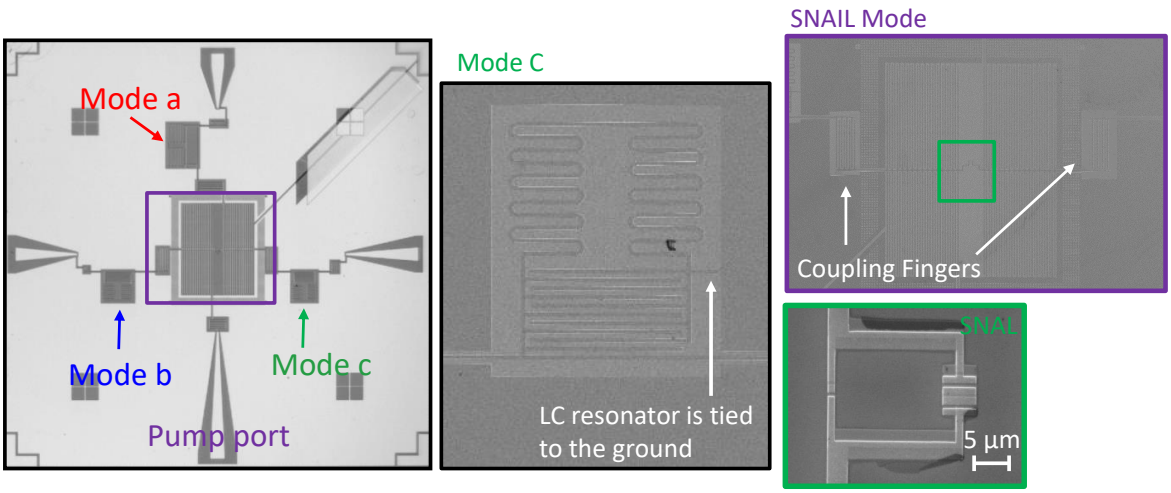

Figure 70: **SHARC optical/SEM images.** SNAIL is surrounded by three modes. Each mode is capacitively coupled to a CPW trace. The SNAIL and linear modes are modestly hybridized with each other through interdigital capacitors, and all LC resonators and the SNAIL share the same ground plane.

figure.

4.4.2 A single parametric process

The simplest way to prove three-wave mixing exists between modes is to test a single parametric process. With knowing all modes' frequencies, we can set a pump's frequency to the sum of two modes and perform a single gain process between two modes, as shown in Fig. 72. We observe 20 dB gain in both reflection and transmission in these three different single pump processes. In this simple experiment, we prove that the gain process indeed exists between mode a, b, and c. Moreover, we can change pump frequency to a difference of modes to perform the conversion process. As we anticipate, about a -20 dB dip appears in reflection while 0 dB unity gain shows up in transmission, see Fig. 73.

Another advantage of using SNAIL as a mixing element is to produce degenerate gain

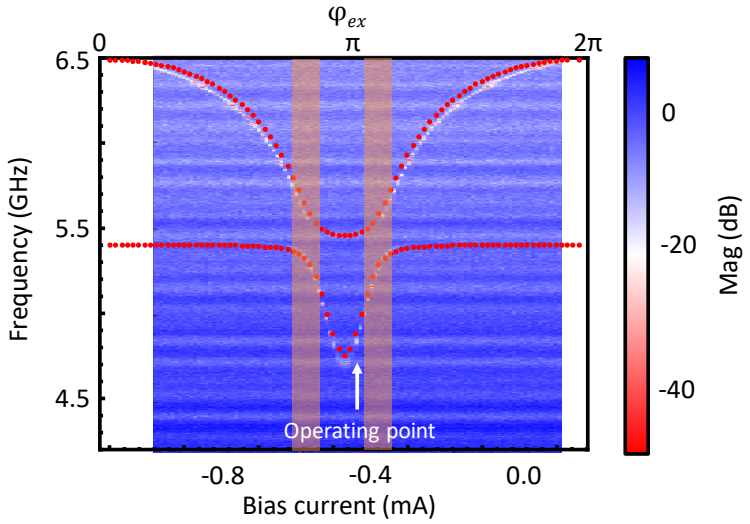

Figure 71: **SHARC resonance modulation.** We observe resonance modulation while varying bias current and fit the result to the theory, which is the red dotted line. The light orange area is the forbidden area where at least 10 % of the mode is hybridized with the SNAIL mode. From the fitting, we obtain a g_2 coupling between the SNAIL and 5.4 GHz mode of about 150 MHz. This operating point is used for the parametric processes shown in this section.

processes naturally. SNAIL has degenerate coupling terms inherent in the Hamiltonian, which will pass to linear modes after hybridization. One can prove this by setting the pump frequency to be twice of mode's frequency, anticipating the gain profile in reflection, as shown in Fig. 74 (a). Furthermore, we have mentioned in the previous section, SNAIL can also be treated as a mode. Three-wave couplings also appear between SNAIL and linear modes. Here, we perform the conversion process to prove that the input photons can convert to SNAIL mode, see Fig. 74 (b).

SHARC is designed to allow easier control of Hamiltonian and addition of eigenmodes to the circuit. For the purpose of creating ideal directional amplifiers, it is convenient to control signal flows and use the SNAIL as a pump port to increase the strength of coupling without worry of running out of generator pump power. Additionally, one can use SHARC

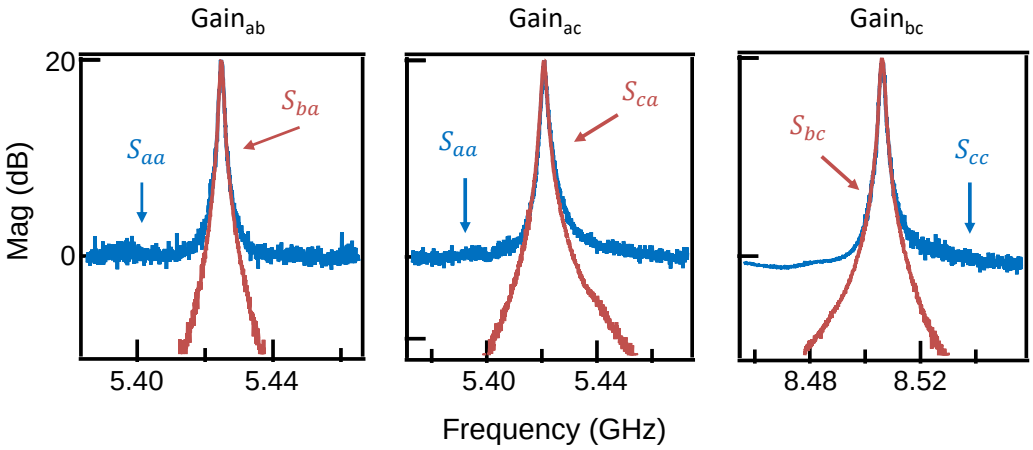

Figure 72: **SHARC: gain.** A single pump gain process performed between different mode. In all cases, 20 dB appears in reflection and transmission.

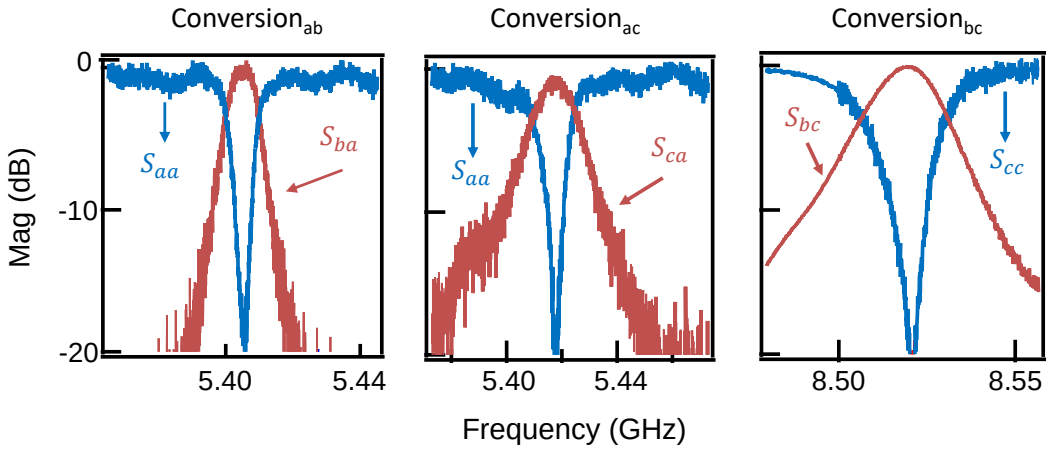

Figure 73: **SHARC: conversion.** A single pump conversion process performed between different mode. In all cases, -20 dB appears in reflection with unity gain in transmission.

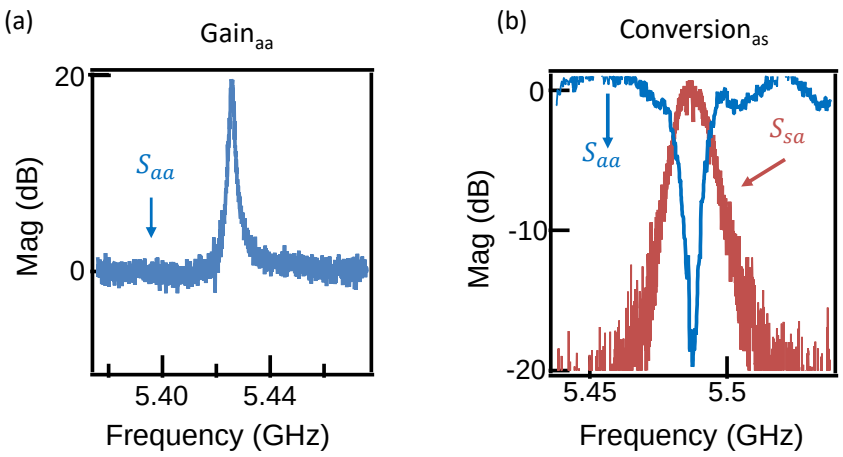

Figure 74: **(a) Degenerate gain process.** Another advantage of using SNAIL as a three-wave mixing element lies in creating degenerate gain processes naturally. This is unlike the JPC, which required asymmetry of the ring to produce a degenerate gain Hamiltonian. **(b) Conversion between linear mode to SNAIL.** Three-wave coupling also exists between SNAIL and linear mode. We use a conversion process as an example.

to read out a multiple qubit system. Each individual linear mode can talk to one qubit cavity system; therefore, one amplifier can readout at least three qubit signals with this particular device. Also, by strongly coupling to the snail mode, we can design large linewidth modes, which leads to larger gain bandwidth. The other advantage of SHARC is that it provides a considerable degree of freedom in terms of fabrication. An individual component can be realized with different fabrication processes. For instance, in this design, modes are lumped LC resonators. However, one can also use $\lambda/2$ resonators instead. As long as they have the same resonance and the same coupling strength to the SNAIL and an output port, then their behavior should be identical.

4.4.3 GC amplifictaion

We can further perform GC amplification to the device. GC gain can be controlled by increasing/decreasing both gain and conversion processes simultaneously. Even though we operate the device at null points of the SNAIL, we still witness the shift of mode frequency when both pumps are on, which might be caused by dynamic Kerrs generated by pumps [65, 94]. With fine-tuning on both pump's power and frequency, we eventually can balance gain and conversion process and reach balanced GC amplification, see Fig. 75. The imbalanced case can be achieved by setting the conversion power to be stronger than that of gain. To achieve directional amplification, we need to have GC imbalanced amplification between not only mode a and b but also a and c, which is also shown in the figure.

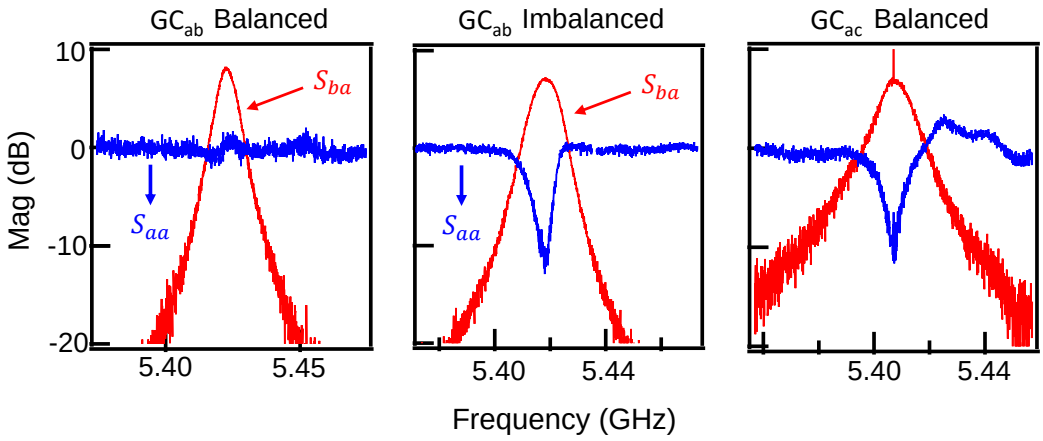

Figure 75: **SHARC: GC.** The balance and imbalanced GC amplification are shown in this plot. The first two are GC between mode a and b while the last one is between mode a and c.

With this device, we have both GC almost aligned on top of each other, meaning the GC$_{ab}$ and the GC$_{ac}$ peaks align at the same frequency. In Fig. 75, they are around 10 MHz away. We believe that we can align these two together if we have more time to operate this device. Unfortunately, all these measurements are taken a few days before the COVID 19 global pandemic. However, at least this is an auspicious result and proves that SHARC has

potential to be a platform for an ideal directional amplifier. The last ingredient required to achieve the ideal amplifier is to prove that SHARC can also be used as a circulator with the conversion process between modes.

4.4.4 Circulator in SHARC device

Since the mode frequency is designed to be different, each mode has its own input/output port. We do not need to use 180° hybrids or engineer bandpass filters to control signals, which indicates that we can measure the whole scattering matrix of the circulator. The data is shown in Fig. 76 where the circulating direction is from c to b to a and then back to c.

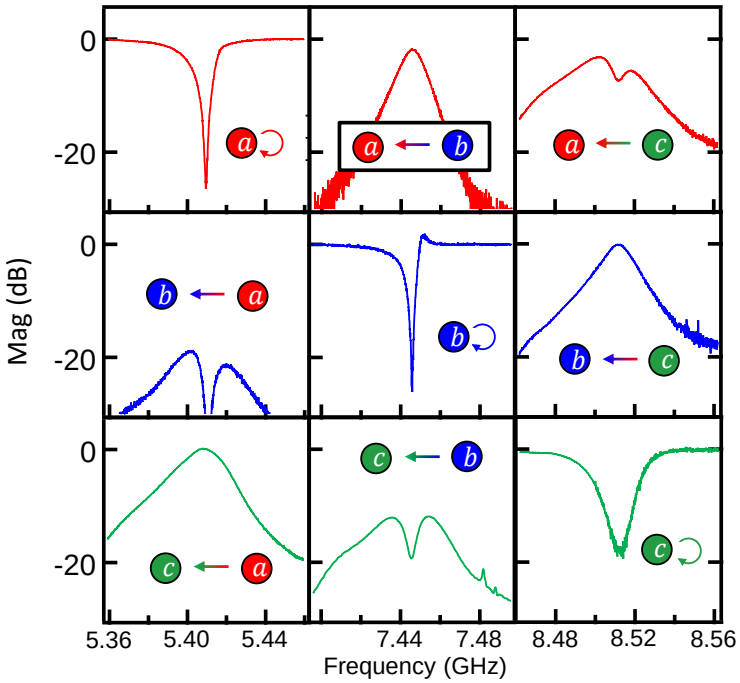

Figure 76: **SHARC: circulator.** Turning on conversion processes between a, b, and c modes, we achieve a circulator on the same SHARC device. This data is taken without external 180° hybrids.

To summarize, SHARC has outstanding flexibility in terms of circuit design and Hamiltonian engineering. Each component on-chip corresponds to a parameter in the Hamiltonian.

It can be generalized to an N-mode system simply by hybridizing N LC resonators to a mixing element that distributes non-linearity between all modes. Also, we have demonstrated multiple parametric processes on SHARC and shown that outcomes behave as we anticipate.

5.0 Saturation power limitation

5.1 Limitation due to Kerr terms

5.1.1 Introduction

A superconducting amplifier's utility is determined by several parameters. These include its quantum efficiency, which describes the noise added during amplification [22], tunability to match the signal frequency of interest, instantaneous bandwidth [95, 96], and the ability to process large amplitude signals. This last parameter is typically referred to as the saturation power, or more precisely as $P_{\text{-1dB}}$, the input power at which the gain falls by 1 dB from its small signal value. Conventionally, saturation in the amplifiers is attributed to depletion of photons from the microwave pump tone [84, 82, 43]. The pump both controls the amplifier gain and serves as the power source for photons created in the amplification process, resulting in a monotonic decrease in gain with increasing signal power.

However, pump depletion has, in almost all cases, failed to give an accurate description of experimental device performance [84, 82]. In this letter we show that, instead, Kerr nonlinearities inherent to Josephson junctions are the dominant factor that limits device saturation power. Our results give good qualitative agreement between a theory which completely neglects pump depletion and experimental data for phase preserving amplification in the Josephson Parametric Converter (JPC) [33, 34]. We find that for typical device parameters, the Kerr terms of the Hamiltonian cause the system to dispersively shift away from its bias point before the effects of pump-depletion become relevant.

Given this understanding, we present a methodology for optimizing device performance in the presence of Kerr nonlinearities while retaining device tunability. Although in this paper we specifically study amplifiers based on three-wave mixing with the Josephson Ring Modulator (JRM) [84], this effect will be equally prominent in three-wave mixing devices based on SQUIDS or other multi-junction circuits with similar-amplitude Kerr terms [64]. We note that a related effect has been studied theoretically for the case of single junction

four-wave mixing based amplifiers [97].

5.1.2 Experimental data and discussion

For all data, an external DC magnetic flux, $\Phi_{\text{ext}} = 1.2\ \Phi_0$, was applied, where $\Phi_0 = h/2e$ is the magnetic flux quantum and we define the flux as applied to the full JRM (which with its four loops is periodic with $4\Phi_0$ total applied flux). At this flux, the resonant frequencies of mode a and b are $\omega_a/2\pi = 5.083$ GHz and $\omega_b/2\pi = 7.452$ GHz, and the linewidths are $\kappa_a/2\pi = 20$ MHz and $\kappa_b/2\pi = 56$ MHz. We first identified the combination of pump powers and frequencies yielding $G = 20$ dB, as shown in Fig. 77 (b). For each pixel, a pump power and frequency combination were applied to the pump port, and the small-signal response for $P_{sig} = -150$ dBm was recorded. Each curve was first fitted to identify the maximum gain and associated signal frequency. We found that the most accurate bias conditions were identified by subsequently fitting all peak-gain points at a given pump frequency to the expected response of G vs. P_p, as shown in the inset. Comparing to Fig. 77 (a), the pump power needed for 20 dB gain increases more rapidly with pump detuning in the data, which is due to impedance variation of the external 50 Ω environment to which the JPC couples [96].

Next, we evaluated the influence of increasing signal power by repeating this protocol for increasing signal powers, as shown in Fig. 77 (c). As the signal power increases, the amplifier response shifts to lower frequency in excellent qualitative agreement with calculated results shown in Fig. 77 (a), including the asymmetry between positive and negative detunings. For positive detunings the modes shift away from the bias point, thus higher pump power is required to maintain 20 dB gain. For negative detunings, the situation is at first reversed as the modes move closer, resulting in an initial shift to *higher* gain before they, too, fall as the modes continue to shift with increasing signal power.

This anomalous behavior requires us to modify how we evaluate saturation, otherwise we may assign very high saturation powers to an amplifier whose response is extremely nonlinear. A more symmetric limit of $P_{\pm 1\text{dB}}$, defined as the power at which the gain first deviates in either direction by 1 dB from its small signal value, will give a much fairer comparison of

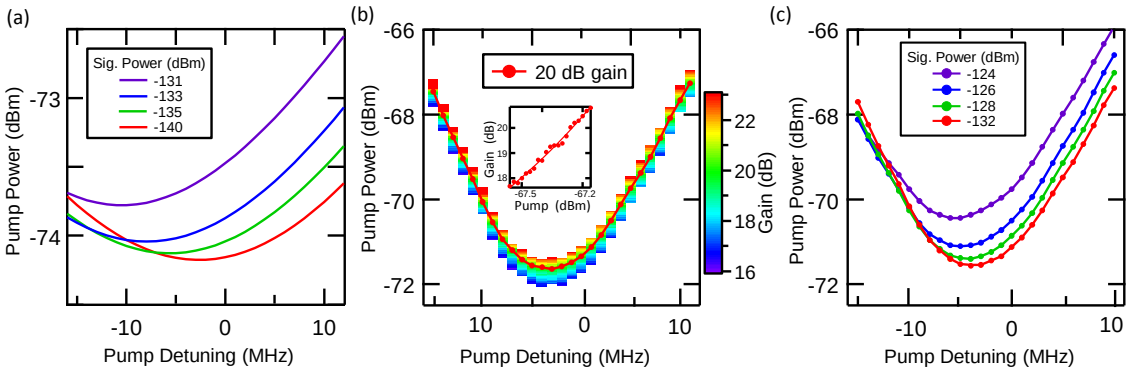

Figure 77: **(a) 20 dB gain curve for different signal powers : theory.** 20 dB gain curve for different signal powers. **(b) 20 dB gain curve for a signal powers : experiments.** Maximum gain vs. pump detuning ($\omega_p - (\omega_a + \omega_b)$) and power for -150 dBm signal power. Each pixel represents the fitted maximum gain for a pump power/detuning combination. The red line connects all the 20 dB points obtained from fitting gain data at each pump detuning vs pump power (see inset for example fit curve). **(c) 20 dB gain curve for different signal powers : experiments.** Experimental $G = 20$ dB points versus pump detuning and power for varying signal powers.

different bias conditions.

The amplifier's saturation behavior was measured as shown in Fig. 78. For each pump frequency we recorded gain vs. signal power while using the pump power and signal frequency determined in Fig. 77 (b). The full data set is shown in Fig. 78 (b); for clarity, representative curves are plotted separately in Fig. 78 (a). The calculated saturation curves using extracted device parameters (see Appendix D) are plotted in Fig. 78 (c). For both data and calculation, the gain initially increases with signal power at negative detuning before finally falling, and for positive detunings the gain monotonically decreases. The ± 1 dB saturation values are indicated by blue diamonds and red triangles, respectively.

At positive detunings the $P_{\text{-1dB}}$ limit is reached first, in both theory and experiment, eventually leveling off at a value $5 - 10$ dB lower (Fig. 78 (a) blue and purple data) than the optimal monotonically decreasing gain point(Fig. 78 (a) in green), which is found very

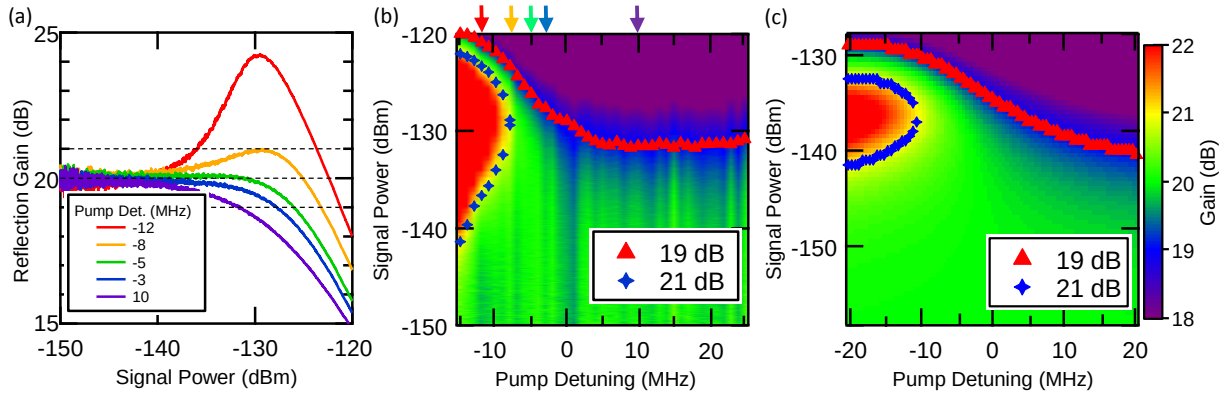

Figure 78: **(a) Measured reflection gain versus signal power.** Measured reflection gain of the JPC vs. signal power at selected pump detunings, showing the variation in saturation response vs pump detuning from the resonant condition. **(b) Measured reflection gain versus signal power and pump detuning: experiments.** Measured gain vs. signal power and pump detuning for 20 dB bias conditions identified in Fig. 77 (b). The colored arrows indicate the dynamic range curves in (a). **(c) Measured reflection gain versus signal power and pump detuning: theory.** Calculated theoretical gain at different signal powers and pump detunings. In both (b) and (c) the saturation values are indicated as red triangles (−1 dB) and blue diamonds (+1 dB).

near the small-signal resonant condition. For negative detunings, the gain rise phenomenon becomes increasingly severe (Fig. 78 (a) in red), eventually resulting in unstable/hysteretic gain conditions (not shown). However, for modestly negative detuning, the gain rise phenomenon can act to enhance the saturation power. Thus, we identify an alternate optimum bias condition (Fig. 78 (a) in orange) which rises to just less than +1 dB before falling. Taken together, these factors can result in amplifier performance that varies by well over 10 dB if the amplifier is biased without knowledge of the Kerr effect. As most amplifiers operate over a modest range of bandwidths (10's-100's of MHz) and critical currents (few μA), these behaviors should be visible in all devices, and are, in fact, visible in previously published data (for example in ref. [84]). The discrepancy between the measured saturation

power and the calculated values are mainly due to uncertainty in the energy participation ratios which determine the Kerr coefficients.

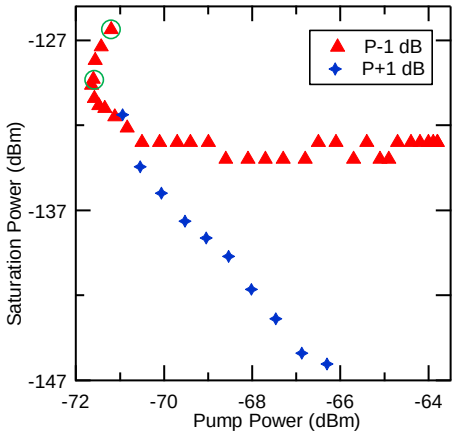

Figure 79: **$P_{\pm 1\mathrm{dB}}$ point for different pump power.** The $P_{\text{-1dB}}$ data shows the saturation of the dynamic range on the positive detuning side, while the $P_{+1\mathrm{dB}}$ data shows that the dynamic range keeps decreasing as the pump power increases. Green circles indicate the two optimal points.

Gain saturation is summarized in Fig. 79, colored by which limit (± 1 dB) is reached first. For positive detuning the $P_{\text{-1dB}}$ (red triangles) limit is relevant and falls to a static value even as P_p continues to climb for increased detuning. For negative detuning, the $P_{+1\mathrm{dB}}$ (blue diamonds) behavior is limiting and falls steadily with increasing P_p as the amplifier's response becomes increasingly distorted. The two optimum points are circled, and are both near the lowest pump powers, in direct contradiction to the expectations of pump depletion theory that bias conditions requiring stronger pump should yield higher saturation powers.

We note that although this result suggests that the JPC possesses only one best bias point for each bias flux, by jointly varying the pump frequency and flux the device should be no less tunable. In fact, our result suggests that the device can be readily tuned by jointly varying flux and pump frequency to minimize the pump power required for a given signal frequency. Finally, we add a caution that this picture can be severely disrupted by variation in the impedance presented by the microwave lines connected to the device modes, unless great care is taken to minimize reflections and mismatches in the microwave cabling. In our

experiment this is the dominant source of disagreement between theory and experiment, as the device bandwidth is observed to vary significantly for the range of frequencies at which we recorded gain data. However, at all bias points the overall behavior of Kerr-based shifts to lower frequencies dominated the device performance and allowed us to identify optimal bias conditions.

5.2 Optimizing JRM-based amplifiers via full Hamiltonian control

In previous works on Josephson parametric amplifiers, it was assumed that saturation power is limited by pump depletion [98, 33, 84, 43, 99]. This is a natural explanation, as the amplifier gain is a very sensitive function of the flux of the applied pump photons. Thus, as the input power is increased, and more pump photons are converted to signal photons, the gain falls. However, in refs. [100, 91, 101] and previous subsection 5.1, it was pointed out that the fourth order nonlinear couplings (i.e. the Kerr terms), inherent in Josephson-junction based amplifiers, can also limit the saturation power. These terms induce a shift in the mode frequencies of the amplifier as a function of signal power, which can cause the amplifier to either decrease or increase its gain. Thus, we adopt the definition of saturation power as the lowest input power that causes the amplifier's gain to either increase or decrease by 1dB, which we abbreviate as $P_{\pm 1\mathrm{dB}}$.

5.2.1 Optimizing β and p

We now discuss the main results of our investigation, which are summarized in Fig. 80. Previously, descriptions of JPCs relied on expanding the nonlinear couplings between the three microwave modes in a power series of cross- and self- couplings. The power series was truncated at the lowest possible order, typically fourth (i.e. corresponding to the cross- and self-Kerr terms) [33, 81]. In the present paper, we compare these power series expansions with the exact numerical solutions in the framework of semi-classic input-output theory. Our first main finding is that there is indeed a sweet spot for operating a JPA, see Fig. 80 (a),

at which $P_{\pm 1\mathrm{dB}}$ is maximized. The sweet spot appears for moderate values of the two circuit parameters: participation ratios $p \sim 1/7$ and shunt inductance ($\beta = L_{\mathrm{J}}/L_{\mathrm{in}} \sim 3.5$, where L_{in} is the shunt inductance, $L_{\mathrm{J}} = \varphi_0/I_0$ is the Josephson inductance, $\varphi_0 = \hbar/2e$ is the reduced flux quantum, and I_0 is the Josephson junction critical current). Our second main finding is that in the vicinity of the sweet spot nonlinear terms up to at least seventh order are comparable in magnitude and hence truncating the power series description at fourth order is invalid, see Fig. 80 (b). The second main result can be interpreted from two complementary perspectives. First, the sweet spot corresponds to high pump powers and hence the energy of Josephson junctions cannot be modeled by a harmonic potential anymore. Second, different orders of the power series expansion have either a positive or a negative effect on the gain as a function of signal power; when the magnitudes of terms at different orders are comparable the terms cancel each other resulting in a boost of $P_{\pm 1\mathrm{dB}}$. We hypothesize that the second main finding is a generic feature for Josephson junction based parametric amplifiers.

5.2.2 JPC with third order coupling, relaxing the stiff-pump approximation

As we increase the input signal strength, the power supplied to the pump mode will eventually be comparable to the power consumed by amplification, where the amplifier will significantly deviate from the ideal parametric amplifier. The pump mode strength is affected by the signal and idler mode strengths, we refer to it as the "Soft-pump" condition.

In Fig. 81, we plot the reflection gain obtained by numerical integration. The reflection gain of the amplifier is no longer independent of the input signal power, instead we see that the reflection gain deviates from 20 dB as we increase the signal mode power. Moreover, as we change the detuning of the pump mode relative to the sum frequency of the signal and idler mode, the deviation of the reflection gain changes from negative to positive. While a deviation towards smaller gain (which occurs at negative or zero detuning) is consistent with the pump saturation scenario, a deviation towards higher gain (which occurs at positive detuning) is not. The "shark fin" feature we observe here, in which the gain first deviates up and then down, has been previously attributed to intrinsic Kerr couplings [46]. The fact that the "shark fin" reappears without an intrinsic Kerr term gives us a hint that SoP-3rd

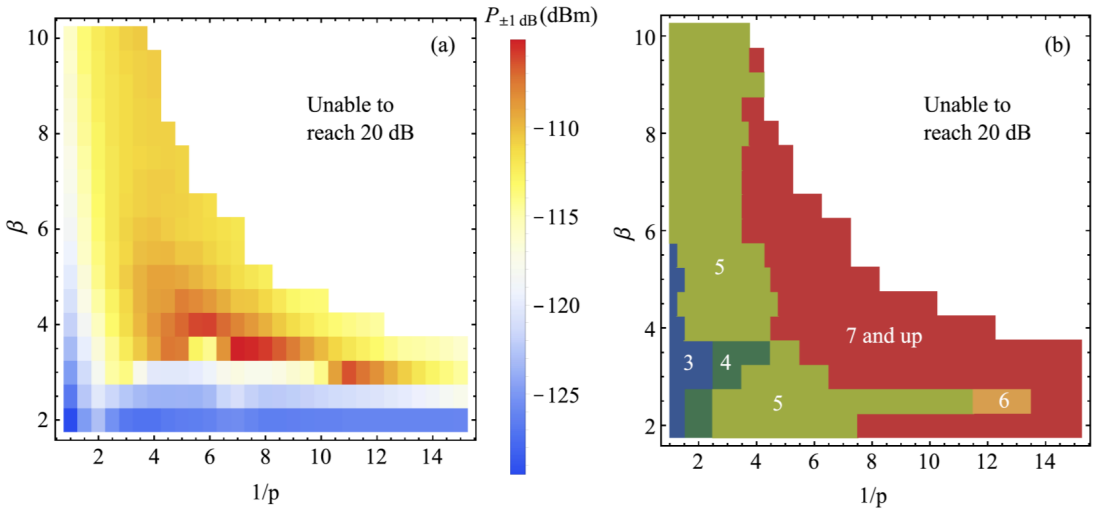

Figure 80: **(a) The saturation power of the amplifier as a function of β and p.** The saturation power of the amplifier has sweet spots in the low β regime. In small participation ratio regime, the amplifier is not able to reach desired reflection gain, i.e. 20 dB. This region is labeled in white. When β is small, in the medium participation ratio ($1/p$ about 4 to 10), because of the extra nonlinear couplings caused by external linear inductance, the reflection gain rises before dropping. The amplifier saturates to 21 dB instead. As we keep decreasing participation ratio, the "shark fin" is suppressed. The sweet spot of the saturation power is located at the edge of the "shark fin". The maximum saturation power is located at $\beta = 3.5$, $1/p = 7.0$, where the saturation power is $P_{\pm 1\ \mathrm{dB}}$ about -104.8 dBm. **(b) The minimum truncation order needed to converge small-signal reflection gain.** We show that the convergence order of small-signal reflection gain gives a good prediction on the convergence order of the saturation power. In the small-β, large-p corner, the third order truncation is enough to make the time-solver converge to the desired 20 dB reflection gain. However, as we decrease the participation ratio, higher and higher order is needed to converge the truncated theory, which shows that full-order simulation is needed to predict the performance of the amplifier near the boundary, especially around the sweet spot.

order couplings can generate an effective Kerr nonlinearity.

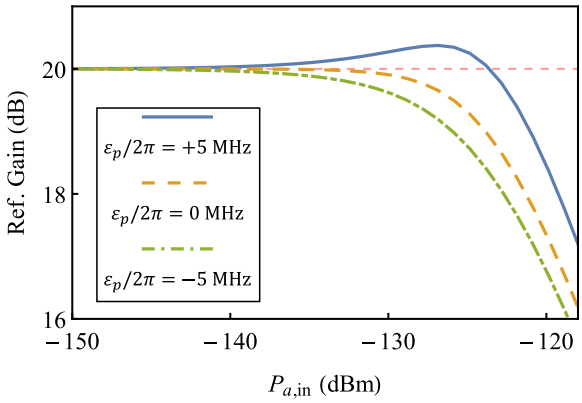

Figure 81: **Saturation power under Soft-pump condition with only third-order coupling.** We consider the soft-pump condition with third order coupling strength and calculate the reflection gain of the amplifier. We slightly detune the pump drive frequency from the sum frequency of the signal and idler mode frequency. When the pump frequency detuning ε_p is negative (green dash-dotted line), the reflection gain is further suppressed compared with on-resonance drive (orange dashed line). However, when the pump frequency detuning is positive (blue line), the "shark fin" feature reappears, which was understood as the consequence of the existence of Kerr nonlinearity in the amplifier system.

5.2.3 The effects of participation ratio to Kerr terms

When there are external resonators connected to the JRM, the flux injected from the microwave ports is shared between the JRM and the external resonators and hence the JRM nonlinearity is attenuated. To model this effect, four outer linear inductors L_{out} are added in series with the JRM circuit, see Fig. 82 (a). These inductors and the JRM can be treated as a "flux-divider" type circuit.

The self-Kerr coupling strength k_{aa} and the cross-Kerr coupling strength k_{ab} are plotted in Fig. 82 (b) and (c), respectively. The Kerr nonlinear coupling strengths (k_{aa} and k_{ab}) are calculated via both numerical method (dots) and the above perturbation method (lines) as shown in [94]. In all three β values, the perturbation analysis matches the numerical solution

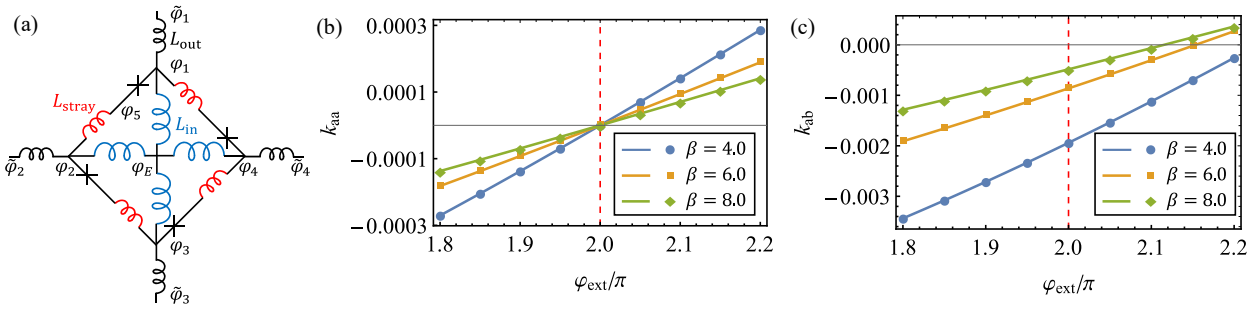

Figure 82: **The effects of participation ratio to Kerr terms.** In (a), we show a more realistic circuit model for JRM, in which we include stray inductance L_{stray} in series of Josephson junctions and outer linear inductance L_{out} in series of JRM. The fluxes associated with each nodes are labeled on the plot. In (b) and (c), we calculate the Kerr coupling strength k_{aa} (b) and k_{ab} (c) as we sweep external magnetic field bias φ_{ext} when participation ratio $1/p = 1.1$. The perturbation solution (lines) and numerical solution (dots) agree well. In (b) for all three β values, the self-Kerr coupling strength k_{aa} can always be turned off at the Kerr nulling point $\varphi_{\text{ext}} = 2\,\pi$. However, in (c), we notice that the the magnetic field bias φ_{ext} to turn off cross-Kerr coupling k_{ab} depends on the choice of β. This means the exact Kerr nulling point of the does not exist any more when the participation ratio is not unity. Parameters chosen: three mode decay rates are $\gamma/(2\,\pi) = 0.1$ GHz, the critial current of the junctions is $i_c = 1.0\ \mu$A. The outer linear inductance ratio $\zeta = 0.1$. The rest of the circuit elements are set by the mode frequencies at $\varphi_{\text{ext}} = 2\,\pi$, and they remain when we tune the external flux bias.

well. Further, we notice that the self-Kerr coupling strength can still be turned off at the $\varphi_{\text{ext}} = 2\ \pi$ (Kerr nulling point) no matter what β value we choose, see Fig. 82 (b). But the cross-Kerr couplings cannot be turned off at this magnetic bias point when participation ratio is not unity, see Fig. 82 (c).

A similar analysis of the JRM with Josephson-junction based shunts, as in [82, 92], shows that the cross-Kerr terms null together at a similar point to our linearly shunted JRM, but the self-Kerr null point is shifted to a larger flux.

5.2.4 Taking advantage of Kerr terms

In section 4.1.5, we have demonstrated that lumped single-ended JPC allows us to fabricate large junctions with a significant amount of three-wave coupling. Also, we can extract the Kerr coefficient and identify nulling points. With this device, we have demonstrated saturation power at three different bias currents, see Fig. 83 (a).

When it is at a nulling point, gain starts at around 20 dB and gradually increase and hit $P_{+1\ \text{dB}}$ point at about -115 dBm. After that, it climbs up and reaches an unstable regime at -105 dBm, which we will come back and discuss later. For another bias current, the blue one shown in Fig. 83 (a), it breaks $P_{+1\ \text{dB}}$ at about -130 dBm and form "shark fin". Based on our discussion is the section, this shark fin might come from the combination of the inherent fourth-order of the Hamiltonian or the dynamic Kerr effects. The purple bias point, on the other hand, has the largest Kerr terms but the greatest saturation power. It starts from 20 dB and forms a tiny "shark fin", which has turnaround point right at 21 dB. We believe at this point, the dynamic Kerr generated by the pump compensates the inherent Kerr terms and results in a massive saturation power.

For the green curve in Fig. 83 (b), we measure with forward and backward sweep of input signal power, see Fig. 84. The backward sweep has a tremendous discrepancy with the forward sweep. At this point, this is still an open question and waiting for us to explain.

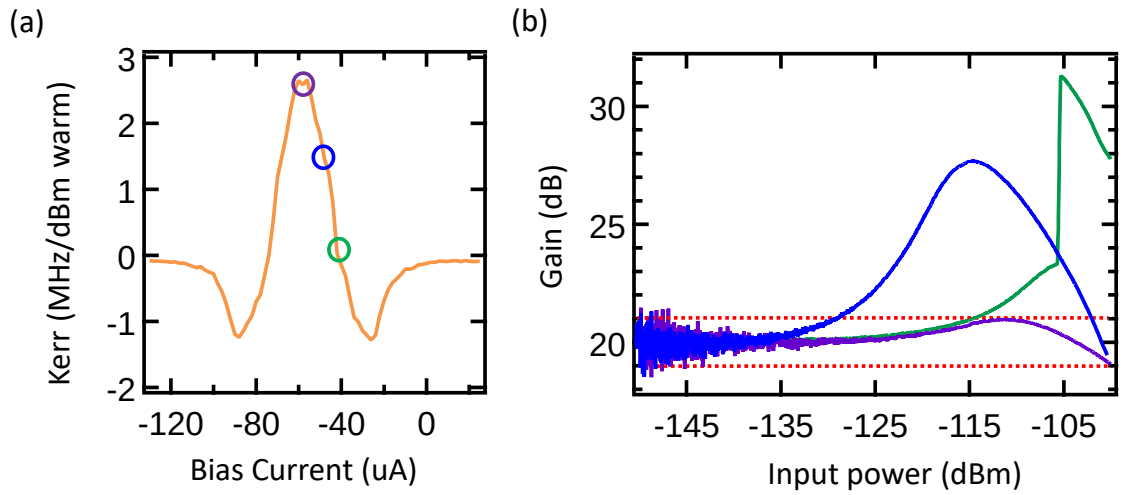

Figure 83: **(a) Kerr coefficient obtained from the Kerr measurement.** We perform the standard Kerr measurement on the aluminum shunted JPC. Three bias points are used to compare the saturation power performance. **(b) Saturation power at different bias currents.** The best saturation happens when the Kerr term is at the maximum. It is possible that the inherent Kerr and dynamic Kerr compensate with each other and yield the best saturation power. Note that typically saturation power for the JRM based device is usually -120 dBm. This result proves that the cavity-based amplifier can have huge saturation power as well.

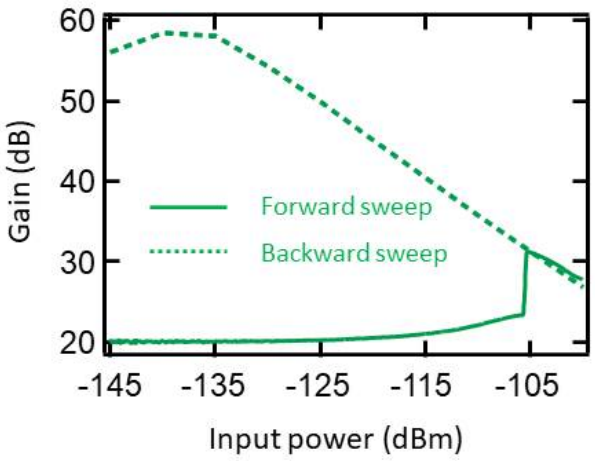

Figure 84: **Saturation hysteresis.** Saturation power is measured with forward and backward sweep of input signal power. The device has hysteresis, which resulted in different values for saturation power in the backward sweep.

6.0 Conclusions and perspectives

The first key element of amplifier design we have demonstrated in this thesis is the use of multiple parametric processes (Ch. 2) applied to an few-mode system to generate both gain and interference which will change the amplifier's functionality. From the scattering matrix derived in a matrix form, the optimal operating conditions are calculated and implemented in an actual devices, as we have shown in chapters 4. Our approach to a quantum-limited, directional amplifier is based on two gain processes applied to a circulator generated by conversion processes between three cavity modes. The pumping scheme generates (a) gain in transmission but not in reserve direction, (b) gain increases linearly with pump power, (c) bandwidth remains the same regardless of gain, and (d) bandwidth is larger than typical single gain process. We can even use it to measure multiple qubits with different cavity frequencies if 20 % of measurement efficiency is sacrificed.

However, creating the optimal operating conditions for the scheme requires precise control of the system's Hamiltonian. Often, the Hamiltonian of Josephson junction-based circuits contains undesired Hamiltonian terms. Using JPC as an example, it has inherent fourth-order or even higher-order terms in the Hamiltonian, which tends to shift mode frequencies causing the pump conditions to no longer be at optimal operating conditions. Fortunately, at the external flux of $\pm 2\ \pi$, the nulling points, our linearly shunted JRM can eliminate fourth- and higher-order even terms. Even though the nulling points will be shifted away from $\pm 2\ \pi$ due to the stray inductance used to connect the Josephson junctions to output ports, we can carefully design the JPC to factor in the inductance ratio between the Josephson junctions and shunted linear components to account for participation ratio and control the Hamiltonian, see chapter 3.

Another challenge for multiple-parametric processes is signal flow control. Detecting modes' signals at their ports has the advantage of simplifying the measurement system, meaning bandpass filters or 180° hybrids are not needed. We invented a new circuit design, SHARC, that achieves signal flow control relatively easily compared to other amplifiers. SHARC provides enormous flexibility in terms of Hamiltonian engineering as well. Each

component has a corresponding variable in the Hamiltonian, which implies that components are not tied together and that changing one will not affect others, see chapter 3.

In chapter 5, we identified the (many) sources of limitations in saturation power. Among them are the pump-dependent shifts of mode frequency caused by Kerr terms, dynamically generated Kerr-like terms due to imperfectly stiff pumps, as well as fifth-order terms which resemble number operators multiplying our third order couplings. Furthermore, a generic optimization of a superconducting circuit is discussed and implemented in order to improve the saturation power. We designed a device based on that optimization method and achieved about -100 dBm saturation power, which is about 20 dBm higher than a typical JRM-based amplifier. Although not yet directional, these devices are very promising and we are building them for both the use of our lab and our collaborator's labs at other universities.

Although the ideal amplifier has not yet been realized, we have made great strides in Hamiltonian engineering, including using parametric processes and designing optimal superconducting circuits. There are several practical challenges that we have to overcome. When applying parametric drives, we have to relate the experimental results to the theory via the scattering matrix. From theoretical calculation, we can predict outcomes by giving pump power and phase. However, when increasing the pump power, the shift of mode frequency becomes significant due to inherent higher even-order terms and dynamic Kerr terms, which are not included in traditional scattering theory.

When designing an amplifier circuit, we need to make sure all gain and conversion frequencies are at least five linewidths away from any mode's resonances or harmonics. By doing so, we avoid accidentally exciting unwanted parametric processes. Moreover, the gain peaks or dips show up only on resonance when the pumps have no detuning, which implies that the peak/dip frequency should relate to pumps' frequencies. We can therefore keep tracking peaks/dips in frequency and pumps' frequencies to avoid losing ourselves in a wild sea of variables.

In the future, members of the Hatlab will implement optimization on SHARC designs to build an robust, practical directional amplifier and use it to measure qubits. More, the SHARC can have many modes, and it may be possible to expand it to have multiple potential input modes, allowing us to measure multiple qubit channels efficiently on a single output

line via time-bin multiplexing. It is also worth exploring the replacement of our single SNAIL mode with either a SNAIL array in a single resonator, or an array of SNAIL-bearing modes (mimicking the participation of many atoms in a LASER or MASER) to produce a more robust gain medium, and further enhance our achievable saturation power.

The SHARC itself is a product of re-examining our conventional JPC amplifiers based on recent results in the lab on parametrically-driven signal routers (see the forthcoming theses of Chao Zhou and Pinlei Lu). Other members of the lab are investigating the potential for SNAIL-based, third-order qubit-qubit gates, as well as bath engineering loss operators for cavities and qubits (Xi Cao, Pinlei Lu, Maria Mucci and Mingkang Xia). Thus, it may be that the tools and knowledge we are developing for amplifiers may find other important applications. Already, we are having fruitful conversation about how the limits we have identified on saturation in amplifiers can apply to these more qubit-centric systems, and it will be exciting to see how the topics converge. It is also exciting to contemplate how we can replace Josephson junctions with other nonlinear elements, such as opto-mechanical or super-semiconducting elements for other applications.

Appendix A Circuit QED

Circuit QED stands for circuit quantum electrodynamics. It is the study of electrical circuits that operate at microwave frequency, comparable to those used in cell phones, for example. These circuits are made of superconducting materials and are cooled to a temperature close to absolute zero so that there is no dissipation of energy. The goal is to design these electrical circuits so that they behave like atoms that have quantized energy levels.

This section briefly reviews the general scheme for circuit quantization, using the classical simple harmonic oscillator as an example. The ideal is to start from a circuit diagram for a non-dissipative circuit.

A.1 The simple harmonic oscillator

Consider a mass m on a spring with spring constant k and a characteristic frequency of $\omega_0 = \sqrt{k/m}$, see Fig. 85 (a). The position of the mass is x and the velocity is $v = dx/dt$. We can obtain the Hamiltonian :

$$H = KE + PE = \frac{p^2}{2m} + \frac{1}{2}kx^2$$

To make the harmonic oscillator quantum, we simply replace x and p by the position and momentum operators, $\hat{x}$ and $\hat{p}$. Since they do not commute, we can also write down the usual commutator, $[\hat{x}, \hat{h}] = i\hbar$. In other words, the quantum simple harmonic oscillator is described by the quantum Hamiltonian:

$$H = \frac{\hat{p}^2}{2m} + \frac{1}{2}m\omega_0^2\hat{x}^2 = \hbar\omega(\frac{1}{2} + \hat{a}^\dagger\hat{a})$$

where

$$\hat{x} = \sqrt{\frac{\hbar}{2m\omega_0}}(\hat{a}^\dagger + \hat{a})$$
$$\hat{p} = i\sqrt{\frac{\hbar m\omega_0}{2}}(\hat{a}^\dagger - \hat{a}) \tag{A.1}$$

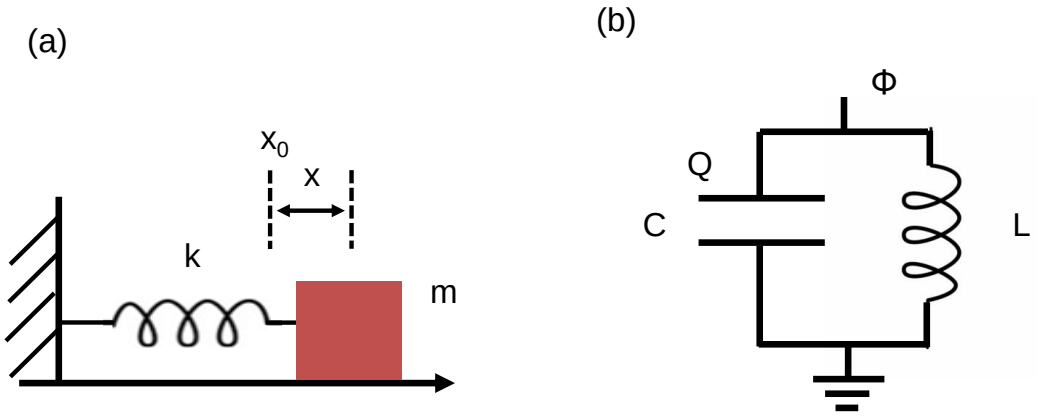

Figure 85: **(a) A mass on a spring system.** A mass m on a spring with spring constant k. **(b) LC circuit.** LC circuit forms a harmonic oscillator.

We can perform the same quantization trick with an LC circuit, see Fig. 85 (b). The Hamiltonian of the circuit is

$$H = \frac{Q^2}{2C} + \frac{\Phi^2}{2L}$$

Similar to the previous example, the LC harmonic oscillator in the quantum form can be achieved by replacing Q and Φ by the charge and flux operators, $\hat{Q}$ and $\hat{\Phi}$. Comparing this expression with the previous example, we realize the commutator, $[\hat{\Phi}, \hat{Q}] = i\hbar$. The Hamiltonian of an LC oscillator in the quantum form is

$$H = \frac{\hat{Q}^2}{2C} + \frac{\hat{\Phi}^2}{2L} = \hbar\omega(\frac{1}{2} + \hat{a}^\dagger\hat{a}) \tag{A.2}$$

where

$$\hat{\Phi} = \Phi_{\text{ZPF}}(\hat{a^\dagger} + \hat{a}), \text{ and } \Phi_{\text{ZPF}} = \sqrt{\frac{\hbar Z}{2}}$$
$$\hat{Q} = iQ_{\text{QPF}}(\hat{a^\dagger} - \hat{a}), \text{ and } Q_{\text{ZPF}} = \sqrt{\frac{\hbar}{2Z}}$$

$\omega = 1/\sqrt{LC}$ and $Z = \sqrt{\frac{L}{C}}$ are resonant frequency and characteristic impedance of the circuit while Φ_{ZPF} and Q_{ZPF} represent the standard deviations of the flux and charge fluctuations of the ground state, respectively. From Eq. A.2, the quantized superconducting LC circuit shows the same expression as a quantum-mechanical harmonic oscillator and we can define the relationships between mechanical and LC oscillator, listed in Table 1. The key point to realise from this calculation is that the quantum LC circuit is just a quantum simple harmonic oscillator, with quadratic potential energy, quantized with equally spaced energy levels and annihilation and creation operators.

Table 1: **Comparison of Hamiltonian between the mechanical and LC oscillator**

Mechanical oscillator	LC oscillator
m	L
k	$1/C$
$\omega_0 \equiv \sqrt{k/m}$	$\omega_0 \equiv \sqrt{1/LC}$
$p \equiv mv$	$p \equiv LI = \Phi$

From this point forward in this dissertation, I will drop the "hats" on the operators when it is clear from context that it is an operator and not a complex number.

A.2 A nonlinear component: Josephson junction

In a linear system of harmonic resonators, the spacing of the energy levels is $\hbar\omega$ for any transition. This is why in practical superconducting circuits, a non-linear component is required: it changes the spacing of the energy levels, which is a necessary criteria for building

a qubit. Also, it generates the capability to couple LC resonators in such a way that one can use it to build practical devices such as amplifiers. The most common non-linear component is the Josephson junction.

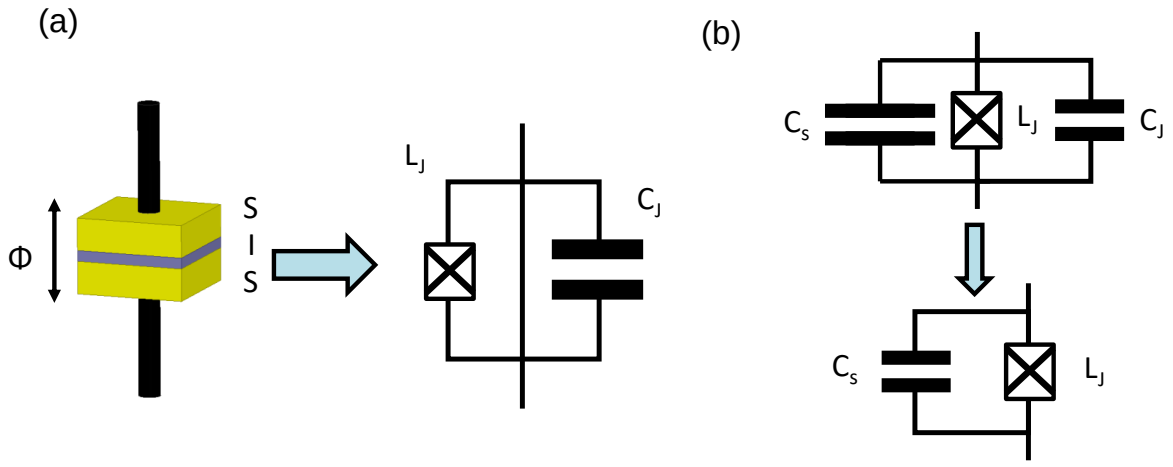

Figure 86: **(a) Schematic circuit of a Josephson junction.** A single Josephson junction consists of two superconducting plates, labeled as L, with an insulator layer (I) in between. The phase across the junction is labeled Φ. In the circuit QED, a single junction is represented by an LC circuit, which has a non-linear inductor, represented by a cross, and capacitance. **(b) Schematic circuit of an LC circuit.** Typically, we shunted the junction with a capacitor, C_S, that has more extensive energy than C_J. By doing so, the resonance of the circuit can be tuned independently.

Josephson junctions are made out of two superconducting electrodes, separated by an insulator see Fig. 86 (a). This means that that a Josephson junction can be represented by a pure capacitor in parallel with a pure tunneling element in between. The Hamiltonian of the junction is

$$H = \frac{\hat{Q}^2}{2C_J} - E_J \cos\left(2\pi \frac{\hat{\Phi}}{\Phi_0}\right) \tag{A.3}$$

where E_J, C_J, and $\Phi_0 = h/2e$ are tunnel coupling energy, junction capacitance and the superconducting flux quantum respectively. This equation also gives the first clue as to what role the junction plays in a circuit theory context. Assuming the junction is perturbed

around the stable point where the phase across the junction is zero, one can expand the cosine term of the tunnelling element in a Taylor series

$$H = \frac{\hat{Q}^2}{2C_J} - E_J\left(1 - \frac{(2\pi)^2}{2\Phi_0^2}\hat{\Phi}^2 + \frac{(2\pi)^4}{24\Phi_0^4}\hat{\Phi}^4 + \cdots\right)$$

Comparing the above equation with Eq. A.2, we see that the pure tunnelling element behaves like a linear inductor

$$H \approx \frac{\hat{Q}^2}{2C_J} + \frac{1}{2}\frac{E_J(2\pi)^2}{\Phi_0^2}\hat{\Phi}^2 = \frac{\hat{Q}^2}{2C_J} + \frac{\hat{\Phi}^2}{2L_J}, \text{ and } L_J = \frac{\Phi_0^2}{(2\pi)^2 E_J} = \frac{\varphi_0^2}{E_J}$$

where $\varphi_0 = \frac{\Phi_0}{2\pi}$ is called the reduced magnetic flux quantum. Moreover, inherent higher-order terms in the expansion provide non-linearity to the junction. Consequently, a single Josephson junction can be a approximately represented by a capacitor in parallel with a nonlinear inductor - it is a nonlinear quantum LC circuit in a single element, see Fig. 86 (a).

To make Josephson junction circuits more configurable, a capacitor, C_S, that usually has a larger capacitance, is used for shunting the junction, see Fig. 86 (b). Due to this reason, one can simplify the Hamiltonian of the junction as only the inductance part

$$H = -E_J \cos\left(2\pi\frac{\hat{\Phi}}{\Phi_0}\right) \tag{A.4}$$

This implies that the Hamiltonian of this circuit is

$$H_{JJ} = \frac{\hat{Q}^2}{2C_S} - E_J\cos\left(2\pi\frac{\hat{\Phi}}{\Phi_0}\right) \approx \frac{\hat{Q}^2}{2C_S} + \left(\frac{1}{2}\frac{E_J(2\pi)^2}{\Phi_0^2}\hat{\Phi}^2 - E_J\frac{(2\pi)^4}{24\Phi_0^4}\hat{\Phi}^4\right)$$

Rewriting the above equation, the Hamiltonian of a transmon can be reached

$$H_{JJ} = \hbar\omega a^\dagger a - \frac{\alpha}{2}a^\dagger a a^\dagger a \tag{A.5}$$

where $\omega = 1/\sqrt{C_S L_S}$ and α are angular frequency and anharmonicity of a transmon, respectively.

In this work, multiple Josephson junctions will be used to design a superconducting circuit that has the desired amount of modes coupled with each other. With these coupling terms, one can build electronic devices such as beam-splitters, isolators, amplifiers, etc. [83].

Using a two-port element as an example, see Fig. 87, we list all variables required when one analyzes an arbitrary superconducting circuit, see Table 2. The dynamics of the element are characterized by the voltage across the component and the current flowing through it, which is the same as in Kirchhoff's laws. It is useful to convert the voltage and the current to the element's flux and charge because the Hamiltonian of a Josephson junction is a function of flux.

Table 2: **Symbols used in circuit element of Fig. 87**

Variable	Symbol used
Voltage at node i	v_i
Voltage across element	$v \equiv v_1 - v_2$
Current through element	i
Node flux	$\phi_i \equiv \int_{-\infty}^{t} v_i(t')dt'$
Generalized element flux	$\Phi = \int_{-\infty}^{t} v(t')dt' + \int_{2}^{1} \vec{A}(t)d\vec{s} = \phi_1 - \phi_2 + \int_{2}^{1} \vec{A}(t)d\vec{s}$
Generalized element charge	$Q = \int_{-\infty}^{t} i(t')dt'$
Reduced branch flux	$\varphi \equiv \frac{\Phi}{\varphi_0}$
Magnetic flux quantum	$\Phi_0 \equiv \frac{h}{2e} \equiv 2\pi\varphi_0$
Reduced magnetic flux quantum	$\varphi_0 \equiv \frac{\hbar}{2e} \equiv \frac{\Phi_0}{2\pi}$
External magnetic flux	Φ_{ext}

The flux, Φ, through the element is defined not only by node flux but also the vector potential $\vec{A}$ along the element. This term usually is not zero when external magnetic filed is applied to the circuit.With all these variables, one can analyze arbitrary superconducting circuits following the Kirchhoff's laws in terms of flux and charge.

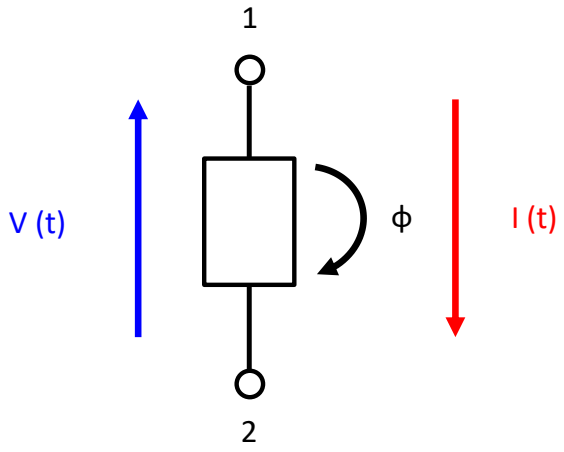

Figure 87: **Schematic of branch element.** The dynamics of the element can be described by the voltage across it and the flowing current, which can be represented by the phase and charge of the component.

Appendix B Cascaded amplifiers

When a microwave input signal travels to a cascade of amplifiers, each stage may degrade the signal to some degree. The noise of the cascaded system can be determined when the noise temperature of the individual stages are known. Noise power, N, at a given temperature, T, is given by

$$N = k_B T_0 B \tag{B.1}$$

where k_B and B are Boltzmann constant and the measurement bandwidth, respectively.

Now, let us consider a cascade of two amplifiers, having gains G_1, G_2 and noise temperature T_1, T_2, as shown in Fig. 88. We can obtain the overall noise power at the output of the first stage as the combination of the noise power that goes through the first amplifier with inherent amplifier noise

$$\begin{aligned} N_1 &= G_1 N_i + G_1 k_B T_1 B \\ &= G_1 k_B T_0 B + G_1 k_B T_1 B \end{aligned}$$

Similary, the output noise power of the second stage is expressed as

$$\begin{aligned} N_0 &= G_2 N_1 + G_2 k_B T_2 B \\ &= G_1 G_2 k_B B \left(T_0 + T_1 + \frac{1}{G_1} T_2 \right) \\ &= G_1 G_2 k_B B \left(T_0 + T_{\text{cas}} \right) \end{aligned} \tag{B.2}$$

The above equations show that the noise temperature of a cascaded system is dominated by the characteristics of the first stage since the effect of the second stage is reduced by the gain of the first amplifier. This implies that if we can have an amplifier before the HEMT with 20 dB gain, which is equivalent to $G = 100$, then the noise from the HEMT and even higher temperature stages can be significantly suppressed. For this reason, we need to introduce a quantum-limited amplifier into the readout chain.

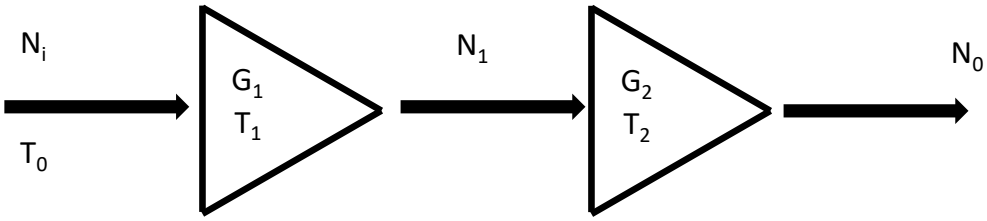

Figure 88: **Cascade amplification.** This schematic shows the noise power at different amplifications stages.

Appendix C Eigenmodes for an N-Junction N-port Josephson junction ring

An easy way to build an N-mode system is to form an N-Junction N-port Josephson junction ring. To design a circuit consists of the ring, one has to identify eigenmodes distribution, which can be constructed through the inductance matrix $\mathcal{L}$. As shown in Fig. 89, the ring has N Josephson junctions with the phase difference, φ_x, where $x \in \{a, b, ..., N\}$. The Hamiltonian is

$$H_{\mathrm{NJJ}} = -\sum_{x=a}^{N} E_J \cos\varphi_x \tag{C.1}$$

By assigning node's phase to all the joint, Eq. C.1 can be re-written as a function of node's phase, φ_i

$$H_{\mathrm{NJJ}} = -\sum_{i=1}^{N} E_J \cos\left(\varphi_{i+1} - \varphi_i + \frac{\varphi_{ext}}{N}\right)$$

where the boundary condition $\varphi_{N+1} = \varphi_1$ is imposed due to the symmetry of the ring [93, 102].

The normal modes of the circuits can be found by expanding the Hamiltonian up to the second order in $\varphi_{1,2,...,N}$. Then it can be expressed as a function of the inductance matrix $\mathcal{L}$ and the flux vector $\boldsymbol{\varphi} = (\varphi_1, \varphi_2, ..., \varphi_N)$.

$$H_{\mathrm{NJJ}} = \boldsymbol{\varphi}\frac{\mathcal{L}^{-1}}{2}\boldsymbol{\varphi}^T + o(|\boldsymbol{\varphi}|^2) \tag{C.2}$$

where

$$\mathcal{L}^{-1} = E_J \cos\left(\frac{\varphi_{ext}}{N}\right) \begin{bmatrix} 2 & -1 & 0 & \cdots & -1 \\ -1 & 2 & -1 & \cdots & 0 \\ 0 & -1 & 2 & \cdots & 0 \\ \vdots & \vdots & \vdots & \ddots & \vdots \\ -1 & \cdots & 0 & -1 & 2 \end{bmatrix} \tag{C.3}$$

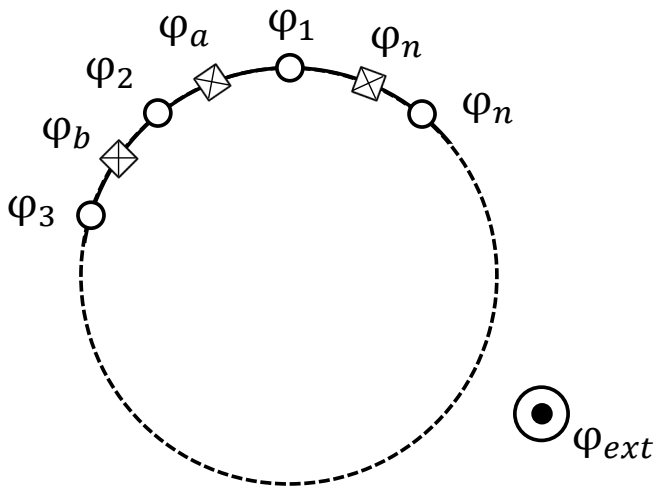

Figure 89: **(a) A schematic circuit of a N-Junction N-Port ring.** A ring consists of N Josephson junctions with N nodes' flux.

The normal modes of the JRM are directly given by the eigenmodes of the inductance matrix. The Hamiltonian can be re-written in terms of eigenmodes. By doing so, the system's motion can be studied and predicted.

C.1 Examples

C.1.1 2-Junction 2-port device: SQUID and SNAIL

An example of a two-junction two port device is Superconducting Quantum Interference Device (SQUID). Using the expression for the inductance matrix for $N = 2$, see Fig. 90

$$\mathcal{L}^{-1} = E_J \cos\Big(\frac{\varphi_{ext}}{2}\Big) \begin{bmatrix} 2 & -1 \\ -1 & 2 \end{bmatrix}$$

$$\begin{cases} \varphi_X = \varphi_2 - \varphi_1 \\ \varphi_Z = \varphi_2 + \varphi_1 \end{cases}$$

Eigenmode's flux configuration can be achieved through the inductance matrix.

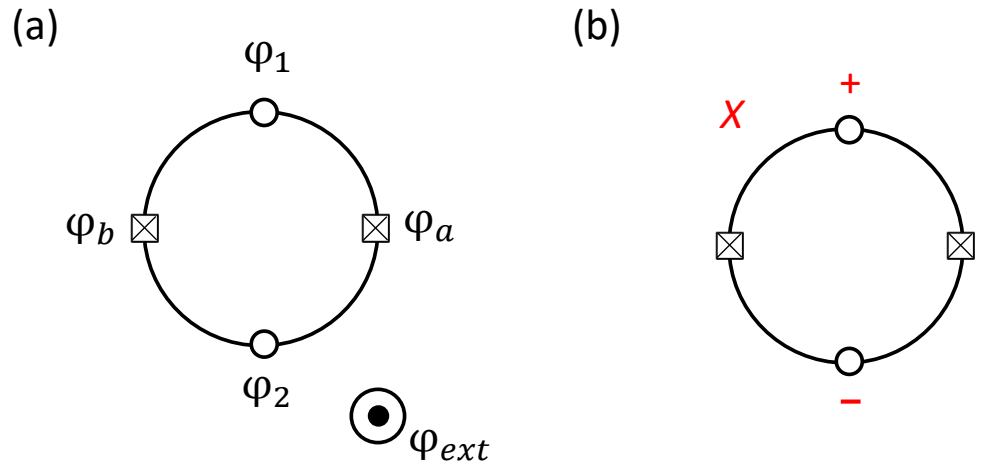

Figure 90: **(a) A schematic circuit of a 2-Junction 2-Port ring.** A ring consists of two Josephson junctions. (b) An eigenmode of the ring. Mode X

C.1.2 3-Junction 3-port device: photon lattice

A 3-junctions 3-port device is used for constructing photon lattices and building a circulator [103, 53, 104]. Because of an additional junction on the ring, an extra eigenmode will be obtained. Using Eq. C.2 with $N = 4$, we obtain the the inductance matrix

$$\mathcal{L}^{-1} = E_J \cos\left(\frac{\varphi_{ext}}{3}\right) \begin{bmatrix} 2 & -1 & -1 \\ -1 & 2 & -1 \\ -1 & -1 & 2 \end{bmatrix}$$

From eigenvectors of the inductance matrix, the flux configuration for all eigenmodes can be constructed, see Fig. 91 (b).

$$\begin{cases} \varphi_X = \varphi_3 - \varphi_1 \\ \varphi_Y = \varphi_2 - \varphi_1 \\ \varphi_W = \varphi_1 + \varphi_2 + \varphi_3 \end{cases}$$

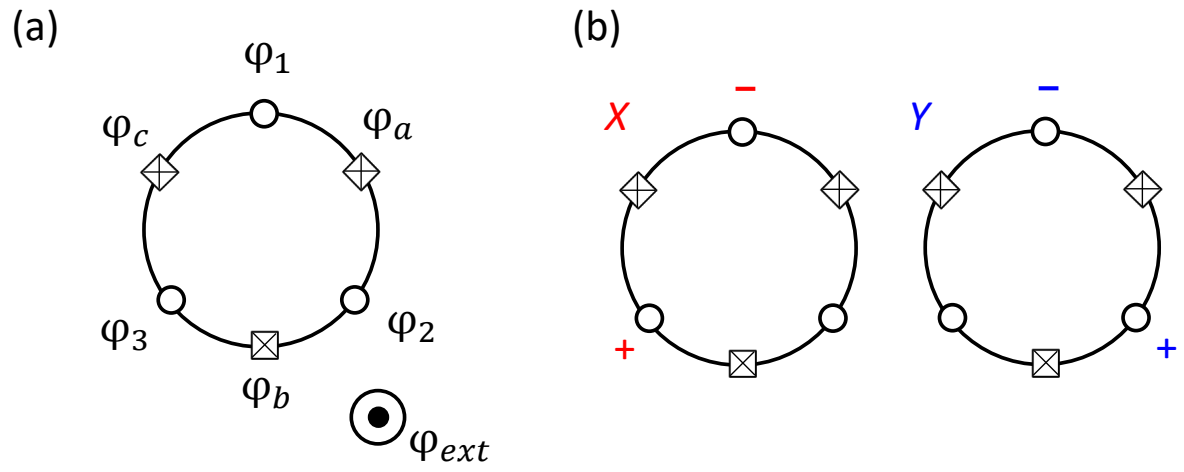

Figure 91: **(a) A schematic circuit of a 3-Junction 3-Port ring.** A ring consists of three Josephson junctions. (b) Eigenmodes of the ring. Two modes, X and Y, share a same node, φ_1.

C.1.3 4-Junction 4-port device : JRM

In this example, we recover the eignemode results for the first version of JRM, the unshunted JRM [33, 34]. It has four Josephson junctions on a ring with four nodes labelled $\varphi_{1,2,3,4}$, see Fig. 92 (a). Applying Eq. C.2 with $N = 4$, we obtain the the inductance matrix

$$\mathcal{L}^{-1} = E_J \cos\left(\frac{\varphi_{ext}}{4}\right) \begin{bmatrix} 2 & -1 & 0 & -1 \\ -1 & 2 & -1 & 0 \\ 0 & -1 & 2 & -1 \\ -1 & 0 & -1 & 2 \end{bmatrix}$$

Again, eigenmodes' flux configuration of the ring are eigenvectors of the inductance matrix.

$$\begin{cases} \varphi_X = \varphi_3 - \varphi_1 \\ \varphi_Y = \varphi_4 - \varphi_2 \\ \varphi_Z = \varphi_2 + \varphi_4 - \varphi_3 - \varphi_1 \\ \varphi_W = \varphi_1 + \varphi_2 + \varphi_3 + \varphi_4 \end{cases}$$

The result is the same as the shunted-JRM. When the ring is shunted, as long as shunted elements are identical, then the symmetry of the ring is preserved. Hence, the same eigenmodes are expected.

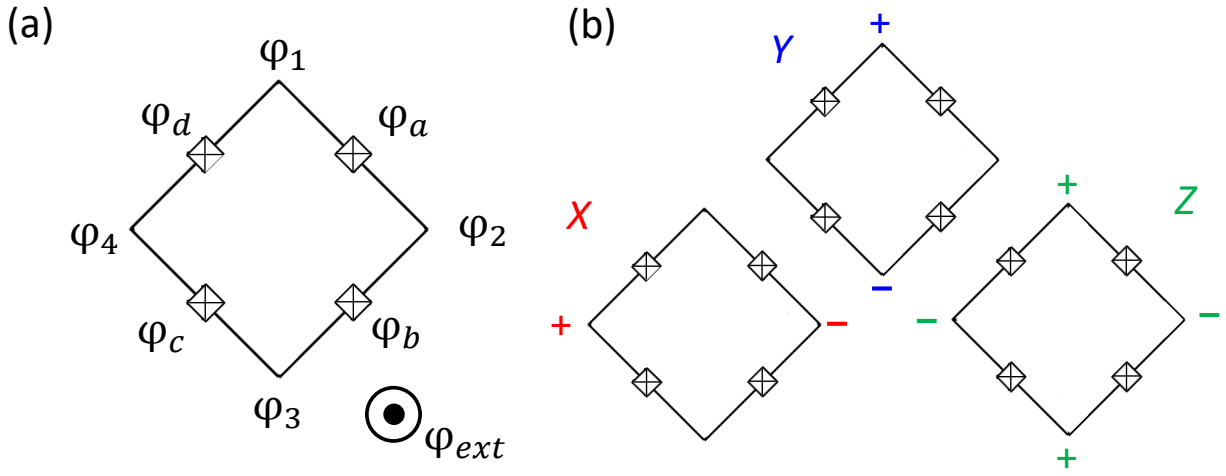

Figure 92: **(a) A schematic circuit of a 4-Junction 4-Port ring.** A ring consists of four Josephson junctions. This is the original design of JRM, a ring without any shunted elements. (b) Eigenmodes of the ring. Eigenmodes are the same as the shunted JRM.

Appendix D Semi-classical solution for the JPC with a single gain process

D.1 Third order

The Josephson Parametric Converter (JPC) consists of a linearly shunted Josephson Ring Modulator (JRM) coupled to microwave resonators. The JRM, which in its simplest form is comprised of four identical Josephson junctions arranged in a superconducting loop, has three different spatial modes (X, Y and Z), each of which couples to an external microwave mode with matching spatial configuration. The Hamiltonian of the JRM can be written as

$$\begin{aligned} H_{\text{ShuntedJRM}} =& -4E_J \cos\Big(\frac{\varphi_X}{2}\Big)\cos\Big(\frac{\varphi_Y}{2}\Big)\cos(\varphi_Z)\cos\Big(\frac{\varphi_{ext}}{4}\Big) \\ & -4E_J \sin\Big(\frac{\varphi_X}{2}\Big)\sin\Big(\frac{\varphi_Y}{2}\Big)\sin(\varphi_Z)\sin\Big(\frac{\varphi_{ext}}{4}\Big) \\ & +\frac{E_L}{4}\left(\varphi_X^2+\varphi_Y^2+2\varphi_Z^2\right), \end{aligned} \tag{D.1}$$

where E_J is Josephson junction energy and $\varphi_i = \Phi_i/\varphi_0$. The reduced flux quantum is $\varphi_0 = \hbar/2e$, Φ_i is the flux for the i-th spatial mode, and φ_{ext} is the external flux applied to the JRM loop . Typically $\Phi_{X,Y,Z} \ll 2\pi\varphi_0$, so the cosine and sine terms can be expanded as power series. By ignoring terms higher than third order in Φ_i, the Hamiltonian of the JRM in the stable regime, $\boldsymbol{\varphi_{min} = 0}$, can be written as

$$\begin{aligned} H_{\text{ShuntedJRM}} =& \frac{1}{4}\left[E_L + 2E_J\cos\Big(\frac{\varphi_{ext}}{4}\Big)\right]\left(\varphi_X^2+\varphi_Y^2\right) \\ & \frac{1}{2}\left[E_L + 4E_J\cos\Big(\frac{\varphi_{ext}}{4}\Big)\right]\varphi_Z^2 \\ & -E_J\sin\Big(\frac{\varphi_{ext}}{4}\Big)\varphi_X\varphi_Y\varphi_Z \end{aligned} \tag{D.2}$$

The third term on the right hand side gives the three-wave coupling between the spatial modes of the JRM which leads to amplification and frequency conversion of microwave photons. Next we add the inductance and capacitance of the microwave resonators, which we approximate on resonance as LC oscillators , see [33]. Their contribution to the total JPC energy is expressed as

$$H_{\text{res}} = \frac{{Q_X}^2}{2C_X} + \frac{{\Phi_X}^2}{2L_X} + \frac{{Q_Y}^2}{2C_Y} + \frac{{\Phi_Y}^2}{2L_Y} + \frac{{Q_Z}^2}{2C_Z} + \frac{{\Phi_Z}^2}{2L_Z}.$$

For the $\lambda/4$ segments of transmission line used in our circuit, the effective inductances are in series with the respective JRM spatial modes. To express the total Hamiltonian of the JPC, we introduce a new set of conjugate canonical variables, $\tilde{\Phi}_i$, $\tilde{Q}_i$ which we calculate using the concept of a series participation ratio (p_i) as in [82] which expresses the fraction of the total mode energy resident in a given JRM mode. The JPC's Hamiltonian can then be expressed as

$$\begin{aligned} H_{\text{JPC}} =& \frac{\tilde{Q}_X^2}{2C_X} + \frac{\tilde{\Phi}_X^2}{2L'_X} + \frac{\tilde{Q}_Y^2}{2C_Y} + \frac{\tilde{\Phi}_Y^2}{2L'_Y} + \frac{\tilde{Q}_Z^2}{2C_Z} + \frac{\tilde{\Phi}_Z^2}{2L'_Z} \\ & - \frac{E_J}{\varphi_0^3} \sin\Big(\frac{\varphi_{ext}}{4}\Big) p_X p_Y p_Z \tilde{\Phi}_X \tilde{\Phi}_Y \tilde{\Phi}_Z \end{aligned} \tag{D.3}$$

where

$$\begin{aligned} & L'_i = L_{\text{JRM}_\text{i}}(\varphi_{ext}) + L_i \ , \\ & L_{\text{JRM}_{\text{X,Y}}}(\varphi_{ext}) = \frac{2{\varphi_0}^2}{E_L + 2E_J \cos\big(\frac{\varphi_{ext}}{4}\big)} \ , L_{\text{JRM}_\text{Z}}(\varphi_{ext}) = \frac{{\varphi_0}^2}{E_L + 4E_J \cos\big(\frac{\varphi_{ext}}{4}\big)} \\ & p_i = \frac{L_{\text{JRM}_\text{i}}(\varphi_{ext})}{L_{\text{JRM}_\text{i}}(\varphi_{ext}) + L_i}, \ i \in \{X, Y, Z\} \end{aligned}$$

Canonical variables can be transformed into creation and annihilation operators through the following relation

$$\tilde{\Phi}_j = \sqrt{\frac{\hbar Z_j}{2}}(j + j^\dagger) \ ; \ \tilde{Q}_j = i\sqrt{\frac{\hbar}{2Z_j}}(j - j^\dagger) \ ; \ Z_j = \sqrt{\frac{L_j + L_J}{C_j}} \ ; \ j \in \{X, Y, Z\}$$

With a strong pump $\omega_p \equiv \omega_1 + \omega_2 \simeq \omega_a + \omega_b$ applied to the c-mode, and under the rotating wave approximation (RWA) we arrive at

$$\frac{H_{\text{JPC}}}{\hbar} = \omega_a a^\dagger a + \omega_b b^\dagger b + \omega_c c^\dagger c + g\left(a^\dagger b^\dagger c + a b c^\dagger\right) \tag{D.4}$$

where

$$g = -\frac{p_X p_Y p_Z E_J \sqrt{\hbar}}{2\sqrt{2}{\varphi_0}^3} \sin\left(\frac{\varphi_{ext}}{4}\right) \left(\frac{L'_X}{C_X}\frac{L'_Y}{C_Y}\frac{L'_Z}{C_Z}\right)^{1/4}$$

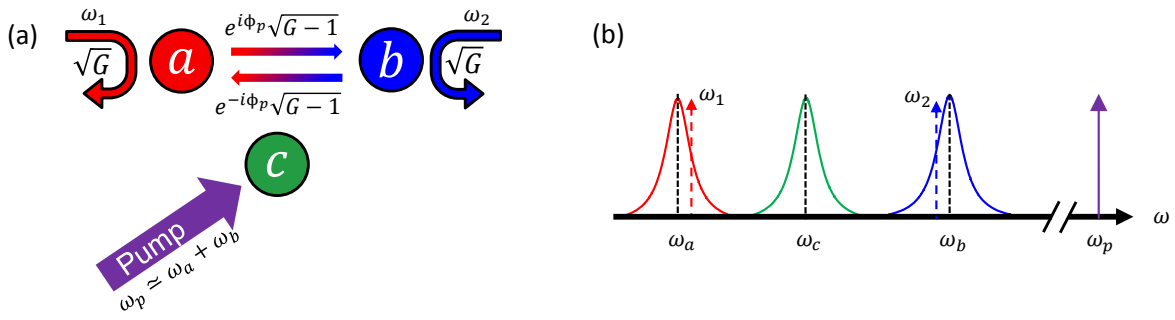

Figure 93: **(a) Diagram of phase-preserving amplification of inputs to modes a and b. (b) Schematic of JPC modes and pump tone in frequency space.** The red and blue Lorentzian line shapes represent mode a and b of the JPC. The purple and blue arrow represent the pump tone and input signal to mode b. The dashed red arrow corresponds to signal generated into mode a through the parametric gain process.

A schematic of the operation of the JPC is given in Fig. 93. Signals incident on port a, b at angular frequency $\omega_{1,2} \simeq \omega_{a,b}$ will be amplified both at the same frequency with voltage gain $\sqrt{G}$ in reflection and transmitted with amplitude $\sqrt{G-1}$ to port b, a at angular frequency $\omega_{2,1} = \omega_p - \omega_{1,2}$ with nonreciprocal phase-shift $\pm\phi_p$ set by the pump tone.

We assume a perfectly 'stiff' pump tone applied to port c, which is to say that the pump is sufficiently intense and detuned from any c-mode resonance that the change in pump amplitude is negligible despite the fact that pump-photons are being converted to signal and idler photons to produce amplification. Then in Eq. D.4, c can be replaced by it's classical average value $\langle c \rangle$. Next, we treat the effect of the mode's coupling to the external environment by constructing semi-classical Langevin equations of the JPC in frequency domain as in [68, 72]. We specialize to the case of no signal incident on the b-mode ($b_{in} = 0$) and express the reflection and transmission voltage gain as $\alpha = a^{out}/a^{in}$ and $\beta = b^{out\dagger}/a^{in}$ respectively. From Eq. 2.5, we obtain

$$\left(\frac{\kappa_a}{2} - i\delta\right)\frac{(1+\alpha)}{\sqrt{\kappa_a}} = -i\frac{g\langle c\rangle}{\sqrt{\kappa_b}}\beta + \sqrt{\kappa_a}$$

$$\left(\frac{\kappa_b}{2} - i\left(-\delta + \epsilon\right)\right)\frac{\beta^*}{\sqrt{\kappa_b}} = -i\frac{g\langle c\rangle}{\sqrt{\kappa_a}}\left(1+\alpha^*\right),$$

where $\delta = \omega_1 - \omega_a = \omega_b - \omega_2 + \epsilon$, and $\epsilon = \omega_p - \omega_a - \omega_b$. Notice that α and β are complex variables. These coupled equations are solved analytically for the reflected power gain:

$$|\alpha|^2 = \frac{16g^4{n_p}^2 + 8g^2 n_p \left(4\delta\left(\delta-\epsilon\right) + \kappa_a\kappa_b\right) + \left(4\delta^2 + {\kappa_a}^2\right)\left(4(\delta-\epsilon)^2 + {\kappa_b}^2\right)}{16g^4{n_p}^2 + 8g^2 n_p \left(4\delta\left(\delta-\epsilon\right) - \kappa_a\kappa_b\right) + \left(4\delta^2 + {\kappa_a}^2\right)\left(4(\delta-\epsilon)^2 + {\kappa_b}^2\right)} \tag{D.5}$$

where $n_p = \langle c^\dagger c \rangle$.

We obtain the signal frequency where peak gain occurs for a given pump frequency and amplitude by solving for the frequency at which $\frac{\partial|\alpha|^2}{\partial\delta} = 0$. The behavior of the maximum gain frequency depends crucially on the difference between κ_a and κ_b, so we make the substitutions $\kappa_{a,b} = \kappa \mp \frac{\Delta\kappa}{2}$. In general, there is a non-linear dependence on the pump detuning ϵ, for small detuning we can write to first order in ϵ the detuning from ω_a at which maximum gain occurs as

$$\Delta_{\max\,\mathrm{G}} = \left(\frac{1}{2} - \frac{\kappa\left(\Delta\kappa/2\right)}{4g^2 n_p + \kappa^2 + \left(\Delta\kappa/2\right)^2}\right)\epsilon + O\left[\epsilon\right]^3$$

We note that for $\Delta\kappa = 0$ this expression greatly simplifies and the peak gain frequency does not vary vs. pump power, and hence gain. However, for dissimilar resonator loss rates, even in this third order treatment the peak frequency will shift vs. pump power if the pump frequency differs from the modes' sum frequency. We experimentally fit each gain curve for a unique peak gain amplitude and $\Delta_{\max\,\mathrm{G}}$, then substitute $\Delta_{\max\,\mathrm{G}}$ into the expression for $|\alpha|^2$ we obtain the familiar result [33]

$$G = |\alpha|^2 = \left(\frac{1 + \frac{P_p}{P_c}}{1 - \frac{P_p}{P_c}}\right)^2,$$

where the pump power $P_p \propto n_p$ and P_c is the critical power at which gain diverges.

D.2 Third and fourth orders

We extend our treatment to include the fourth order terms of the JRM. The Hamiltonian of the JPC becomes

$$\frac{H_{JPC}}{\hbar} = \omega_a{}'a^\dagger a + \omega_b{}'b^\dagger b + \omega_c{}'c^\dagger c + g\left(a^\dagger b^\dagger c + abc^\dagger\right) - \frac{1}{2}\mathrm{K}_{aa}a^\dagger a^\dagger aa - \frac{1}{2}\mathrm{K}_{bb}b^\dagger b^\dagger bb - 8\mathrm{K}_{cc}c^\dagger c^\dagger cc - 2\mathrm{K}_{ab}a^\dagger ab^\dagger b - 8\mathrm{K}_{ac}a^\dagger ac^\dagger c - 8\mathrm{K}_{bc}b^\dagger bc^\dagger c \quad \text{(D.6)}$$

in which the mode frequencies shift slightly to

$$\omega_a{}' = \omega_a - \frac{1}{2}\mathrm{K}_{aa} - \mathrm{K}_{ab} - 4\mathrm{K}_{ac},\ \omega_b{}' = \omega_b - \frac{1}{2}\mathrm{K}_{bb} - \mathrm{K}_{ab} - 4\mathrm{K}_{bc} \text{ and } \omega_c{}' = \omega_c - 8\mathrm{K}_{cc} - 4\mathrm{K}_{ac} - 4\mathrm{K}_{bc}$$

and

$$\mathrm{K}_{ii} = \frac{\hbar E_J}{32\varphi_0^4}\cos\left(\frac{\Phi_{ext}}{4\varphi_0}\right){p_i}^4\frac{L_i}{C_i}$$
$$\mathrm{K}_{ij} = \sqrt{\mathrm{K}_{ii}\mathrm{K}_{jj}}$$

defined as the 'self' and 'cross' Kerr terms for the system, respectively. As before, we assume a 'stiff' pump and no input signal on mode b, yielding the modified semi-classical quantum Langevin equations for the JPC:

$$\left[\frac{\kappa_a}{2}\text{-}i\left(\delta + \frac{\mathrm{K}_{aa}}{\kappa_a}|1+\alpha|^2|a^{in}|^2 + 2\frac{\mathrm{K}_{ab}}{\kappa_b}|\beta|^2|a^{in}|^2 + 8\mathrm{K}_{ac}\langle c^\dagger c\rangle\right)\right]\frac{(1+\alpha)}{\sqrt{\kappa_a}} = \text{-}i\frac{g\langle c\rangle}{\sqrt{\kappa_b}}\beta + \sqrt{\kappa_a}$$

$$\left[\frac{\kappa_b}{2}\text{-}i\left(-\delta + \epsilon + \frac{\mathrm{K}_{bb}}{\kappa_b}|\beta|^2|a^{in}|^2 + 2\frac{\mathrm{K}_{ab}}{\kappa_a}|1+\alpha|^2|a^{in}|^2 + 8\mathrm{K}_{bc}\langle c^\dagger c\rangle\right)\right]\frac{\beta^*}{\sqrt{\kappa_b}} = \text{-}i\frac{g\langle c\rangle}{\sqrt{\kappa_a}}\left(1+\alpha^*\right).$$

We note that these equations can no longer be expressed in terms of α and β alone, and the explicit dependence on a^{in} will result in gain saturation effects absent from the third-order stiff pump expressions. The unsaturated reflection gain for sufficiently small signal power can be calculated from theses two equations by assuming $a^{in} = 0$ as

$$|\alpha|^2 = \frac{16g^4{n_p}^2 + 8g^2n_p\left(-4\delta_m\delta_n + \kappa_a\kappa_b\right) + \left(4{\delta_m}^2 + {\kappa_a}^2\right)\left(4{\delta_n}^2 + {\kappa_b}^2\right)}{16g^4{n_p}^2 + 8g^2n_p\left(-4\delta_m\delta_n - \kappa_a\kappa_b\right) + \left(4{\delta_m}^2 + {\kappa_a}^2\right)\left(4{\delta_n}^2 + {\kappa_b}^2\right)}$$

where $\delta_m = 8\mathrm{K}_{ac}n_p + \delta$ and $\delta_n = 8\mathrm{K}_{bc}n_p - \delta + \epsilon$.

Again substituting $\kappa_{a,b} = \kappa \mp \Delta\kappa/2$, we can solve $\Delta_{\max\,\mathrm{G}}$ to first order in ϵ and $\Delta\kappa$ and find

$$\Delta_{\max\,\mathrm{G}} \simeq (K_{bc} - K_{ac})\, n_p + \frac{(K_{bc} + K_{ac})}{x_-}\frac{\Delta\kappa}{2}\kappa n_p + \left(\frac{1}{2} - \frac{\kappa\Delta\kappa}{2{x_-}^2}x_+\right)\epsilon$$

where $x_\mp = 4g^2 n_p \mp 4\left(K_{bc} + K_{ac}\right)^2 {n_p}^2 + \kappa^2$. In this fourth order expression there is a net pump-dependent frequency shift except in the special case where the pump-dependent cross-Kerr terms $K_{ac,bc}$ are equal and resonator bandwidths $\kappa_{a,b}$ are equal.

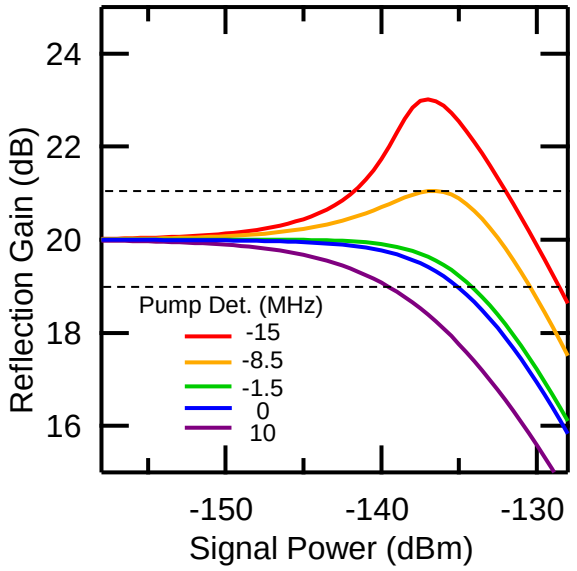

Figure 94: **Saturation of gain curves with different pump detuning.** From this figure, optimal points can be defined in two ways. Max dynamic range happens when pump detuning is -8.5 MHz while max flatness appears at -1.5 MHz pump detuning.

Appendix E Fabrication and characterization

We fabricate Josephson junctions using the standard Dolan bridge technique, a.k.a. double angle deposition, which uses a mask that is suspended above the substrate. The mask is formed from two layers of resist. Depending on the evaporation angle, the shadow image of the mask is projected onto different positions on the substrate. By carefully choosing the angle for each material to be deposited, adjacent opening in the mask can be projected on the same spot, creating an overlay of two thin films with a well-defined geometry [105, 106].

E.1 Dolan bridge technique

We can break the deposition into several steps. (a) spin-coating, (b) exposure and development, (c) metal deposition, and (d) stripping resist. In the following subsections, I will go through the detail of each step. This technique can apply on either silicon or sapphire substrates. The difference between these two is that sapphire substrates are not conductive causing the charging effect [107]. This effect can be solve by depositing a 10 nm thin conducting film on top of resist.

Double-side polished silicon wafers with thickness 250 μm, resistance 3000-5000 ohm/cm, and crystal direction (100) are used most in amplifier design. Sapphire substrates are used for qubit design due to less internal loss in the substrates. Sapphire substrates have thickness 430 μm and it is also double-side polished with crystal direction in C-M plane 0.2°.

The recipe discussed in this section is generally for Josephson junction larger than 1 μ m^2. With slight modification, the recipe can also apply to qubit design [private communication with Pinlei, Xi, and Chao].

E.1.1 Spin-coating

Two layers of resist form the mask for the Dolan bridge technique. We have chosen methyl methacrylate (MMA) and poly-methyl methacrylate (PMMA). Due to the relatively weak chemical bond, MMA is sandwiched by PMMA and a substrate. For creating a suspending bridge, this is critical. To be specific, we use MMA EL13 and PMMA 950K A4.

Before the spinning, it is better to clean the spinner with IPA and acetone, then use argon to dry the machine and blow away tiny particles.It is important to place the wafer at the center of the spinner. The thickness of resist depends on spinning speed, which determine different the central force. To let substrates experience the same central force in radius direction, one has to place center of a wafer at the center of the spinner.

To spin the first layer, MMA EL 13, on a substrate, we follow this recipe for a resist spinner.

Table 3: **First layer: MMA EL 13**

Step	Description
1	ramp up the spinner to 500 rpm in 10 sec
2	speed up to 2000 rpm in 5 sec
3	maintain at 2000 rpm for 90 sec
4	slow down to 0 rpm in 10 sec
5	bake the substrate for 90 sec at 175°

While the substrate sits on the baker, one can clean the spinner, including the lid, to make sure no MMA residual is left in the spinner.

When the first layer is finished, it is better to cool down the substrate before putting down the second layer. Right after baking, the substrate is still above 100°. To make sure the fabrication process is repeatable, we have to make sure each step is controllable and the same.

The recipe for the second layer, PMMA 950K A4, is similar to the first one

Table 4: **Second layer: PMMA 950K A4**

Step	Description
1	ramp up the spinner to 500 rpm in 10 sec
2	speed up to 3000 rpm in 5 sec
3	maintain at 3000 rpm for 90 sec
4	slow down to 0 rpm in 10 sec
5	bake the substrate for 900 sec at 175°

E.1.2 Anti-charge layer : only for sapphire substrate

Sapphire is not a conductive substrate, so that electrons tend to accumulated on substrate. We typically deposit a 10 nm thin aluminum film as a conductive layer to solve this problem.

E.1.3 Exposure and development

We use an E-beam exposed on resist to form a mask generated in a mask design software, such as KLayout. The idea is to break resist molecules with accelerated electrons. By controlling the strength of the beam, we can precisely determine which layers need to be destroyed. The strength of the beam is referred to E-beam dose controlled by two variables

$$Dose = (Dose \;\; factor) * (Area \;\; dose)$$

The area dose typically is set in the machine, and the users modify dose by assigning a dose factor to a designed mask. We can separate E-beam into two parts, strong dose, and weak dose. The strong dose beam can destroy both resist molecules while the weak dose beam only affects MMA but leave PMMA alone, see Fig. 95. The weak dose beam is critical for creating a suspending bridge. It cleans MMA beneath PMMA and creates hollow patterns (undercut in the figure).

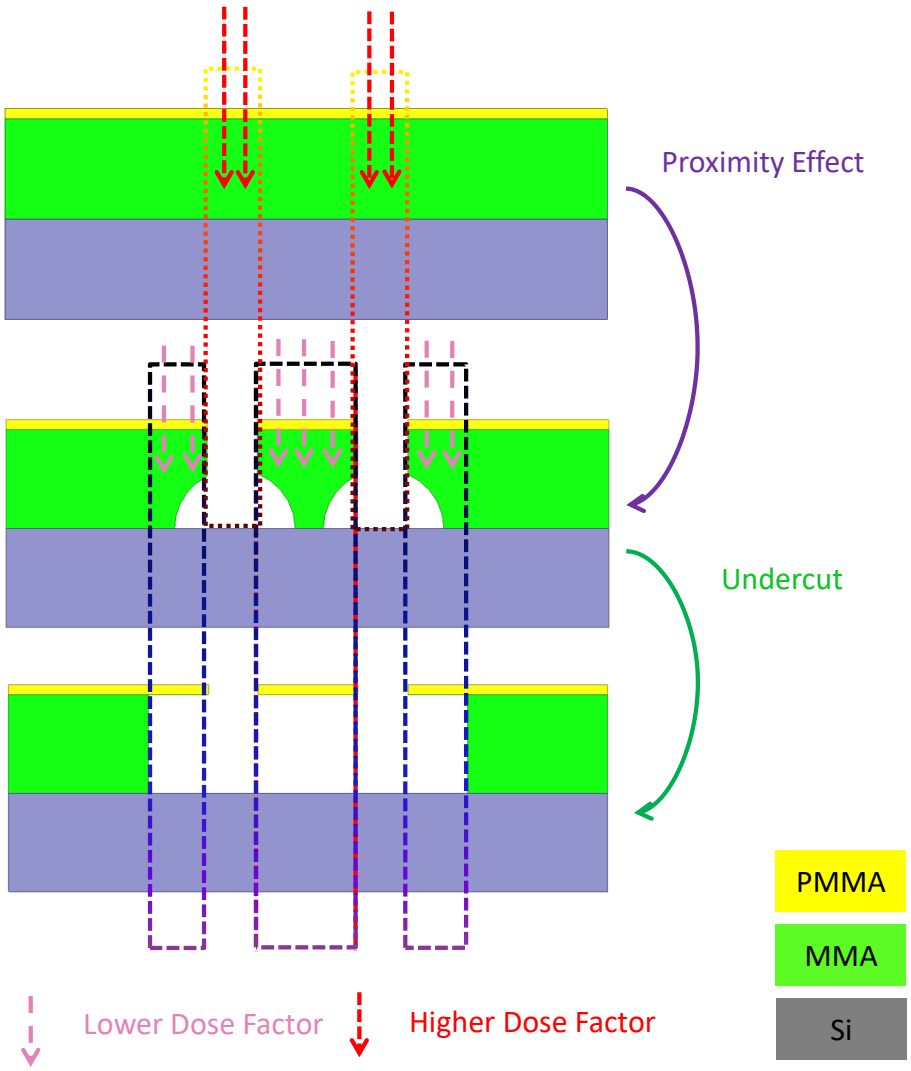

Figure 95: **E-beam exposure.** When writing a mask (where resist is removed)with an E-beam, typically, we assign different E-beam strength controlled by dose. Dose is associated with the number of electrons exposed to the target. We usually set an area dose in the machine and use the dose factor to control the number of electrons. The strong dose is used for destroying both layers of molecules while the weak dose is for the purpose of removing MMA but PMMA.

The design pattern can also separate into two parts. The large pattern typically is for metal traces or capacitor's pads, which can be written with a strong beam. These patterns

often are a few hundred μm^2, written with 200 μm by 200 μm write field and 120 μm aperture. For the critical patterns, usually are for junctions, both strong and weak beams need to be applied with smaller write field, 110 μm by 110 μm and 30 μm aperture.

The Raieh e-LiNE we used has highest accelerating voltage up to 30 kV and the area dose we setup in the machine is 300 μC/cm. The dose factor for the strong beam is around 1.3. The right dose factor for the weak beam is different between designs. Usually, before writing a real device, we have to dose test. The test has the same designed pattern but with different dose factors, one of which should produce the same pattern as design and should be repeatable.

Backward scattering needs to be considered when E-beam hits the substrate. The backscattering electrons will damage resist molecules again and cause additional shallow pattern, as shown in Fig. 95. This indicates the pattern does not experience the same dose: corners of the patterns, particularly, have a weaker dose, which generates the round corner patterns. This effect is called the proximity effect. The way to solve this problem is to use the software to perform the proximity correction, break patterns into small pieces with different dose factor, but overall patterns experience the uniform dose. However, this correction is time-consuming and requires delicate simulation. Another way to solve this problem is by adding other patterns around corners.

After E-beam writing, we use solution to flush away destroyed resist.

Table 5: **Developing recipe**

Step	Description
1	rinse the chips with IPA plus DI water with mass ratio 2.4 to 1 for 2min
2	clean with DI water for 30 sec

Note: if chip has an anticharge layer, we have to dissolve it in MF-CD 26, which only affects aluminum but not resist. This process usually is 1 min, but it really depends on solution. Since the solution will not damage resist, we can soak chips in MF-CD 26 till aluminum is all gone (chips become transparent.

E.1.4 Metal deposition

The superconducting material used to form Josephson junctions in our lab is aluminum. The idea of the Dolan bridge technique is to deposit metal twice from different angles, as shown in Fig. 96. The first deposition indicated by the red dashed lines put down metal on the substrate through a mask formed by two layers resist (green and yellow). The second deposition (green dashed lines) comes from another angle and is at least about four times thicker than that of the first layer. In the figure, we assume two angles are the same. The junction is formed at the place where two deposition overlay. Junction's dimension is determined by x and another edge (edge's direction is into the page), where x is associated with resist thickness, deposition angle, and gap between masks.

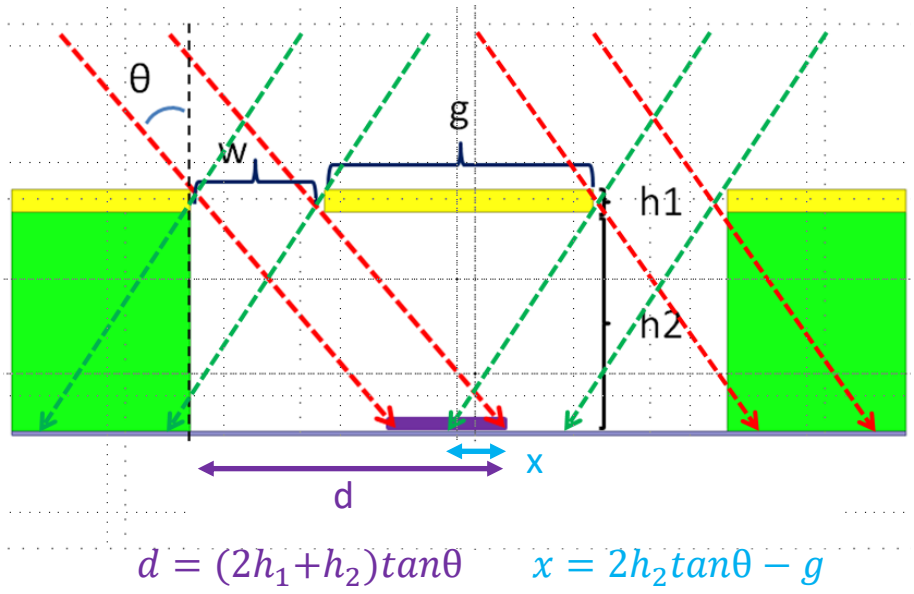

Figure 96: **Double angle deposition.** First deposition (red lines) and second deposition (gree lines) overlay at the center and form a junction.

Before the deposition, we perform another step called conditioning. The purpose of this step is to make sure the machine always starts with the same environment.

Ti thin film mentioned in step 3 in Table 6 is used as an adhesive thin film to hold particles on the chamber wall. This thin film can prevent unwanted particles fall on the chips.

Table 6: **Conditioning recipe**

Step	Description
1	inject argon/oxygen till the chamber reach XXX mbar
2	ion-mill for 30 sec at XX kV.
3	Ti sweep.

After the conditioning, we start depositing aluminum on the chips. Note, the oxidation layer between two aluminum pads is achieved by injecting pure oxygen into the chamber and letting the oxidation layer grow on the top of the first layer. Also, the last step in Table 7 is to form a protecting oxidation layer on the whole chip.

Table 7: **Double angle deposition**

Step	Description
1	35 nm Al at the rate 1 nm/sec with 40°to the normal of subtrate surface
2	pure oxygen at the pressure 13.5 mbar for X min
3	120 nm Al at the rate 1 nm/sec with -40°to the normal of subtrate surface
4	pure oxygen at the pressure 13.5 mbar for 5 min

E.1.5 Stripping resist

We use hot acetone to remove the resist.Typically, the chip is immersed in the acetone for at least 30 min, but sometimes aluminum residual can still be found on chips, so longer time might be needed. Using room temperature acetone can also strip the resist. It is safer with room temperature acetone, however, the process requires about twice time.

Table 8: **Stripping resist**

Step	Description
1	70°acetone for 30 min at least
2	clean the wafer in hot acetone with syringe
3	clean with IPA
4	clean with DI water
5	blow dry the chips

E.2 Fabrication details for JPCs

E.2.1 JRM

Here are a few details I can think of for the JRM design for now. I have learned these details in a hard way, so hopefully, this discussion can help readers and not make the same mistakes.

E.2.1.1 Edges of the JRM

A typical design of the JRM is shown in Fig. 97. It has four Josephson junctions (black box) on the edge of the ring. However, wherever two metals overlap are Josephson junctions, including the edge of the ring (blue) and the arm extending to outside (red). These accidental junctions are unavoidable, however, we can design these junctions bigger so that it still acts as a piece of metal. In this figure, junctions size is 1 μm^2, and we make the edge junctions larger (8.5 μm^2) so that it does not contribute too much inductance. A similar ideal goes to the arm extending to the outside of the ring.

To do even better, we can connect the junction on edge with the junction outside of JRM together. In Fig. 97, the blue box is connected with the top junction. By doing so, this becomes a huge junction, hence it acts as a piece of metal.

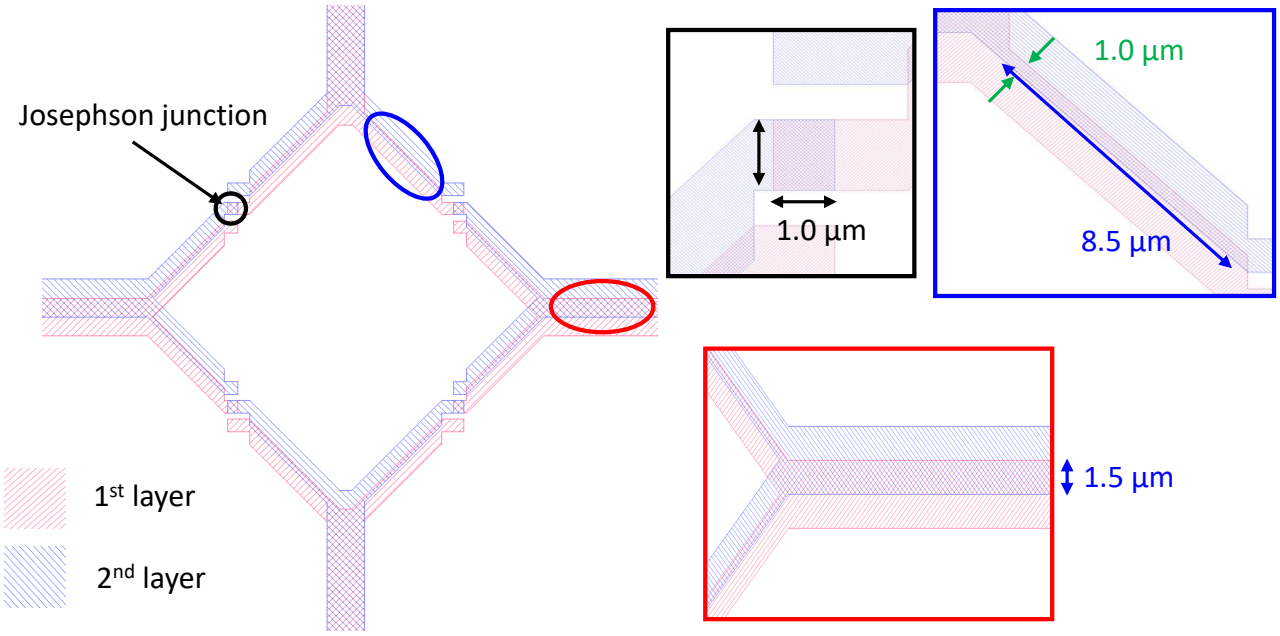

Figure 97: **JRM design in KLayout.** After double angle deposition, any place where two metals meet is a Josephson junction, i.e. black, blue, and red circles.

E.2.1.2 Kinetic inductance shunted JRM

For the kinetic inductance shunted JRM, we have to fabricate kinetic inductance, the cross in the ring, see Fig. 53 (a). The ring is made out of two different materials, NbTiN, and aluminum, which means that alignment markers for EBL are required.

The fabrication process has two parts. The first one is to fabricate the center cross made out of NbTiN; then, the second part is to complete the ring with the Dolan bridge technique recipe. The second part is already covered in the previous discussion.

In this design, we fabricate the cross and the alignment markers together. Note the alignment markers will be used for the second part of the process, which implies that it will be exposed under E-beam while performing an alignment. When the markers are exposed with E-beam, resist molecules will be damaged. Because of this reason, we design the markers underneath of resonators, see Fig. 98.

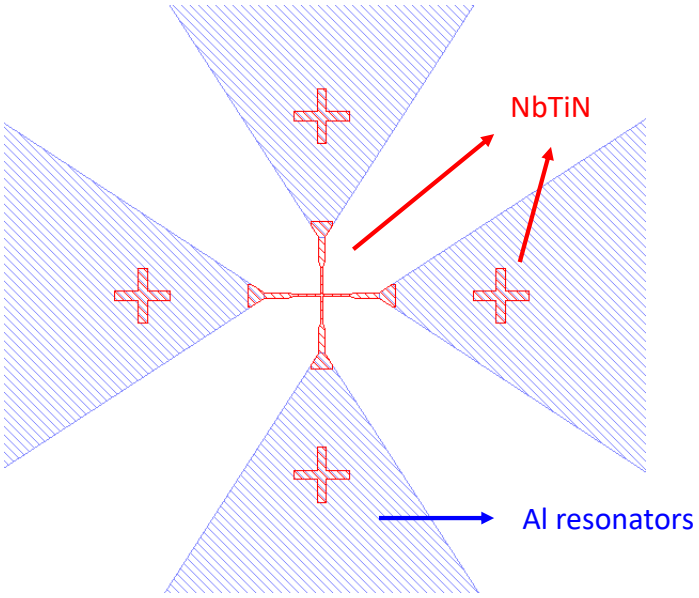

Figure 98: **Kinetic inductance shunted JRM design in KLayout.** The figure only shows the cross of the ring (red pars). The blue area is from part of $\lambda/2$ resonator.

Since we use EBL to fabricate the first part, therefore EBL resist is required. Here, we only need a layer of resist (PMMA 950K A4).

Table 9: **Spin recipe for a thin NbTiN: PMMA 950K A4**

Step	Description
1	ramp up the spinner to 500 rpm in 10 sec
2	speed up to 6000 rpm in 8 sec
3	maintain at 6000 rpm for 60 sec
4	slow down to 0 rpm in 10 sec
5	bake the substrate for 300 sec at 175°

Then, we use E-beam to write the cross and markers. The writing only takes about a min. After that, we develop the chip

Table 10: **Develop recipe for a thin NbTiN**

Step	Description
1	MIBK for 1 min
2	IPA for 1 min
3	blow dry the chips with compressed air

At this point, we are ready to deposit NbTiN, which is done by a sputter machine, AJA. The recipe for this step is recorded in the machine and I am locked at apartment due to Covid. The final step is strip the resist in room temperature acetone. We do not have to use hot acetone for this step.

Table 11: **Stripping resist**

Step	Description
1	room temperature acetone for 5 min at least
2	clean with IPA
3	clean with DI water
4	blow dry the chips

E.2.2 Microstrip JPC

For the microstrip JPC, the coupling capacitor that defines the linewidth of mode is achieved by leaving a gap between a $\lambda/2$ resonator and a feeding port. The gap size determines the coupling capacitance; hence a precise control of the gap is essential.

Since Dolan bridge technique is used for forming a device, we have to include depositions shift caused by depositing with an angle. With the recipe mentioned in E.1.1, the shift is around 1.5 μm, see Fig. 99.

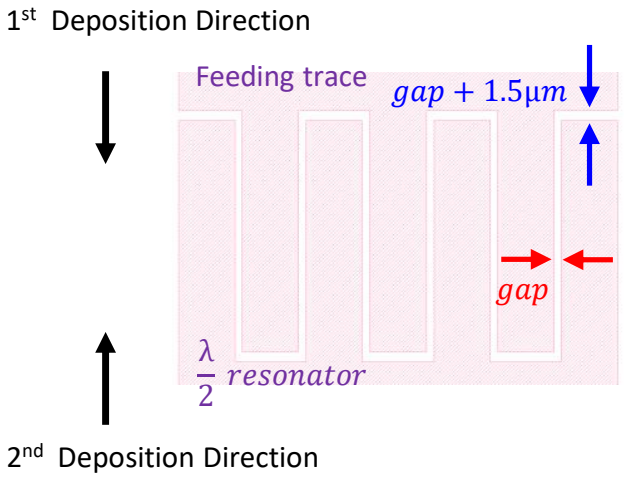

Figure 99: **Coupling capacitor for a microstrip JPC.** Coupling capacitance is determined by the gap between feeding trace to $\lambda/2$ resonator. The gap in perpendicular to the deposition direction has to include the shift caused by double angle deposition.

E.2.3 Single-ended lumped JPC

Lumped JPC requires us to fabricate extra two steps, one for a ground plane and the other for dielectric material. These two steps are done by optical lithography and the recipe for spinning resist is the same.

Table 12: **First layer spin recipe: LOR 5B**

Step	Description
1	ramp up the spinner to 500 rpm in 5 sec
2	speed up to 3000 rpm in 45 sec
4	slow down to 0 rpm in 10 sec
5	bake the substrate for 540 sec at 195°

Before moving to the next step, we cool the chips with compressed air.

Table 13: **Second layer spin recipe: S1805**

Step	Description
1	ramp up the spinner to 500 rpm in 5 sec
2	speed up to 4000 rpm in 60 sec
4	slow down to 0 rpm in 10 sec
5	bake the substrate for 180 sec at 115°

After spinning resist, we expose the wafer with MLA (MaskLess Aligner). The exposure is similar to E-beam, instead of electron beam, laser is used. Dose also controls the number of photons in a given area.

Next step is developing

Table 14: **Develop recipe for MLA**

Step	Description
1	solvent 351 with DI water (1:4) for 75 sec
2	DI water for 10 sec
3	400K for 45 sec
4	DI water for 10 sec
5	blow dry with compressed air

Next step is to deposit metal. For the ground plane, 150 nm NbTiN is used with AJA while 100 nm sapphire is deposited by PLASSYS.

The final step is to strip the resist

Table 15: **Strip resist for MLA**

Step	Description
1	PG remover for at least 2 hrs
2	sonicate with acetone for 5 min
3	sonicate with IPA for 5 min
4	sonicate with DI water for 5 min
5	blow dry with compressed air

E.3 Ambegaokar-Baratoff relation

Typically, we fabricate at least 2 amplifiers or 15 qubits at a time, but to make sure the junction has the inductance as expected, we can not cool down all devices (well for amplifiers, this is doable, but not so much for qubits.). Fortunately, we can use the Ambegaokar-Baratoff relation, which links junction's room temperature resistance to junction's inductance at cold. The relation is

$$L_J = 1.12\frac{\hbar}{\pi\Delta}R_J = \frac{\varphi_0}{I_c} \tag{E.1}$$

where Δ and I_c are half of the superconducting energy gap and critical current of Junctions, respectively.

The coefficient 1.12 is the correction we used in the lab, this number might be different from other labs. From Eq. E.1, we can calculate L_J once we measure R_J. Also, we can calibrate density current of junction based on this equation. We fabricate different size of junctions at the same time and measure it's resistance at the room temperature. Using this measurement, we can figure out the density current, see Fig. 100.

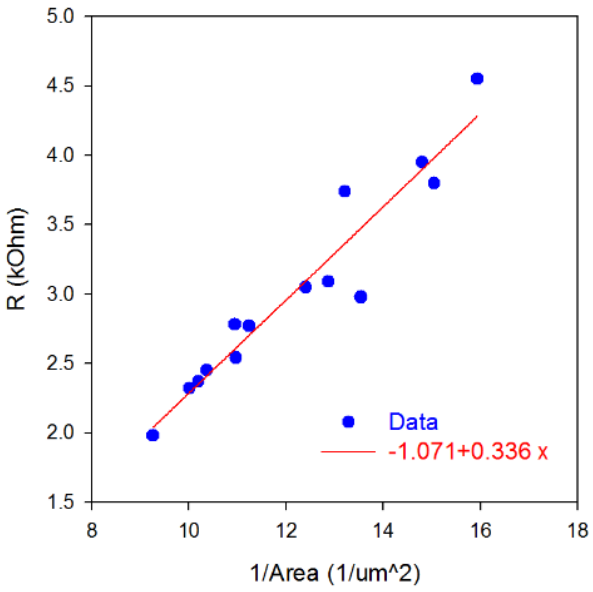

Figure 100: **Density current measurement.** We measure room temperature resistance from different size of junctions and calculate the density current.

Appendix F Mathematica

This mathematica code is for generating a scattering matric for giving modes and couplings. Using the calculation method based on ref [55], we create a code that can construct an M matrix and obtain a scattering matrix. We have tested this code to a three-mode system with different multiple parametric processes, including circulator, directional amplification with gain-bandwidth limitation (GGC). This file can be used for an arbitrary number of modes and pumps.

Define Functions

```
(* This function is to define all variables *)
prefunc[amountmode_, amountpump_] := Module[{coup, modes, κarray, ωarray, ωnarray},
  coup = {gain, conversion, self};
  modes = Alphabet[][[1 ;; amountmode]];
  κarray = Join[Table[Symbol[ToString[κ] <> ToString[modes[[i]]]], {i, amountmode}],
    Table[Symbol[ToString[κ] <> ToString[modes[[i]]]], {i, amountmode}]];
  ωarray = Join[Table[Symbol[ToString[modes[[i]]]], {i, amountmode}],
    Table[Symbol[ToString[modes[[i]]]], {i, amountmode}]];
  ωnarray = Join[Table[Symbol[ToString[Alphabet[][[1 ;; 2 * amountmode]][[i]]] <>
      ToString[1]], {i, 2 * amountmode}]];
  Return[{coup, modes, κarray, ωarray, ωnarray}]
 ]
(* This function is to define all pumps *)
couplings[amountmode_, amountpump_] := Module[{para, coup, modes, vals},
  para = prefunc[amountmode, amountpump];
  coup = para[[1]];
  modes = para[[2]];
  vals = Partition[Range@(amountpump * 3), 3];
  Dynamic[
   Grid[
    Table[
     With[{r = ṛ, c = ç},
      {PopupMenu[Dynamic[vals[[r, c]]], If[c == 1, coup, modes]], Dynamic[vals[[r, c]]]}]
     , {ṛ, amountpump}, {ç, 3}]
    , Frame → True, Dividers → {True, All}, Background → {None, {{Pink, Yellow}}}]
  ]
 ]
gensMtx[amountmode_, amountpump_, pumps_] := Module[
  {para, coup, modes, blah, vals, κarray, ωarray, ωnarray, γMtx, res, mMtx, sMtx,
   sub, aG1, gP, detuneδ, checkmodes, totedges, startmode, startpoint, stmdetun,
   edges, soldetune, endpoint, check, pumpfreq, numedges, reversdetuneδ},
  (* Define all variables *)
  para = prefunc[amountmode, amountpump];
  coup = para[[1]];
  modes = para[[2]];
  κarray = para[[3]];
  ωarray = para[[4]];
  ωnarray = para[[5]];
  vals = Setting[pumps[[1, 1]][[All, 1 ;; -1, 2]]];
  γMtx = DiagonalMatrix[Flatten[Table[√(κarray[[1 ;; amountmode]]), {i, 2}]]];
  res = Table[
    type = Position[coup, vals[[i, 1]]][[1, 1]];
    copmode = Sort[{vals[[i, 2]], vals[[i, 3]]}];
    mode1 = Position[modes, copmode[[1]]][[1, 1]];
    mode2 = Position[modes, copmode[[2]]][[1, 1]];
    func[g_] := Symbol[ToString[g] <> ToString[copmode[[1]]] <> ToString[copmode[[2]]]];
    Which[
```

```
    type == 1,
    {{mode1, mode2 + amountmode} → i func[f] Exp[-i func[θ]],
     {mode2 + amountmode, mode1} → -i func[f] Exp[i func[θ]],
     {mode1 + amountmode, mode2} → -i func[f] Exp[i func[θ]],
     {mode2, mode1 + amountmode} → i func[f] Exp[-i func[θ]]},
    type == 2,
    {{mode1, mode2} → i func[g] Exp[-i func[ϕ]],
     {mode2, mode1} → i func[g] Exp[i func[ϕ]],
     {mode1 + amountmode, mode2 + amountmode} → -i func[g] Exp[i func[ϕ]],
     {mode2 + amountmode, mode1 + amountmode} → -i func[g] Exp[-i func[ϕ]]},
    type == 3,
    {{mode1, mode2 + amountmode} → i func[f] Exp[-i func[θ]],
     {mode2 + amountmode, mode1} → -i func[f] Exp[i func[θ]]}
   ]
   , {i, amountpump}];

(* Here is for producing m and s matrix *)
mMtx = Normal[Quiet[SparseArray[
     Join[
      {{i_, j_} /; i == j && i ≤ amountmode →
         (κarray[[i]] / 2 - i (ωnarray[[i]] - ωarray[[i]]))},
      {{i_, j_} /; i == j && i > amountmode → (κarray[[i]] / 2 -
          i (ωarray[[i]] - ωnarray[[i]]))},
      Flatten[res]]
     , {2 * amountmode, 2 * amountmode}]]];


(* This part is for ploting diagram *)
damodes = Table[Symbol[ToString[modes[[i]]] <> ToString[†]], {i, amountmode}];
allmodes = Join[modes, damodes];
allmode = Join[modes, modes];
sub = Table[
   If[Length[mMtx[[i, j]]] == 0, 0, 1]
   , {i, Length[mMtx]}, {j, Length[mMtx]}];
aG1 = AdjacencyGraph[allmodes,
   sub - IdentityMatrix[2 * amountmode], VertexLabels → "Name", ImagePadding → 20];
gP = GraphPlot[Rule @@@ EdgeList[aG1], VertexLabeling → True,
   PlotLabel → Style["Red : Conversion ; Blue : Gain ; Black : Self", 16, Purple, Bold],
   EdgeRenderingFunction →
    (If [Union[Map[MemberQ[modes, #] &, {First[#2], Last[#2]}]][[1]] == True ||
        Union[Map[MemberQ[damodes, #] &, {First[#2], Last[#2]}]][[1]] == True,
       {Red, Line[#1]},
       If[Abs[Position[allmodes, First[#2]][[1, 1]] - Position[allmodes, Last[#2]][[
            1, 1]]] == amountmode, {Black,  Line[#1]}, {Blue,  Line[#1]}]
      ] &
    )];
```

```
(* detine used variables *)
solmodes = Alphabet[][[1 ;; 2 * amountmode]];
detuneδ =
 Join[Table[Symbol[solmodes[[i]] <> ToString[1]], {i, 2 * Length[modes]}]] /. a1 → a + δ;

(* organize the total edges in order *)
checkmodes = {};
totedges = Table[
  If[
   (Position[allmodes, Last[EdgeList[aG1][[i]]]][[1, 1]] -
      Position[allmodes, First[EdgeList[aG1][[i]]]][[1, 1]]) > 0,
   EdgeList[aG1][[i]],
   Last[EdgeList[aG1][[i]]] ↤ First[EdgeList[aG1][[i]]]]
  , {i, Length[EdgeList[aG1]]}];
startmode = allmodes[[1]];
startpoint = Position[allmodes, startmode][[1, 1]];
stmdetun = detuneδ[[1]];
edges = EdgeList[aG1, startmode ↤ _];

  (* using edges to calculate detuning for the end points *)
For[itera = 1, itera ≤ amountpump,
 soldetune = Table[
   endpoint = Position[allmodes, Last[edges[[i]]]][[1, 1]];
   check = If[endpoint ≤ amountmode && startpoint ≤ amountmode || endpoint > amountmode &&
       startpoint > amountmode, 2, If[Abs[endpoint - startpoint] == amountmode, 3, 1]];
   If[check == 1,
    (* this part is for gain coupling *)
    pumpfreq = Symbol[ToString[allmode[[startpoint]]]] + Symbol[
       ToString[allmode[[endpoint]]]] + Symbol[ToString[Δ] <> ToString[g] <> ToString[
         modes[[Mod[startpoint, amountmode + 1]]]] <> ToString[allmode[[endpoint]]]];
    solm = Symbol[ToString[solmodes[[endpoint]]] <> ToString[1]];
    Simplify[Solve[pumpfreq == stmdetun + solm, solm]][[1]],
    If[check == 2,
     (* this part is for conversion coupling *)
     pumpfreq = Symbol[ToString[allmode[[startpoint]]]] - Symbol[
        ToString[allmode[[endpoint]]]] + Symbol[ToString[Δ] <> ToString[c] <> ToString[
          modes[[Mod[startpoint, amountmode + 1]]]] <> ToString[allmode[[endpoint]]]];
     solm = Symbol[ToString[solmodes[[endpoint]]] <> ToString[1]];
     Simplify[Solve[pumpfreq == stmdetun - solm, solm]][[1]],
     (* this part is for self coupling *)
     pumpfreq = Symbol[ToString[allmode[[startpoint]]]] + Symbol[
        ToString[allmode[[endpoint]]]] + Symbol[ToString[Δ] <> ToString[s] <> ToString[
          modes[[Mod[startpoint, amountmode + 1]]]] <> ToString[allmode[[endpoint]]]];
     solm = Symbol[ToString[solmodes[[endpoint]]] <> ToString[1]];
     Simplify[Solve[pumpfreq == stmdetun + solm, solm]][[1]]
    ]]
   , {i, 1, Length[edges]}];
 detuneδ = detuneδ /. soldetune[[All, 1]];
 reversdetuneδ = soldetune[[All, 1]];

 reversemodes = Join[Table[Symbol[modes[[i]] <> ToString[1]], {i, Length[modes]}],
```

```
    Table[Symbol[modes[[i]] <> ToString[1]], {i, Length[modes]}]];
  reversdetuneδ = Flatten[Table[
     reversdetuneδ /. {ωnarray[[i]] → reversemodes[[i]]}
     , {i, Length[detuneδ]}]];



  (* check totedges have no repetition *)
  checkmodes = Union[Flatten[Append[checkmodes,
       Flatten[Table[{edges[[i, 1]], edges[[i, 2]]}, {i, Length[edges]}]]]]];
  totedges = Table[
    If[
     (MemberQ[checkmodes, First[totedges[[i]]]] == True &&
        MemberQ[checkmodes, Last[totedges[[i]]]]) == True,
     Nothing,
     totedges[[i]]
    ]
    , {i, Length[totedges]}];

  (* determine next start mode from the new totdeges *)
  numedges =
   Table[Length[EdgeList[totedges, Last[edges[[i]]] ⟻ _]], {i, Length[edges]}];
  startmode = Last[edges[[Flatten[Position[numedges, Max[numedges]]][[1]]]]];
  startpoint = Position[allmodes, startmode][[1, 1]];
  stmdetun = detuneδ[[startpoint]];
  edges = EdgeList[totedges, startmode ⟻ _];
  itera++,
  If[Length[totedges] == 0 || Length[edges] == 0, Break[]]
 ];


 (* Adding pump detuging into δ *)
 Table[
  mMtx[[i, i]] = mMtx[[i, i]] /. {ωnarray[[i]] → detuneδ[[i]]}
  , {i, Length[detuneδ]}];


 Table[
  mMtx[[i, i]] = mMtx[[i, i]] /. {ωnarray[[i]] → reversemodes[[i]]}
  , {i, Length[detuneδ]}];
 detuneδ = detuneδ /. Flatten[Table[
        {ωnarray[[i]] → reversemodes[[i]]}
        , {i, Length[detuneδ]}]] /. reversdetuneδ /. {a1 → a + δ};
 Table[
  mMtx[[i, i]] = mMtx[[i, i]] /. {reversemodes[[i]] → detuneδ[[i]]}
  , {i, Length[detuneδ]}];
 (* This is the final scattering matrix *)
 sMtx = γMtx.Inverse[mMtx].γMtx - IdentityMatrix[2 * amountmode];
 (* Retuen scattering matrix and the graph. *)
 Return[{sMtx, gP, detuneδ, mMtx}]
]
```

After defining all the functions listed in previous pages, we execute the cell In[4] listed on the next page to start constructing a scattering matrix. A window will pop out and ask for a number of modes and parametric processes, and users need to type in the desired amount, then a table with dropdown lists will show up, see Out[7] as an example on the next page. A column with three dropdown lists is for a parametric process. The first dropdown list defines the type of parametric process with the option of gain, conversion, and self (degenerate gain) process. The second and third droplists are for modes you want to couple with. Once all parametric processes are defined, double click on the gray box to finish up the calculation. All variables used in the scattering matrix are summarized in the Table 16.

Table 16: **Variables for a scattering matrix**

Variable	Description
δ	frequency detuned away from mode's resonance
κ_i	decay rate of i mode
fij	gain strength between i and j mode
θij	gain phase between i and j mode
gij	conversion strength between i and j mode
ϕij	conversion phase between i and j mode
Δfij	gain detuning between i and j mode
Δcij	conversion detuning between i and j mode
Δsij	self detuning between i and j mode

Generate sMtx and graph representation.

In[4]:=
```
ClearAll[amountmode, amountpump, pumps];
(* Define the amount of modes and pumps *)
amountmode = Input["Please input the amount of modes"];
amountpump = Input["Please input the amount of pumps"];
(* Define all pumps *)
pumps = couplings[amountmode, amountpump]
(* Construct scattering matrix and the graph. *)
EventHandler[
 MouseAppearance[Panel["Double click here when you finish"], "Arrow"],
 {
  "MouseClicked" :> If[CurrentValue@"MouseClickCount" == 2,
    Print[Column[{"Scattering : res[[1]]", "Graph : res[[2]]"}]];
    res = gensMtx[amountmode, amountpump, pumps]]
 }
]
```

Out[7]=

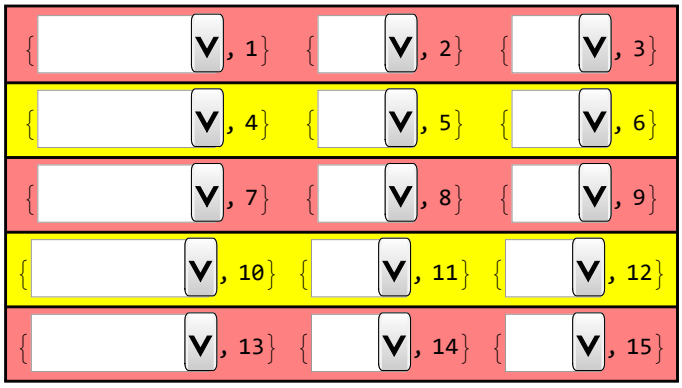

Out[8]=

Double click here when you finish

Bibliography

[1] R. L. Rivest, A. Shamir, and L. Adleman. A method for obtaining digital signatures and public-key cryptosystems. *Commun. ACM*, 21(2):120–126, February 1978.

[2] Peter W. Shor. Polynomial-time algorithms for prime factorization and discrete logarithms on a quantum computer. *SIAM Review*, 41(2):303–332, 1999.

[3] R. P. Feynman. There's plenty of room at the bottom [data storage]. *Journal of Microelectromechanical Systems*, 1(1):60–66, 1992.

[4] Isaac Chuang and Michael Nielsen. Quantum computation and quantum information, 2000.

[5] Lov K. Grover. A fast quantum mechanical algorithm for database search. page 212–219, 1996.

[6] K. Mattle M. Eibl H. Weinfurter A. Zeilinger D. Bouwmeester, J.-W. Pan. Experimental quantum teleportation. *Nature*, 390:575–579, 1997.

[7] W. Pfaff, B. J. Hensen, H. Bernien, S. B. van Dam, M. S. Blok, T. H. Taminiau, M. J. Tiggelman, R. N. Schouten, M. Markham, D. J. Twitchen, and R. Hanson. Unconditional quantum teleportation between distant solid-state quantum bits. *Science*, 345(6196):532–535, 2014.

[8] M. Fuwa P.Loock S. Takeda, T. Mizuta and A. Furusawa. Deterministic quantum teleportation of photonic quantum bits by a hybrid technique. *Nature*, 500:315–318, 2013.

[9] X.L. Wang, X.D. Cai, Z.E. Su, M.C. Chen, D. Wu, L. Li, N.L. Liu, C.Y. Lu, and J.W. Pan. Quantum teleportation of multiple degrees of freedom of a single photon. *Nature*, 518:516–519, 2015.

[10] Kamyar Saeedi, Stephanie Simmons, Jeff Z. Salvail, Phillip Dluhy, Helge Riemann, Nikolai V. Abrosimov, Peter Becker, Hans-Joachim Pohl, John J. L. Morton, and Mike L. W. Thewalt. Room-temperature quantum bit storage exceeding 39 minutes using ionized donors in silicon-28. *Science*, 342(6160):830–833, 2013.

[11] C Monroe. Quantum information processing with atoms and photons. *Nature*, 416:238–246, 2002.

[12] D Kielpinski, C Monroe, and D J Wineland. Architecture for a large-scale ion-trap quantum computer. *Nature*, 417:709–711, 2002.

[13] L Petit, H G J Eenink, M Russ, W I L Lawrie, N W Hendrickx, S G J Philips, J S Clarke, L M K Vandersypen, and M Veldhorst. Universal quantum logic in hot silicon qubits. *Nature*, 580:355–359, 2020.

[14] Alex I. Braginski and John Clarke. The squid handbook: Fundamentals and technology of squids and squid systems, 2004.

[15] Michel H. Devoret, Andreas Wallraff, and John M. Martinis. Superconducting qubits: A short review. 2004.

[16] Morten Kjaergaard, Mollie E. Schwartz, Jochen Braumüller, Philip Krantz, Joel I.-J. Wang, Simon Gustavsson, and William D. Oliver. Superconducting qubits: Current state of play. *Annual Review of Condensed Matter Physics*, 11(1):369–395, 2020.

[17] D. P. DiVincenzo. The physical implementation of quantum computation. *Fortschr. Phys.*, 48:771, 2000.

[18] Michael A. Nielsen and Isaac L. Chuang. *Quantum Computation and Quantum Information*. Cambridge University Press, 2004.

[19] M. D. Reed, B. R. Johnson, A. A. Houck, L. DiCarlo, J. M. Chow, D. I. Schuster, L. Frunzio, and R. J. Schoelkopf. Fast reset and suppressing spontaneous emission of a superconducting qubit. *Appl. Phys. Lett.*, 96(20):203110, 2010.

[20] Vladimir B. Braginsky, Yuri I. Vorontsov, and Kip S. Thorne. Quantum nondemolition measurements. *Science*, 209(4456):547–557, 1980.

[21] M. H. Devoret and R. J. Schoelkopf. Superconducting circuits for quantum information: An outlook. *Science*, 339:1169, 2013.

[22] Carlton M. Caves. Quantum limits on noise in linear amplifiers. *Phys. Rev. D*, 26:1817–1839, Oct 1982.

[23] T. Mimura. The early history of the high electron mobility transistor (hemt). *IEEE Transactions on Microwave Theory and Techniques*, 50(3):780–782, 2002.

[24] R. Vijay, D. H. Slichter, and I. Siddiqi. Observation of quantum jumps in a superconducting artificial atom. *Phys. Rev. Lett.*, 106:110502, Mar 2011.

[25] K W Murch, S J Weber, C Macklin, and I Siddiqi. Observing single quantum trajectories of a superconducting quantum bit. *Nature*, 502:211–214, 2013.

[26] S J Weber, A Chantasri, J Dressel, A N Jordan, K W Murch, and I Siddiqi. Mapping the optimal route between two quantum states. *Nature*, 511:570–573, 2014.

[27] N. Roch, M. E. Schwartz, F. Motzoi, C. Macklin, R. Vijay, A. W. Eddins, A. N. Korotkov, K. B. Whaley, M. Sarovar, and I. Siddiqi. Observation of measurement-induced entanglement and quantum trajectories of remote superconducting qubits. *Phys. Rev. Lett.*, 112:170501, Apr 2014.

[28] P. Campagne-Ibarcq, P. Six, L. Bretheau, A. Sarlette, M. Mirrahimi, P. Rouchon, and B. Huard. Observing quantum state diffusion by heterodyne detection of fluorescence. *Phys. Rev. X*, 6:011002, Jan 2016.

[29] P. Campagne-Ibarcq, E. Flurin, N. Roch, D. Darson, P. Morfin, M. Mirrahimi, M. H. Devoret, F. Mallet, and B. Huard. Persistent control of a superconducting qubit by stroboscopic measurement feedback. *Phys. Rev. X*, 3:021008, May 2013.

[30] G. de Lange, D. Ristè, M. J. Tiggelman, C. Eichler, L. Tornberg, G. Johansson, A. Wallraff, R. N. Schouten, and L. DiCarlo. Reversing quantum trajectories with analog feedback. *Phys. Rev. Lett.*, 112:080501, Feb 2014.

[31] Y. Liu, S. Shankar, N. Ofek, M. Hatridge, A. Narla, K. M. Sliwa, L. Frunzio, R. J. Schoelkopf, and M. H. Devoret. Comparing and combining measurement-based and driven-dissipative entanglement stabilization. *Phys. Rev. X*, 6:011022, Mar 2016.

[32] M. Hatridge, S. Shankar, M. Mirrahimi, F. Schackert, K. Geerlings, T. Brecht, K. M. Sliwa, B. Abdo, L. Frunzio, S. M. Girvin, R. J. Schoelkopf, and M. H. Devoret. Quantum back-action of an individual variable-strength measurement. *Science*, 339:178, 2013.

[33] N. Bergeal, R. Vijay, V. E. Manucharyan, I. Siddiqi, R. J. Schoelkopf, S. M. Girvin, and M. H. Devoret. Analog information processing at the quantum limit with a josephson ring modulator. *Nat. Phys.*, 6(4):296–302, April 2010.

[34] N. Bergeal, F. Schackert, M. Metcalfe, R. Vijay, V. E. Manucharyan, L. Frunzio, D. E. Prober, R. J. Schoelkopf, S. M. Girvin, and M. H. Devoret. Phase-preserving amplification near the quantum limit with a josephson ring modulator. *Nature*, 465(7294):64–68, May 2010.

[35] R. Vijay. *Josephson BifurcationAmplifier: Amplifying quantum signals using a dynamical bifurcation*. PhD thesis, Yale University, 2008.

[36] M. R. Vissers, R. P. Erickson, H.-S. Ku, Leila Vale, Xian Wu, G. C. Hilton, and D. P. Pappas. Low-noise kinetic inductance traveling-wave amplifier using three-wave mixing. *Applied Physics Letters*, 108(1):012601, 2016.

[37] S. Chaudhuri, D. Li, K. D. Irwin, C. Bockstiegel, J. Hubmayr, J. N. Ullom, M. R. Vissers, and J. Gao. Broadband parametric amplifiers based on nonlinear kinetic inductance artificial transmission lines. *Applied Physics Letters*, 110(15):152601, 2017.

[38] J D Teufel, T Donner, Dale Li, J W Harlow, M S Allman, K Cicak, A J Sirois, J D Whittaker, K W Lehnert, and R W Simmonds. Sideband cooling of micromechanical motion to the quantum ground state. *Nature*, 475:031001, 2011.

[39] G. A. Peterson, F. Lecocq, K. Cicak, R. W. Simmonds, J. Aumentado, and J. D. Teufel. Demonstration of efficient nonreciprocity in a microwave optomechanical circuit. *Phys. Rev. X*, 7:031001, Jul 2017.

[40] O. Noroozian, A. R. Kerr, J. G. Mangum, P. K. Day, H. G. Leduc, J. Zmuidzinas, D. P. Woody, A. W. Lichtenberger, M. Cyberey, and R. Weikle. Superconducting parametric amplifiers: The next big thing in (sub)millimeter-wave receivers. pages 1–2, 2018.

[41] C. Macklin, K. O'Brien, D. Hover, M. E. Schwartz, V. Bolkhovsky, X. Zhang, W. D. Oliver, and I. Siddiqi. A near-quantum-limited josephson traveling-wave parametric amplifier. *Science*, 350(6258):307–310, 2015.

[42] T. C. White, J. Y. Mutus, I.-C. Hoi, R. Barends, B. Campbell, Yu Chen, Z. Chen, B. Chiaro, A. Dunsworth, E. Jeffrey, J. Kelly, A. Megrant, C. Neill, P. J. J. O'Malley, P. Roushan, D. Sank, A. Vainsencher, J. Wenner, S. Chaudhuri, J. Gao, and John M.

Martinis. Traveling wave parametric amplifier with josephson junctions using minimal resonator phase matching. *Appl. Phys. Lett.*, 106(24):242601, 2015.

[43] Christopher Eichler and Andreas Wallraff. Controlling the dynamic range of a josephson parametric amplifier. *EPJ Quantum Technology*, 1(1):2, 2014.

[44] B. Yurke. Squeezed-state generation using a josephson parametric amplifier. *J. Opt. Soc. Am. B*, 4(10):1551–1557, Oct 1987.

[45] M. A. Castellanos-Beltran, K. D. Irwin, G. C. Hilton, L. R. Vale, and K. W. Lehnert. Amplification and squeezing of quantum noise with a tunable josephson metamaterial. *Nat. Phys.*, 4(12):929–931, December 2008.

[46] G. Liu, T.-C. Chien, X. Cao, O. Lanes, E. Alpern, D. Pekker, and M. Hatridge. Josephson parametric converter saturation and higher order effects. *Applied Physics Letters*, 111(20):202603, 2017.

[47] Alice C Mahoney, James I Colless, Lucas Peeters, Sebastian J Pauka, Eli J Fox, Xufeng Kou, Lei Pan, Kang L Wang, David Goldhaber-Gordon, and David J Reilly. Zero-field edge plasmons in a magnetic topological insulator. *Nature Communications*, 8:1836, 2017.

[48] A. Metelmann and A. A. Clerk. Quantum-limited amplification via reservoir engineering. *Phys. Rev. Lett.*, 112:133904, Apr 2014.

[49] A. Metelmann and A. A. Clerk. Nonreciprocal photon transmission and amplification via reservoir engineering. *Phys. Rev. X*, 5:021025, Jun 2015.

[50] K. M. Sliwa, M. Hatridge, A. Narla, S. Shankar, L. Frunzio, R. J. Schoelkopf, and M. H. Devoret. Reconfigurable Josephson Circulator/Directional Amplifier. *Phys Rev X*, 5:041020, 2015.

[51] Leonardo Ranzani and José Aumentado. Graph-based analysis of nonreciprocity in coupled-mode systems. *New J of Phys*, 17:023024, 2015.

[52] Baleegh Abdo, Nicholas T Bronn, Oblesh Jinka, Salvatore Olivadese, Antonio D Córcoles, Vivekananda P Adiga, Markus Brink, Russell E Lake, Xian Wu, David P Pappas, and Jerry M Chow. Active protection of a superconducting qubit with an interferometric josephson isolator. *Nature Communications*, 10:3154, 2019.

[53] L. Ranzani and J. Aumentado. Circulators at the quantum limit: Recent realizations of quantum-limited superconducting circulators and related approaches. *IEEE Microwave Magazine*, 20(4):112–122, 2019.

[54] Wen-An Li, Guang-Yao Huang, and Yuan Chen. Directional amplifiers in a hybrid optomechanical system. *J. Opt. Soc. Am. B*, 36(2):306–311, Feb 2019.

[55] Leonardo Ranzani and José Aumentado. A geometric description of nonreciprocity in coupled two-mode systems. *New Journal of Physics*, 16:103027, 2014.

[56] Xiu-Xiu Xia, Qi-Chao Sun, Qiang Zhang, and Jian-Wei Pan. Long distance quantum teleportation. *Quantum Science and Technology*, 3(1):014012, dec 2017.

[57] Ji-Gang Ren, Ping Xu, Hai-Lin Yong, Liang Zhang, Sheng-Kai Liao, Juan Yin, Wei-Yue Liu, Wen-Qi Cai, Meng Yang, Li Li, Kui-Xing Yang, Xuan Han, Yong-Qiang Yao, Ji Li, Hai-Yan Wu, Song Wan, Lei Liu, Ding-Quan Liu, Yao-Wu Kuang, Zhi-Ping He, Peng Shang, Cheng Guo, Ru-Hua Zheng, Kai Tian, Zhen-Cai Zhu, Nai-Le Liu, Chao-Yang Lu, Rong Shu, Yu-Ao Chen, Cheng-Zhi Peng, Jian-Yu Wang, and Jian-Wei Pan. Ground-to-satellite quantum teleportation. *Nature*, 549:70–73, 2017.

[58] Allen Mottershead. *Electronic Devices and circuits*. 2003.

[59] William B. Case. The pumping of a swing from the standing position. *American Journal of Physics*, 64(3):215–220, 1996.

[60] Baleegh Abdo, Flavius Schackert, Michael Hatridge, Chad Rigetti, and Michel Devoret. Josephson amplifier for qubit readout. *Appl. Phys. Lett.*, 99(16):162506, 2011.

[61] Byeong Ho Eom, Peter K Day, Henry G LeDuc, and Jonas Zmuidzinas. A wideband, low-noise superconducting amplifier with high dynamic range. *Nature Physics*, 8:623–627, 2012.

[62] P. T. Parrish and R. Y. Chiao. Amplification of microwaves by superconducting microbridges in a four-wave parametric mode. *Applied Physics Letters*, 25(10):627–629, 1974.

[63] M. Hatridge, R. Vijay, D. H. Slichter, John Clarke, and I. Siddiqi. Dispersive magnetometry with a quantum limited squid parametric amplifier. *Phys. Rev. B*, 83:134501, Apr 2011.

[64] F. Lecocq, L. Ranzana, G. A. Peterson, K. Cicak, R. W. Simmonds, J. D. Teufel, and J. Aumentado. Nonreciprocal microwave signal processing with a field-programmable josephson amplifier. *Phys. Rev. Appl.*, 7:024028, 2017.

[65] V.V. Sivak, N.E. Frattini, V.R. Joshi, A. Lingenfelter, S. Shankar, and M.H. Devoret. Kerr-free three-wave mixing in superconducting quantum circuits. *Phys. Rev. Applied*, 11:054060, 2019.

[66] E SCHRÖDINGER. Are there quantum jumps ?: Part ii. *The British Journal for the Philosophy of Science*, 3:233–242, 1952.

[67] Carlton M. Caves, Joshua Combes, Zhang Jiang, and Shashank Pandey. Quantum limits on phase-preserving linear amplifiers. *Phys. Rev. A*, 86:063802, Dec 2012.

[68] A. A. Clerk, M. H. Devoret, S. M. Girvin, Florian Marquardt, and R. J. Schoelkopf. Introduction to quantum noise, measurement, and amplification. *Rev. Mod. Phys.*, 82:1155–1208, Apr 2010.

[69] Nadeem A. Ansari. Theory of a two-mode phase-sensitive amplifier. *Phys. Rev. A*, 46:1560–1564, Aug 1992.

[70] E. Flurin, N. Roch, F. Mallet, M. H. Devoret, and B. Huard. Generating entangled microwave radiation over two transmission lines. *Phys. Rev. Lett.*, 109:183901, Oct 2012.

[71] Matti Silveri, Evan Zalys-Geller, Michael Hatridge, Zaki Leghtas, Michel H. Devoret, and S. M. Girvin. Theory of remote entanglement via quantum-limited phase-preserving amplification. *Phys. Rev. A*, 93:062310, Jun 2016.

[72] A. Roy and M. H. Devoret. Introduction to parametric amplification of quantum signals with josephson circuits. *Comptes Rendus Physique*, 17(7):740–755, 2106.

[73] F. D. Bennett. Optimum source size for the mach-zehnder interferometer. *Journal of Applied Physics*, 22(2):184–190, 1951.

[74] Yang Ji, Yunchul Chung, D Sprinzak, M Heiblum, D Mahalu, and Hadas Shtrikman. An electronic mach–zehnder interferometer. *Nature*, 422:415–418, 2003.

[75] T.-C. Chien, O. Lanes, C. Liu, X. Cao, P. Lu, S. Motz, G. Liu, D. Pekker, and M. Hatridge. Multiparametric amplification and qubit measurement with a kerr-free josephson ring modulator. *Phys. Rev. A*, 101:042336, Apr 2020.

[76] K. Sliwa. *Improving the Quality of Heisenberg Back-Action of Qubit Measurements made with Parametric Amplifiers*. PhD thesis, Yale University, 2016.

[77] Alexandre Blais, Steven M Girvin, and William D Oliver. Quantum information processing and quantum optics with circuit quantum electrodynamics. *IEEE Microwave Magazine*, 16:247–256, 2020.

[78] John M Martinis, Michel H Devoret, and John Clarke. Quantum josephson junction circuits and the dawn of artificial atoms. *Nature Physics*, 16:234–237, 2020.

[79] Alexandre Blais, Ren-Shou Huang, Andreas Wallraff, S. M. Girvin, and R. J. Schoelkopf. Cavity quantum electrodynamics for superconducting electrical circuits: An architecture for quantum computation. *Phys. Rev. A*, 69:062320, Jun 2004.

[80] S Haroche, M Brune, and J M Raimond. From cavity to circuit quantum electrodynamics. *Nature Physics*, 16:343–346, Jun 2020.

[81] N. Roch, E. Flurin, F. Nguyen, P. Morfin, P. Campagne-Ibarcq, M. H. Devoret, and B. Huard. Widely tunable, nondegenerate three-wave mixing microwave device operating near the quantum limit. *Phys. Rev. Lett.*, 108:147701, Apr 2012.

[82] Flavius Dietrich Octavian Schackert. *A Practical Quantum-Limited Parametric Amplifier Based on the Josephson Ring Modulator*. PhD thesis, Yale University, 2013.

[83] Uri Vool and Michel Devoret. Introduction to quantum electromagnetic circuits. *International Journal of Circuit Theory and Applications*, 45(7):897–934, 2017.

[84] Baleegh Abdo, Archana Kamal, and Michel Devoret. Nondegenerate three-wave mixing with the josephson ring modulator. *Phys. Rev. B*, 87:014508, Jan 2013.

[85] R Barends et al. Superconducting quantum circuits at the surface code threshold for fault tolerance. *Nature*, 508:500, 2014.

[86] T. Walter, P. Kurpiers, S. Gasparinetti, P. Magnard, A. Potocnik, Y. Salathe, M. Pecha, M. Mondal, M. Oppliger, C. Eichler, and A. Wallraff. Rapid high-fidelity single-shot dispersive readout of superconducting qubits. *Phys Lett A*, 2017.

[87] A. B. Zorin. Josephson traveling-wave parametric amplifier with three-wave mixing. *Phys. Rev. Applied*, 16:034006, 2016.

[88] M. Castellanos-Beltran and K. Lehnert. Widely tunable parametric amplifier based on a superconducting quantum interference device array resonator. *Appl. Phys. Lett.*, 91:083509, 2007.

[89] N. E. Frattini, U. Vool, S. Shankar, A. Narla, K. M. Sliwa, and M. H. Devoret. 3-wave mixing josephson dipole element. *Appl. Phys. Lett.*, 110:222603, 2017.

[90] N. Roch, E. Flurin, F. Nguyen, P. Morfin, P. Campagne-Ibarcq, M. H. Devoret, and B. Huard. Widely tunable, nondegenerate three-wave mixing microwave device operating near the quantum limit. *Phys. Rev. Lett.*, 108:147701, Apr 2012.

[91] N. E. Frattini, V. V. Sivak, A. Lingenfelter, S. Shankar, and M. H. Devoret. Optimizing the nonlinearity and dissipation of a snail parametric amplifier for dynamic range. *Phys Rev Applied*, 10:054020, Nov 2018.

[92] G. Liu, T.-C. Chien, X. Cao, O. Lanes, E. Alpern, D. Pekker, and M. Hatridge. Josephson parametric converter saturation and higher order effects. *Appl. Phys. Lett.*, 111:202603, 2017.

[93] E. Flurin. *The Josephson Mixer, a Swiss army knife for microwave quantum optics.* PhD thesis, 2015.

[94] C. Liu, T.-C. Chien, M. Hatridge, and D. Pekker. Optimizing josephson-ring-modulator-based josephson parametric amplifiers via full hamiltonian control. *Phys. Rev. A*, 101:042323, 2020.

[95] J. Y. Mutus, T. C. White, R. Barends, Yu Chen, Z. Chen, B. Chiaro, A. Dunsworth, E. Jeffrey, J. Kelly, A. Megrant, C. Neill, P. J. J. O'Malley, P. Roushan, D. Sank, A. Vainsencher, J. Wenner, K. M. Sundqvist, A. N. Cleland, and John M. Martinis. Strong environmental coupling in a josephson parametric amplifier. *Appl. Phys. Lett.*, 104:263513, 2014.

[96] T. Roy, S. Kundu, M. chand, A. M. Vadiraj, A. Ranadive, N. Nehra, M. P. Patankar, J. Aumentado, A. A. Clerk, and R. Vijay. Broadband parametric amplificiation with impedance engineering: Beyond the gain-bandwidth product. *Appl. Phys. Lett.*, 107:262601, 2017.

[97] Bogdan A. Kochetov and Arkady Fedorov. Higher-order nonlinear effects in a josephson parametric amplifier. *Phys. Rev. B*, 92:224304, Dec 2015.

[98] Archana Kamal, Adam Marblestone, and Michel Devoret. Signal-to-pump back action and self-oscillation in double-pump josephson parametric amplifier. *Phys. Rev. B*, 79:184301, May 2009.

[99] Ananda Roy and Michel Devoret. Quantum-limited parametric amplification with josephson circuits in the regime of pump depletion. *Phys. Rev. B*, 98:045405, Jul 2018.

[100] Bogdan A. Kochetov and Arkady Fedorov. Higher-order nonlinear effects in a josephson parametric amplifier. *Phys. Rev. B*, 92:224304, Dec 2015.

[101] Saeed Khan, A. Metelmann, and Hakan Türeci. Quantum nonlinear dynamics of nondegenerate parametric amplification beyond the stiff-pump approximation. In *APS March Meeting Abstracts*, Jan 2019.

[102] Tanay Roy, Madhavi Chand, Anirban Bhattacharjee, Sumeru Hazra, Suman Kundu, Kedar Damle, and R. Vijay. Multimode superconducting circuits for realizing strongly coupled multiqubit processor units. *Phys. Rev. A*, 98:052318, Nov 2018.

[103] Clemens Müller, Shengwei Guan, Nicolas Vogt, Jared H. Cole, and Thomas M. Stace. Passive on-chip superconducting circulator using a ring of tunnel junctions. *Phys. Rev. Lett.*, 120:213602, May 2018.

[104] Jens Koch, Andrew A. Houck, Karyn Le Hur, and S. M. Girvin. Time-reversal-symmetry breaking in circuit-qed-based photon lattices. *Phys. Rev. A*, 82:043811, Oct 2010.

[105] J. Niemeyer and V. Kose. Observation of large dc supercurrents at nonzero voltages in josephson tunnel junctions. *Applied Physics Letters*, 29(6):380–382, 1976.

[106] G. J. Dolan. Offset masks for lift-off photoprocessing. *Applied Physics Letters*, 31(5):337–339, 1977.

[107] Ki Hyun Kim, Zentaro Akase, Toshiaki Suzuki, and Daisuke Shindo. Charging effects on sem/sim contrast of metal/insulator system in various metallic coating conditions. *MATERIALS TRANSACTIONS*, 51(6):1080–1083, 2010.